STUDIES ON HEXAFERRITE BASED NANOCOMPOSITES FOR RADAR/MICROWAVE ABSORPTION APPLICATIONS

A THESIS

Submitted in partial fulfilment of the
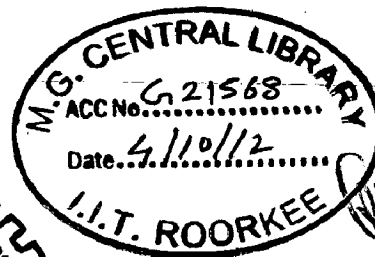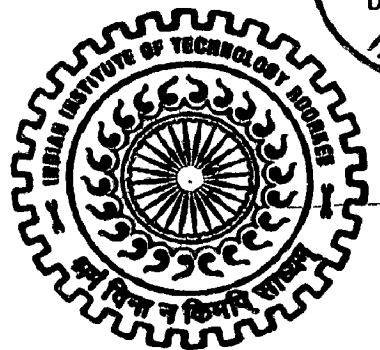*requirements for the award of the degree*

of

DOCTOR OF PHILOSOPHY
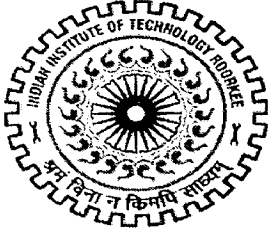
in

METALLURGICAL AND MATERIALS ENGINEERING

by

SACHIN TYAGI

DEPARTMENT OF METALLURGICAL AND MATERIALS ENGINEERING
INDIAN INSTITUTE OF TECHNOLOGY ROORKEE
ROORKEE-247 667 (INDIA)
DECEMBER, 2011

INDIAN INSTITUTE OF TECHNOLOGY ROORKEE
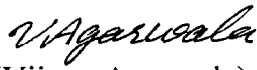## ROORKEE
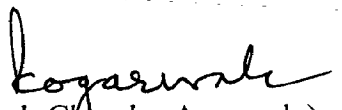
CANDIDATE'S DECLARATION

I hereby certify that the work which is being presented in the thesis entitled, **"STUDIES ON HEXAFERRITE BASED NANOCOMPOSITES FOR RADAR/MICROWAVE ABSORPTION APPLICATIONS"** in partial fulfilment of the requirements for the award of the degree of Doctor of Philosophy and submitted in the Department of Metallurgical and Materials Engineering of the Indian Institute of Technology Roorkee, Roorkee is an authentic record of my own work carried out during the period from July 2007 to December 2011 under the supervision of Prof. Ramesh Chandra Agarwala and Prof. (Mrs.) Vijaya Agarwala, Department of Metallurgical and Materials Engineering, Indian Institute of Technology Roorkee, Roorkee.

The matter presented in this thesis has not been submitted by me for the award of any other degree of this or any other institute.

(SACHIN TYAGI)

This is to certify that the above statement made by the candidate is correct to the best of our knowledge.

(Vijaya Agarwala)
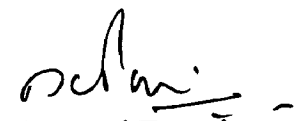Supervisor

(Ramesh Chandra Agarwala)
Supervisor

Date:

The PhD Viva-Voce Examination of **Mr. Sachin Tyagi**, Research Scholar has been held on...30...3..2.0.1.2

Supervisor

Chairman SRC

External Examiner

Head of the Department & Chairman ODC

Radar is a sensitive detection tool and since its development, methods for reducing microwave reflections have been explored. In defense, the primary objective is to detect enemies' equipment/arms as early as possible in order to employ weapons effectively. In current, radar cross section (RCS) designs, shaping techniques are considered to be the first step of RCS control. The objective of shaping is to design the platform's surfaces and the edges to reflect or diffract the incident wave in directions away from the radar, and is primarily applied to establish a low RCS in the main threat sectors. However, the modification of an aircraft's shape is limited to certain aerodynamic principles and within last three decades, the shaping techniques have been applied excessively in the design of fighter aircrafts. Recent design approaches generally opt for a balance between shaping and other reduction techniques. Therefore, radar absorbing material (RAM) engineering has become an important area of research. Radar absorbing materials reduce the energy reflected back to the radar by means of absorption.

Thus radar absorbing materials have become the essential part of defense system for their contribution to survivability of air vehicle. Like defense, these materials are equally important in industries for use as a commercial product for the electromagnetic interference (EMI) shielding. EMI is a specific type of environmental pollution which is caused by the extensive use of electromagnetic (EM) waves in wireless communications such as EM waves of 0.8–1.2 GHz are used for mobile phones, 2.45 GHz for electronic ranges, 5.6–8.2 GHz (G-band) for synthetic aperture radar (SAR) or microwave communication on the ground, 8.2–12.4 GHz (X-band) and 12.4–18 (Ku-band) for SAR or electron spin resonance (ESR) apparatus. The emergence of nanoscience and nanotechnology opened the door for newer opportunities to further involve the functionality of electromagnetic absorber. The use of magnetic , non magnetic and composite of magnetic/non magnetic materials in polymer resin matrix system has become a subject of interest in engineering applications due to potential changes in physical, chemical, magnetic and dielectric properties of nanocomposite. These changes in the properties come from unique morphology, increased surface area, exchange interaction existing between hard and soft magnetic phases and quantum size effect associated with nano size particles.

ACKNOWLEDGMENTS

At this momentous occasion of binding my thesis I would like to acknowledge the contribution of all those benevolent people, I have been blessed to associate with. All the data collection, theories, models would have failed to serve their purpose for me if blessing of God would not have joined hands with my efforts.

My first and foremost offering of thanks goes to the architects who shaped my dreams into the reality, my guides and mentors **Dr. Ramesh Chandra Agarwala** and **Dr. Vijaya Agarwala,** Professors, Department of Metallurgical and Materials Engineering, IIT Roorkee. Perseverance, exuberance, positive approaches are just some of the traits they have imprinted on my personality. They steered me through this journey with their invaluable advice, positive criticism, stimulating discussions and consistent encouragement. Their meticulous attention toward my proceedings, their devoted time and their ideas has enabled me to make the project a success. Their faith in me has always made me more confident. Their blessings always made me optimistic. If I will stand proud of my achievement then undeniably they are the main creditors. It had been my privilege to be under their tutelage.

Deep sense of gratitude is acknowledged to **Dr. P. K. Ghosh**, Professor and Head of the Department of Metallurgical and Materials Engineering, IIT Roorkee, for his help and providing excellent facilities in the department for research work.

The author would like to express his acknowledgment to Ministry of Human Resource and Development, IIT Roorkee for providing the fellowship during this period.

Profound sense of appreciation is acknowledge to all the members of Departmental Research Committee (DRC) and Student Research Committee (SRC), **Dr. Vijaya Agarwala,** Chairman, DRC, **Dr. B. S. S. Daniel**, Chairman, SRC, **Dr. K. L. Yadav**, External Member, **Dr. R. Jayaganthan**, Internal Member for their precious assessment throughout.

The author would like to express his sincere thanks to technical and administrative staff of Department of Metallurgical and Materials Engineering, Mr. T. K. Sharma, Mr. Rajendra Sharma, Mr. R. K. Sharma, Mr. Shakti Gupta, Mr. S. M. Giri, Mr. Ramvir Singh, Mrs. Suman, Mr. Kuldeep Sharma, Mr. Ashish, Mr Narendra Kumar and Mr. Sanjay who helped in all possible ways during the Ph.D work.

Deep sense of admiration is acknowledge to the Head, Institute Instrumentation Centre (IIC) for their co-operation in extending the necessary facilities and supports during

CONTENTS

LIST OF FIGURES

NOMENCLATURE

α_d	Attenuation Constant
α	Transformed Fraction
B	Magnetic Field Density in (Wb/m^2)
β	Heating Rate
CC	Chemical Co-Precipitation
CNT	Carbon Nano Tubes
C	Velocity of Electromagnetic Wave
CNF	Carbon Nano Fiber
CVD	Chemical Vapour Deposition
D	Electric Flux Density (C/m^2)
dB	Decibels
d	Thickness of Coating
DSC	Differential Scanning Calorimetry
DTG	Differential Thermo Gravimetry
E	Electric Field Intensity (V/m)
δ	Skin Depth
E	Activation Energy
ED	Electron Diffraction
EL	Electroless
EM	Electromagnetic
EMI	Electromagnetic Interference
EP	Epoxy
ESR	Electron Spin Resonance
ε_r	Relative Complex Permitivity
ε'	Real Part of Complex permitivity
ε''	Imaginary Part of Complex permitivity
f_r	Resonance Frequency
FSS	Frequency Selective Surfaces
FESEM	Field Emission Scanning Electron Microscopy

G-N	Gel-Nanocrystalline
GHz	Giga-Hertz
HARP	Halpren Anti-Radar Paint
H	Magnetic Field Intensity (A/m)
H_c	Coercivity
HT	Heat Treatment
J	Electric Flux Density (A/m^2)
JCPDS	Joint Committee for Powder Diffraction Data Society
LCS	Low Combustion Synthesis
MA	Mechanical Alloying
MFM	Modified Flux Method
M_s	Saturation Magnetization
μ_o	Absolute Permeability
μm	Micrometer
μ_r	Relative Complex Permeability
μ'	Real Part of Complex Permeability
μ''	Imaginary Part of Complex Permeability
λ	Wavelength
λg	Guide Wave Length
n	Avrami Index Parameter
nm	Nano Meter
P	Electric Charge Density
R	Gas Constant (8.314 J/mol/K)
RAM	Radar Absorbing Material
RCS	Radar Cross Section
RAS	Radar Absorbing Structure
RL	Reflection Loss
rpm	Revolution Per Minute
SAR	Synthetic Aperture Radar
SE	Shielding Effectivness
SWNTs	Single Wall Carbon Nano Tubes
S-G	Sol-Gel

σ	Conductivity of Material
ρ	Electric Charge Density (C/m^3)
t	Time of Transformation
T	Absolute Temperature
T_m	Temperature of Reaction
TEM	Transmission Electron Microscopy
Tan $\lvert \delta_m \rvert$	Magnetic Loss Tangent
Tan $\lvert \delta_d \rvert$	Dielectric Loss Tangent
Tan $\lvert \delta_h \rvert$	The Hysteresis Loss Tangent
Tan $\lvert \delta_e \rvert$	Eddy Current Loss Tangent
Tan $\lvert \delta_r \rvert$	Residual Loss Tangent
TG	Thermo Gravimetry
Θ	Bragg's Angle
VSM	Vibrating Sample Magnetometer
VNA	Vector Network Analyzer
W_h	Hysteresis Energy Loss
w	Angular Frequency of Applied Field
XRD	X-Ray Diffractometer
γ	Gyromagnetic Ratio
Z	Wave Impedence
Z_o	Impedance of Air

LIST OF PUBLICATIONS

PUBLICATIONS IN JOURNALS

1. **Sachin Tyagi**, Himanshu B. Baskey, R. C. Agarwala, Vijaya Agarwala and T. C. Shami, "Synthesis and characterization of $SrFe_{11.2}Zn_{0.8}O_{19}$ nanoparticles for enhanced microwave absorption ", *Journal of Electronics Materials,* doi: 10.1007/s11664-011-1693-y (2011).

2. **Sachin Tyagi**, Himanshu B. Baskey, R. C. Agarwala, Vijaya Agarwala and T. C. Shami, "Reaction Kinetic, Magnetic and Microwave Absorption Studies of $SrFe_{12}O_{19}/CoFe_2O_4$ Ferrite Nanocrystals", *Transaction of Indian Institute of Metals (springer publication),* Vol. 64, Issue 3, pp 271-277 (2011).

3. **Sachin Tyagi**, Himanshu B. Baskey, R. C. Agarwala, Vijaya Agarwala and T. C. Shami, "Development of hard/soft ferrite nanocomposite for enhanced microwave absorption ", *Ceramics International,* Vol 37, pp 2631-2641 (2011).

4. **Sachin Tyagi**, Himanshu B. Baskey, R. C. Agarwala, Vijaya Agarwala and T. C. Shami, "Microwave Absorption Studies of $SrFe_{12}O_{19}/ZnFe_2O_4$ Ferrite Nanocrystals", *Transaction of Indian Institute of Metals,* doi:10.1007/s12666-011-0068-7 (2011).

5. **Sachin Tyagi**, R. C. Agarwala and Vijaya Agarwala, " Reaction Kinetics magnetic and microwave absorption study of $SrFe_{11.2}Ni_{0.8}O_{19}$ hexaferrite nanoparticles", *Journal of Materials Science: Materials in Electronics,* Vol 22, pp 1085-1094 (2011).

6. **Sachin Tyagi**, R. C. Agarwala and Vijaya Agarwala, " Reaction Kinetics Study of Strontium Hexaferrite Nanoparticles Synthesized by Co-Precipitation Method" , *Transaction of Indian Institute of Metals (springer publication),* Vol 63, pp 15-19 (2010).

7. **Sachin Tyagi**, R. C. Agarwala and Vijaya Agarwala, " Reaction Kinetics Study of Barium Hexaferrite Nanoparticles Synthesized by Co-Precipitation Method" , *International Journal of Material Science,* Vol 4, pp 125-134 (2009).

8. **Sachin Tyagi**, R. C. Agarwala and Vijaya Agarwala " A Comparative Study on the Morphology and Magnetic Properties of Barium and Strontium Hexaferrite Nanoparticles Synthesized by Co-precipitation Method" , *Advance Materials Research,* Vol 67, pp 203-208 (2009).

9. **Sachin Tyagi,** R. C. Agarwala and Vijaya Agarwala " Microwave Absorption and Magnetic Studies of Strontium Hexaferrite Nanoparticles Synthesized by Modified Flux Method" , *Journal of Nano Research* Vol 10, pp 19-27 (2009).

10. **Sachin Tyagi,** Himanshu B. Baskey, R. C. Agarwala, Vijaya Agarwala and T. C. Shami, "Microwave absorption study of carbon nano tubes dispersed hard/soft ferrite nanocomposite", *Ceramics International* (**Under Review**)

11. **Sachin Tyagi,** Himanshu B. Baskey, R. C. Agarwala, Vijaya Agarwala and T. C. Shami, "Microwave absorption study of carbon black nanoparticles dispersed hard/soft ferrite nanocomposite", *Solid State Communication* (**Under Review**).

12. **Sachin Tyagi,** Himanshu B. Baskey, R. C. Agarwala, Vijaya Agarwala and T. C. Shami, "Microwave absorption study of silicon carbide nanoparticles nanoparticles dispersed hard/soft ferrite nanocomposite", *Solid State Communication* (**Under Review**).

PUBLICATIONS IN CONFERENCES

1. **Sachin Tyagi** and Kulvir Singh, " Development and In-Vitro Characterization of Melt Quenched Derived Silica Based Bioglasses" in the proceedings of International conference on *"Processing and Fabrication of Advanced Materials-XVII"*, Vol 2, p 830, (2008).

2. **Sachin Tyagi,** R. C. Agarwala and Vijaya Agarwala " Morphological Evaluation and Magnetic Properties of Ba-M Hexaferrites" *International conference on NMD-ATM 2008* (Oral Presentation).

3. **Sachin Tyagi,** R. C. Agarwala and Vijaya Agarwala " Morphological Evaluation and Magnetic Studies of Strontium Hexaferrite Nanoparticles Synthesized by Co-Precipitation Method" in *National Seminar on Special Purpose, Strategic and Futuristic Materials for High Technology Sectors*, Organised by Indian Institute of Metals, Trivandrum Chapter, 2008 (**Awarded 2nd Prize in Oral Presentation**)

4. **Sachin Tyagi,** R. C. Agarwala and Vijaya Agarwala "Reaction Kinetic and Magnetic Studies of RADAR Absorbing $SrFe_{11.2}Ni_{0.8}O_{19}$ Hexaferrite Nanoparticles" as a poster at *Seetharaman-Seminar on 'Materials processing towards properties'* at Sweden during 14-15 June 2010.

5. **Sachin Tyagi,** R. C. Agarwala and Vijaya Agarwala "Reaction Kinetic and Magnetic Studies of RADAR Absorbing $SrFe_{11.2}Ni_{0.8}O_{19}$ Hexaferrite Nanoparticles" at IIM (Delhi Chapter) on 31 July 2010.

6. Vijaya Agarwala R. C. Agarwala and **Sachin Tyagi** "Nano Grained Materials Produced by Co-Precipitation and Gas Reduction Methods for Electronic Applications '*at Seetharaman-Seminar on Materials processing towards properties'* at Sweden during 14-15 June 2010.

7. **Sachin Tyagi,** R. C. Agarwala and Vijaya Agarwala "Development of $SrFe_{12}O_{19}/ZnFe_2O_4$ Nanocrystalline Nanocomposite for Enhanced Microwave Absorption" *at ICMAT 2011, Singapore* (Accepted for oral presentation).

8. **Sachin Tyagi,** R. C. Agarwala and Vijaya Agarwala "Development of Microwave Absorptive $SrFe_{12}O_{19}/NiFe_2O_4$ Ferrite Nanocomposite" *at ICMAT 2011, Singapore* (Accepted for oral presentation)

In recent times development of microwave absorbing material has regained considerable importance as these play key role in stealth technology where these materials are used in the form of paint coated on the surface of the object to reduce radar cross section (RCS) effectively. Apart from radar cross section reduction, microwave absorber find applications in other fields as well, such as in electronic applications for antenna's side lobe reduction, construction of anechoic chamber, preservation of electromagnetic interference, as protective sheets in microwave oven, removal of ghost images in TV pictures, noise suppression in cellular phones etc (Meshram, 2002; 2004). Radar absorbing materials reduce the energy reflected back to the radar by means of absorption. The technique is based on an arrangement of dielectric or magnetic materials that present the appropriate impedance to the incident wave. The general idea is to establish impedance at the RAM surface that posses good matching and absorbing qualities, so that it can attenuate the radar wave once it enters the material. The use of radar absorbing material is one aspect of a comprehensive platform design approach. It is a trade-off in which advantages are balanced against disadvantages, and the systems engineering approach is applied. The use of radar absorbing materials enables remarkable reduction in the platform's radar cross section. On the other hand, it has disadvantages like added weight, cost, and the requirement of high maintenance (Meshram, 2002; 2004).

The absorption and the interference shielding of electromagnetic wave have become very important issue for defense applications. The two most often employed radar cross section reduction (RCSR) techniques are shaping and use of radar absorbing materials. In current radar cross section (RCS) designs, shaping techniques are considered the first step of RCS control. Altering the shape of the airframe can reduced the RCS considerably. There are two approaches that may be adopted, a highly angular faceted shape whereby the radar signals are reflected away from the source, an example of this is the F117A Stealth Fighter; alternatively a smooth rounded shape whereby little of the surface will be perpendicular to the signal source and so will be reflected away, an examples of this are the B2 bomber and the A12 Fighter (Pitkethly, 1992). The drawback to these approaches is

that, aerodynamically the performance and agility of the aircraft is reduced. Recent design approaches generally opt for a balance between shaping and other reduction techniques. Therefore, radar absorbing material (RAM) engineering has become an important area of research. Radar absorbing materials reduce the energy reflected back to the radar by means of absorption (Pitkethly, 1992).

The RCS reduction technique using RAM engineering is based on matching of dielectric or magnetic parameters that present the appropriate impedance to the incident wave. The absorbing material must satisfy two important properties with the purpose of attenuating the strength of EM wave. First is matched characteristic impedance, in which intrinsic impedance of material is made equal to impedance of free space. This makes the dielectric loss tangent and magnetic loss tangent equal to each other and leads to zero reflection. Second, incident electromagnetic wave must enter and get attenuate rapidly through the material layer, thus reducing the emergent wave to an acceptable low magnitude (Wang, 2011).

There are several types of materials used for microwave absorber including dielectric and magnetic materials. As far as thickness and working frequency bandwidth is concerned, magnetic composite have obvious advantage over non magnetic materials (Ghasemi, 2008). Magnetic loss depends on imaginary part of the permeability. The higher the values of imaginary part of complex permeability, more is the loss (Ghasemi, 2008). The magnetic fillers often used in such composites are ferrite materials, such as spinel ferrites and hexaferrites (Kwon, 1994; Ghasemi, 2008). As compared to the spinel ferrite, the hexaferrites with large planar magnetic anisotropy are of great interest for use as electromagnetic energy dissipation in GHz range. Hexaferrites are classified into four classes, depending on chemical composition and crystalline structure. These include hexaferrites of M, W, Y and Z type, which correspond to (SrO + MeO): Fe_2O_3 ratios of 1:6, 3:8, 4:6 and 5:12 respectively. The class of hexagonal ferrite with formula $MFe_{12}O_{19}$, where M is usually barium, strontium, calcium or lead is widely studied as microwave absorbing material (Sharma, 2007; 2008; Ghasemi, 2008; Fu, 2005). The crystal structure of M type hexagonal ferrite is complex but it can be describes as hexagonal with unique c axis, which is the easy axis of magnetization in the basic structure. Hexagonal ferrites are referred to as hard as the direction of magnetization can not be changed easily to another axis. Initially theses materials were studied for their use as permanent magnet or as magnetically soft core at frequencies in UHF region. Later on it was realized that due to their large "built in" biasing field, these material have good prospect

2

for application at microwave frequencies. Though $BaFe_{12}O_{19}$ referred to by its commercial trade name Ferroxdure and Inbox V has been studied as a traditional microwave absorbing material. Recently $SrFe_{12}O_{19}$ has received wide attention and it has been claimed that strontium ferrite based electromagnetic attenuation material are superior to barium based electromagnetic attenuation material. In the literature, the strontium hexaferrite is observed to have higher magnetic parameter like saturation magnetization, coercivity, magnetic anisotropy, curie temperature with low density than barium hexaferrite (Shirk, 1969). The large magnetic loss with low density increased the use of strontium hexaferrite over barium hexaferrite as a stealth material (Shirk, 1969).

Recently, demand for various EM wave absorbers has increased; single material cannot meet these demands such as large absorption peak, wide working frequency range and thin absorption layer. In order to improve electromagnetic absorption properties of magnetic materials, new systems have been evolved comprising of composite powder including hard and soft magnetic materials (Chen, 2007; Masala, 2006). It is reported that (Masala, 2006) exchange interaction existing between hard and soft magnetic phases improves the microwave absorption properties of composite. Spinel ferrite like $CoFe_2O_4$, $ZnFe_2O_4$ and $NiFe_2O_4$ having cubic spinel structure is a kind of soft magnetic material and has widely studied as EM wave absorbing material at relatively low frequencies (Sunny, 2010; Giannakopoulou, 2002; Peng 2005). The synthesis of magnetic composite containing hard and soft ferrite could be a good attempt to develop a magnetic RAM composite.

Electromagnetic response of the substance is the result of complex mutual interaction between electron system of material and EM wave. The EM wave absorption characteristic of composite depends on its material properties particularly its electric properties (complex permitivity) and magnetic properties (complex permeability). Dielectric composite absorber depend on the ohmic loss and polarization loss of energy which can be achieved by adding losing filler like carbon, graphite, silicon carbide or metal particle/powder to a matrix. Magnetic particle absorbers are dependent on the type of magnetic hysteresis loss which is obtained when magnetic particles such as hard ferrite, soft ferrite or composite of hard and soft ferrite is added to the matrix. Thus composite having perfect match of dielectric and magnetic loss tangent to give large absorption can be fabricated by using the magnetic and non magnetic fillers.

The emergence of nanoscience and nanotechnology opened the door for new opportunities to further improve the functionality of EM absorbers (Sharma, 2007; 2008). However, the challenge

3

of incorporating nanoparticles into a coating matrix is to overcome the difficulty of dispersing larger volume fractions of nanoparticles into the suitable matrix without sacrificing the mechanical properties of the resulting composite. The use of nanoparticles in matrix system has become a subject of interest in engineering applications due to potential changes in physical properties of nanocomposites. These changes in properties come from two aspects of nanoparticles: increased surface area and quantum effects associated with the structure of nano-dimensional particles. These factors can change or enhance properties such as reactivity, strength, magnetic and dielectric properties etc. of nanocomposites. Out of various composites/nanocomposites coating technologies, electroless, EL coating technology is one of the best that withstands with recent development in the nanosciene and nanotechnology to provide coatings for various applications. EL (Electro+ Less i.e. without using electrical energy) nickel-phosphorus deposits are produced by the autocatalytic electrochemical reduction of nickel ion onto the substrate from the solution of coating bath (Agarwala, 2006). An extensive literature exists, dealing with the virtues of EL Ni-P for microwave absoption applications.

The properties of hexaferrite ferrite are largely dependent on processing routes used for fabrication (Cullity, 2008). Traditionally, hexaferrite are synthesized by mixed oxide ceramic method, which involve the solid state reaction between $SrCO_3$ and Fe_2O_3 at high calcinations temperature (~1300°C) (Cullity, 2008). However this technique has disadvantages like large particle size; agglomerates and non uniformity in particle size distribution. Also, the subsequent millings of the calcined ferrite powder undoubtedly introduced a high level of contamination and, therefore, degrade the magnetic, dielectric and microwave absorption properties of ferrite. Thus the preparation of strontium hexaferrite and composite of hexaferrite and spinel ferrite with refined particle size, narrow particle size distribution and minimal particle agglomeration is a challenging task. In order to improve material properties, numerous non conventional soft synthetic routes have been devised, including hydrothermal synthesis (Primc, 2009), sonochemical synthesis (Shafi, 1999), modified flux method (Sharma, 2008), low combustion synthesis (Hasab, 2007; 2007), microwave induced combustion synthesis (Fu, 2005), oxalate precursor method (Mohsen, 2010) etc.

The present investigation has been focused on the development of nanocomposite containing magnetic phase and composite of both magnetic and non magnetic phases in the polymer matrix (epoxy resin). The magnetic RAM particles have been synthesized by different chemical routes like chemical coprecipitation (CC) method, modified flux method (MFM) and low combustion synthesis (LCS) method. The 'as synthesized' particles have

4

been given a heat treatment at elevated temperatures in the range of 800 to 1200°C for 4h in nitrogen atmosphere to achieve the desirable magnetic phases with increased crystallinity. The reaction kinetics of the endothermic reaction resulting in the synthesis of desirable magnetic phase during heat treatment also have been studied using differential scanning calorimetry (DSC) data at the various heating rate of 10, 30 and 50 K/min. The empirical activation energy is an important experimental parameter. It yields the temperature dependence of the transformation rate and mechanism of transformation. The calculation of Avrami index parameter give the number of growth dimensions of nano sized magnetic RAM synthesizing after heat treatment. Non magnetic RAM like multiwalled carbon nano tubes used in the present investigation have been synthesized by chemical vapour deposition technique (CVD) using acetylene gas as a source of carbon. The commercialized carbon black and silicon carbide (procured from Merck and Sigma Aldrich India) has been reduced in size using high energy planetary ball mill at 300 rpm for 50hrs milling time. All the developed magnetic and non magnetic RAM have been characterized using various techniques like XRD for phase analysis, FESEM/TEM for morphological analysis, VSM/SQUID for magnetic measurement and DSC/DTG/TG for thermal study. Finally dielectric and microwave absorption properties has been measured for X band (8.2-12.2 GHz) using vector network analyzer. Out of all the magnetic RAM powder (hexaferrite and composite of hexaferrite and spinel ferrite), best powder based on their RL properties have been selected to fabricate the composite containing dielectric (CB, SiC and CNT) and magnetic phases (magnetic composite of hexaferrite and spinel ferrite). In continuation of the previous study carried out by our group (Sharma, 2007; 2008) an attempt also have been made to study the effect of Ni-P coating on the microwave absorption properties of barium and strontium hexaferrite nanoparticles (Sharma, 2007; 2008). All the mechanisms for the enhancement of microwave absorption at the various stages of magnetic-RAM, composite of magnetic and non magnetic RAM and coated RAM also have been explained.

LITRATURE REVIEW

2.1 INTRODUCTION

A critical literature review has been carried out in the area of RAM nano particles namely magnetic RAM, non magnetic RAM, composite of magnetic and non magnetic RAM and coated RAM. The synthesis of fine and uniform particle size magnetic RAM powder without impurity is a challenging task. So a critical literature review also has been presented for the various non conventional techniques available for the synthesis of magnetic and non magnetic RAM with small and uniform particle size distribution.

2.2 A HISTORY OF RAM DEVELOPMENT

Since mid 1930's, both theoretical and experimental work has been carried out on EM wave absorber (Emerson, 1973). The first absorber to be patented was designed and fabricated at the Namaalooze Vennootschap Machineries, in Holland in 1936 (Scade, 1945). This was made of quartz wave resonant material in 2 GHz region, in which carbon black was used to achieve dissipation and titania, to achieve a high dielectric constant. Purpose was to reduce the radar cross section (RCS) of the target so that enemies' radar could not detect it, during the World War II, the mission for absorbers intensified to cover a wide bandwidth as well as having good absorption qualities. This was necessitated mainly because of the increased use of radar in battlefield. During this period USA and Germany launched projects to implement the EM wave absorber ideas emerging from research through development and design tests and field evaluation for use in a limited number of defense applications. The effort in USA was primarily directed towards developing absorbers that would enhance the radar performance by reducing interfering reflection from the nearby objects (Simmons and Emeson, 1953; Stonier, 1991). Germany, concerned with radar camouflage for submarines, developed "Wesch" material, a carbonyl iron powder loaded rubber sheet about 0.3 inches thick and a resonant frequency of 3 GHz. The front surface of this material was waffled to produce a larger bandwidth. They also produced the Jaumann Absorber, a multilayer device of alternating resistive sheets and rigid plastic. This device was about 3 inches thick with

resistances decreasing exponentially from the front to the back. This device achieved a reduction in the reflectivity of –20 dB over 2-15 GHz.

Between 1941 and 1945, a coating material called "HARP" (Halpren Anti-Radar Paint) was developed in Radiation Laboratory of M.I.T. under the leadership of Halpern (Halpren, 1945). Although the HARP coating was only 0.6 mm thick, it achieved a return loss of -15 dB to -20 dB in X-band range (8-12 GHz). This material was suitable for aircraft applications because of its small thickness. Small thickness was a tribute to the development of an artificial high dielectric constant material such as barium titanate. The real part of the relative dielectric constant of barium titanate is about 150 at 10 GHz, the central frequency of X-band. The main components of HARP were carbon black, disc shaped aluminum flakes and barium titanate in a polymer matrix. Besides HARP coating, Radiation Laboratory of M.I.T. also developed the now well-known "Salisbury" screen absorber. This screen showed zero refection when a 377 ohms (impedance) resistive sheet was placed in front of a metal plate at a distance of quarter wave length. Although Salisbury absorbers were effective only for normal incident waves, its absorbing mechanism motivated scientist to continue the development of EM wave absorbers (Salisbury, 1952).

During World War II, the quality of anechoic chambers became very important to obtain accurate indoor measurements. Apart from the test equipment, a perfect free space environment was required for precise measurements. Therefore, wide bandwidth and high absorption performance of EM wave absorber were required. The long pyramidal shapes loaded with carbon black were developed to cover the walls of a rectangular room so as to achieve an artificial free space environment (Simmons and Emeson, 1953). From the absorbing mechanism of pyramidal shapes foam absorbers, broadband absorber was developed by gradually tailoring the required effective EM properties near that of free space at the front surface to those of a dissipative medium at the back surface. From 1945-1950, these broadband absorbers satisfied most of the requirements for anechoic chambers. The broadband absorber had been developed from the knowledge of the previous art of "dummy load" design that inspired the scientists and engineers to develop a lot of typical "dummy load materials" (Simmons and Emeson, 1953).
Other dissipative component such as metal and graphite powder, iron oxide, metal wire and steel wool had also been experimented in the development of absorbers. Subsequently, lots of experimental work has been carried out on various surface geometrics including pyramids, cones, hemispheres and wedges.

R. W. Wright, a scientist of U.S. Naval Research Laboratory, has been one of the most successful workers in this field (Wright and Emerson, 1954). In early 1950's, Emerson of the U.S.Naval Research Laboratory developed an effective broad-band absorber which could be made by dipping or spraying tiny conducting powders such as carbon black onto a base of loosely spun animal hair. Lightweight and easy-to-make were the advantages of this kind of absorbers. The Sponge Products Company produced the first commercial product, "Spongex", in 1951. A Spongex material with 2 inch thickness offered a reflection loss (RL) of about -20 dB for normal incidence at the frequency range from 2.4 to 10 GHz. In the late 1950's, Emerson & Cuming Inc. produced absorbers for anechoic chamber, higher than -40 dB RL at a wide frequency range (Simmons and Emeson, 1953).

Research into circuit analog devices was started by Severin and Meyer during this decade. (Severin, 1956; Emerson, 1973; Meyer, 1954; Meyer, 1956). The term circuit analog comes from the use of circuit theory to represent the components/processes occurring in the absorber, and hence to model the reflectivity. This technique was adopted from research programs on acoustical absorbers. Severin and Meyer made experimental absorbers based on resistance loaded loops, slots in resistive foil, resistance loaded dipoles, strips of resistive material with various orientations, surface shaping and magnetic loading of resonant materials. This started a new field of research into frequency selective surfaces, FSS (Munk, 2000).

In 1960's R.E.Hiatt, Head of the Radiation Laboratory, University of Michigan, Ann Arbor, demonstrated significant reduction absorber thickness using magnetic ferrite as under layers, his work was sponsored by NASA. As those happened to be the days of satellite projects, the anechoic chamber had to be useful for making many types of measurements for multi-purposes. The 100-400 MHz frequency region was important for tracking and telemetry. At lower frequencies it is difficult to obtain the high absorbing performance. High permeability and high permittivity magnetic materials contribute for high refraction index at low frequency region and reduce the thickness of absorbers. This development made it possible to obtain up to -40 dB RL from 100 MHz- 1 GHz (Scade, 1945; Johnk, 1988).

In 1970's, Japanese used magnetic ferrite to make EM wave absorbing paint and applied it on the outside wall of high buildings to reduce the ghost image on television screen. The Plessy Company in UK, a renowned manufacturer of EM wave absorbers, developed a new generation EM wave absorbers to satisfy the requirements of British Navy including camouflage and minimizing EMI. All these efforts have resulted in the development of "Stealth material" which plays a significant role in the development of advanced bomber and fighter aircrafts as well as the development of RAM for naval vessels.

These developments have been achieved because of a synergistic approach. The reduction of the RCS of the target has been obtained by a number of methods such as adjusting geometrical shapes to reduce the reflection at certain sensitive angles and applying the RAM onto the target surfaces (Varadan, 1990).

During 1980's the absorber design process was improved by optimization techniques (Fante, 1988). Bandwidth improvement of Jaumann absorbers was evaluated by using graded layers (Gaylor, 1989, Nortier, 1987) and different resistive profiles to achieve maximum bandwidths. Computers and transmission line models were used to calculate reflectivity from material properties, and for frequency selective surfaces which can be represented as equivalent circuits, the transmission line model is applied (Lederer, 1986). Circuit analog materials are designed (Kasevich, 1993) and the scattering of these materials is analysed based on the Floquet theorem (Van, 1989). Materials continue to use carbon black or graphite, carbonyl iron and ferrites, though now artificial dielectrics are being made by adding inclusions such as rods, wires, disc and spheres (Gaylor, 1989). Helical inclusions are found to improve absorption and resulted in research into chiral materials (Jaggard 1989). Mixing theory of magnetic and non magnetic materials is now being used to obtain the desired complex permittivity and permeability for enhanced microwave absorption.

2.3 FUNDAMENTAL OF ELECTROMAGNETIC WAVE THEORY

Microwaves are EM waves that have a frequency range from ~0.3 GHz (there is no actual specified lower frequency limit) to 300 GHz with corresponding wavelengths ranging from 1m to 1mm. Microwaves are transverse electromagnetic waves in which the disturbance is a time-variation of the electric and magnetic fields, E and B at a point. They are generated by accelerated (often oscillating) electrical charges, or by magnetic dipoles. Microwaves are coherent and polarized in contrast to visible waves (apart from lasers). They obey the laws of optics and can be transmitted, absorbed or reflected depending on the type of materials (Kittel, 1971; Born, 1984). The EM aspects of microwave absorber design focus principally on the synthesis of an arrangement of dielectric or magnetic materials that provide a specified impedance profile to an incident wave. The evolution of microwave absorber design is the study of the materials and techniques employed to achieve desirable impedance properties and, hence a good absorbing characteristic with increasing bandwidths (Sadiku, 1995; Knott, 1977).

The propagation and energy transfiguration of EM waves are governed by the well known "Maxwell's Equation". The differential forms are as follow:

Faraday's Law of Induction: $\qquad \nabla \times \bar{E} = -\dfrac{\partial \bar{\mathbf{B}}}{\partial t}$ $\qquad$ .... $\qquad$ (2.1)

Ampere Law: $\qquad \nabla \times \bar{E} = -\dfrac{\partial \bar{\mathbf{H}}}{\partial t} + \mathbf{J}$ $\qquad$ ....(2.2)

Gauss's Law of Magnetic Field: $\qquad \nabla \times \bar{\mathbf{B}} = 0$ $\qquad$ ....(2.3)

Gauss's Law of Electric Field: $\qquad \nabla \times \bar{\mathbf{D}} = \rho$ $\qquad$ ....(2.4)

Where E is the electric field intensity in [V/m], H is the magnetic fields intensity in [A/m], B is the magnetic field density in [Wb/m^2], D is the electric flux density in [C/m^2], J is the electric current density in [A/m^2] and ρ is the electric charge density in [C/m^3].

Solution of any EM problems requires the following EM constitutive equation:

$$\bar{\mathbf{D}} = \varepsilon_r \varepsilon_0 \bar{\mathbf{E}}, \quad \bar{\mathbf{B}} = \mu_r \mu_0 \bar{\mathbf{H}}, \quad \bar{\mathbf{J}} = \sigma \bar{\mathbf{E}} \qquad ......(2.5)$$

Where $\varepsilon_0 = 8.85 \times 10^{-12}$ F/m, $\mu_0 = 0.4\pi \times 10^{-6}$ H/m are absolute permittivity and permeability of air, ε_r and μ_r are complex relative permittivity and permeability and σ is the conductivity of the material with the unit of S/m. The material is assumed to be isotropic. The electric and magnetic properties of a dielectric material are characterized by the relative complex permittivity and permeability written as:

$$\varepsilon_r = \frac{\varepsilon}{\varepsilon_0} = \varepsilon_r' + i\varepsilon_r'' \qquad ....(2.6)$$

$$\mu_r = \frac{\mu}{\mu_0} = \mu_r' + i\mu_r'' \qquad ....(2.7)$$

For lossy media, imaginary parts of the complex permittivity and permeability are nonzero. Generally these imaginary parts represent the absorbing performance. The actual absorption not only depends on the electric and magnetic field but also random scattering effect and chirality effect of conducting chirals. When the alternating electric field is applied across a dielectric slab (or layer), an alternating displacement current is observed which results from the oscillation of the electric dipoles within the field.

Applying the Gauss's Law of electric field: $\nabla \times \bar{\mathbf{D}} = \rho$, the dielectric slab or layer, possesses an alternating conductivity. It is independent of other direct displacement current that has a relationship with the total conductivity that is due to the summation of the above

two kinds of displacement currents. This is $\varepsilon_r'' = \sigma/\omega$, where ω is the angular frequency of the applied field.

In magnetic materials, the magnetic tangent loss is due to the hysteresis phenomenon. This loss tangent can be summarized as follows:

Magnetic loss tangent: $\qquad \tan|\delta_m| = \dfrac{\mu_r''}{\mu_0}$ $\qquad$ .... (2.8)

Dielectric loss tangent: $\qquad \tan|\delta_d| = \dfrac{\varepsilon_r''}{\varepsilon_0}$ $\qquad$ .... (2.9)

From the loss tangents one can also calculate the attenuation constant α_d of the absorbers. For dielectric materials,

$$\alpha_d = \frac{\omega\sqrt{\mu_r \varepsilon_r}}{\sqrt{2}}\left[\sqrt{1+(\sigma/\omega\varepsilon_r)^2}-1\right]^{1/2} \qquad .... (2.10)$$

For magnetic materials,

$$\alpha_d = \frac{\lambda\omega^2}{4\pi}(\varepsilon'\mu_r'' + \varepsilon''\mu_r') \qquad .... (2.11)$$

Equation (2.1) can be rearranged to yield the following EM wave equations:

$$\nabla \times \nabla \times \vec{E} + \frac{1}{c^2}\frac{\partial^2 \vec{E}}{\partial t^2} = -\mu_0\mu\,\frac{\partial \vec{J}}{\partial t} \qquad .... (2.12)$$

$$\nabla \times \nabla \times \vec{H} + \frac{1}{c^2}\frac{\partial^2 \vec{H}}{\partial t^2} = \nabla \times \vec{J} \qquad .... (2.13)$$

Where c is the speed of light,

$$c = \frac{1}{\varepsilon\mu} \qquad .... (2.14)$$

For a time harmonic field expressed in complex notation as $\vec{E}(r,t) = \vec{E}(r)e^{j\omega t}$, the wave equation reduces to

$$\nabla^2\vec{E} = j\omega\omega\mu\vec{E} - \omega^2\mu\varepsilon\vec{E} \qquad .... (2.15)$$

Where ω is the radiation frequency. In free space or in dielectric medium where, the plane wave solution of equation becomes

$$\vec{E}(\vec{r},t) = E_0 e^{-j(\hat{k}.\vec{R}-\omega t)} \qquad .... (2.16)$$

Where $\hat{k}$ is the direction vector of the wave propagation with wavelength $\lambda = 2\pi c/\omega$. The corresponding solution for the magnetic field is obtained as

$$\vec{H}(r) = \frac{k}{\omega\mu}.\hat{k}x\vec{E}(r) \qquad .... (2.17)$$

11

With $k = (\omega^2 \mu\varepsilon)^{1/2}$. The magnitude of E to H is the wave impedance Z and is given by

$$\frac{E}{H} = \frac{\omega\mu}{k} = \sqrt{\frac{\mu}{\varepsilon}} = Z \qquad \ldots\ldots\ldots (2.18)$$

This suggests that the impedance depends on the permeability and permittivity of the medium that the wave propagates in. For the normalized impedance where the wave impedance is divided by the impedance of air, Z_0, Equation becomes

$$\frac{Z}{Z_o} = \frac{\sqrt{\dfrac{\mu}{\varepsilon}}}{\sqrt{\dfrac{\mu_0}{\varepsilon_0}}} = \sqrt{\frac{\mu_r}{\varepsilon_r}} \qquad \ldots\ldots\ldots (2.19)$$

To summarize, the EM wave equation is derived from Maxwell's equation and shows that an EM wave has both electric and magnetic field components that are perpendicular to each other, oscillating in time and space in phase. The ratio of E to H is the wave impedance determined by the permeability and permittivity of the medium. Figure 2.1 illustrates characteristics of an EM plane wave (Sadiku, 1995).
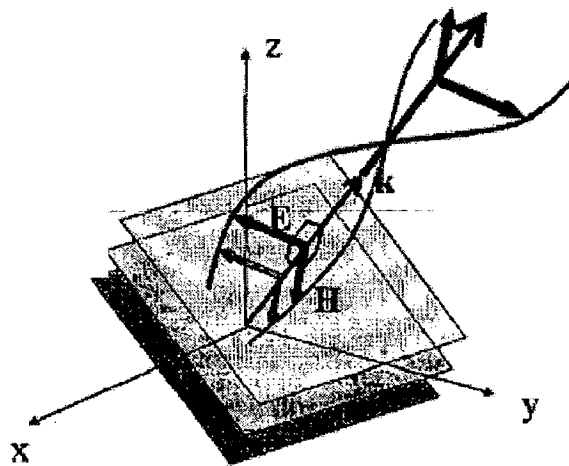
Fig. 2.1:   Electromagnetic (EM) wave propagation

2.3.1 Reflection Coefficient

When a wave impinges on the surface of an object which is semi-infinite, part of the wave is reflected and part is transmitted. The refection coefficient from the part depends not only on the material properties but also on the propagation frequency. The reflection coefficient, R, for normal incidence can be calculated by using the normalized Z/Z_0.

$$R = \frac{Z/Z_0 - 1}{Z/Z_0 + 1} \qquad \dots\dots\dots (2.20)$$

R is a complex number since the normalized impedance is a function of relative permittivity and permeability. When discussing the reflection coefficient, it is customary to ignore the plane angle and refer only to the amplitude of R in decibels. Thus the reflection coefficient can be written as

$$|R|(dB) = 20\log_{10}|R| \qquad \dots\dots\dots (2.21)$$

Wave impedance provides us insight into how material properties, ε_r and μ_r, can affect the reflection coefficient. If the material is very good conductor, Z approaches 0 due to high $\varepsilon_r^{''}$ (= $\sigma/\omega\varepsilon_0$). In this case, Equation (2.20) tells us that R=-1, meaning the wave is entirely reflected with a phase change of 180^0. Now if the material has an EM property of $\varepsilon_r = \mu_r$, Equation (2.19) suggests Z=Z_0, and there will be no reflection from the material (R=0).

For a flat metallic surface coated with a layer of dielectric material, the normalized impedance is modified as

$$\frac{Z}{Z_o} = \sqrt{\frac{\mu_r}{\varepsilon_r}} \tanh(-ik_0 d\sqrt{\mu_r\varepsilon_r}) \qquad \dots\dots\dots (2.22)$$

Where d is the thickness of the layer and $k_0 = 2\pi\lambda_0$. Now substituting Equation (2.22) into Equation (2.20) we get the reflection coefficient R,

$$R = \frac{Z}{Z_o} = \frac{\sqrt{\mu_r/\varepsilon_r}\ \tanh(-ik_0 d\sqrt{\mu_r\varepsilon_r}) - 1}{\sqrt{\mu_r/\varepsilon_r}\ \tanh(-ik_0 d\sqrt{\mu_r\varepsilon_r}) + 1} \qquad \dots\dots\dots (2.23)$$

It is seen that the reflection coefficient depends on two material properties, relative permeability and permittivity, the design parameters and layer thickness. As ε_r and μ_r changes with frequencies, the design of an absorber involves optimizing microwave absorption at a target frequency using its EM properties and thickness. Figure 2.2 showed reflection coefficient with different thicknesses for an artificial material with ε_r =12, $\varepsilon_r^{''}$ = 1, μ_r =2 and $\mu_r^{''}$=1.

Reflection Loss (dB)

Frequency (GHz)

t = 1.0 mm
t = 1.5 mm
t = 2.0 mm

$\varepsilon = 12\varepsilon' + 1\varepsilon''$
$\mu = 2\mu' + 1\mu''$
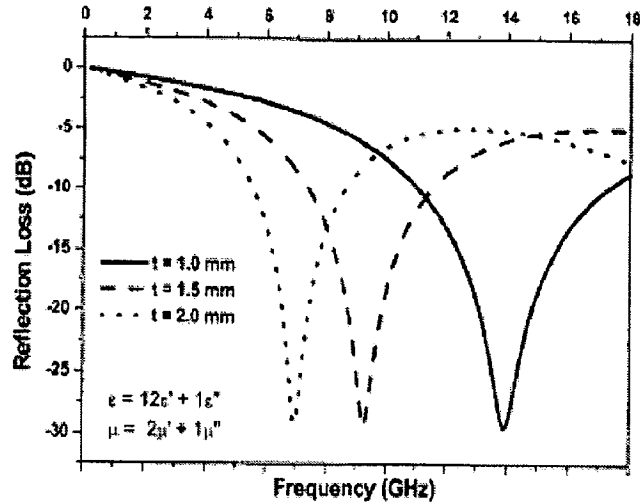
Fig. 2.2:   Effect of thickness of microwave absorber on refection coefficient.

This illustrates a general rule of thumb in microwave absorber: a thicker absorber was needed to absorb effectively at low frequencies than at higher frequencies.

2.3.2 Loss Mechanism of Microwave Absorber

The two main loss mechanisms for non- magnetic materials are dielectric (dipolar) losses and conduction losses. Conduction losses dominate in metallic, high conductivity materials and dipolar losses dominate in dielectric insulators. Magnetic materials also exhibit conduction losses with additional magnetic losses such as eddy current loss, hysteresis loss, domain wall resonance and electron spin resonance.

2.3.2.1   LOSSES DUE TO OSCILLATING MAGNETIC FIELD

In dielectric (electrically insulating) materials such as industrial ceramics and the bulk matrix of lava, the absorption (degree of interaction) of microwaves is related to the material's relative complex permittivity is given in equation (2.6).

When microwaves penetrate and propagate through a dielectric material the internal field generated within the effected volume induces translational motions of free or bound charges such as electrons or ions, and rotates charge complexes such as dipoles. Inertial, elastic and frictional forces resist these induced motions and cause losses, a consequence of which is volumetric heating. These loss mechanisms are combined together for convenience to give

one electric loss parameter ε_r''. Figure 2.3 illustrates the variation in ε_r' and ε_r'' for a dielectric showing 'Debye' relaxation.
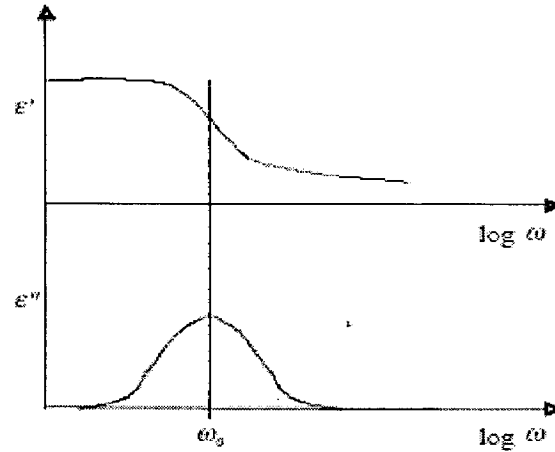
Fig. 2.3: Variation in permittivity with frequency for a dielectric showing 'Debye' relaxation, w_0 being the resonance frequency.

The loss tangent is also commonly used to describe these losses, which is defined as Dielectric loss tangent:

$$\tan|\delta_d| = \frac{\varepsilon_r''}{\varepsilon_0} = \frac{\sigma}{\omega\varepsilon_0\varepsilon_r'} \qquad \ldots\ldots\ldots (2.24)$$

The power P that is absorption per unit volume (W/m^3) of the sample at any instant of time can be described by

$$P = \sigma|\vec{E}|^2 = \omega\varepsilon_0\varepsilon_r'|\vec{E}|^2 \tan|\delta_d| \qquad \ldots\ldots (2.25)$$

It has been assumed that the power is uniform throughout the volume and that thermal equilibrium has been achieved. This is not always the case and in addition $|\vec{E}|$, $\tan|\delta_d|$, ε_r' and ω are all in fact interdependent. However, it does provide a useful approximation for the power absorbed and describes the basic relationships between the four variables. It can be seen that the power absorbed varies linearly with frequency, the relative dielectric constant, loss tangent varies with the square of the electric field.

2.3.2.2 LOSSES DUE TO OSCILLATING MAGNETIC FIELD

The permeability μ, of a material is defined as

$$\vec{B} = \mu_r\mu_0\vec{H} = \mu(H + M) \qquad \ldots\ldots\ldots (2.26)$$

15

M is the magnetization (A/m), For small fields the magnetization is proportional to the field intensity which means that the initial relative permeability, μ_r, is a constant.

$$\mu_r = \frac{\mu}{\mu_0} = \mu_r{'} + i\mu_r{''} = 1 + \frac{\mathbf{M}}{\mathbf{H}} = 1 + \chi \qquad \dots\dots\dots (2.27)$$

In an analogous way to the electric losses, the losses that occur due to a time varying magnetic field can be described by a complex relative permeability. An analogous magnetic loss tangent, can also be defined where

$$\tan|\delta_m| = \frac{\mu_r{''}}{\mu_0} \qquad \dots\dots\dots (2.28)$$

In a similar way, the power P that is absorbed per unit volume (W/m³) of the sample at a given instant of time can be described by

$$P = \omega\mu_0\mu_r{''}\left|\vec{\mathbf{H}}\right|^2 = \omega\mu_0\mu_r{'}\left|\vec{\mathbf{H}}\right|^2 \tan|\delta_m| \qquad \dots\dots\dots (2.29)$$

It can be seen that the power absorbed varies linearly with frequency, permeability, loss tangent and with the square of the magnetic field.

For a ferrite the loss tangent can be expressed in terms of three main contributors,

$$\tan|\delta_\mu| = \tan|\delta_h| + \tan|\delta_e| + \tan|\delta_r| \qquad \dots\dots\dots (2.30)$$

Where, $\tan|\delta_h|$, $\tan|\delta_e|$ and $\tan|\delta_r|$ are the hysteresis, eddy current and 'residual' loss tangents respectively. The processes that contribute to the residual losses include the resonance losses and at high frequencies these will often dominate.

2..3.2.3 HYSTERESIS LOSSES

As a result of hysteresis, energy is dissipated as heat in a magnetic material as it travels around a **B-H** hysteresis loop. The hysteresis energy loss W_h per unit volume of material is

$$\mathbf{W}_h = \oint\mathbf{B}d\mathbf{H} \qquad \dots\dots\dots (2.31)$$

This loss is controlled by factors that control low frequency permeability and coercivity such as porosity, grain size and impurities as well as the intrinsic properties.

2.3.2.4 EDDY CURRENT LOSSES

The conductivity of the material is important as it determines the extent of losses due to eddy currents. For ferrites the conduction mechanism is believed to be electron hopping between ions of the same type of equivalent lattice sites, e.g. for magnetite $Fe^{3+} \leftrightarrow Fe^{2+}$. This

mechanism is also known as valence exchange mechanism. Magnetite is one of the most conductive oxides with the conductivity, σ, approximately 10^4 S/m at room temperature. The skin depth, δ, in a conductive material is the depth of penetration of the magnetic field (as well as the current density) at which its value decreases by $1/e$ of its surface value. (This is analogous to the penetration depth for a dielectric in which case it is the electric field that penetrates.) The skin depth is given by

$$\delta = \sqrt{\frac{2}{\sigma\omega\mu}} \qquad \qquad \ldots\ldots\ldots (2.32)$$

When the skin depth is large compared to the sample size, the influence of eddy currents on the magnetic field is entirely negligible. Hence, in calculations an infinite skin depth can be assumed and the energy dissipation for various shapes evaluated (Smith, 1959; Vinoy, 1996). The energy dissipation W can be evaluated using the equation;

$$\mathbf{W} = \sigma \oint |\mathbf{E}|^2 \, dV \qquad \qquad \ldots\ldots\ldots (2.33)$$

2.3.2.5 DOMAIN WALL RESONANCE LOSSES

For magnetic materials, the energy loss is associated with the relaxation mechanisms which control the magnetization motion during flux reversal (Patton, 1967). Whenever there is a change in magnetization motion due to a dynamic external field applied, it is accompanied with energy loss. The loss of energy comes from two major sources: a domain wall movement and ferromagnetic resonance. A ferromagnetic material consists of many magnetic regions, called domains, within which the magnetization is constant in magnitude and direction. However, the magnitude and direction of magnetization varies from domain to domain in such a way that the net magnetization vanishes. When an external field is applied, these domains change their volume through the displacement of the boundary walls between adjacent domains (Aharoni, 2000). The transition of domain walls depends upon the magnetic anisotropy energy, which is the interaction energy between atomic moments. The competition between these two energies provides the finite thickness of the wall. The transition of the domain wall is associated with an energy loss as its movement dissipates energy to the crystal lattice of the material.

Another form of energy loss comes from ferromagnetic resonance which involves the precession of magnetic moments. When a magnetic material is disturbed from the equilibrium state, the magnetic moments undergo precession as a result of the torque exerted

17

on the magnetization by the external field. When a sinusoidal magnetic field is applied, it excites precessional motion. At a frequency near precessional frequency of the magnetic materials, the energy coupled from the excitation field to the process of magnetization will be large and the energy is absorbed from the magnetic field by the crystal lattice. For ferrites or ferromagnetic materials, the precession frequency falls under the regime of microwave frequencies. This makes these materials an excellent choice for microwave absorbers.

2.4 CLASSIFICATION OF FERRITES

Ferrites are metal oxides, which contain magnetic ions arranged in a manner that produces magnetization spontaneously while maintaining good dielectric properties (Kojima, 1982). Ferrites are magnetic oxides of iron, providing the best available combination of electrical insulation and magnetic characteristics with a remarkable flexibility in controlling magnetic, conductive and crystal lattice parameters by appropriate doping (Smith, 1959; Wilhelm, 1965).

The magnetic properties that make ferrites useful in application as an absorber arises from an interaction of dipole moment of electron associated with its spin and EM wave. High value of electrical resistivity and permeability play a major role in making this interaction strong. High resistivity enables an EM wave to penetrate the material and high permeability increases the magnetic moment of the ferrite (Pozar, 1998). Ferrite can be classified into three categories depending upon crystal structure namely; spinel, hexagonal and garnet ferrite (Wilhelm, 1965).

2.4.1 Spinel

General chemical formula of spinel is MFe_2O_4, where M denotes a divalent atom and Fe a trivalent ion. The crystal structure of this type of compounds is isomorphic with the classical spinel $MgAl_2O_4$, which is a well-known mineral found in nature (Sharma, 2008). The crystal structure is preserved when the trivalent aluminum of the spinel is replaced by the trivalent iron to produce $Mg^{2+}O.Fe_2^{3+}O_3$, which is called magnesium ferrite. The divalent magnesium can then be replaced by divalent iron to yield iron ferrite, or magnetite. Nearly any divalent metal ion such as nickel, cobalt, manganese, zinc, copper, barium or cadmium can be used to form a pure spinel ferrite.

The unit cell of a spinel contains eight units of MFe_2O_4. Thus, it consists of thirty two oxygen, sixteen trivalent iron and eight divalent metal ions. The most important feature of the unit cell is that its array of oxygen ions leaves open two kinds of interstices that can be filled

by metal ions. These interstices are referred to as tetrahedral or 'A' sites and octahedral or 'B' sites. The smallest three-dimensional building block of the crystal structure is shown in Figure 2.4.
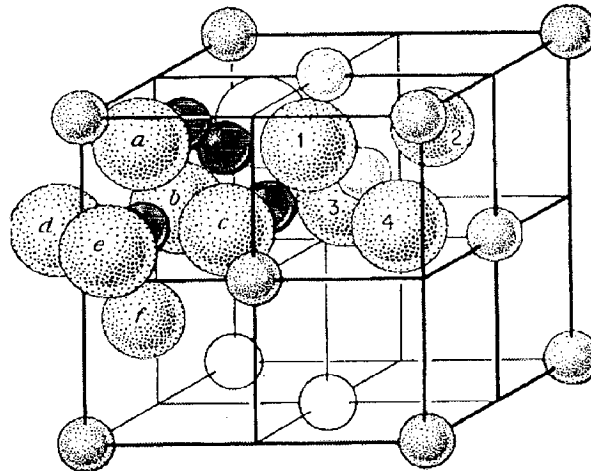
Fig. 2.4:   The unit cell of spinel structure. The oxygen anions are shown as large spheres. The small lightly shaded spheres are metal cations in tetrahedral sites, one of which is shown surrounded by a metal ion (black) on an octahedral site. The ions have been drawn only in two of the eight octants of the unit cell (Sharma, 2008).

The definition of the normal spinel arrangement requires that the eight divalent metal ions of the unit cell occupy the eight 'A' sites of the unit cell and the sixteen trivalent metal ions occupy the sixteen B sites. It has been found, however, that the magnetic ferrite have a structure known as the inverted spinel in which 8 of the 16 trivalent ions occupy the entire 'A' sites. The other half of the trivalent ions and all of the divalent ions occupy the B sites in random order.

2.4.2 Hexagonal Ferrite

The ferromagnetic oxides having a crystal structure similar to the mineral magnetoplumbite, $PbFe_{7.5}Mn_{3.5}Al_{0.5}Ti_{0.5}O_{19}$, are also referred to as the "hexagonal ferrites". The chemical composition of hexagonal ferrite is $MeFe_{12}O_{19}$, where Me is a divalent metal ion (i.e. Ba, Sr, Pb), which can be replaced by any of these elements. The chemical

compositions of these oxides are displayed by the triangular diagram in Figure 2.5. The corners of the diagram are labeled by three constituent's oxide, SrO, MeO and Fe_2O_3, but this does not imply that a compound is actually prepared from such materials. Each point within the diagram represents a different mixture of the component, but only a few points represent actual compounds. The composition corresponding to any given point is determined in the following manner: Perpendiculars are drawn from the point to each of the three sides. The length of the perpendicular to any side then represents the relative proportion of the constituent indicated in the corner opposite to that side.
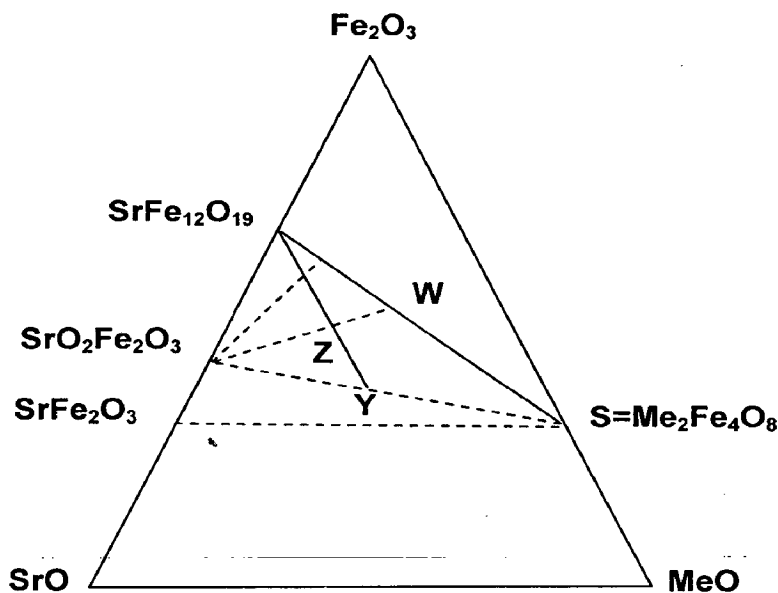
Fig. 2.5:   Triangular diagram and chemical composition of hexagonal ferrite.

Consider a point on the boundary, such as S, the SrO content is zero. Since the lengths of the two remaining perpendiculars are proportional to the adjacent proportions of the side in question, the length of the side between S and a corner represent relative contents of the constituents at the opposite corner. Thus, S corresponds to the composition MeO or Fe_2O_3 or $MeFe_2O_3$, the composition of a spinel ferrite.

2.5 CRYSTAL STRUCTURE OF HEXAGONAL FERRITE

Each of the ferrimagnetic hexagonal oxides has a different crystal structure. It is possible to represent them as different stacks of only three relatively simple blocks of ions, designated as S, R and T.

2.5.1 The S Block

The S block is the smallest and contains no strontium. The oxygen anion and interstitial metal cation are so distributed that they form precisely the spinel arrangements. The chemical formula of S block is Fe_6O_8.

2.5.2 The R Block

The two strontium containing blocks are bound by the same type of the plane that demarks the boundaries of the S block; the plane lies halfway between two oxygen layers in a region free of tetrahedral ions and contains three octahedral ions. The R block, $SrFe_6O_{11}$ includes three oxygen layers.

2.5.3 The T Block

The third type of block is the T block; it has the chemical formula $Sr_2Fe_8O_{14}$ and subsumes four oxygen layers. In each of the two middle layers of the T block, one of the four O^{2-} ions is replaced by Sr^{2+}. The T blocks contain six octahedral ions. Three of these lie on the boundary planes. The internal three lie on the vertical line, one halfway between each pair of oxygen planes. One of the two tetrahedral ions in the T block lies between the first and second oxygen planes directly above the lower Ba^{2+} ions. The other is between the third and fourth planes directly below the upper Ba^{2+} ions.

2.6 CLASSIFICATION OF HEXAGONAL FERRITES

From the block R, S, R^*, S^* and T hexagonal ferrite have classified into six categories as shown in Table 2.1. Where, M is the divalent transition metal ion (Stadeley, 1971).

Table 2.1: Classification of Hexagonal Ferrites

S. No.	Type	Unit cell structure	Formula
1.	M	SR S*R*	$SrFe_{12}O_{19}$
2.	W	SSR* S* S*R	$Sr\,M_2^{2+}Fe_{16}O_{27}$
3.	Y	STSTST	$Sr_2\,M_2^{2+}Fe_{12}O_{22}$
4.	Z	RSTSR*S*T*S*	$Sr_3\,M_2^{2+}Fe_{24}O_{41}$
5.	X	3(RSR*SS)	$Sr_2\,M_2^{2+}Fe_{28}O_{46}$
6.	U	RSR*S*T*S*	$Sr_4\,M_2^{2+}Fe_{36}O_{60}$

2.7 RADAR ABSORBING MATERIALS (RAMs)

The work reported in open literature can be summarized in to four broad categories namely:

i)   Magnetic RAM

ii)   Non magnetic RAM

iii)   Composite of magnetic and non magnetic RAM.

iv)   Coated magnetic RAM

The details are discussed subsequently.

2.7.1 Magnetic RAM

A large number of investigations have been carried out to develop microwave absorber by dispersing ferrite powder (magnetic RAM) into polymer matrix (Varadan, 1990; Vaia, 2001; Verma, 2002). Natio (1971) experimentally exhibited that for a given ferrite polymer composite, the frequency at which absorption is maximum and the matching thickness at which maximum absorption was achieved are different and independent of each other. Knott (1977) reported theoretically that for maximum absorption, the thickness of the layer should be equal to the quarter of a wavelength for predominantly dielectric material and one half-wave length for the predominantly magnetic material. Absorbers, which satisfy the above thickness criterion, are commonly known as resonant absorber. Ishino (1987) reported the development of magnetic ferrite for absorption of microwave. They reported the microwave absorption of -32 dB at 200 MHz for a thickness of 9 mm in Ni-Zn ferrite based absorber. Musal (1990) reported the universal design chart that gave overall view of interrelated numerical values of material properties required to implement an optimum design of EM wave absorber using a single homogeneous layer of materials. This chart is still being used for design and development of microwave absorber. Yashuhiro (1989) reported the fundamental treatment of a thin absorber in the spatial network model. The validity of this treatment has been verified by comparing computed results with the experimental results as a function of parameters namely, the medium constant of the absorber, the frequency, the incidence angle and the polarization of the wave. Nedkov (1990) investigated the effect of orientation and particle size of scandium (Sc) and cobalt titanium (CoTi) substituted barium hexaferrite ($BaM_xFe_{12-x}O_{19}$, where M=(Sc) and (CoTi), while x=O-1.8) on microwave absorption in a wide frequency range (5-70 GHz) and reported that peak absorption was available for the particle sizes of 1 to 7 micron. Further they have also reported that

imaginary part of complex permittivity (ε'') will increase if manganese in very small quantity is doped with cobalt and titanium. Ahmad (1990) published a work on the theoretical analysis and design of an absorbing layer coating on the radar target, in order to reduce RCS. A new mathematical model describing a single absorbing layer has been developed. This model was based on Maxwell's equation and evaluation of overall refection coefficient.

Kim (1990) reported the measurement of complex permeability and permittivity of Ni-Zn ferrite in X-band. They have also presented the complex permeability and permittivity spectra of ferrite-polymer composite material. Gupta (1993) developed microwave absorber by dispersing cobalt substituted barium hexagonal ferrite powder into rubber matrix. They have reported minimum absorption of -8 dB for normal incidence in the range of 12-18 GHz. They have also reported single layer absorber sheet of thickness less than 7 mm in S-band, 4 mm in C band, 4 mm in X band and 3 mm in Ku band to give the minimum of -10 dB absorption. Pitkethly (1992) reported that radar absorbing material have a significant role to play in reducing the radar cross section of military aircraft. They represented the several techniques namely shaping, Parasitic RAM, Internal RAM and integral structure RAM of reducing the RCS. They concluded that shaping alone is not sufficient to provide the required reductions and to maintain the desired operational flight envelope. Shin (1993) developed the complex permeability dispersion and the microwave absorbing phenomenon in hexagonal Y, Z type hexaferrite and spinel (NiZnCo) based microwave absorber in the frequency range of 200 MHz to 16 GHz. They observed one or two matching frequencies exist in the ferrite absorbers. This phenomenon strongly depends on the complex permeability locus of ferrite absorber on the impedance matching solution map. They also observed that first matching frequency of the ferrite absorber strongly depends on its spin resonance frequency (f_{r2}) and the second matching frequency is independent of the resonance frequency.

Wallace (1993) reported computer simulated results for multilayer microwave absorber and concluded that it is impossible to obtain broad absorption with the homogeneous single layer material which obey the Kramers-Kronig conditions (i.e. materials in which large values of μ'' are invariably accompanied by rapidly changing values of μ'). They reported that excellent performance can be obtained from properly designed multilayer structures. The investigation of Dishovski (1994) has showed that cobalt and titanium substituted barium hexaferrite improves the absorption properties of microwave absorber. They also studied the absorption characteristics of composites with different filler ratio of rubber, ferrite, magnetite and graphite in the frequency range of 8 to 15 GHz for rubber: ferrite:

magnetite: graphite = 1.0:1:5:0.6:0.75 systems. They concluded that, the introduction of a highly anisotropic magnetic component in the magnetic absorber leads to the improvement of the long-range order in the arrangement of the absorbing fillers in the polymer matrix and, as a result, the hysteresis losses and microwave absorption in the substance increase. Chaitanya (1994, 1995) developed add on type of EM interference absorber in the frequency range from 8 to 18 GHz and added thickness restriction of 2 mm. They have also presented the design criteria for matched absorber and resonant absorber. Kim (1996) reported that a microwave absorber with reflection loss of -40 dB can be designed by controlling the ferrite volume fraction of $0.26 \leq V_r \leq 0.45$ in Mn-Zn ferrite polymer composite in the frequency range of 0.8 to 12 GHz. Matsumoto (1996) developed a grid type EM wave absorber using Y and Z type barium based hexagonal ferrites They concluded that the hexagonal ferrite retains high permeability even in the GHz range. They also studied effect of introduction of free space in the direction perpendicular to the electric field, which was found to decrease the total permittivity of the material. They observed that, absorber consist of $Ba_3Co_2Fe_{24}O_{41}$ and $Ba_2(Zn_{0.8}Mn_{0.2})_2Fe_{12}O_{22}$ showed wide bandwidths of 1.8–5 GHz and 1.5–4.5 GHz ($RL \geq 15$ dB) respectively, when the free space was 37% (v/v) and the thickness of the ferrite was about 5 mm. Increasing the free space to a 50% (v/v) of free space led to a wider bandwidth (1.7–9 GHz) when the thickness of the $(Zn_{0.8}Mn_{0.2})_2Y$ increased to 7 mm.

Ruan (2000) developed microwave absorber by synthesizing W type hexagonal ferrite powder $(Ba(Zn_{0.7}Co_{0.3})Fe_{16}O_{27})$ by citrate method. They have also investigated the effect of particle size on microwave absorption and reported that microwave is absorbed more effectively by material with nano scale than with micron size absorber. The maximum reflection reaches -28.5 dB and for a reflection loss above -10 dB, the bandwidth reached about 5 GHz compared to only 3.5 GHz for that using barium hexaferrite powder with the size of 5μm. The investigation of Takabayashi (2000) pointed the effect of crystal orientation on the electromagnetic wave absorption properties of barium M-type-hexaferrites in which Fe^{3+} was substituted by $(Ti_{0.5}Mn_{0.5})^{3+}$. The $BaFe_9(Ti_{0.5}Mn_{0.5})O_{19}$ sintered samples were prepared by a conventional powder metallurgy technique, in which, c-axes of the powder particles were aligned in a magnetic field during compaction. After sintering, toroidally shaped samples were formed whose c-axes were aligned at certain angles to the sample thickness. It was concluded that the degree of crystallographic alignment of the sample and the sintering time used are important factors in obtaining good electromagnetic wave absorption properties with a smaller matching thickness. They observed that the complex permeability depend on the angle of incidence. At normal incidence the ferrite sample

exhibited highest value of imaginary part of complex permeability. They have also reported the maximum reflection loss of -20 dB at 12.5 GHz for a coating thickness of 0.57 mm.

Iijima (2000) developed millimeter wave absorber using M-type aluminum substituted strontium based hexagonal ferrite [$SrFe_{12-x}Al_xO_{19}$] for x=0 to 2. They reported peak absorption of -20 dB at 60 GHz for coating thickness of 0.39 mm in the frequency range of 52 to 83 GHz. Giannakopoulou (2002) synthesized Ni-ferrites ($NiFe_2O_4$) by sol gel technique followed by heat treatment at different temperature for the formation of single phase ferrite with increased crystallinity. They reported that the permeability spectra of nickel ferrites exhibit broadening with the increase of annealing temperature. This happen due to the appearance of domain wall resonance, and displacement of spin resonance to higher frequencies which in turn leads to extending the absorptivity of nickel ferrite layers to higher microwave frequencies. The same results were observed for $CoFe_2O_4$, $Li_{0.07}Ni_{0.93}Fe_2O_4$, $Li_{0.15}Ni_{0.85}Fe_2O_4$ compounds connected with permeability spectra. The absorptions broaden move towards the X-band frequencies as the annealing temperature moves to higher values. They reported that nickel ferrite achieves the satisfactory reflection loss of -25 dB (thickness=3.1mm) at 9.64GHz for the material heat treated at 1600°C. Yang (2003) reported the microwave absorption performance of W-type hexagonal ferrite ($Ba(Zn_{0.5}Co_{0.5})_2Fe_{16}O_{27}$) based microwave absorbing paint in the frequency range of 2 to 18 GHz. The ferrite particle were synthesized by combination of coprecipitation and mechanical alloying methods and observed to posses excellent hexagonal shape and are well separated from one another. The reflection loss is found to depend sensitively on the absorber thickness. The attenuation peak shifts to low frequency when the thickness of composite materials increases. This shows that attenuation peak frequency of the ferrite–epoxy composites can be manipulated easily by changing the thickness of materials. The maximum reflection loss of -13 dB at 10 GHz is observed for the coating thickness of 3.5 mm.

Haijun (2002) reported the development of $Ba_2Zn_xCo_{2-x}Fe_{28}O_{46}$ hexaferrites with X =2:0; 1.6, 1.2, 0.8, 0.4 and 0.0 by citrate sol gel process. They concluded that the substitution of zinc ion had a close effect on the microwave properties of $Ba_2Zn_xCo_{2-x}Fe_{28}O_{46}$ ferrites, as increasing zinc ion content lowered the natural resonance frequency.

Meshram (2002, 2004) has reported the design, development and characterization of the hexagonal ferrite powder $BaCo_{0.58}Ti_{0.58}Mn_{0.1}Fe_{(11.87-\delta)}O_{19}$, $Ba(MnTi)_xFe_{(12-2x)}O_{19}$ at x =1.6 as a microwave absorber. The developed ferrite powder (60% by weight) has been mixed in epoxy resin to form a microwave-absorbing paint. This paint was coated on a conducting aluminum sheet to study the absorption characteristics of a linearly polarized

wave at X-band. The results for single- and two-layer microwave absorbers for different coating thicknesses have been reported. It has been found the broad-band characteristics with minimum absorption of -8 dB at 8 to 12 GHz for a coating thickness of 2 mm. The Ni-Zn ferrite with chemical composition $Ni_{0.5-x}Zn_{0.5-x}M_{2x}Fe_2O_4$ (M = Co, Cu, or Mg, and $x = 0$ or 0.05) were synthesized by a low combustion synthesis method (Peng, 2005). The crystallite sizes were observed to increase from 20 nm for the as-synthesized powders to ~35–45 nm for the annealed samples. They reported that the Co-doped, Mg-doped, and Cu-doped NiZn ferrite-TPU (thermalplastic polyurethane) composites have more effective absorption effect than the undoped ferrite. The doping of cobalt results in highest reflection loss (-42.15dB, d= 5mm) than those observed for cu, Mg doped Ni-Zn ferrite. The nano size nickel zinc ferrite is observed to exhibits higher reflection loss than micro sized powder.

Kim (2005) reported that, dispersing ferromagnetic iron particles as the absorbent fillers in rubber matrix, thin-layer electromagnetic wave absorbers with appreciable attenuation could be designed in the quasi microwave frequency band (1–2 GHz). The addition of iron particle-improves the magnetic permeability and dielectric constants of the composite materials which in turn decreases the eddy current loss and enhance the space charge polarization of the composite. With the iron particles controlled in size and shape (flakes), the thickness of absorbing layer could be reduced to as low as 1 mm with respect to −5 dB reflection loss (70% power absorption) in the frequency band of 1–2 GHz. Nie (2006) reported the static magnetic and microwave characteristics of hexagonal ferrite ($BaZn_{1.1}Co_{0.9}Fe_{16}O_{27}$) particles for application in a microwave absorber. The complex permeability and permittivity of ferrite-wax composites were measured over the frequency range of 2–8 GHz. The microwave intrinsic permeability and permittivity spectra have been presented, which were calculated on the basis of the measured data of the ferrite–wax mixtures using the Bruggeman equation. Li (2006) studied the effects of CuO additive, particle size, and filler concentration on the complex permittivity, permeability, and microwave-absorbing properties of CO_2Y hexaferrite composites. Co-Y-type hexaferrites ($Ba_2Cu_xCo_{2-x}Fe_{12}O_{22}$, x=0, 1) particle were synthesized by the conventional ceramic process. They reported that reducing particle size of hexaferrite broadens the bandwidth below -10 dB from 4 to 8 GHz and improves the absorption. When the volume concentration of $Cu_{1.0}Co_{1.0}Y$ (4 µm) hexaferrites was increased to 60%, RL values less than -5 and -10 dB were observed in the 6–18 and 9–18 GHz range and minimum RL value of -35 dB at 13 GHz is observed. Hwang (2006) developed NiZn-ferrite by conventional solid state reaction route using waste iron oxide as a catalyst which is thrown away as an

industrial waste in the styrene monomer process. Nickel oxide and zinc oxide powders were mixed with finely ground and acid refined waste catalysts, and spinel type ferrite ($Ni_xZn_{1-x}Fe_2O_4$, x=0.36, 0.50 and 0.66) is synthesized by calcination at 900 °C for 2 h followed by sintering at 1325 °C for 5 h. They reported that reflection losses at a zero-reflection frequency are as low as −45 dB at several hundreds MHz frequencies. The minimum reflection loss for calcined ferrite (1 μm. with irreregular spherical shape) found to be -20dB at 6.2 GHz for the thickness of 5.5mm. Their study showed feasibility of recycling waste iron oxide catalyst as an electromagnetic wave absorber.

It is reported that (Masala, 2006) exchange coupling interaction existing between hard and soft magnetic phases improved the microwave absorption of ferrite by changing the complex permeability of composite material. The composite powder including hexagonal ferrite (hard magnetic phase) and spinel ferrite (soft magnetic phase) coupled to each other by exchange through interface of ferrite particles. There will be more interfaces if the particle size is smaller, and there will be stronger exchange coupling interaction at the interface. $SrFe_{12}O_{19}$ is a hard magnetic material and zinc ferrite is a cubic spinel structure is a kind of soft magnetic material and has been widely studied as microwave absorbing material in a relatively low frequency range (Peng, 2005; Yusoff, 2004; Verma, 2002). Chen (2007) fabricated the composite powders with different weight ratios of hard strontium hexaferrite and soft zinc ferrite (weight percents of $ZnFe_2O_4$ are 0, 15 and 30, respectively) using sol–gel technique. They observed that composite powder with 15 wt% zinc ferrite in $SrFe_{12}O_{19}$ powder possesses minimum reflection loss of −37 dB at the thickness of 2.2 mm. They reported that additions of $ZnFe_2O_4$ make the minimum reflection loss frequency of the composite powders shift to a higher frequency than that of pure strontium ferrite.

Sharma (2008) synthesized single phase M-type barium hexaferrite nano crystals of radar absorbing material i.e., $BaFe_{12}O_{19}$ by a modified flux method under cyclic microwave irradiation. They observed uniform and ultrafast morphological transformation from spherical to pyramidal-faced nano crystals during the cyclic microwave irradiation power for constant time. Significant increments in reflection loss from −15.23 to −53.63 dB over a wide bandwidth were noticed during symmetric morphological growth of single phase nano crystals. The strongest RL of −53.69 dB is observed at 14.75 GHz for complete grown nano crystals of pyramidal face. This finding adds that not only the formation of single phase hexaferrite nanoparticles but also the morphology of the particles obtained (pyramidal face) play very important role in the enhancement of microwave absorption. Bueno (2008) developed $Ni_{0.5-x}Zn_{0.5-x}Me_{2x}Fe_2O_4$ (Me = Cu, Mg, Mn; x = 0.00 and 0.10) ferrite by the

nitrate-citrate precursor method. They conclude that the improvement in microwave-absorbing properties and bandwidth are achieved by Mn^{2+} and Cu^{2+} substitution. They observed that the minimum reflection loss was improved from -20.14 dB in the non-substituted NiZn ferrite to about -29.56 dB in the Mn-substituted NiZn ferrite, and to about -35.02 dB in Cu-substituted NiZn ferrite. The bandwidth increased to at least 1.15 GHz. They also reported that Mg substitution reduces microwave absorption in the X-band as compared to non substituted NiZn ferrite.

Ghasemi (2008) studied the structural and electromagnetic characteristics of strontium hexaferrite nano particles by doping with Mn, Co, Zr. The single phase strontium hexaferrite and single phase strontium hexaferrite nano particle doped with Mn, Co, Zr $(SrFe_9(Mn_{0.5}Co_{0.5}Zr)_{3/2}O_{19})$ with hexagonal fine platelet structure, narrow particle size distribution with an average diameter of 30 nm were synthesized by sol–gel method. They observed that doped strontium hexaferrite nanoparticles found to have higher reflection loss (−31 dB at matching frequency of 8.5GHz) than undoped strontium hexaferrite nanoparticles (-11.6dB). The doped strontium hexaferrite composite found to have two absorption peaks. First is at matching frequency of 8.5GHz with reflection loss of −31 dB and second is at 9.35GHz with reflection loss of -30 dB. This dispersion is due to the domain-wall motion at lower frequency (8.5GHz) and spin resonance at higher frequency (9.35GHz). It is concluded that the doped ferrite-containing composites have much more effective electromagnetic absorption effects. Zhao (2009) fabricated nano crystallites NiFe$_2$O$_4$ spinel ferrite by poly acrylamide gel method with acrylamide as the monomer and N N'-methylenediacrylamide as the lattice agent. The average particle sizes observed to increase from 10 to 50nm with spherical morphology when heat treatment temperature increased to 800°C. They observed that composite with 65wt% ferrite in polymer matrix showed a minimum reflection loss of -13dB at 11.5GHz with a -10dB band width over the extended frequency range of 10.3–13GHz. They also demonstrate that multilayer ferrites exhibits higher reflection loss with wide microwave absorbing band than single layer ferrite. They developed three kind of Ni–Zn spinel ferrite namely $(Ni_{0.5}Zn_{0.5})Fe_2O_4$, Cu-doped $(Ni_{0.4}Cu_{0.2}Zn_{0.4})Fe_2O_4$ and Co-doped $(Ni_{0.4}Co_{0.2}Zn_{0.4})Fe_2O_4$) by a conventional ceramic processing method (Zhao, 2009). The single layer $(Ni_{0.4}Co_{0.2}Zn_{0.4})Fe_2O_4$ spinel ferrite absorber with a thickness of 3mm achieved a reflection loss below −10 dB (90% absorption) at 3.9–11.5 GHz, and the minimum value was −17.01 dB at 6.1 GHz. Compared with the performances of the single layer spinel ferrite absorbers, not only the matching frequencies of the double layer spinel ferrite absorbers were

shifted to higher values, but also the microwave absorbing frequency bands were expanded. When the first layer and second layer are $(Ni_{0.5}Zn_{0.5})Fe_2O_4$ and $(Ni_{0.4}Co_{0.2}Zn_{0.4})Fe_2O_4$ spinel ferrites, respectively, the laminated double layer spinel ferrite absorber with a thickness of 3mm achieved a reflection loss below -10 dB at 3.3–12.7 GHz, and the minimum value was -49.1 dB at 11.8 GHz.

Zhang (2009) developed core-shell structure nanocomposites by using coprecipitation method. They developed the coating of $CoFe_2O_4$ on the surface of $SrFe_{12}O_{19}$ nanoparticles. The core of strontium ferrite is spherical or elliptical with diameter in the range of 20–35 nm and the thickness of the shell is about 7nm. They observed that the saturation magnetization and the coercivity decrease from 31.7 emu/g and 4362Oe for $SrFe_{12}O_{19}$ to 27.9 emu/g and 3567Oe for $SrFe_{12}O_{19}/CoFe_2O_4$ nanocomposites. The decrease in saturation magnetization was attributed to the non-collinearity of the magnetic moments at the interface of two phases while for coercivity, the particles contact closely, the interphase exchange coupling occurs, with which the rotation of the domains on one particle as the field is reversed induces domains in contiguous particles to rotate, and thereby decreasing the coercivity (Zeng, 2004). They reported that $SrFe_{12}O_{19}/CoFe_2O_4$ nanocomposites has the strongest microwave absorption (-2.5 dB at 15.4 GHz) in comparison with core material $SrFe_{12}O_{19}$ (0.5 dB at 16.6 GHz) and the shell material $CoFe_2O_4$ (1.4 dB at 16.5 GHz).

Tabatabaie (2009) studied the microwave absorption properties of Mn and Ti doped strontium hexaferrite nanoparticles. They synthesized single domain (average particle size is less than 1μm) M-type strontium hexaferrites ($SrFe_9Mn_{1.5}Co_{1.5}O_{19}$ and $SrFe_9Co_{1.5}Ti_{1.5}O_{19}$) by solid-state method. They observed that the composite containing 70% ferrite and 1.8mm thickness possesses a reflection loss below -15 dB in the frequency range of 16.4–19.4 GHz. The maximum reflection loss observed for $SrFe_9Mn_{1.5}Co_{1.5}O_{19}$ is -26 dB at frequency of 18.84 GHz. Sharbati (2010) fabricated nanocrystalline strontium hexaferrite doped with Zr–Mg ($SrMg_xZr_xFe_{12-2x}O_{19}$, x = 0, 0.5, 1.0 and 1.5) synthesized by the citrate sol–gel process. The particles obtained possess irregular non-spherical shapes with a broad size distribution. They observed that the ferrite with a composition of $SrMg_{1.5}Zr_{1.5}Fe_9O_{19}$ exhibits a larger reflection loss and a wider bandwidth (1.8 GHz for RL more than -20dB) than those obtained from other compositions. They observed the minimum reflection loss of -43 dB at the matching frequency of 9.2 GHz, and also there is another matching frequency at 10.1 GHz with a reflection loss of -27 dB. Davoodi (2011) fabricated single phase Sn–Mg substituted strontium hexaferrites ($SrFe_{12-x}(Sn_{0.5}Mg_{0.5})_xO_{19}$) nanoparticles with irregular spherical shape by co-precipitation method. They observed that mean particle size of samples was decreased

from 82 to 56nm with increasing the Sn–Mg content from x = 0.0 to x = 0.8. It was found that increasing the Sn–Mg content from x = 0.0 to x = 0.8 led to a reduction in the coercivity from 4728.9 to 1455.5Oe and increasing the saturation magnetization from 51.34 to 65.49 emu/g. The composites which contained doped ferrite with x = 0.8 exhibited the largest reflection loss (-35 dB at 11.44 GHz) and the widest bandwidth (0.65GHz for reflection loss more than -15dB) relative to other specimens. This led to the conclusion that the composites containing doped ferrites had much more effective electromagnetic absorption properties than undoped constituent ferrite. Fannin (2011) reported the effect of synthesis method on the morphology and microwave absorption properties of ferrite. They studied the microwave absorbent properties of nanosized cobalt ferrite powders prepared by coprecipitation and subjected to different thermal treatments. They synthesized cobalt ferrite nano powders by means of two methods using a common precipitating agent. After coprecipitation, in the first method the cobalt ferrite was calcined (CC) at 200°C for 4h, whilst in the second method the precipitation was followed by a hydrothermal treatment (CHT). They observed that sample obtained by CC shows large particle agglomerations (with mean diameter in the order of 600 nm), whilst the second shows that the sample consists of smaller particles, with a mean diameter of 28 nm. They reported that over the frequency range 0.1–6 GHz, the sample obtained by the CC method (-10dB<RL<-15dB) has a smaller attenuation constant than that of the sample obtained by the CHT method (RL>-15dB), up to an approximate frequency of 2.7 GHz. Ting (2011) developed Ni-Zn ferrite magnetic particles by the sol–gel auto combustion method at room temperature followed by coating with polyaniline, using in situ polymerization at different aniline/Ni-Zn ferrite weight ratio (Ani/Ni-Zn ferrite = 1/1, 2/1, 3/1) and introduced into epoxy resin to be a microwave absorber. The calculated crystallite sizes of the Ni-Zn ferrite particles range from 0.2 to 0.5µm. They observed that specimen of the Ni-Zn ferrite showed only one band at 7.5GHz with −13 dB in reflection loss while polyaniline/Ni-Zn ferrite composites, exhibited a pronounced absorption bands at 14GHz with the reflection losses of −20 dB. They concluded that polyaniline/Ni-Zn ferrite powder showed better absorption bands than Ni-Zn ferrite at 2–18 GHz.

This section concluded that most of the studies are focusing on microwave absorption study of hexaferrite (BaFe$_{12}$O$_{19}$, SrFe$_{12}$O$_{19}$) and spinel ferrite (CoFe$_2$O$_2$, NiFe$_2$O$_4$ and ZnFe$_2$O$_4$) alone. A very few studies are focusing on the composite containing hexaferrite and spinel ferrite together as a magnetic composite. The attempt to develop a magnetic composite containing hard ferrite with large magnetic anisotropy (SrFe$_{12}$O$_{19}$) and soft spine ferrite (CoFe$_2$O$_4$, NiFe$_2$O$_4$ and ZnFe$_2$O$_4$) could be better microwave absorbing medium.

2.7.2 Non Mgnetic RAM

Composites added with dielectric material should be designed not only to carry loads but also to perform electromagnetic wave absorption. The dielectric RAMs like CB, CNTs, SiC and graphite etc. has the advantage that they are lighter than magnetic loss material such as iron nanoparticles, hexaferrite, spinel ferrite and composite hexaferrite and spinel ferrite etc. Kumar (1987) developed single layer microwave absorber using acetylene black and reported the increase in real and imaginary part of the complex permittivity with addition of carbon. Motojima (2003) examined the EM wave absorption properties of carbon micro coils (CMCs) with a three-dimensional-helical/spiral chiral structure (1–10 mm coil diameter and 0.1–10 mm coil length) in the range 12–110 GHz. They observed that multilayer absorption composites showed a higher EM absorptivity than that of single-layer composites. Also longer the coil length higher is the absorptivity obtained. Materials generally absorb the EM waves by the three mechanisms, i.e., dielectric loss, conductive loss and magnetic loss. The CMCs are typical chiral materials with a microcoiling morphology and shows different interactions from unchiral materials against EM waves. They proposed that when EM waves are irradiated on CMCs, the CMCs will act as chiral micro coils (microsolenoid) and an inductive electromotive force producing an inductive current in the CMCs and result in higher attenuation of EM waves. They concluded that for most effective generation of an inductive current, the coiling-chiral morphology of the fibers is considered to be a more favorable form than that of the straight or powder-like form. It is an important issue not only for military purposes but also from commercial point of view, whether or not the reflective wave from an incident electromagnetic wave can be nullified. By blending conductive carbon black with the binder matrix of glass/epoxy composite, a radar absorbing structure (RAS) which can support loads and absorb the electromagnetic wave can be designed (Oh, 2004). The specimens of the glass fabric are impregnated by epoxy mingled with carbon black. First, the mixing of epoxy matrix and carbon black was accomplished and the premixed matrix was uniformly applied to the glass fabrics. Oh et al fabricated radar absorbing structure in the following manner; the first layer of CB7, 7 wt% CB (thickness 0.6 mm) and second layer of CB5, 5 wt % CB (thickness 1.9 mm). The optimum structure showed 2.4 GHz in -10 dB absorbing bandwidth and 0.64 GHz in -20 dB absorbing bandwidth within the X-band frequency range. A thin and broad-band microwave absorber using synthesized $BaTiO_3$, polyaniline and commercial conducting carbon has been fabricated, and successfully

demonstrated for a maximum reflection loss of -25 dB (>99% power absorption) at 11.2 GHz with a bandwidth of 2.7 GHz in a sample thickness of 2.5 mm (Abbas, 2006).

Fan (2006) stated that the microwave absorption of CNTs composites is mainly attributed to the dielectric loss rather than magnetic loss. They prepared the different CNTs/polymer composites as microwave absorbing materials. They observed that position of reflectivity peak moves to a lower frequency and the loss factors of composites increase with increasing concentration of CNTs. When concentration of CNTs is increased to 4 wt%, there is a sharp increase of loss tangent. 4 wt% CNTs/PET and 8 wt% CNTs/varnish displayed considerable absorbing peak at 7.6 GHz, 15.3 GHz and achieved maximum absorbing value of -17.61 dB, -24.27 dB, respectively. In addition, the frequency range for absorbing values exceeding -5 dB of CNTs/ (PET, PP, varnish) composites are 13 GHz, 10 GHz and 6 GHz, respectively. They concluded that in order to select and design a microwave absorbing material in the specified frequency range; one should take into account not only the CNTs concentration, but also the kind of polymer and the thickness of materials. Wang (2008) studied the electromagnetic properties of carbon black and barium titanate nano composite material synthesized by sol–gel method. It was observed that $BaTiO_3$ powder is tetragonal phase and its grain was oval shape with average particle size of 80–100 nm which was coated by carbon black film (thickness about 5–20 nm). From electromagnetic (EM) complex permittivity, permeability and reflection loss (RL) data, it was concluded that composite is a kind of dielectric loss material (mainly come from polarization relaxation) and exhibits a minimum RL value of −23 dB at 13.4 GHz (with 30 wt. % CP). They also concluded that content of carbon species in the composite also play a very important role in the microwave absorption properties of composite. When the content of CB in the matrix is too higher, it can cause an increase of the amount and size of the CB contacting aggregates which in turn rapidly decrease the absorption properties of the composite. (Wu, 2008). A core shell structure of carbon black coated with polyaniline was introduced into epoxy resin to prepare a microwave absorbing medium. The core shell structural PANI/CB composites exhibiting electromagnetic properties were synthesized by in situ polymerization method. It is concluded that PANI/CB (20 and 30 wt.%) composites exhibit good absorption performances (-40 dB) over a broadband range in the radar band (2-40 GHz). The changes in microwave absorbing properties of composites are due to the dielectric and magnetic loss generated by the magnetic dipoles and by the changes of boundary condition of the microwave field at the interface between the PANI/CB particle and polymer matrix.

The dielectric absorbers utilize conductive fillers like CB (carbon black), MWNT (multiwalled carbon nano tube), CNF (carbon nano fiber), SCF (short carbon fiber), silver powder, etc (Oh, 2004). The conductive fillers are used to control the complex permittivity only. The conductive fillers are relatively of low density and their mixing ratios are very low in comparison with those of the magnetic fillers. The microwave absorbers for RCS reduction are usually used in external surface of structure, so that they need to have good characteristics such as light weight, lower thickness, high structural strength and chemical resistance, as well as good absorbing performance. The E-glass fabric/epoxy composite laminate can be a good candidate for the microwave absorbers, because of its good structural and chemical performance, low dielectric constant and capability to be absorbent by adding magnetic and/or conductive fillers in the epoxy matrix (Kim, 2008). Microwave absorption of E-glass/epoxy composite laminates containing three different types of carbon nano materials such as carbon black (CB), carbon nano fiber (CNF) and multi-wall carbon nano tube (MWNT) in X-band (8.2–12.4 GHz) is studied. The experimental results showed that the real and imaginary parts of the complex permittivity of the composites are proportional to the filler concentrations and, they observed that, the electrical properties including dc conductivity and complex permittivity of composites depend on the filler characteristics (configuration, dimension, intrinsic electric property, etc). The orders of increasing rates of the dc conductivities and complex permittivity with respect to filler concentrations were all CNF > MWNT>>CB. The excellence of CNF is due to its straightness and length, in addition to the high conductivity. The straightness of CNF offered the big electric dipoles and induces higher dielectric constant of composites. The complex permittivity for single-layer absorbers were obtained and they showed that the real part of complex permittivity has greater effect on the absorber thickness than the imaginary part. The optimal thicknesses of composite materials for single-layer absorbers were obtained using the Cole–Cole plot of the complex permittivity ($\varepsilon = \varepsilon' - j\varepsilon''$) of single-layer absorber and experimental complex permittivity data. The order of the optimal thickness of the composite materials was CNF < MWNT<<CB. It can be noted that the increasing rate of real part in comparison with that of imaginary part is the meaningful factor for thin matching thickness rather than the increasing rates themselves. Phang (2008) fabricated a nanomaterial possessing moderate conductivity, magnetic and dielectric property. It was fabricated by using novel hexanoic acid (HA)-doped, polyaniline (PAni) nanocomposites containing TiO_2 nanoparticles (dielectric filler) and carbon nanotubes, CNTs (magnetic fillers such as single-walled carbon nanotube, SWNT and multi-

33

walled carbon nanotube, MWNT). They reported that PAni/HA/TiO$_2$/SWNT with 20% of SWNT exhibits the best microwave absorption property (~99.2% absorption) with reflection loss of−21.7 dB at 6 GHz due to its moderate conductivity (1.27 S/cm), magnetization (Ms = 1.01 emu/g), highest tan δ and heterogeneity. Cao (2010) reported the dielectric measurement of short carbon fiber/silica composite in the frequency range from 8.2 to 12.4 GHz at temperatures between 30 and 600°C. The composite was prepared by conventional ceramic processing. The shortened relaxation time of electron polarization in CF/SiO$_2$ attributed to enhance ε' with increasing temperature, and the effect of enhanced electrical conductivity in CFs could be considered as a dominating factor enhancing ε". The shielding effectiveness was greater than -10 dB which indicates that CF/SiO$_2$ could be applied in microwave devices and apparatus. Micheli (2010) stated that composite materials have different dielectric losses as function of the size and shape of the granular carbon matter added to the polymeric matrix. They developed several carbon species: micro-sized granular graphite, fullerenes, carbon nanofibers, single- and multi-walled carbon nanotubes in the matrix of epoxy resin. They observed that CNFs have shown higher dielectric permittivity then SWCNTs, and SWCNTs in turn higher permittivity than MWCNTs and micro-graphite. They found that the loss factor of a composite reinforced with 1 wt.% of carbon nanostructures (CNF and SWCNT) inclusions is even three times greater than that of 'heavy graphite-reinforced' (10 wt.%) composite. These results are very important in order to build advanced and lightweight microwave absorbing structures. The results obtained show that in the most part of bandwidth the reflection coefficient has a value lower than -20 dB, with two peaks under -35 dB. This latter surely represents an interesting result for both the low RC of the proposed RAS over the whole X band and the thinness of the four layer structure.

Liu (2011) prepared absorbing medium using nanosize carbon black (CB) blended with nanosize silicon carbide (SiC). SiC particles are shaped into irregular cubes with an average size of around 80–100 nm by template technique. It was observed that the CB particles with original average diameter of 18 nm are severely aggregated and prone to form multi-pore secondary structures. These specific structures, possessing high surface areas, lead to plenty of interfacial polarization to weaken the energy of EM waves. They also reported that addition of certain mass of SiC improved the microwave absorption of the composite. When 5 wt.% carbon black is blended with 50 wt.% SiC to fabricate a composite with a 2 mm thickness, the maximum reflection loss becomes -41 dB at 9 GHz, and the -10 dB bandwidth reaches 6 GHz.

2.7.3 Composite of Magnetic and Non Magnetic RAM

Srivastava (1992) developed microwave absorber using polymer, carbon and ferrite in the frequency range of 2.5 to 4 GHz. They reported the material showing the microwave losses comprising of magnetic and dielectric loss. They reported maximum of RL of -18 dB at 3.38 GHz for a thickness of 4.9 mm, the mixing ratio of rubber: carbon: ferrite was 1:0.4: 0.6.

Miyata (1997) developed double layer EM wave absorber with a 1.5 mm carbonyl iron and 0.5 mm barium titanate loaded rubber. They have reported -29 dB RL at 0.9 GHz and concluded that the matching frequency can easily be designed to any frequency in quasi microwave band by controlling the thickness of the layer of ferroelectric substance. Such material was found to have applications in quasi-microwave-band applications such as cellular phones and personal data assistants. Choi (2004) prepared Fe_3O_4-encapsulated $BaTiO_3$ composite powders with ultrasound-enhanced ferrite plating. Fe_3O_4 particles of 20-30nm in diameter grew in a spherical form and coated quite densely on the $BaTiO_3$ grains. The coating thickness was ~40 nm. Each Fe_3O_4 particle appeared to be of a single magnetite crystal. The specimen of the $BaTiO_3$ powder showed only one band at 9GHz with -27 dB in reflection loss. Among the composite powders, the powder prepared from the buffer concentration of 0.2M exhibited the two relatively pronounced absorption bands at 8 and 13 GHz, with the reflection losses of -24 dB and -8 dB, respectively. In addition, the matching thickness of the $BaTiO_3$ specimen was 2.33mm at 9 GHz, while in the $Fe_3O_4/BaTiO_3$ composite one, the matching thickness reduced to 1.83 mm.

Tang (2006) reported the novel magnetic–dielectric composites, the anatase titania-coated barium ferrite particles. The barium ferrite particles were having hexagonal platelet crystals which were stacked each other due to magnetic attraction between the particles. The results showed that the titania coverage on barium ferrite has a great influence on its microwave properties. Comparing the anatase titania-coated barium ferrite composites with the uncoated barium ferrite, the complex permittivity of the composites was higher than that of the uncoated barium ferrite. The enhancement of the complex permittivity is attributed to dipolar polarization and interfacial polarization. The complex permeability of composites was found to decrease with increase in frequency as well as with the molar ratio of Ti to Ba. The maximum reflection loss (-19 dB at 7.5 GHz) was obtained for Ti: Ba ratio of 1:10, the position of the maximum reflection loss peak shifts to a lower frequency value with the

increasing titania fraction. It has been observed that the properties of interfaces could have a dominant role in determining dielectric performance. Additionally, joule heating loss will also occur due to finite conductivity of the composites comprising magnetic and non magnetic phases (Tang, 2006). Since the titania-coated barium ferrite composite is a heterogeneous system, and interfacial polarization is another important polarization process, associated relaxation also will give rise to loss mechanism.

Soft magnet $CoFe_2O_4$ ferrite has a large saturation magnetization and high Snoek's limit, which results in high complex permeability values at a wide frequency range. This factor makes $CoFe_2O_4$ highly useful as a thin absorber working at a high-frequency band. Che (2006) fabricated large-scale $CNT/CoFe_2O_4$ nanocomposite by chemical vapor deposition method using $CoFe_2O_4$ nanoparticles as catalysts. Microwave absorption of the $CNT/CoFe_2O_4$ nanocomposites at 2–18 GHz is observed to enhanced, as compared with that of both pure CNTs and $CoFe_2O_4$ nanoparticles. The enhancement mechanism is explained on the basis of magnetization hysteresis loop measurement and electromagnetic theory. It is stated that, this improvement may originate from the better match between dielectric loss (due to CNTs) and magnetic loss (cobalt spinel ferrite).

Shen (2007) synthesized M-type $BaFe_{12}O_{19}$ and W-type $BaCo_2Fe_{16}O_{27}$ hexaferrites by citrate sol–gel technique. M-type ferrite, showed the average size of about 80 nm and W-type ferrite showed the perfect hexagonal crystal with size of about 3–5 μm. The diameter of the carbon fibers is about 7.5 μm and their dimensions are very uniform. Double-layer microwave absorbers composed of W-type ferrite composite and M-type ferrite composite filled with short carbon fiber were designed based on their own better absorption properties. It is concluded that addition of short carbon fiber largely improved microwave absorption properties of M type ferrite composite, and the absorption of double-layer absorbers depend on the combination of different layer. The absorption is excellent when the W-type composite was used as inner layer. Absorbing bandwidth less than −10 dB can reach 3.2 GHz, and absorbing peak value of −22.0 dB at about 12.7 GHz is observed. These composites have magnetoelectric effects and electromagnetic properties that are absent in their constituent phases. Wu (2008) fabricated bamboo charcoal (BC) coated with $Ni_{0.5}Zn_{0.5}Fe_2O_4$ spinel ferrite nanoparticles. This was forming a core–shell structure which with different bamboo charcoal content (10, 20 and 30 wt%) was introduced into epoxy resin to prepared a microwave absorbing medium. Pure BC had a porous surface. After coating with NiZn ferrite, a continuous overlayer of magnetic powders was produced on the BC particle surface.

The $Ni_{0.5}Zn_{0.5}Fe_2O_4$ particles were almost spherical with diameters ranging from 8 to 20 nm. In the frequency range of 18–40 GHz, the absorption bands of three samples appeared at frequency of 27.8, 34.0 and 33.3 GHz with -8.5, -13.5 and -32.7 dB respectively. The Ni-Zn ferrite/BC-30 observed to exhibits the largest reflection loss and the widest bandwidth than those obtained from other specimen. Zhang (2009) studied the microwave absorbing properties (in the frequency range of 2–18 GHz) of Sm_2O_3-filled MWCNTs, which were prepared by wet chemical method. Sm_2O_3 nanoparticles encapsulated in the nanotubes are considered to play an important role in improving the magnetic loss of MWCNTs. Compared to unfilled MWCNTs, the maximum absorbing peak of Sm_2O_3-filled MWCNTs shifts to higher frequency range, and the absorbing bandwidth becomes much broader. With increasing thickness, the maximum RL of Sm_2O_3-filled MWCNTs shifts to lower frequency and multiple absorbing peaks appear. For raw MWCNTs, the maximum absorbing peak of −21.58 dB at 9.40 GHz (d_m = 2.0 mm) is observed with band width of 1.58 GHz (for RL below −10 dB). In contrast, under the same d_m, the absorbing peak of Sm_2O_3- filled MWCNTs becomes broader and the maximum absorbing peak decreases to -12.22 dB at 13.4 GHz, which is in the frequency range of Ku wave band. Zhao (2009) filled the carbon nanotubes (CNTs) with Fe nanoparticles using a wet-chemical method. The CNTs were prepared by catalytic decomposition of benzene using floating transition at 1100–1200°C. CNTs were found to have inner diameter in the range of 20–40nm and an outer diameter in the range of 40–60nm with lengths of 5–15μm. The saturation magnetization M_s, remanent magnetization M_r, and coercivity H_c, were $50.70 Am^2 kg^{-1}$, $3.16 Am^2 kg^{-1}$ and $21.78 KAm^{-1}$ for Fe-filled CNTs, respectively. The reflection loss of the CNT/epoxy composites is below −10 dB (90% absorption) at 10.1–13.1 GHz, and the minimum value is −22.89 dB at 11.4 GHz. The bandwidth corresponding to the reflection loss below −10 dB is 3.0 GHz. For the Fe-filled CNTs, the reflection loss of the corresponding composites is below −10 dB at 11.8–14.7 GHz, and the minimum value is −31.71 dB at 13.2 GHz. The bandwidth corresponding to the reflection loss below −10 dB reached to 2.9 GHz for the thickness of 1mm. Qi (2009) synthesized carbon nanotubes of high helicity (H-CNTs, Sample A) by pyrolysis of acetylene at 450°C over Fe nanoparticles derived from coprecipitation / hydrogen reduction method. With controlled introduction of hydrogen during acetylene pyrolysis, CNTs of low helicity (L-HCNTs, Sample B) and worm-like CNTs (Sample C) were obtained in large quantities. Good absorption of electromagnetic wave (reflectionlosso-20 dB) was observed in the 7.18–10.68 and 7.5–10.7GHz range over composites B and C (2.0–3.0mmthickness), respectively.

The diameters of the tubes were in the 80–180nm range. In the case of Sample A, The RL value reaches its maximum (-25.78 dB) at 7.18GHz and at thickness dm ¼ 3:0mm, while the absorption range below -10dB is roughly 4–18GHz. The inner diameter and wall thickness of the worm-like CNTs range from 120 to 350nm and 30 to 50 nm, respectively (sample C). The maximum RL value (at composite thickness dm ¼ 2.8mm) reaches -26.39 dB at 7.71GHz, higher than that of composite A or B. Also, RL values below -20 dB are obtained in 7.5–10.7GHz with thickness of composite C in the 2.0–3.0 mm range. At d_m= 2.0mm, the band width corresponding to RL values below -5 dB is about 10.0GHz. Clearly, composite C is superior to composites A and B in microwave absorption.

Qiang (2010) used carbon fibers with a diameter of 5–10 μm to prepare Fe_3O_4/CFs composites by wet chemical method. The lowest reflectivity of the Fe_3O_4/CFs composites was found to be −35 dB at 6.37GHz for a layer of 4.41mm in thickness. The strong absorption (RL <−10 dB and −20 dB) is broadened from the 3.52 to 10.01GHz and 5.49 to 7.75GHz with the thickness varying from 5.12 to 2.90mm, respectively. Liu (2009) fabricated (Fe, Ni)/C nanocapsules with soft magnetic (Fe, Ni) nanoparticles as cores and graphite as shells by a modified arc discharge technique in ethanol. They stated that, the graphite shell plays the double role that makes the (Fe, Ni) nanoparticles free from oxidation and the separator for suppressing the eddy current loss. They observed that, for the (Fe, Ni)/C nanocapsules, the RL values exceeding -10 dB are achieved in the whole Ku-band (12.4–18 GHz) for d_m = 2.0 mm, and an optimal RL value of -26.9 dB is observed at f_m = 16 GHz with the -20 dB bandwidth over the frequency range of 13.6– 16.6 GHz. Liu (2010) developed a single-layer wave-absorbing coating employing complex absorbents composed of carbonyl-iron powder (CIP) and carbon black (CB) with epoxy resin as matrix to prevent serious electromagnetic interference. The results showed that the higher thickness, CIP or CB content could make the absorption band shift towards the lower frequency range. So the wave-absorbing coating could be applied in desired frequency range through adjusting the content of CIP or CB in composites. The minimum reflection loss for this composite reached to -17.5 dB at 15.9 GHz.

Hou (2011) fabricated the polymer matrix composites with the different rarer metal - doped MWCNTs and the pure MWCNTs as the absorber in the first and second layer respectively (4 mm in thickness). The raw MWCNTs, with the length up to several μm and the diameter about 30–50 nm, intertwined with each other. The double-layer EM wave absorption composites with the MWCNTs doped different RM (Co/La/Ni) as absorber in the

first layer and the pure MWCNTs as absorber in the second layer showed better absorption properties when the total thickness was 4 mm. Based on the absorption bandwidth (maximum is 5.28 GHz), the reflection loss (<-10 dB or >90%) of the MWCNTs doped Ni was the widest. Wang (2011) studied the effect of MWCNT content on the magnetic and microwave absorption properties of strontium hexaferrite. Different mass ratios of $SrFe_{12}O_{19}$-MWCNTs composites were prepared by sol–gel method, where $SrFe_{12}O_{19}$ nanoparticles were coated on the surface of MWCNTs. It is observed that composites exhibit good absorption performances in the lower frequency (0–6000 MHz) with good electromagnetic properties. Comparison the pure $SrFe_{12}O_{19}$ with the $SrFe_{12}O_{19}$-MWCNTs composites observed to have large coercive force and low saturation magnetization. Measurements of electromagnetic parameters and wave absorbing characteristic indicate that magnetic loss mechanism caused by strontium ferrite plays a dominant role in the low-frequency. Meanwhile, the existence of MWCNTs increases the anisotropy of the composites, which enhances the wave absorbing strength. $SrFe_{12}O_{19}$-MWCNTs (6wt.% CNT) composite observed to possesses the best magnetic and wave absorbing properties (-19 dB at 3GHz).

Liu (2011) synthesized cobalt oxides/carbon fibers (CoOx/CFs) composites by thermal oxidation of cobalt coated carbon fibers (Co/CFs). The diameter of the carbon fiber is about 8μm.When annealed at 350ºC for 3 h, all carbon fibers remain intact and have been coated with cobalt-oxides layers of about 0.7μm. The reflectivity of cobalt covered carbon fibers is more than −2.57 dB with the thickness varying from 1.0mm to 5.0mm which indicates the Co/CFs composites have poor microwave absorption property. The reflectivity of the prepared CoOx/CFs composites is less than −10 dB over the frequency range of 4.04–18GHz when the thickness of sample is between 1.11mm and 5.12mm, and less than −20 dB over the range of 11.54–14.77GHz (1.36–1.83mm in thickness). The lowest reflectivity of the CoOx/CFs composites is −45.16 dB at 13.41GHz and the corresponding thickness is 1.5mm.

This section concluded that most of the studies are focusing on microwave absorption study of composite comprising of metal particle filled in non magnetic species like carbon nanotube. A very few studies are focusing on the composite containing hexaferrite and non magnetic carbon species like CB, CNT and SiC. The attempt to develop a composite containing hard ferrite with large magnetic anisotropy ($SrFe_{12}O_{19}$) and non magnetic material (CB, CNT and SiC) could be better microwave absorbing medium.

2.7.4 Coated RAM

Liu (2006) has coated hollow glass microspheres with thin nickel films of various thicknesses (about 50–250 nm) by electroless (EL) coating technique. The permittivity and permeability increased with increasing microsphere content in the composite and with increasing Ni film thickness. These composites had ferromagnetic resonance peak in the range of 5–12 GHz. Zhang (2006) has reported the development of carbon-coated Ni(C) nanocapsules prepared by a modified arc-discharge method in methane atmosphere. Its electromagnetic parameters were measured at 2–18 GHz. It was observed that the natural resonance which appeared at 5.5 GHz is dominant among microwave absorption properties of Ni(C) nanocapsules, as the consequence of the increased surface anisotropic energy for nanosized particles. The measured relative complex permittivity indicates that a high resistivity existed in Ni(C) nanocapsules samples. The maximum RL for of Ni(C) nanocomposites can reach a value of -32 dB at 13 GHz with 2 mm thickness.

Pan (2007) has developed a new type of Co–Ni–P coated strontium ferrite nanocomposite with EL plating enhanced by ultrasonic stirring at room temperature. The maximum microwave loss of the composite powder reaches -44.12 dB. The bandwidth with the loss above 10 dB exceeds 13.8 GHz. The plated powders possess more effective microwave absorption properties than the conventional strontium ferrite powder. Especially, the microwave absorption ability was improved greatly with the heat treatment at 400 °C for 1 h in the N_2 flow.

Zhao (2008) investigated microwave absorbing property, complex permittivity, and permeability of epoxy composites containing Ni-coated and Ag nanowires filled carbon nanotubes (CNTs). CNTs were coated with nickel by an electroless plating technique, also CNTs were filled with Ag nanowires using wet chemical method. Compared with the CNTs/epoxy composites, the real part (ε') and imaginary part (ε") of the complex permittivity as well as dielectric dissipation factor ($\tan\delta = \varepsilon"/\varepsilon$') of the epoxy composites containing the Ni–P coated CNTs were much smaller, while the real part (μ') and imaginary part (μ") of the complex permeability and the magnetic dissipation factor ($tg\delta\mu = \mu"/\mu$') were greater. The microwave absorption enhancement of Ni-coated CNTs/epoxy composites resulted from dielectric and magnetic losses. In contrast, the microwave absorption of Ag nanowire-filled CNTs/epoxy composites was mainly attributed to the dielectric loss rather than magnetic loss. The absorption peak frequency of the CNTs/epoxy composites can be controlled by plating CNTs with nickel or by filling Ag nanowire into CNTs. It is observed that the epoxy

composites containing CNTs achieved a reflection loss below -10 dB (90% absorption) over 3.0 GHz in the range of 10.1–13.1 GHz, and the minimum value was -22.89 dB at 11.4 GHz. When the CNTs were coated with nickel (before heat treatment), the microwave absorption peaks from the corresponding composites moved to the higher frequency (-11.58dB at 14.0 GHz). But after the Ni–P (-13.36dB at 7.59 GHz) and Ni–N (-19.19dB at 8.59 GHz) coated CNTs were heat-treated at 600°C in hydrogen atmosphere for 5 h, the microwave absorption peaks from the corresponding composites shifted to the lower frequency. Li (2008) prepared silicon carbide particles reinforced nickel–cobalt–phosphorus matrix composite coatings by two-step electroless plating process (pre-treatment of sensitizing and subsequent plating) for the application to lightweight microwave absorbers. Due to the conductive and ferromagnetic behavior of the Ni–Co thin films, high dielectric constant and magnetic loss can be obtained in the microwave frequencies. The maximum microwave loss of the composite powder less than -32 dB was found at the frequency of 6.30 GHz with a thickness of 2.5 mm when the initial atomic ratio of Ni–Co in the plating bath is 1.5.

Sharma (2008) coated Ni-, Ti-substituted nanocrystalline M-type barium hexaferrite powder ($BaNi_xTi_xFe_{12-2x}O_{19}$ ($x = 0.4$) of size ~10 nm) with Ni-P by using electroless (EL) coating technique to form EL $Ni-P/BaNi_{0.4}Ti_{0.4}Fe_{11.2}O_{19}$, a radar absorbing material (RAM) nanocomposite powder. They observed that the particle size of RAM powders before and after Ni-P coating were found to be in the range of 10–15 nm and 15–25 nm respectively. A uniform layer of 5–10 nm thick coating is deposited due to the controlled growth of EL Ni-P nanoglobules onto the powder. The reflection loss (RL) of the EL (Ni-P)/RAM nanocomposite powder in Ku band (12.4 –18 GHz) was evidently enhanced to −28.70 dB, as compared to the EL Ni-P nano globules (−16.20 dB) and nano crystalline RAM powder (−24.20 dB). After annealing at 400°C for 4 h, the RL and bandwidth of EL (Ni-P)/RAM nanocomposite powder was further improved from −24.20 to −35.90 dB and 1.50 to 4.00 GHz respectively.

Park (2011) investigated the microwave absorbing hybrid composites containing metal coated one-dimensional carbon nanomaterials for wider absorption bandwidth (BW) with thinner thickness. The optimally designed dielectric carbon nanofibers (CNFs)/epoxy composites had -10 dB absorbing band width of 2.8 GHz (8.8–11.6) in the X-band with the content of 3.0 wt.% (2.30 mm thickness). For the improvement of the magnetic characteristics of the fillers, Ni–Fe coated CNFs were prepared by electroless plating. The typical thickness of Ni–Fe deposited layers was about 200–300 nm. Using the prepared

41

hybrid nanofillers, optimally designed Ni–Fe coated CNFs/epoxy composites had -10 dB absorbing band width of 3.7 GHz (8.3–12.0) in the X-band with the content of 40.0 wt.% (2.40 mm thickness). The -10 dB absorbing band width per unit thickness is about 1.54 GHz/mm. The hybrid composites showed about 26% improvement over the dielectric composites. This study illustrates effective electroless plating for the manufacturing of metal-coated CNFs as new composite fillers for EM wave absorption.

This section concluded Ni-P coated barium hexaferrite nanoparticles using electroless coating technology are observed to be potential material for microwave absorption applications (Sharma, 2009). An attempt could be made to developed Ni-P coated strontium hexaferrite nanoparticle system for microwave absorption application. This can also be compare with data available for Ni-P coated barium hexaferrite nanoparticle.

2.8 ELECTROLESS COATING TECHNOLOGY

Electroless, EL (Electro+ Less i.e. without using electrical energy) nickel-phosphorus deposits are produced by the autocatalytic electrochemical reduction of nickel ion onto the substrate from the solution of coating bath (Agarwala, 2006). The EL coating process that led to the practical application of these deposits was developed by Brenner and Riddell in 1946, and the first patent for it was awarded in 1950 (Brenner and Riddell, 1946; 1963).

During past five decades, EL coating has gained popularity due to its ability to produce coatings that possess excellent corrosion, wear and abrasion resistance. Although EL Ni–P deposits give satisfactory performance for several applications, enhancing their performance to suit different end uses warrant further development. The composite coatings were first carried out in pursuing for improved corrosion resistance for electrodeposited nickel-chromium by Odekerken (1966), in which an intermediate layer, containing finely divided particles including: aluminum oxide and polyvinyl chloride resin (PVC) distributed within a metallic matrix. Further electroless nickel coating containing alumina (Al_2O_3) particles was enunciated by Mallory (1979) in the year 1966. This is achieved either by adding second phase element(s) or by incorporating hard/soft particles in the Ni–P matrix. A detailed account of EL nickel composite coating was presented earlier by Feldstein (1983). The co-deposition efficiency of the second phase particles reinforced in the matrix depends on the size, shape, density, polarity, concentration and method of suspension of these particles in the bath. During last five years, several researchers have controlled these

parameters for EL Ni-P based composite coatings successfully and were able to co-deposit second phase nano particles in the EL Ni-P matrix and this led this classical EL coating technology to a further step that is EL nanocomposite coatings, ELNCC.

2.8.1 Development of El-NiP Coating Matrix

EL nickel is primarily used for engineering applications where uniform thicknesses, high hardness, wear resistance and improved corrosion resistance of the surface are required (Mallory, 1974; Pai, 1975; Mahoney, 1985; Bakonyi, 1986; Baczewska, 1996; Agarwala, 2005; Bangwei, 1999; Bozzini, 1997; 1999; Abraham, 1990; 1992) . Thus, the coating can be used (a) to deposit on complex shapes; (b) on large surfaces, especially large interior surfaces; (c) on surfaces subjected to wear; (d) to replace expensive stainless steel vessels in some processing industries; (e) to repair or salvage nickel-plated machine parts; (f) for nickel depositions where electrical power is not available or possible; (g) for improving the adhesion of enamels on steel; and (h) on printed circuit boards and electronics industries for corrosion resistance and solderability and to replace gold coating (Brenner, 1963; Gaurilov,, 1979; Catuala, 1995). With increased use of aluminum alloys in industrial machinery, EL nickel-plated aluminum has a bright future. Aluminum or beryllium parts coated with EL nickel and precision turned to an accuracy of 0.05 and 1.0 μm smoothness are used in parabolloid mirrors in space vehicles (Baudrand, 1994). Beryllium hemispheres coated with diamond turnable EL nickel are used in gyroscopes (Henry, 1985; Balaraju, 2003).

EL nickel is now being advocated as a prelate for additives and semi additive circuitry because of its faster rates of build up, greater solution stability, and consistent results. EL nickel is found to be one of the metals that possesses a low catalytic effect on hydrazine and methyl hydrazine decomposition and has been used as a surface coating on steel to delay the pressure build up during prolonged storage. The excellent corrosion resistance of high phosphorus nickel coatings has found wide application in many industries because it is a cheaper substitute for construction materials like nickel, monel, or stainless steel (Mallory, 1974). The cost for nickel or titanium cladding as a construction material in the manufacture of reaction vessels in some chemical industries is prohibitive. Hence, EL nickel, with high phosphorus, offers a cheaper alternative. EL nickel phosphorus has found application as a solar absorber in solar collectors. The bright Ni-P deposits can be blackened with dilute acids and black coating produced possesses good optical properties.

2.8.2 Recent Development in El Ni-P Coating Matrix

EL deposition nanotechnologies for the first time allows one to produce photo masks and micro devices with nanosized adjacent elements of different thicknesses made of various materials by single conventional optical photolithography (Khoperia, 2003; Harikrishnan, 2006; Crobu, 2008). These advantages significantly extend functional capabilities of the device, simplify removal of undesirable gases, and heat dissipation. The proposed nanotechnologies are much more advantageous and simpler than other expensive and complicated methods such as e-beam, X-ray lithography, or production of the devices using light phase shift photo masks. Methods of fabricating the ultrathin void-free and pore-free EL coatings on micro-, meso- and nanosized particles (carbides, borides, nitrides, oxides, diamond, graphite, etc.) are also proposed. These methods allow one to obtain nanostructured composite materials and coatings with the specified properties. The developed technologies will be applied in these industries soon (Shacham, 2007). Wear tests on self-mated pairs of Ni, Cu, and Ni-P deposits have been carried out during the Ni-P EL plating process onto the friction surfaces. The in-situ EL plating of Ni-P enhanced the growth process of transfer particles during Cu/Cu and Ni/Ni rubbing. It also increased the coefficient of friction in both cases. In the rubbing of Ni-P, Ni-P plating had no effect on the growth of transfer particles and coefficient of friction. The hardness test showed that the transfer particles at the interface of pin and disk were harder than the bulk of pin and disk. The effect of Ni-P plating during wear is due to the enhancement of the shear strength of transfer particles compared to the original surface (Harikrishnan, 2006).

The EL nickel deposition bath is known to have a major problem of sudden bath decomposition, which results in an increase in the operating cost of the process. Bath stabilizers have normally been added to extend its life and smoother operation. It has been demonstrated that the addition of thiourea and maleic acid significantly improved the stability of the EL nickel bath. It has been observed that the stabilizers have a minor major effect on phosphorus content and the morphology of the electroless nickel deposits, respectively. It has also been shown that the addition of the stabilizers has an effect on the nano grain size of the EL nickel deposit (Cheong, 2004). EL nickel plating on hollow glass micro spheres with hypophosphite as a reducing agent in an alkaline bath has been studied (Zhang, 2006). The hollow glass spheres adsorbed more palladium induced active catalytic centers on their surfaces during pretreatment. Hence, continuous and uniform coated microspheres have been achieved. The magnetic property of microspheres was improved by adjusting the pH and the concentration of

the reducing agent in an optimum range. The morphology, composition, and structure of deposits have been investigated, and it has been found that the deposits on hollow glass microspheres grew thicker with prolonged plating time. Post treatment of the coated Ni glass spheres improved the crystalline structure of the plated Ni layer. EMI shielding effectiveness (SE) of single-layer or double-layers of EL coatings, such as nickel phosphorus–pure nickel (NiP-Ni), Ni-NiP, NiP-Cu, Ni-Cu, and coated carbon fiber reinforced acrylonitrile-butadiene-styrene (ABS) composites have been investigated. The resistivity and antioxidization of conductive fillers were important factors for EMI shielding composites. Although the electrical resistivity of electroless copper coated carbon fiber (ECCF) is much lower than that of EL Ni-P coated carbon fiber (ENCF), electroless copper films on the carbon fibers readily oxidized during compounding processes. The resistivity of combined ECCFyABS composites increased significantly after ECCF and ENCF composite fabrication. As a result, the EMI SE of the ECCFyABS composite showed a poor EMI SE (37 dBm) as compared to those EL metals-coated carbon fiber–reinforced ABS composites. The coated double-layer EL metals on the conductive fillers were obtained by the EL method. The outside metal layer, which possessed better antioxidizing properties, provided suitable protection for the conductive fillers. Thus, the EMI SE of the ECCFyABS composite improves effectively. The best EMI SE of double-layer EL coated metals yABS composites has been reached to 65 dBm.

2.8.3   EI NI-P Micro/Nanocomposite Coating Bath

An example of an experimental set-up used for producing EL nickel composite coatings, similar to the one described by Sharma (2005, 2002, 2002) is shown in Figure 2.6 used a similar alkaline EL Ni-P bath assembly for incorporating in-situ co-precipitation reaction successfully to deposit Ni-P-nX (nX=ZrO_2-Al_2O_3-Al_3Zr) particles in Ni–P matrix. This arrangement consists of a copper beaker placed the silicon oil bath circulated by a motor. The temperature of the bath is controlled at an accuracy of ± 0.2 °C. The pH is measured by a pH meter with accuracy ±0.01. A corning glass beaker is placed tight inside the copper beaker to maintain the uniform temperature. Other EL bath constructions have also been used successfully by many groups reported in literature (Agarwala, 1987; Rajagopal, 1989; Grosjean, 1997; Sharma, 2002; Necula, 2007; Srivastava, 1992; 1992) to coat EL Ni-P and Ni-B based composite coatings.
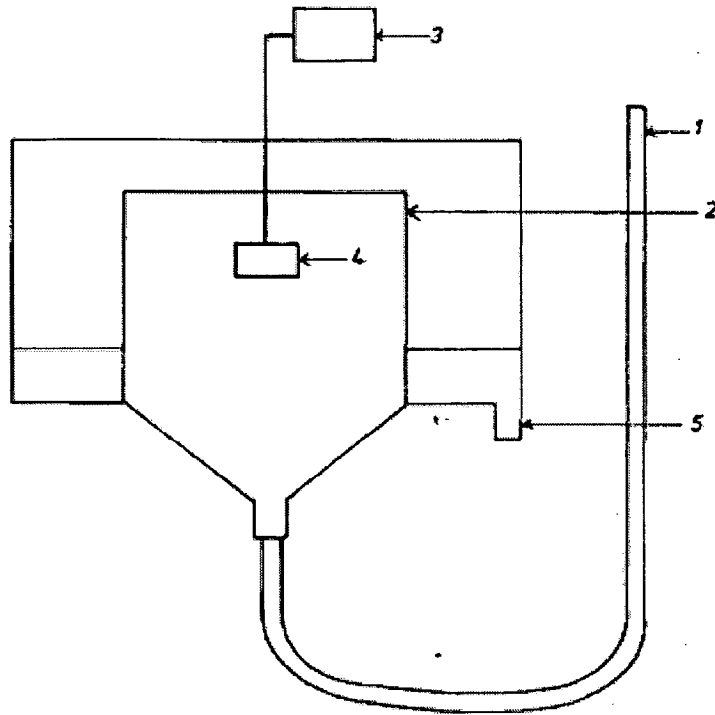
Fig. 2.6: Experimental set-up recommended for producing EL composite coatings. (Rajagopal 1989) Key: (1) inlet for thermostated electroless composite bath, (2) overflow level, (3) Mechanical arrangement for the slow rotation of component, (4) component subjected to EL composite coating, and (5) outlet for solution.

2.8.4 Factors Influencing El Ni-P Composite Coating Process

Several factors influence the incorporation of hard and soft second phase particles in an EL Ni–P matrix including, particle morphology (size and shape), relative density of the particle, particle charge, inertness of the particle, the concentration of particles in the coating bath, the method and degree of agitation, the compatibility of particle with the matrix, and the orientation of the part being plated and the most important of these all is the time spend by the particle onto the surface of the substrate (Balaraju 2003; Agarwala,2006)

2.8.4.1 SIZES OF NI-P MATRIX AND SECOND PHASE PARTICLE

The size of the particles has a definite impact on their incorporation in the EL Ni–P matrix (Grosjean, 1997; Apachitei, 1998). In general, it is recommended that particles must be large and heavy enough to settle in the solution yet not so large as to make the deposit rough or make it difficult for them to be held in suspension. Also, the size of the particles should be

selected with reference to the thickness of the EL Ni-P deposition, as attempts made to incorporate 10 µm size particles in a 7 µm thick EL nickel deposit resulted in unsatisfactory deposit and incorporation of 10 µm size particles even in a 25 lm thick deposit physically weakened the deposit. It is suggested that particles in the size range of 2-7 µm might be suitable for co-deposition in an EL Ni-P matrix, with particles in the size range 4-7 µm being easiest to work with. Grosjean (1997) has suggested that whatever the concentration of silicon carbide particles in the bath, the majority of the particles incorporated in the Ni-P matrix are in the range 0.3-1.8 µm diameter. Apachitei (1998) has found that, under similar operating conditions, smaller particles in a narrow size distribution yield maximum incorporation and also recommended that for achieving a better integrity between the particles and the EL Ni-P matrix, the size of the particles should be small so that they can be firmly held by the matrix.

2.8.4.2 MORPHOLOGY OF SECOND PHASE PARTICLES

Particle shape also plays a vital role in determining their incorporation level. It is generally believed that angular shaped particles will have a greater tendency to hold on to the surface upon impingement than round ones. Apachitei (1998) has, however, shown that spherical shaped alumina particles resulted in better incorporation than irregular ones. The difference in particle shape also has a bearing on the type of finish of the deposit. Very smooth and very rough surfaces were obtained, respectively, from small rounded particles and large angular particles.

2.8.4.3 ORIENTATION OF SUBSTRATE IN THE EL BATH

The other important factor that determines particle incorporation is the orientation of the substrate. Samples held vertically under uniform agitation, showed good incorporation. However, surfaces held horizontally and facing upwards were found to contain twice as many particles in comparison with those obtained using the vertical orientation (Grosjean, 1997). Nevertheless, in such an orientation, very few particles were incorporated on the surface facing downwards. Hence it is recommended that the objects be rotated and/or tumbled in such a way that all parts of the surface are regularly presented upwards (Balaraju 2003; Sharma 2002; 2005)

2.8.4.4 AGITATION OF EL BATH

Agitation of the coating solution is also a key factor in determining particle incorporation. Various methods of agitation employed include circulation by pumping, purging

of air, oxygen, nitrogen, ultrasonic agitation, and the plate-pumper technique. In practice, circulation by pumping or controlled air purging is the best way to agitate the coating bath for obtaining maximum incorporation of particles in the Ni–P matrix. In general if the agitation is too slow (laminar flow), the particles in the bath may not disperse completely, except when their density is low. On the other hand, if the agitation is too high (turbulent), particles will not have sufficient time to spend onto the surface, and this results in poor particle incorporation. The level of incorporation is obtained for silicon nitride, ceria and titania in a Ni–P matrix obtained at a fixed stirring speed (600 rpm) (Balaraju 1999). The lesser incorporation levels obtained for titania particles are due to the fact that these particles, being relatively smaller in size (2.7 μm) compared to silicon nitride (7.0 μm) and ceria (7.9 μm), were swept away from the activated surface. This shows that the stirring speed should be optimized on the basis of size of the second phase particles to be incorporated. Further has suggested that the laminar turbulent transition region is the most effective agitation condition for maximizing incorporation of particles in EL composite coating. The effects of various modes of agitation on the level of incorporation of nano-sized diamond particles in the Ni–P matrix were studied (Xu 2005). Mechanical agitation resulted in lesser incorporation due to the directional flow in the bath. Although agitation by nitrogen avoids the directional flow, it does not help to decrease the extent of aggregation of nano-sized diamond particles in the bath. Injection agitation mode helps to shatter the aggregation of nano-sized diamond particles and results in higher levels of incorporation of particles in the EL Ni–P matrix.

2.8.4.5 CONCENTRATION OF SECOND PHASE PARTICLES

Concentration of the dispersed particles in the EL Ni-P bath also plays a major role in influencing the incorporation level. Incorporation of Si_3N_4 (Balaraju, 1999), CeO_2 (Yu, 2000) and TiO_2 (Shibli, 2007) particles in EL Ni–P matrix was found to increase with increase in their concentration in the bath up to 10 g/l, beyond which there seems to be saturation in spite of a continuous increase in their concentration up to 25 g/l. Several researchers (Balaraju, 2003; Sharma 2002; 2005) have also observed a similar trend of saturation in the incorporation level of various hard and soft particles. However, the critical concentration at which these particles exhibit saturation in incorporation is not very different. Hence, it is evident that the particle flux available for impingement at the activated surface, as well as the time these particles are held on the surface, determines their level of incorporation rather than their type and nature. The observed increase in incorporation level up to a critical concentration can be ascribed to the increased flux of

particles adjacent to the substrate surface. However, beyond this critical concentration, there is a possibility of grouping or agglomeration of these second phase particles due to the decrease in the mean distance between them resulting in settlement of the particles, causing either a saturation or slight decrease in the level of incorporation. Compared to electrodeposited nickel composite coatings, incorporation of particles for a given concentration is considerably higher for EL Ni–P deposits. Moreover, it is observed that to obtain a particular level of incorporation, a greater amount of particles in the bath is required in the case of electrocodeposition than EL co-deposition (Balaraju, 2003; Agarwala, 2006).

2.8.4.6 SPECIAL ADDITIVES

Besides the above factors, some special additives, mostly surfactants, also play a major role in deciding the incorporation of second phase particles. These additives are especially important in the incorporation of soft particles like polytetra fluoroethylene (PTFE), graphite and molybdenum disulphide (Moonir-Vaghefi, 1997). Grosjean (1997) have shown that with the addition of 'Forafac-500', the incorporation of silicon carbide particles could be raised from 19 to 53 vol %. Ger (2002) have suggested that, though surfactant additives enable a higher level of incorporation of PTFE particles, their concentration in the bath is critical. Beyond a certain concentration, the adsorption of surfactant additives on the substrate leads to increased surface coverage and acts as a barrier for the co-deposition of PTFE particles in the Ni–P matrix. Hence, it is recommended that while modifying the EL Ni-P coating bath using special additives, such as, surfactants, a better understanding of the adsorption of surfactants and the resultant surface coverage on the substrate is essential to achieve higher levels of incorporation.

The amount of hard and soft particles incorporated in the EL Ni–P matrix is determined by dissolving a known weight of the deposit in nitric acid and then filtering the particles through a weighed 0.1 μm membrane. From this, the percentage weight of particles incorporated in the deposit can be estimated and used an electron microprobe analyzer (EPMA) to determine the incorporation level of Cr_3C_2 in EL Ni–P matrices. The proportion of the particles in the Ni–P matrix could also be quantitatively determined from the cross-section of the coating using image analysis. This method, developed by Bozzini (1997, 1999) was also used by Grosjean (1997) to determine the extent of particle incorporation in the coating. The method of particle counting by observation of the coating surface morphology was adopted in the case of TiO_2 and PTFE particles. Serhal in 2001 has used infrared

reflection absorption spectroscopy to determine the PTFE content of electrodeposited Au–Co–PTFE coatings. These methods could be extended for determining the particle content of composite coatings prepared by EL deposition (Balaraju, 2003).

2.9 SYNTHESIS OF RAM

There are many different chemical routes of producing the magnetic and non magnetic RAM. These routes are divided as conventional and non conventional and are discussed subsequently.

2.9.1 Synthesis of Magnetic RAM (Ferrite)

The conventional way of synthesizing hexaferrites involves solid state reaction route at high heat treatment (HT) temperature ($\geq 1200°C$), which results in powders with coarse particle size, limited chemical homogeneity and low sinterability (Cullity, 2008). So, the preparation of nano size ferrite particle with uniform particle size distribution without impurity is a challenging task. There are several other non conventional processing routes as reported in the literatures (Primc, 2009; Shafi,, 1999; Sharma 2008; Fu, 2005; Mohsen, 2010). These are discussed in the subsequent section.

2.9.1.1 HYDROTHERMAL SYNTHESIS

In this method (Primc, 2009) the solution of metal salts is prepared by dissolving the iron nitrate and metal nitrate in deionized water. The suspension of precipitated precursors is then sealed in the autoclave vessel and heated with a heating rate of $3°C$ min^{-1} to various temperatures ranging from 150 to 290°C. The autoclave is then maintained for different times at different temperature before the heating is turned off. Because of the relatively large thermal capacity, the temperature inside the autoclave started to decrease after ~10 min. After this synthesis, each product was thoroughly washed with a diluted aqueous solution of acetic acid (10%). Acetic acid easily dissolves any metal-rich compounds formed as a consequence of the metal excess, whereas hexaferrite is completely insoluble. Finally, the particles were washed with deionized water, and dried at 60°C in ambient air. The use of expensive autoclaves, good quality seeds of a fair size and the impossibility of observing the crystal as it grows is the drawback associated with this technique. Moreover surfactant like oleic acid has to use to block the secondary re-crystallization of the nanoparticles during the hydrothermal treatment.
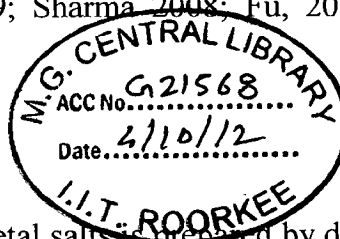
2.9.1.2 SONOCHEMICAL SYNTHESIS

In this method (Shafi,, 1999), a decane solution of $Fe(CO)_5$ and Barium ethylhexanoate, $Ba[OOCCH(C_2H_5)C_4H_9]_2$ in stochiometric ratio, is decomposed by high intensity ultrasonication at 273 K, under air atmosphere, with a high intensity ultrasonic probe. After four hours of irr-radiation, a reddish brown colored homogeneous colloidal solution was obtained. The precursor was extracted as powder from the solution by evaporation and or precipitation, which was then centrifuged and washed with pentane. Centrifuging and washing were repeated at least five times, and the product was then dried under vacuum. The precursor was then calcined at low temperature (700°C) to get the final $BaFe_{12}O_{19}$ crystalline nano particles. Sonochemical synthesis can generate a transient localized hot zone with extremely high temperature gradient and pressure (Suslick, 1988) which can assist the destruction of the sonochemical precursor and the formation of nanoparticles.

2.9.1.3 MODIFIED FLUX METHOD

In this method (Sharma, 2008), ferric chloride ($FeCl_3.6H_2O$), barium chloride ($BaCl_2$), nickel chloride ($NiCl_2$) and NaOH are used for synthesizing nickel substituted barium hexaferrite nanoparticles. Stochiometric amounts of barium and nickel chloride are dissolved completely into ultra pure water to make an aqueous solution (I) and ferric chloride is separately mixed in ultra pure water to make an aqueous solution (II). Both the above solutions are mixed in a 1:1 M ratio. The brownish coloured ferrite particles are precipitated from this mixture by gradually adding sodium hydroxide, NaOH (7.5 M) solution at room temperature (pH = 12.5). The aqueous suspension was stirred gently for 15 min to achieve good homogeneity. The precipitates so formed are filtered off, washed with water and dried at 100°C overnight. The precipitated nanocrystalline powder is mixed thoroughly with NaCl in 1:2 ratios (by weight). Since the melting point of NaCl is about 800°C, so the 'as synthesized' particles are given a heat treatment of 800 and 1,200°C for 4 h to achieve a uniform growth. During annealing, there is liquid phase diffusion of particles surrounding the molten NaCl salt which makes the process fast and hexaferrite particles crystallize out completely with uniform morphology after cooling in the furnace. The cooled mixture of nanoparticles and NaCl was then washed by ultra pure water. NaCl was dissolved and barium hexaferrite nanoparticles were filtered out. This method needs four to five times washing followed by filtration after heat treatment to remove the impurity like NaCl.

2.9.1.4 LOW COMBUSTION SYNTHESIS

In this method M-type nickel substituted barium hexaferrite was synthesized by (Sharma, 2008) citrate precursors using sol to gel (S–G) followed by gel to nanocrystalline (G–N) conversion. Stoichiometric amount of metal nitrates ($Fe(NO_3)_3.9H_2O$ and $Ni(NO_3)_2.6H_2O$) were dissolved completely into ultra pure water to make an aqueous solution (I), barium carbonate was dissolved into minimum amount of acetic acid to make another transparent solution (II). Both the above solutions (I) and (II) were mixed with citric acid in a 1:1 molar ratio. The pH of the solution was increased to 7 by addition of ammonia solution. The resulting sol was heated at constant temperature of $80°C$ on magnetic stirrer to complete the reaction to form barium nickel iron citrate precursor. The mixed solution (I+II) was evaporated very slowly over a period of 5 h to dryness. As soon as the solvent removal was completed, dried precursor undergoes a self ignition reaction to form a very fine brown foamy powder of nanocrystalline ferrite. The precursor thus obtained is given a heat treatment of $1000°C$ for 4 h in nitrogen atmosphere. Low temperature combustion synthesis is complex, takes long time for self ignition reaction to occur and needs cationic surfactants to remove the impurity like hematite phase ($\alpha\ Fe_2O_3$) (Hasab, 2007; Hasab, 2007).

2.9.1.5 MICROWAVE INDUCED COMBUSTION SYNTHESIS

This synthesis process involved the combustion of redox mixtures (Fu, 2005) in which metal nitrate acted as an oxidizing reactant and urea as a reducing one. The initial composition of the solution containing strontium nitrate, ferric nitrate, and urea was based on the total oxidizing and reducing valences of the oxidizer and the fuel using the concepts of propellant chemistry. Stoichiometric amounts of strontium nitrate [$Sr(NO_3)_2$], iron nitrate [$Fe(NO_3)_3·9H_2O$], and urea [$CO(NH_2)_2$] dissolved in a minimum quantity of water are set in a crucible. Initially, the solution boils and undergoes dehydration followed by decomposition with the evolution of large amount of gases (N_2, NH_3, and HNCO). After the solution reaches the point of spontaneous combustion, it began burning and released lots of heat, vaporized all the solution instantly and became a solid burning at the temperature over $1000°C$. The entire combustion process produced strontium ferrite powders in a microwave-oven taking only 30 min. A stoichiometric combustion reaction of metal nitrate with urea to form strontium ferrite is given below.

$$Sr(NO_3)_2 + 12Fe(NO_3)_3 + 31CO(NH_2)_2 \rightarrow SrFe_{12}O_{19} + 31CO_2 + 50N_2 + 62H_2O$$
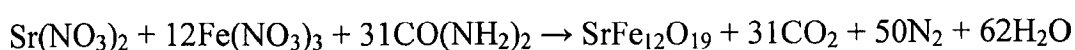
2.9.1.6 OXALATE PRECURSOR METHOD

In this method (Mohsen, 2010) chemically graded ferric chloride ($FeCl_3. 6H_2O$), barium chloride ($BaCl_2.H_2O$) and oxalic acid as source of organic were used as starting materials. A ferric chloride and barium chloride solution with Fe^{3+}/Ba^{2+} molar ratio of 12, and containing equivalent amount of oxalic acid were prepared. A mixture of barium chloride and ferric chloride solutions were prepared and then stirred for 15 min on a hot-plate magnetic stirrer, followed by addition of an aqueous solution, which was heated to 80°C with constant stirring until dry. The dried powders obtained as barium ferrite precursors. For the formation of the barium ferrite phase, the dry precursors were annealed at the rate of 10°C/min in static air atmosphere up to different temperatures (900–1200°C) and maintained for annealing time of 2 h.

2.9.2   Synthesis of Non Magnetic RAM

2.9.2.1 CHEMICAL VAPOUR DEPOSITION TECHNIQUE (Radhakrishan, 2009)

The multiwalled CNT arrays were grown over the Si-wafer in a CVD system. The carbon source gas (acetylene), reducing gas (ammonia) and inert gases (argon) entered the reactor from one side of tube. The reaction products escaped from the other side of the reactor tube. The tip of a chromel–alumel thermocouple was positioned below the substrate. The CVD reactor was housed inside a fume hood, and a bank of mass flow controller controlled the flow of carbon source gas, reducing gas and the inert gas into the reactor. The Si-wafer deposited with Fe-catalyst film was placed in the middle of a quartz boat and loaded into the quartz reactor tube. Here, thermal annealing of the Fe-catalyst film occurred in the temperature range 750-800°C under reducing gas atmosphere, to break it into nanosized particles. Then, a carbon source gas, acetylene (10 ccm) was introduced, which undergo catalytic decomposition and the growth of carbon nanotubes occurred over the catalyst nanoparticles. At the end of the scheduled carbon nanotube growth period (30 minutes), argon gas (100 ccm) flow was commenced again, the flow of other gases was stopped, the furnace switched-off, and the reactor cools down to room temperature, under the flow of argon gas.

FORMULATION OF PROBLEM

The *'Literature Review'* has been carried out in four distinct areas namely magnetic RAM, non magnetic RAM, composite of magnetic and non magnetic RAM and coated RAM. It has been observed that most of the studies carried out in various composites/nanocomposites revolve around the composites comprising either magnetic phase or non magnetic phase and few of them concern to the composite of magnetic and non magnetic phase development. Single magnetic and non magnetic materials known by critical literature review namely; barium hexaferrite (Nedkov, 1990; Dishovski, 1994; Ruan, 2000, Sharma, 2008), strontium hexaferrite (Ghasemi, 2008; Tabatabaie, 2009; Sharbati, 2010; Davoodi, 2011), nickel ferrite (Hwang, 2006; Zhao, 2009) , zinc ferrite (Ting, 2011), cobalt ferrite (Zeng, 2004), silicon carbide (Liu, 2011), or materials contain carbon (charcoal, carbon black, graphite or carbon nano tubes) (Fan, 2006; Wang, 2008; Oh, 2004; Phang, 2008; Cao, 2010; Liu, 2011) alone are not fulfilling the demand of large absorption peak, wide working frequency range and thin absorption layer.

Electromagnetic (EM) wave absorption property of composite depends on electric (complex permitivty) and magnetic (complex permeability) properties of material. The electric loss of composite depends on ohmic and polarization loss of energy, which can be obtained by adding fillers like silicon carbide, carbon black, graphite, CNTs or carbon fiber to a matrix. The magnetic loss depends on big hysteresis attenuation, which can be obtained when magnetic material like hexaferrite or spinel ferrite or a composite of hard and soft ferrite is added to a matrix.

In view of this, the present study, attempts to develop a RADAR absorbing medium containing magnetic and non magnetic phases. In the present work strontium hexaferrite ($SrFe_{12}O_{19}$), which is a hard hexagonal magnetic material and has less density and large magnetic anisotropy as compared to the barium hexaferrite (traditional magnetic microwave absorbing ferrite) is proposed to be the base composition.

The details of the proposed study are worked out considering the following facts.

1. The base composition, $SrFe_{12}O_{19}$ and composite of strontium hexaferrite hexaferrite and spinel ferrite ($NiFe_2O_4$, $ZnFe_2O_4$ and $CoFe_2O_4$, $SrFe_{12}O_{19}$) are proposed to be

synthesized by different chemical routes namely; chemical co-precipitation, modified flux method and low combustion synthesis techniques.

2. Thus 'as synthesized' RAM are proposed to be heat treated at various heat treatment temperatures (800, 900, 1000, 1100 and 1200°C) under the N_2 atmosphere for different time durations for attaining single crystalline phase.

3. The magnetic RAM particles are proposed to be coated by Ni-P using electroless (EL) coating technology.

4. The non magnetic RAM like carbon nanotubes are proposed to be synthesized by chemical vapour deposition technique (CVD). The commercialized silicon carbide and carbon black particle are proposed to reduce in size by mechanical alloying technique (MA).

5. There is no study reported on reaction kinetics of endothermic reaction resulting in the synthesis of nano magnetic phases (hexaferrite, composite of hexaferrite and spinel ferrite). So basic study of endothermic reaction kinetics is proposed for enabling the synthesis of various nano magnetic phases during the heat treatment process using differential scanning calorimtery data.

6. All these developed RAM are proposed to be characterized using various instruments like XRD, FESEM-EDAX, TEM, VSM, SQUID, DSC/TG/DTG etc.

7. To study the dielectric properties, all the RAM samples (80 wt. %) are to be mixed with epoxy resin (18 wt%) and hardener (2 wt %). The RAM epoxy mixture thus obtained is to be cast into rectangular pellet of various thicknesses (2- 2.5 mm) and cured at 75°C for 30 minutes. The composite thus prepared was polished and mounted on an aluminum foil (to obtain a single layer metal- backed absorber) to exactly fit into the measuring wave guide. The complex permitivity and permeability measurements are to be carried out on Network Analyzer (Agilent E8364B PNA series) using Material measurement software 85071 in the frequency range of 8.2 to 12.2 GHz at room temperature.

The flow chart showing the details of proposed research plan is shown in Figure 3.1.

Synthesis of Magnetic RAM
(Hexaferrite and composite of hexaferrite/ Spinel ferrite)

Synthesis of Non-Magnetic RAM

Co-Precipitation Method

Modified Flux Method

Low-Combustion Synthesis Method

Chemical Vapor Deposition

Mechanical Alloying

Development of Ni-P-RAM

Optimized Parameter of magnetic RAM

Composite of Magnetic & Non-Magnetic RAM

Optimized Parameter of non magnetic RAM

Characterization

Phase & Morphological Study (XRD, FESEM, TEM)

Non-Isothermal DSC study for Reaction Kinetics

Magnetic Study (VSM, SQUID)

Dielectric and Reflection Loss Measurements (VNA)

3.1: Flow chart showing the details of proposed research plane.

56

4.1 INTRODUCTION

The present work is based on the synthesis and characterization of hexaferrite (strontium hexaferrite and barium hexaferrite), composite of hexaferrite and spinel ferrite, non magnetic RAM (carbon nanotube, silicon carbide and carbon black) and composite of magnetic and non magnetic RAM. This chapter deals with the study of experimental tools adopted for characterization of RAM materials developed in the present investigation. Also the details of synthesis method of magnetic RAM and the heat treatment parameters required for the formation of desired phases with increased crystallinity are presented. The details of electroless coating set up, and plating bath required to coat the magnetic RAM have been described. The coating of Ni-P on the magnetic RAM (strontium hexaferrite and barium hexaferrite) powder has been explained in respect of pretreatment process required for coating. The synthesis of non magnetic RAM (carbon nanotube, silicon carbide and carbon black) by chemical vapour deposition technique and mechanical alloying techniques are also presented.

The different analytical tools like X-ray diffractometer, DSC/DTG/TG, FESEM, TEM VSM/SQUID, VNA required for phase analysis, thermal analysis, morphological evaluation, magnetic properties measurement, dielectric and reflection loss properties measurement respectively (both qualitative and quantitative) have also been summarized. The complete processing was carried out in simple and adaptable way considering the technological restraints and requirement.

4.2 SPECIFICATIONS

Eight different compositions of hexaferrite and magnetic composite of hexaferrite and spinel ferrite prepared for present study are presented in Table 4.1.

Table 4.1: The details of composition and sample code of magnetic RAM developed in present investigation

S.No	Compositions	Sample code
1	$BaFe_{12}O_{19}$	B1
2	$SrFe_{12}O_{19}$	S1
3	$SrFe_{12}O_{19}$, $CoFe_2O_4$	SC
4	$SrFe_{12}O_{19}$, $NiFe_2O_4$	SN
5	$SrFe_{12}O_{19}$, $ZnFe_2O_4$	SZ
6	$SrFe_{12}O_{19}$, $NiFe_2O_4$, $ZnFe_2O_4$	SNZ
7	$SrFe_{12}O_{19}$, $NiFe_2O_4$, $CoFe_2O_4$	SNC
8	$SrFe_{12}O_{19}$, $CoFe_2O_4$, $ZnFe_2O_4$	SCZ

4.3 SYNTHESIS TECHNIQUE

The different chemical routes adopted for synthesizing magnetic and non magnetic RAM for the present study are summarized in the subsequent sections.

4.3.1 Magnetic RAM

The conventional way of synthesizing hexaferrite involves solid state reaction route which needs calcinations at high temperature ($\geq 1200°C$). This results in powders with large particle size, limited chemical homogeneity and low sinterability (Cullity, 2008). So, the preparation of fine and uniform hexaferrite powder without impurity is a challenging task. Several non conventional synthesis routes reported for synthesis of nano sized magnetic RAM are discussed in the chapter 2 (Primc, 2009; Shafi,, 1999; Sharma 2008; 2007; Fu, 2005; Mohsen, 2010). Hydrothermal method employs expensive autoclaves, good quality seeds of small size and the impossibility of observing the crystal as it grows (Primc, 2009). Sonochemical synthesis can generate a transient localized hot zone with extremely high temperature gradient and pressure (Suslick, 1988) which can assist the destruction of the sonochemical precursor and the formation of nanoparticles. Low temperature combustion synthesis is complex, takes long time for self ignition reaction to occur and needs cationic

surfactants to remove the impurity like hematite phase (α Fe_2O_3) (Hasab, 2007; Hasab, 2007). Mechanical alloying leads to impurity and lattice strains (Cullity, 2008).

In view of this, in the present investigation, hexaferrite and composite of hexaferrite and spinel ferrite nanoparticles are synthesized by modified flux method and low combustion synthesis methods. These methods are observed to be economical and are quite suitable for mass production as compared to the other methods (Hessien, 2008).

4.3.1.1 MODIFIED FLUX METHOD

In the present study, various magnetic RAM (hexaferrite) and composite of hexaferrite and spinel ferrite were synthesized by this method. Here the typical method is being explained for composite containing strontium hexaferrite, nickel and zinc spinel ferrite phases. Analytical grades of ferric chloride ($FeCl_3.6H_2O$), strontium chloride ($SrCl_2$), nickel chloride ($NiCl_2$), zinc chloride ($ZnCl_2$) and NaOH (procured from Merck and Sigma Aldrich India) were used for synthesizing magnetic composite containing $SrFe_{12}O_{19}$, $NiFe_2O_4$ and $ZnFe_2O_4$ phases by modified flux method. Stochiometric amounts of strontium chloride, nickel chloride and zinc chloride were dissolved completely into ultra pure water to make an aqueous solution (I). Ferric chloride was separately mixed in ultra pure water to make another aqueous solution (II). Both the above solutions were mixed in a 1:1 molar ratio. The brownish colored ferrite particles were precipitated from this mixture by gradually adding sodium hydroxide, NaOH (7.5 M) solution at room temperature (pH=12.0). The aqueous suspension was stirred gently for 15 minutes to achieve chemical homogeneity. The precipitates so formed were filtered off, washed with water and dried at 100°C overnight. The precipitated nanocrystalline powder was mixed thoroughly with NaCl in 1:2 ratios (by weight). Since the melting point of NaCl is about 800°C, so the 'as synthesized' particles were given a heat treatment of 900 and 1200°C for 4h in nitrogen atmosphere to achieve a uniform growth. During annealing, there was liquid phase diffusion of particles surrounding the molten NaCl salt which makes the process fast and hexaferrite particles crystallize out completely with uniform morphology after cooling in the furnace. The cooled mixture of nanoparticles and NaCl was then washed by ultra pure water. NaCl was dissolved and ferrite nanoparticles were filtered out. It is concluded that under the given co-precipitation reaction, ferric chloride is converted to $\alpha Fe(OH)_3$ and NaCl, which is then dehydrated to form αFe_2O_3. Nickel chloride is converted to $Ni(OH)_2$ and NaCl which further dehydrated to nickel oxide. Zinc chloride is converted to $Zn(OH)_2$ and NaCl which further dehydrated to zinc oxide; and strontium chloride is also dehydrated to $Sr(OH)_2$ which further converted to strontium oxide. Finally,

$SrFe_{12}O_{19}$, $NiFe_2O_4$ and $ZnFe_2O_4$ phases are formed during the post synthesis calcinations stage and can be described by the following chemical reactions

Neutralization with Sodium hydroxide

$$12FeCl_3 + 36\ NaOH \rightarrow 12Fe\ (OH)_3 + 36NaCl$$

$$NiCl_2 + 2\ NaOH \rightarrow Ni(OH)_2 + 2NaCl$$

$$ZnCl_2 + 2\ NaOH \rightarrow Zn(OH)_2 + 2NaCl$$

$$SrCl_2 + 2\ NaOH \rightarrow Sr(OH)_2 + 2NaCl$$

Nucleation of Nano Crystals

$$12Fe(OH)_3 \rightarrow 6Fe_2O_3 + 18H_2O$$

$$Ni(OH)_2 \rightarrow NiO + H_2O$$

$$Zn(OH)_2 \rightarrow ZnO + H_2O$$

$$Sr(OH)_2 \rightarrow SrO + H_2O$$

Growth of Nano Crystals

$$NiO + Fe_2O_3 \rightarrow NiFe_2O_4$$

$$ZnO + Fe_2O_3 \rightarrow ZnFe_2O_4$$

$$SrO + 6Fe_2O_3 \rightarrow SrFe_{12}O_{19}$$
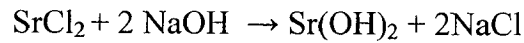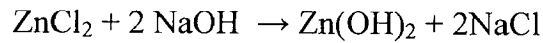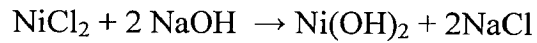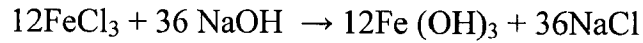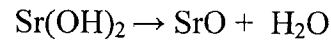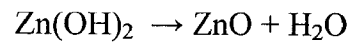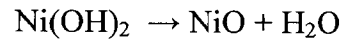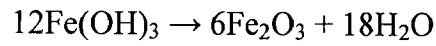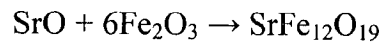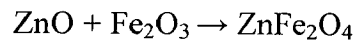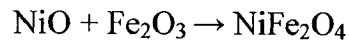
The flow chart showing the different stages of method is shown in Figure 4.1. All magnetic RAM synthesized by modified flux method are given in Table 4.2.

```
┌─────────────────────────────────────────────────────────┐
│           Step 1: Neutralization of Chloride Salts        │
│       SrCl₂ + NiCl₂ + ZnCl₂ +FeCl₃ +Deionized water       │
│  Time- 60minutes                                          │
│  Color- Light Brown              7.5 M NaOH               │
│                                                           │
│        SrFe₁₂O₁₉ + ZnFe₂O₄ + NiFe₂O₄ + NaCl + H₂O        │
└─────────────────────────────────────────────────────────┘
```

Step 1: Neutralization of Chloride Salts

$SrCl_2 + NiCl_2 + ZnCl_2 + FeCl_3 +$ Deionized water

Time- 60minutes
Color- Light Brown   7.5 M NaOH

$SrFe_{12}O_{19} + ZnFe_2O_4 + NiFe_2O_4 + NaCl + H_2O$

Step 2: Nucleation of grains
Complete precipitation and formation spherical and needle shaped nanograins

Color- Light Brown   Time- 12h
Temperature-80⁰C
Washing and filtration

Step 3: Growth of Nanograins

HT Temperature	Morphology of Nanograins	Color
800⁰C	Small hexagonal	Brown
1000⁰C	Small hexagonal plate	Dark brown
1200⁰C	Large hexagonal/pryramidal	Ash black

Fig. 4.1: Flow chart showing the procedure for synthesis of strontium hexaferrite nanoparticles using 'modified flux' method.

Table 4.2: The details of constituents used for synthesizing 100 gm of various magnetic RAM using modified flux method.

S. No.	Composition	Weight in gm						
		SrCl₂	BaCl₂	FeCl₃	NiCl₂	ZnCl₂	CoCl₂	NaOH
1	BaFe₁₂O₁₉	------	18.874	179.43	-------	-------	-------	137.49
2	SrFe₁₂O₁₉	14.935	-------	183.391	-------	-------	-------	143.180
3	SrFe₁₂O₁₉ , CoFe₂O₄	14.888	-------	167.577	-------	-------	12.207	-------
4	SrFe₁₂O₁₉ , NiFe₂O₄	14.891	-------	167.610	12.175	-------	-------	138.990
5	SrFe₁₂O₁₉ , ZnFe₂O₄	14.799	-------	166.568	-------	12.731	-------	138.990
6	SrFe₁₂O₁₉ , NiFe₂O₄, ZnFe₂O₄	14.895	-------	167.088	6.068	6.385	-------	142.310
7	SrFe₁₂O₁₉ , NiFe₂O₄, CoFe₂O₄	14.890	-------	167.593	6.087	-------	6.097	142.310
8	SrFe₁₂O₁₉ , CoFe₂O₄, ZnFe₂O₄	14.843	-------	167.070	-------	6.384	6.078	142.295

4.3.1.2 LOW COMBUSTION SYNTHESIS METHOD

To compare the morphology and its effect on the magnetic, dielectric and microwave absorption properties of the particle, one magnetic RAM is also synthesized by low combustion synthesis method. In this method, composite of strontium hexaferrite and spinel ferrite ($NiFe_2O_4$ and $CoFe_2O_4$) were synthesized by citrate precursors using sol to gel (S–G) method followed by gel to nanocrystalline (G–N) conversion. Stoichiometric amount of metal nitrates ($Fe(NO_3)_3.9H_2O$, $Co(NO_3)_2.6H_2O$) and $Ni(NO_3)_2.6H_2O$) were dissolved completely into ultra pure water to make an aqueous solution (I), strontium carbonate was dissolved into minimum amount of acetic acid to make another transparent solution (II). Both the above solutions (I) and (II) were mixed with citric acid in a 1:1 molar ratio. The pH of the solution was increased to 7 by addition of ammonia solution. The resulting sol was heated at constant temperature of 80°C on a magnetic stirrer to complete the reaction to form strontium nickel cobalt iron citrate precursor. The mixed solution (I+II) was evaporated slowly over a period of 5 h to dryness. As soon as the solvent removal was completed, dried precursor undergoes self ignition reaction to form a very fine brown foamy powder of nanocrystalline ferrite (Figure 4.2). The combustion reaction can be described as follows:

$$SrCO_3 + 2Ni(NO_3)_2.6H_2O + 10Fe(NO_3)_3.9H_2O + C_6H_8O_7.H_2O$$

$$\downarrow$$

$$SrFe_{12}O_{19} + NiFe_2O_4 + CoFe_2O_4 + CO_2 + NO$$
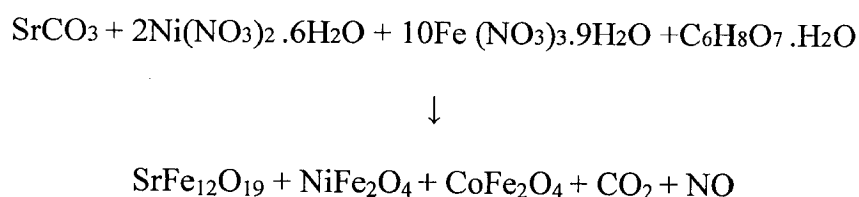
The flow chart showing the synthesis of magnetic composite of strontium hexaferrite and nickel cobalt spinel ferrite using low combustion synthesis method is shown in Figure 4.3.
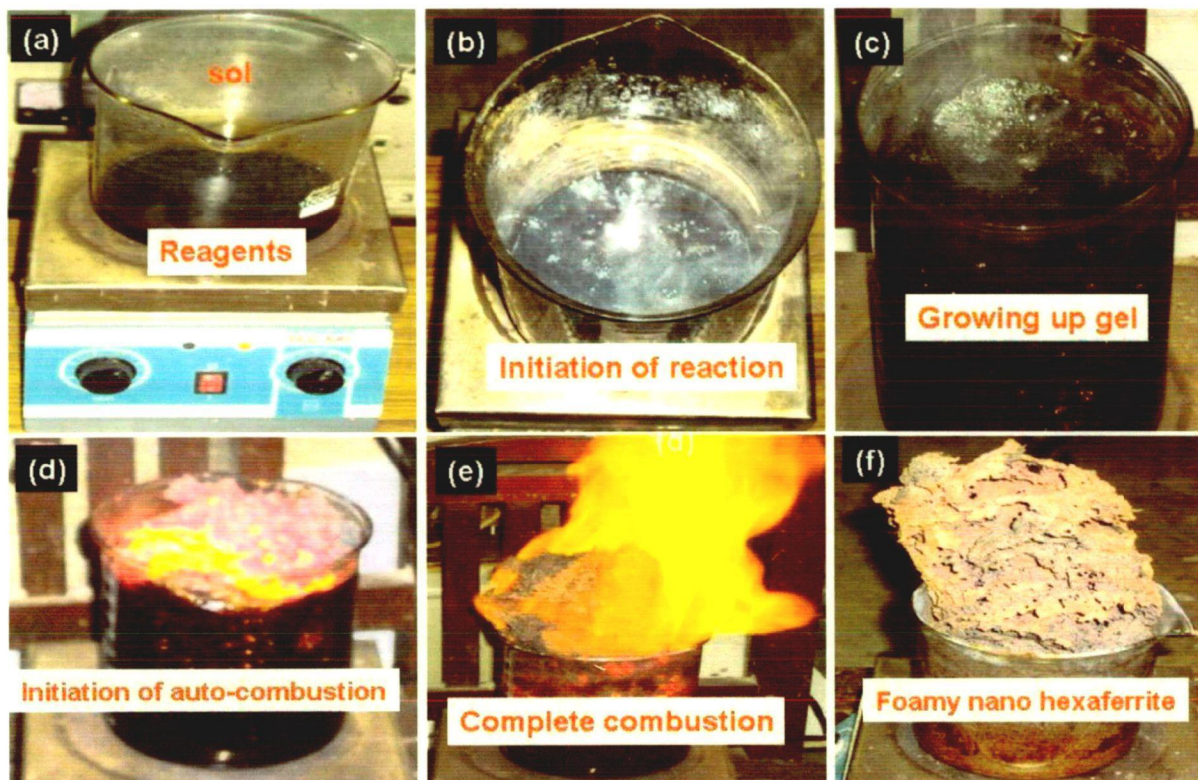
Fig. 4.2: Showing the different stages of low combustion synthesis reaction a) reagents, b) initiation of reaction, c) growing up gel, d) initiation of auto-combustion, e) complete combustion, and f) foamy nano ferrite.
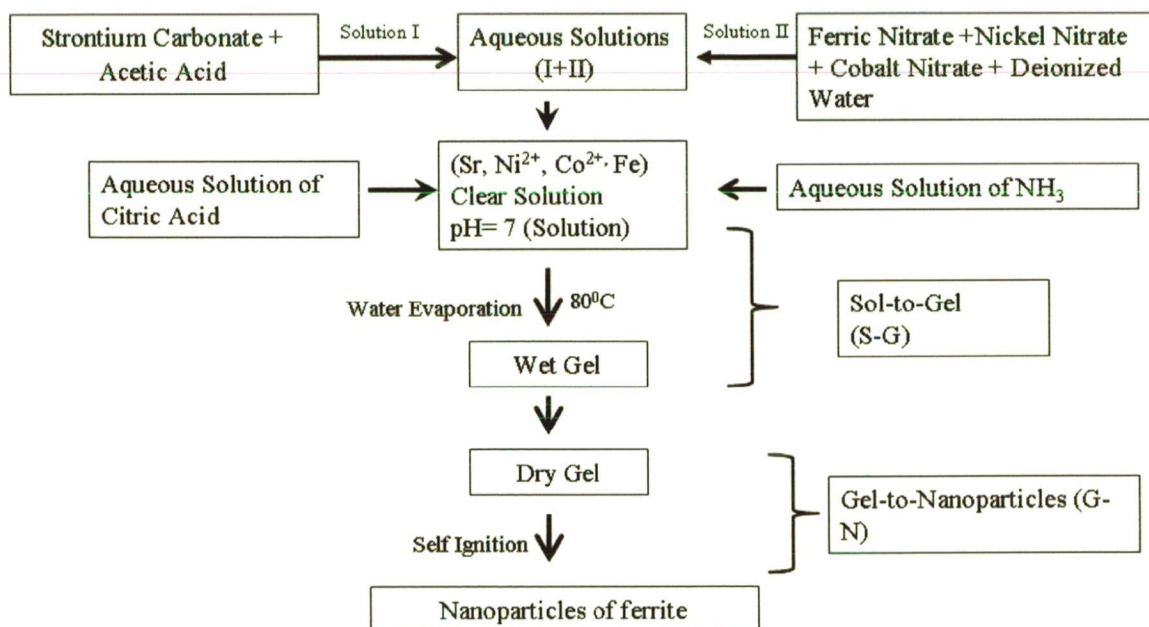
Fig. 4.3: The flow chart showing the synthesis of magnetic composite containing strontium hexaferrite and cobalt, nickel spinel ferrite using 'low combustion synthesis' method.

4.3.1.3 HEAT TREATMENT STUDY OF 'AS SYNTHESIZED' MAGNETIC RAM

As explained earlier that, in both the adopted methods for the synthesis of magnetic RAM, the temperature of reaction is not enough for the formation of desired phases. So the post calcinations are needed for synthesis of desired magnetic phases. The heat treatment was carried out in a tubular furnace at the heating rate of 10 K/min in nitrogen atmosphere. Nitrogen gas with 99.993% purity and 1.5 Kg/cm^2 pressure was used for heat treatment of 'as synthesized' powder.

4.4 SYNTHESIS OF NON MAGNETIC RAM

In the present study multiwalled carbon nanotube, commercialized silicon carbide and carbon black (procured from Merck and Sigma Aldrich, India) were used as non magnetic filler for fabricating the RAM composite. The method for synthesizing carbon nanotubes and the technique adopted for reducing the particle size of commercialized RAM to nano range is summarized below.

4.4.1 Chemical Vapour Deposition Technique

The multiwalled CNT arrays were grown over the Si-wafer in a CVD system. The carbon source gas (acetylene), reducing gas (ammonia) and inert gases (argon) entered the reactor from one side of tube. The reaction products escaped from the other side of the reactor tube. The tip of a chromel–alumel thermocouple was positioned below the substrate. The CVD reactor was housed inside a fume hood, and a bank of mass flow controller controlled the flow of carbon source gas, reducing gas and the inert gas into the reactor. The Si-wafer deposited with Fe-catalyst film was placed in the middle of a quartz boat and loaded into the quartz reactor tube. Here, thermal annealing of the Fe-catalyst film occurred in the temperature range 750-800°C under reducing gas atmosphere, to break it into nanosized particles. Then, a carbon source gas, acetylene (10 ccm) was introduced, which undergo catalytic decomposition and the growth of carbon nanotubes occurred over the catalyst nanoparticles. At the end of the scheduled carbon nanotube growth period (30 minutes), argon gas (100 ccm) flow was commenced again, the flow of other gases was stopped, the furnace switched-off, and the reactor cools down to room temperature, under the flow of argon gas.

4.4.2 Mechanical Alloying Method

The elemental powders were weighed in a precision balance of Denver Instrument (model no S1-234) Germany make. Reduction in particle size of elemental powder from micron to nano size range was carried out using P5 High Energy Planetary Ball Mill of Fristsch, German make (Figure 4.4). Agate jar and agate balls were used for mechanical alloying. Total 50 hrs of cycle was executed for each powder in twenty five segments comprising 2 hrs milling and 30 miniutes pause. The mechanical alloying was carried out at 300 rpm using balls to charge ratio of 5:1 (by weight) to achieve desirable nano size powder.

Fig. 4.4:   Photograph of high energy planetary ball mill (model no S1-234) used for reducing the micron size particle to nano size range.

4.5 NI-P COATED RAM

Electroless, one of the best coating technologies in which deposition is purely systematic chemical process. It includes sensitization, activation, nucleation and growth of nanosized alloy or composite globules first horizontally and then vertically during the reduction process onto the catalytic surface of the substrate. Here it is important to state that the deposition rate in the horizontal direction is faster than vertical direction and this makes the coating almost pore free (Agarwala 2006).

4.5.1 Processing: Ni-P Deposition Using Electroless Technology

To develop a universal EL Ni-P bath, all the systematic coating process parameters like surface pretreatment, bath composition, pH, temperature, bath loading factor, dipping time are kept constant for all the substrates used. Each parameter is optimized extensively and finally the common values were obtained for all the parameters to get the universal EL Ni-P bath i.e. EL Ni-P deposition onto all substrates (Agarwala, 2006).

4.5.1.1 PRETREATMENT AND ACTIVATION

Since EL coating is a chemical reduction process, proper surface preparation of every substrate onto which coating has to be carried out is essential for achieving a sound EL deposit. Surface preparation was followed by the pretreatment of the surface of the substrate. Surfaces were sensitized and then activated by immersing hexaferrite powder into the solution of $SnCl_2$ and $PdCl_2$ respectively for a specific optimized time period at room temperature. All the details are mentioned in the Table 4.3

Table 4.3: Optimized systematic surface preparation and pretreatment processes prior to EL Ni-P deposition on magnetic RAM.

Surface Treatment	Reagents	Time (s)
Sensitization	0.5 ml HCl + 0.5 % $SnCl_2$	180
Activation	0.05 ml HCl + 0.005 % $PdCl_2$	60
Cleaning	Distilled water	30

4.5.1.2 THE EL Ni-P BATH

Schematic diagram and photograph of the experimental set-up used for EL coating bath is shown in Figure 4.5 and 4.6 respectively. The temperature of the bath is controlled to an accuracy of ± 2°C. The pH is measured by a pH meter with accuracy of ±0.25. A corning glass beaker is placed tight inside a copper beaker to maintain the uniform temperature. In the present investigation, uniform EL Ni-P bath composition was used to deposit Ni-P on barium and strontium hexaferrite nanoparticles. The pH of bath is maintained at 9.0 (alkaline bath using NH_3 solution drop-by-drop) and temperature at 90°C. All the details for uniform EL Ni-P bath are mentioned in the Table 4.4.
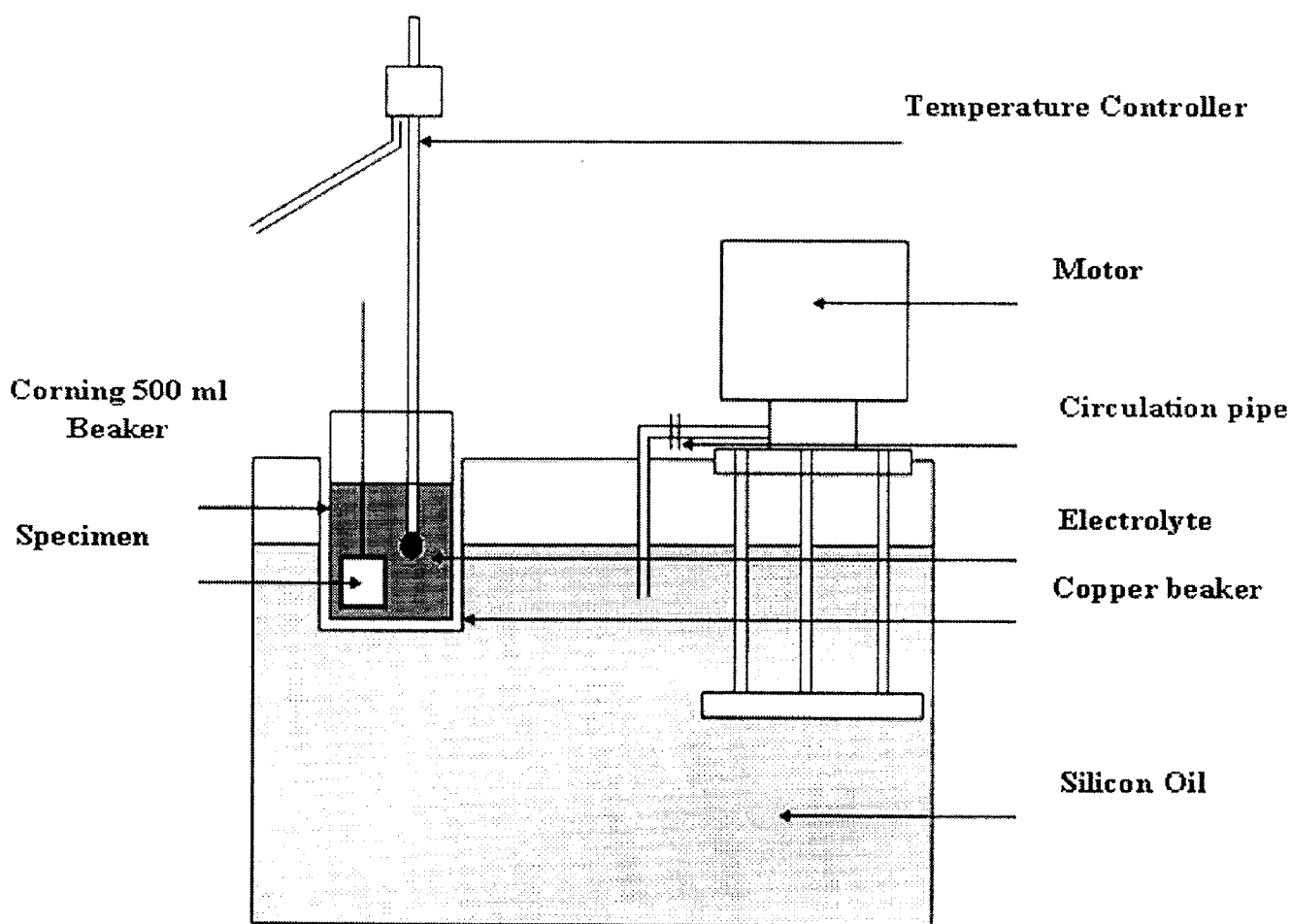
Fig. 4.5: Schematic diagram of the experimental set-up used for EL Ni-P deposition on magnetic RAM (Agarwala, 1987; 2005).

Fig. 4.6: Photograph showing the coating bath set-up with accessories used for EL Ni-P deposition on magnetic RAM (Agarwala, 1987; 2006).

Table 4.4: Details of universal EL Ni-P bath components and their role during deposition for 3 minutes at 90 °C on magnetic RAM ($BaFe_{12}O_{19}$ and $SrFe_{12}O_{19}$).

Bath component/ Reagents Name	Concentration (gm/l)	Role in EL Bath
Metal salt/ Nickel sulphate	24	To provide Ni ions inside the bath to get deposited onto the catalytic (Pd ions) surface (target). After that Ni ion itself work as a catalyst for further deposition.
Reducing agent/ Sodium hypophosphite	15	To supply free electron for the Ni ions reduction and P also goes to Ni lattice and form Ni-P nano globules.
Complexing agent/ Sodium succinate	12	To control the free Ni available during the reaction and avoid spontaneous decomposition so that it occurs only on the catalytic surface.
Stabilizer/Succinic acid	4	To avoid the spontaneous decomposition of EL bath
pH control reagent/ Ammonia solution	pH: 9 maintained	To control the pH of the bath during deposition.
Surfactant/ Oleic acid	16 ml	To avoid the agglomerations and maintain the suspension of NRAMs powders inside the bath during EL Ni-P deposition.
Substrate (Hexaferrite powder)	8	Dried activated (Sn/Pd ions) surface

4.6 CHARATERIZATION

Different tools used for characterizing the magnetic and non magnetic RAM developed in this study are explained in the subsequent sections.

4.6.1 Phase Analysis

X-Ray diffraction analysis was conducted to find out different phases present in the composite powders, which were under study. A Bruker AXS D8 differactometer with Cu-Kα radiation (Figure 4.7) with a current of 20 mA and accelerating voltage of 35 kV was used for

study were obtained for 2θ angle ranging from 20 to 80° for magnetic RAM and 5 to 100 for non magnetic RAM. The intensity of the diffracted beam against 2θ angle was recorded at the speed of 1 cm/min, keeping the Goniometer speed of 1°/min for all the samples. Peaks of different phases in samples were identified using XRD X'pert high score plus software. The average crystallite size of the powder was measured by X-ray line broadening technique employing Scherrer's formula (Khanna, 1983). These analyses were conducted for 'as synthesized' magnetic RAM, heat treated magnetic RAM, multiwalled carbon nanotubes and non magnetic RAM (SiC and CB) obtained after the mechanical alloying.
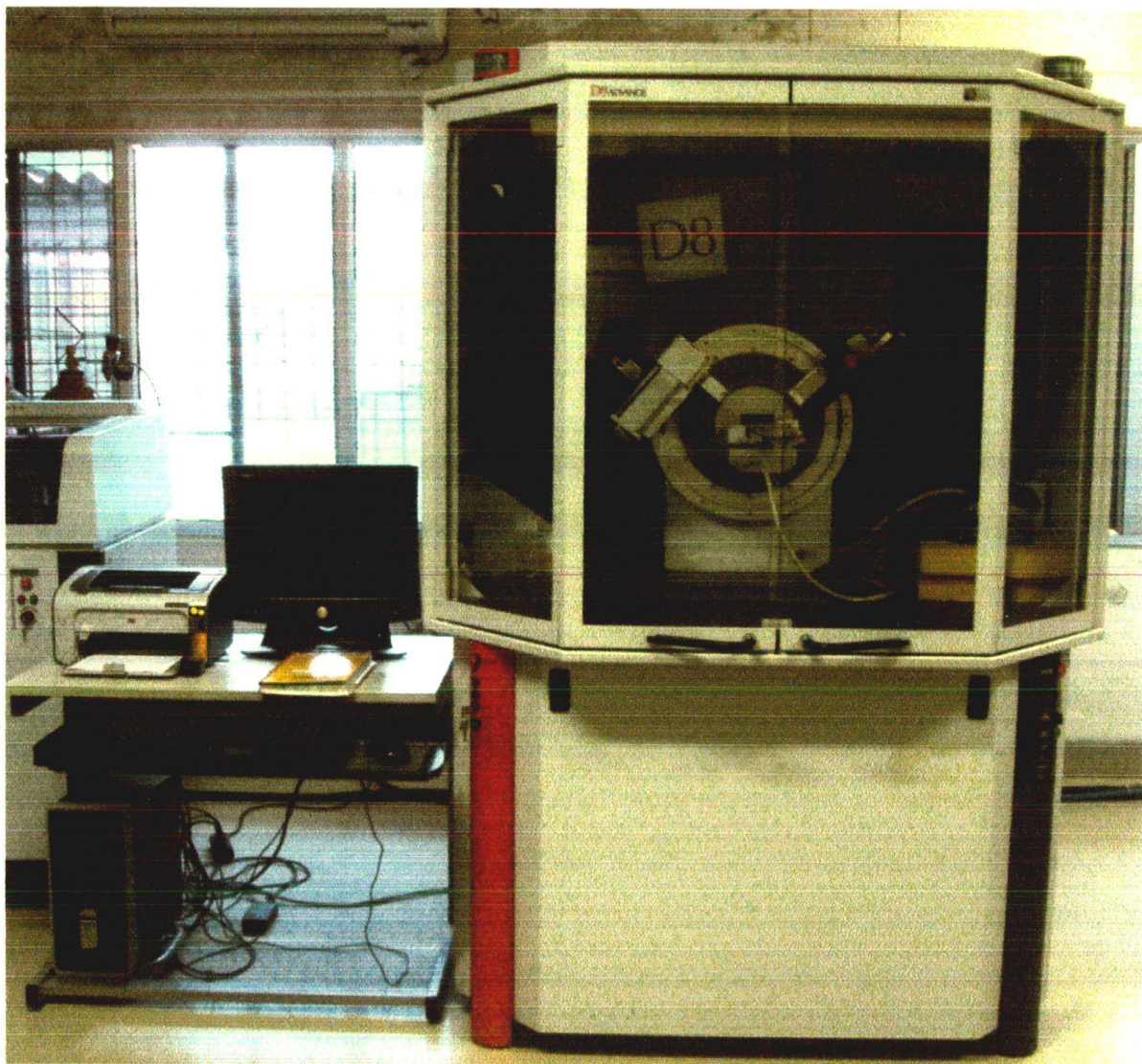
Fig. 4.7: The photograph of X-ray diffractogram set- up (Bruker AXS D8) used for phase analysis.

4.6.2 Thermal Analysis

In the present study it was observed that formation and crystallization of magnetic RAM is highly endothermic process, therefore, their kinetics were suitably studied by use of differential scanning calorimeter (Perkin Elmer, Pyris Diamond). It is an instrument in which physical properties of materials are measured while the material is subjected to a temperature controlled program. All three DSC, DTG and TG were carried out simultaneously on the same sample under the same experimental conditions. Here thermocouple (platinium-platinium-rhodium) for DSC measurement was incorporated in the end of each of the balance beam ceramic tube (Figure 4.8), and the temperature difference between the holder on the sample side and the holder on the reference side is detected. This signal is amplified and become the temperature difference signal used to measure the thermal change of the sample.

Non isothermal kinetic of magnetic RAM synthesized by co precipitation method was investigated using DSC data. The specimen were subjected to DSC study for three heating rates (β), i.e. β = 10, 30 and 50 °C/min in nitrogen atmosphere. The heating was carried out up to 1400°C so as to attain the peak indicating the maximum transformation rate. The activation energy (E) and the Avrami index parameter (n) were calculated using Johnson-Mehl-Avrami (JMA) kinetic model. Reaction mechanism has been proposed in accordance with kinetic parameter (n) values using Criedo and Ortega criterion (Criado, 1987; Doyle, 1962). The photograph of DSC/TG/DTG setup used in this study is shown in Figure 4.8. Theoretical background for determining the activation energy and reaction kinetics parameter using JMA kinetic model is presented the chapter 5.

Fig. 4.8: The photograph of differential scanning calorimetry (Perkin Elmer, Pyris Diamond) used for thermal analysis in the present study.

4.6.3 Morphological Evaluation

Morphological study of all powder samples under study was carried out by field emission scanning electron microscope, FESEM (QUANTA FEG 200 FEI) and transmission electron microscope, TEM (Philips, EM 400; TECHNAI 20G2-S-TWIN).

Powder specimens were mounted on the specimen holder and were placed inside the electron beam chamber. Different regions were viewed on the screen and micrographs are taken. The elemental mapping and EDAX analysis was done to study the distribution and content of various elements present in the composite powder used in the study. The photograph of FESEM-EDAX setup used in this study is shown in the Figure 4.9.
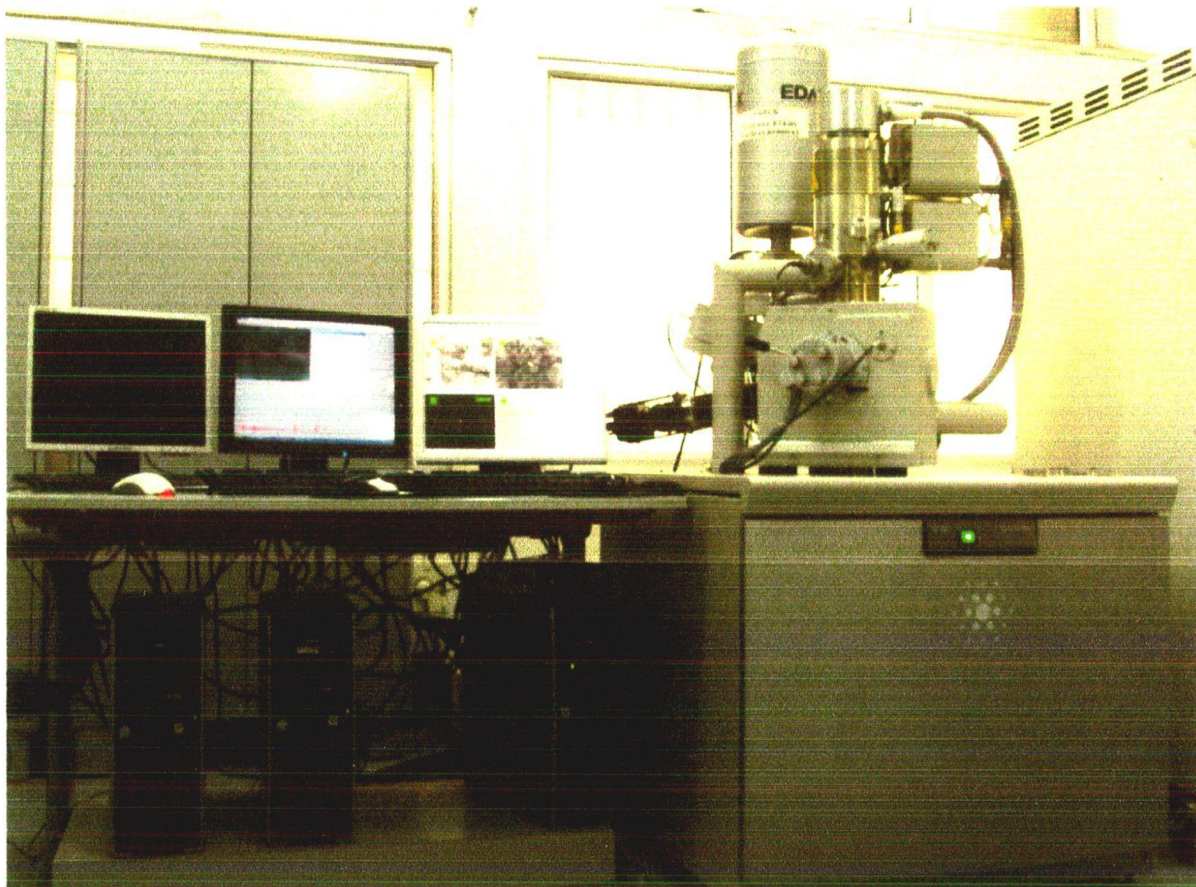
Fig. 4.9: The photograph of FESEM-EDAX setup (QUANTA FEG 200 FEI) used for morphological evaluation of RAM developed in this study.

4.6.4 Magnetic Properties Measurement

The magnetic properties of solids are very important and, an attempt to understand them has led to a deep insight into the fundamental structure of many solids, both metallic and non metallic. The VSM is the instrument used to measure the magnetic moment, the most fundamental quantity in magnetism of solid samples.

In the present study, magnetic measurements were taken at room temperature in the applied field range of -10000 to +10000 gauss using vibrating sample magnetometer, VSM (155, PAR). The powder sample was weighed (25-50 mg by wt) in a precision balance of Denver Instrument (model no S1-234) German make. The photograph of VSM setup used in this study is shown in the Figure 4.10.

4.6.5 Dielectric and Reflection Loss Measurement

To study the dielectric properties, the nanoparticles (80 wt. %) were mixed with epoxy resin (18 wt. %) and 2% hardener. The ferrite epoxy composite thus obtained was cast into a rectangular pellet of thickness 2.5mm and cured at 75°C for 30 minutes. The composite

thus prepared was polished and mounted on an aluminum foil (to obtain a single layer metal-backed absorber) to exactly fit into the measuring wave guide. The complex permittivity and permeability measurements were carried out on Network Analyzer (Agilent E8364B PNA series) using material measurement software 85071 in the frequency range of 8.2 to 12.2 GHz at room temperature. The reflection loss curves were calculated from complex permitivity and permeability at given frequency and absorber thickness with following equations:

$$Z_{in} = Z_o \, (\mu_r / \varepsilon_r)^{1/2} \tanh \{ j \, (2\pi fd/c) \, (\mu_r \varepsilon_r)^{1/2} \}$$

$$RL = 20 \log | (Z_{in} - Z_o)/ (Z_{in} + Z_o)|$$

Where

f is frequency, d is the **thickness of absorber (d= 2.0 mm for all samples)**, c is the velocity of light, Z_{in} is the characteristic impedance of absorber and Z_0 is the characteristic impedance in a vacuum, $Z_0 = 120 \, \pi$. The impedance matching condition is given by $Z_{in} = Z_0$ to represent the perfect absorbing properties. The photograph of VNA setup used for dielectric and reflection loss properties measurement of RAM is shown in Figure 4.11.
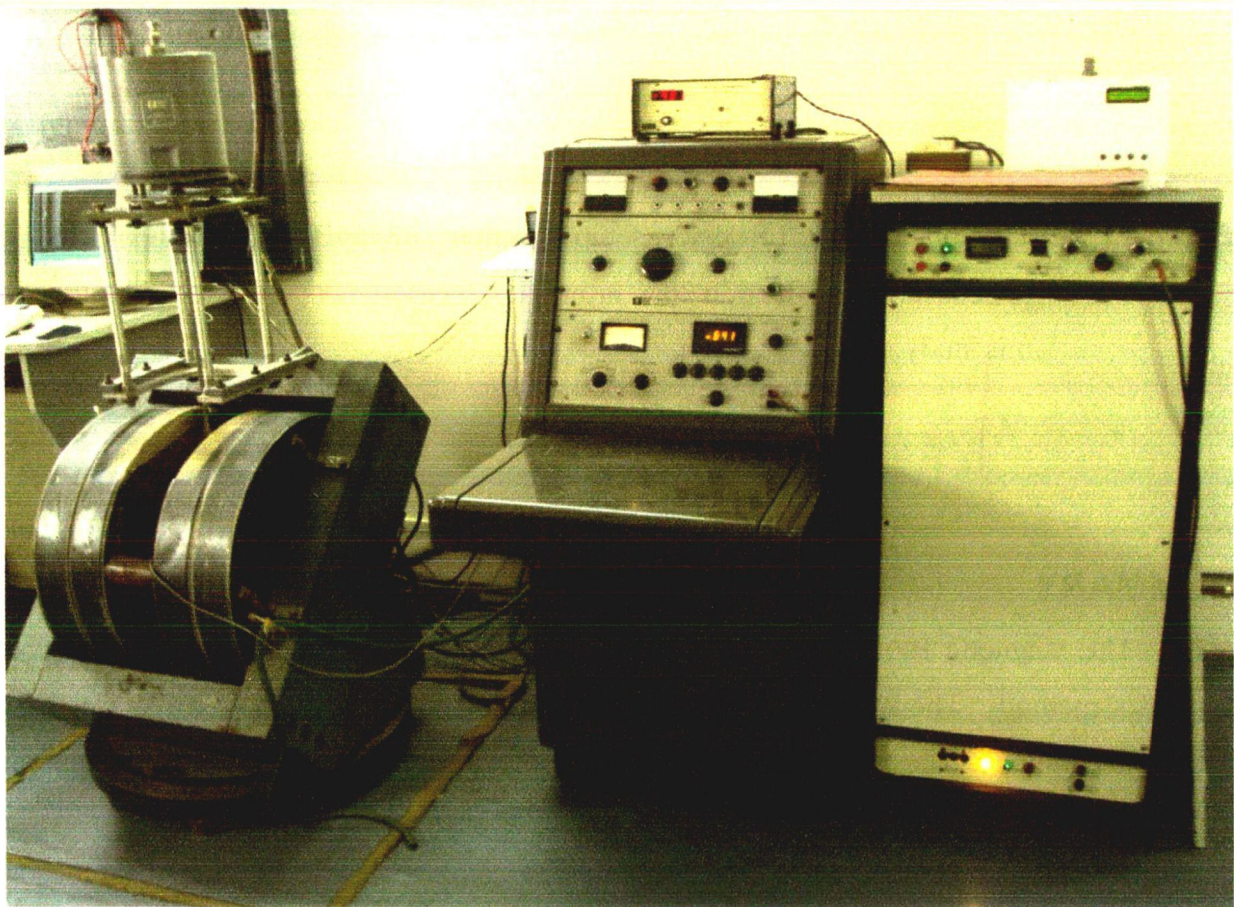
Fig.: 4.10: The photograph of VSM setup (155, PAR) used for magnetic properties measurement of RAM developed in this study.
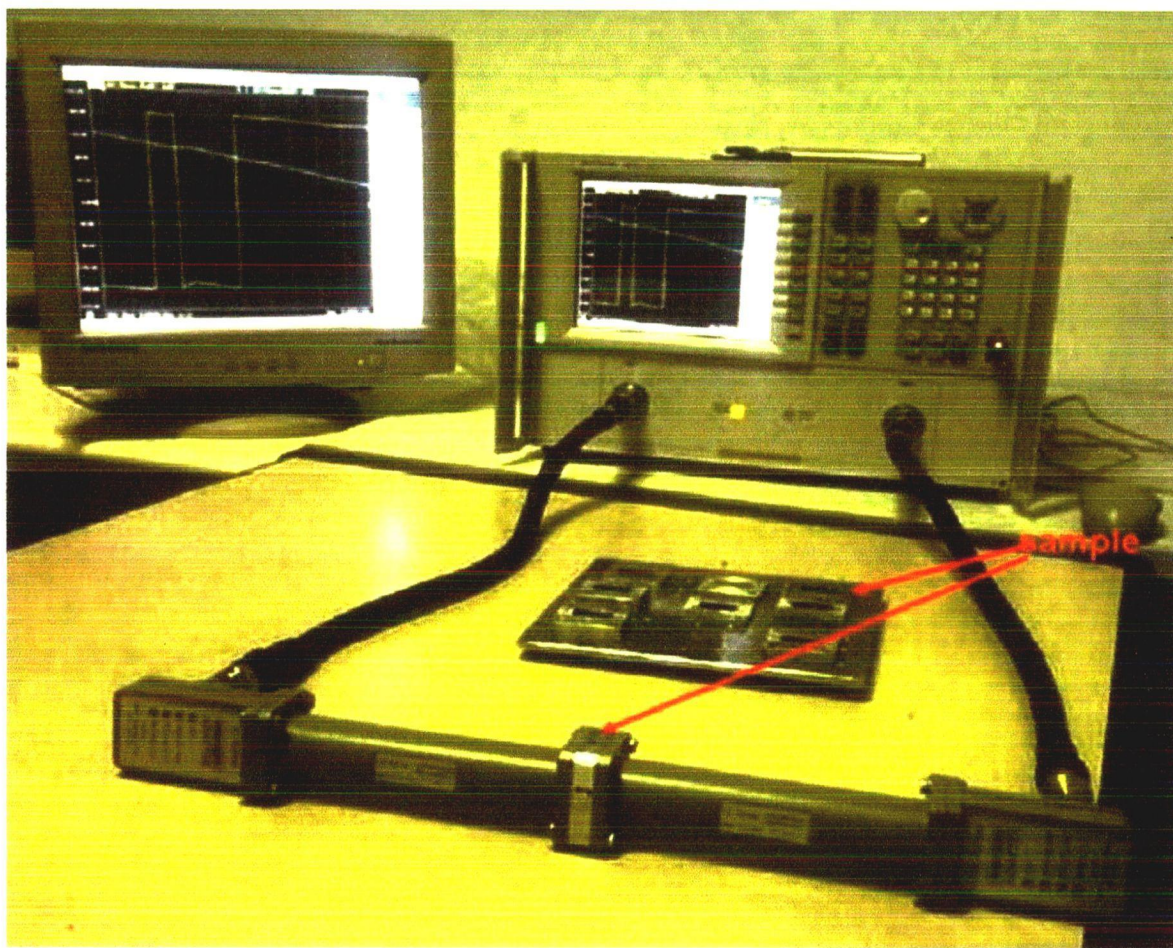
Fig. 4.11: The photograph of VNA setup (Agilent E8364B PNA series) used for dielectric and reflection loss properties measurement of RAM developed in this study.

SUMMARY

The magnetic RAMs have been synthesized by modified flux and low combustion synthesis methods. The magnetic RAMs have been coated by Ni-P alloy using electroless coating technology. The bath composition and the method of coating including pretreatment process also have been explained. Non magnetic RAMs like CNT were synthesized by chemical vapour deposition technique. The commercialized SiC and CB were reduced in particle size using mechanical alloying. The entire developed magnetic and non magnetic RAMs were characterized by different analytical tools like X-ray diffractometer, DSC/DTG/TG, FESEM, TEM, VSM/SQUID, VNA.

NON-ISOTHERMAL STUDY THROUGH DSC ANALYSIS

5.1 INTRODUCTION

In this chapter the reaction kinetics of the endothermic reaction resulting in the synthesis of desired magnetic RAM phases (hexaferrites and magnetic composite of hexaferrite and spinel ferrite) has been studied. This study includes the determination of activation energy and Avrami index parameter of the endothermic reaction resulting in the synthesis of desired magnetic RAM phases. The empirical activation energy is an important experimental parameter. It yields the temperature dependence of the transformation rate and mechanism of transformation (Jena, 1992).

In the present investigation, the magnetic RAM nanoparticles are synthesized by modified flux method. It is observed that temperature of reaction (80°C) during coprecipitation reaction is not enough for the formation and crystallization of desirable magnetic RAM phases. Therefore, post calcinations of 'as synthesized' powder is needed for the formation of desirable magnetic RAM phases wherein endothermic heat absorbed during reaction is utilized for the phase formation. The endothermic reaction during heat treatment process start and end at specific temperatures. It has important role in obtaining desirable phases which influenced morphology and enhanced magnetic, dielectric and microwave absorption properties of magnetic RAM particles. Reaction kinetics for the formation of magnetic RAM phases is studied in nitrogen atmosphere by differential scanning calorimetry (DSC) with various heating rates of 10, 30 and 50 K/min. The specifications of the prepared composition used in reaction kinetics study, theoretical background for calculating the activation energy, Avrami index parameter and the thermal behaviour of each magnetic RAM is discussed in the subsequent sections.

5.2 SPECIFICATIONS

Eight different compositions of hexaferrite and magnetic composite of hexaferrite and spinel ferrite prepared for reaction kinetics studies are presented in Table 5.1.

Table 5.1: The details of composition and sample code of magnetic RAM developed in present investigation

Compositions	Sample code
$BaFe_{12}O_{19}$	B1
$SrFe_{12}O_{19}$	S1
$SrFe_{12}O_{19}$, $CoFe_2O_4$	SC
$SrFe_{12}O_{19}$, $NiFe_2O_4$	SN
$SrFe_{12}O_{19}$, $ZnFe_2O_4$	SZ
$SrFe_{12}O_{19}$, $NiFe_2O_4$, $ZnFe_2O_4$	SNZ
$SrFe_{12}O_{19}$, $NiFe_2O_4$, $CoFe_2O_4$	SNC
$SrFe_{12}O_{19}$, $CoFe_2O_4$, $ZnFe_2O_4$	SCZ

5.3 THERMAL STUDY

The Differential Scanning Calorimetry (DSC), Differential Thermogravimetry (DTG) and Thermogravimetry (TG) traces of the sample B1 ($BaFe_{12}O_{19}$) carried out at the heating rates of 10, 30 and 50 K/min in nitrogen atmosphere are shown in Figures 5.1 (a-c) respectively. In all the three cases only endothermic peaks are observed indicating that barium hexaferrite nanoparticles are synthesized by the endothermic reaction. The endothermic peak at $63°C$ is attributed to the loss of moisture during heat treatment. The endothermic peak at about $784°C$ (Figure 5.1a) is attributed to the synthesis of various phases like αFe_2O_3 (JCPDS Card No.05-637) and $BaFe_{12}O_{19}$ (JCPDS Card No. 7-276) which was confirmed by the XRD analysis of the powder heat treated at $800°C$ in the nitrogen atmosphere (Figure 5.2). The endothermic peak at $971°C$ is attributed to endothermic reaction resulting in the synthesis of single phase, $BaFe_{12}O_{19}$, with increasing crystallinity and is also confirmed by the XRD analysis of the powder heat treated at $1100°C$ (temperature of completion of reaction) in nitrogen atmosphere (Figure 5.2). TG analysis of 'as synthesized' powder (Figure 5.1a) shows a weight loss of ~28% in the temperature range of 23 to $978°C$. It may be due to degassing and loss of moisture during the heat treatment process (Tyagi, 2009; 2010; 2011; 2011). Thereafter no weight loss is observed. The differential thermogravimetry

(DTG) curve indicates the derivative of themogravimetry data which is attributed to the rate of weight loss during the endothermic reactions occurring at 784 and 971°C (for the DSC carried out at 10 K/min). The endothermic reaction occurring at 971°C shows the weight loss of about 11 % at the rate of 132.3ug/min (shown by DTG curve). Thereafter both TG and DTG curves become smoother; this indicates the completion of reaction as M type barium hexaferrite (BaFe$_{12}$O$_{19}$) nanoparticles have formed. The same behaviour is observed for the 'as synthesized' powder carried out under DSC/DTG/TG at 30 and 50 K/min with slight change in the temperature of the reaction (Figures 5.1b-5.1c). For the endothermic peak resulting in the synthesis of single phase barium hexaferrite, the area under the DSC curve (enthalpy of reaction) and T$_m$ (temperature of reaction) for various heating rates (10, 30 and 50 K/min) are given in Table 5.2 Hence the present investigation contributes towards the selection of heat treatment temperature, proper heating rate and required atmosphere for synthesizing single phase BaFe$_{12}$O$_{19}$ nanoparticles.

Table 5.2: Details of enthalpy of reaction (area under the DSC curve) and T$_m$ (temperature of reaction) for various heating rates (10, 30 and 50 K/min).

Sample	T$_m$ (K)			Enthalpy (J/gm)		
	10	30	50	10	30	50
B1	1244	1327	1351	57.9	62.2	37.2
S1	1324	1417	1457	130	147	170
SC	1395	1519	1580	173	88.2	126
SN	1401	1491	1539	124	70.6	93.1
SZ	1356	1448	1490	69.5	95.9	14.5
SNZ	1392	1478	1534	82.5	186	43.7
SNC	1347	1429	1467	421	448	291
SCZ	1384	1521	1548	191	166	89.2

(a)

59Cel
162.0ug/min

176Cel
43.3ug/min

DTG

964Cel
132.3ug/min

94.5 mJ/mg

63Cel
-4.9uW

DSC

23Cel
99.96 %

100Cel
92.19 %

200Cel
88.33 %

300Cel
85.90 %

499Cel
84.71 %

TG %

-30.7 mJ/mg

784Cel
-35.6uW

57.9 mJ/mg

971Cel
-50.6uW

802Cel
83.81 %

899Cel
80.46 %

978Cel
72.51 %

1196C
71.80

DSC uW

TG %

DTG mg/min

Temp Cel

(b)

81Cel
0.340mg/min

199Cel
0.130mg/min

DTG

1047Cel
0.389mg/min

109 mJ/mg

92Cel
-8.6uW

DSC

731Cel
-6uW

13.5 mJ/mg

-23.2 mJ/mg

790Cel
-19uW

932Cel
-26.7uW

62.2 mJ/mg

1081Cel
-36.6uW

1054Cel
-39uW

26Cel
99.94 %

102Cel
92.93 %

200Cel
88.98 %

301Cel
86.12 %

400Cel
85.11 %

600Cel
84.32 %

TG %

800Cel
83.84 %

900Cel
82.56 %

1067Cel
70.65 %

1218Cel
69.94 %

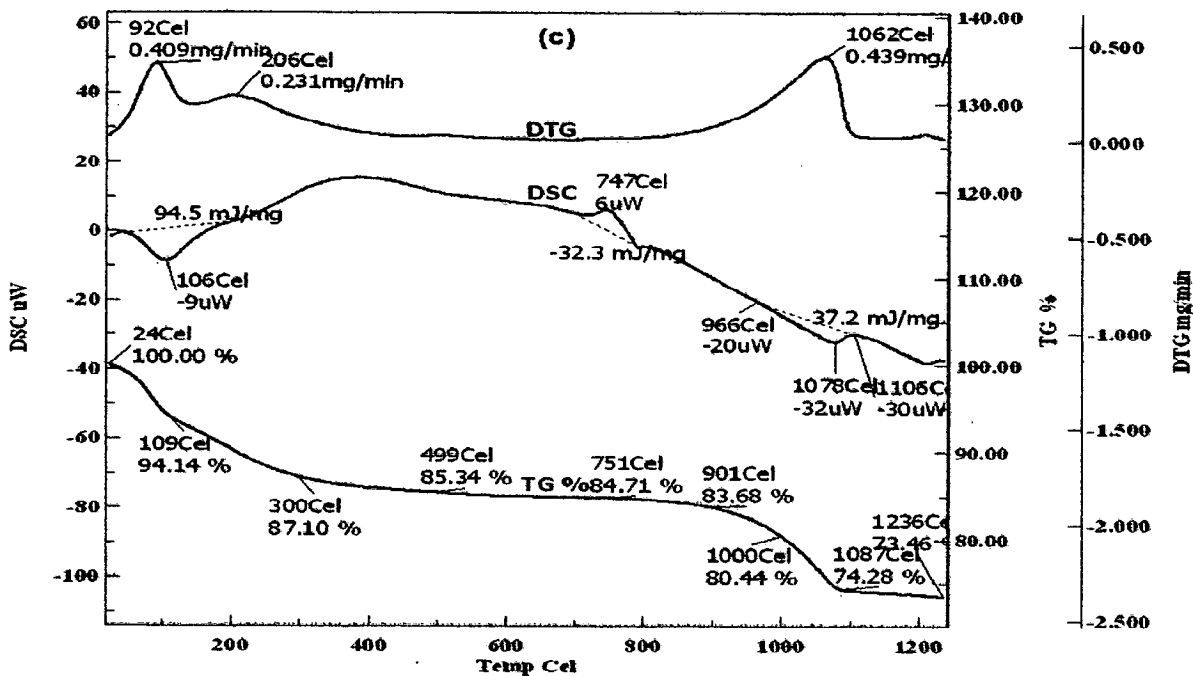DSC uW

TG %

DTG mg/min

Temp Cel

79

Fig. 5.1: The DSC/DTG/TG traces of the samples B1 synthesized by Co-Precipitation method at the heating rate of a) 10, b) 30, and c) 50 K/min.
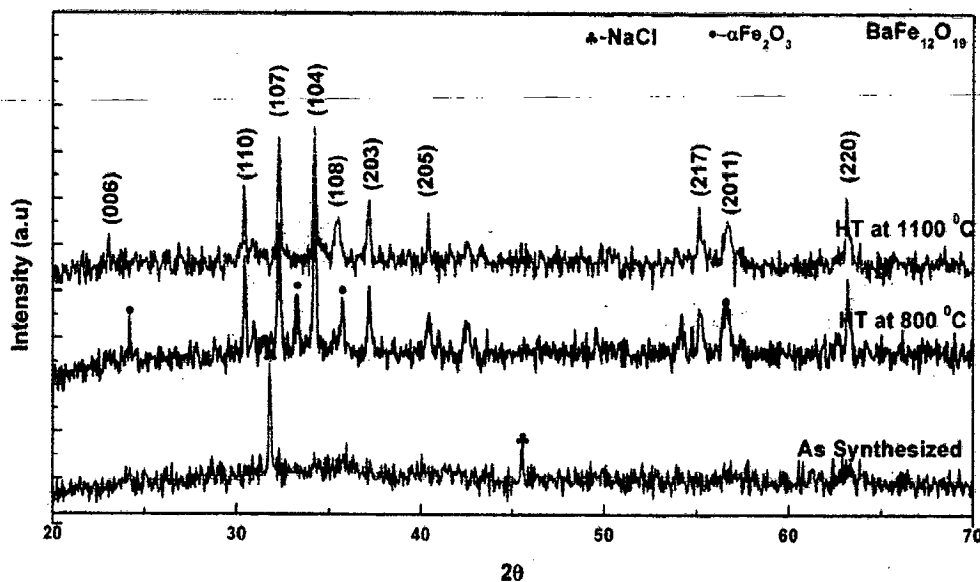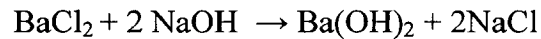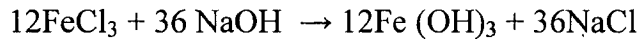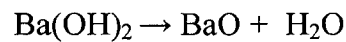

Fig. 5.2: XRD patterns of sample B1 in 'as synthesized' and heat treated at 800 and 1100°C in nitrogen atmosphere.

From the XRD and DSC results, it may be concluded that under the given co-precipitation reaction, the ferric chloride is converted to $\alpha Fe(OH)_3$ and NaCl, which is then dehydrated to form αFe_2O_3. Barium chloride is also dehydrated to $Ba(OH)_2$ which further converted to barium oxide. Finally, $BaFe_{12}O_{19}$ nanoparticles were formed during the post synthesis calcinations stage and can be described by the following chemical reactions.

Neutralization with Sodium hydroxide

$$12FeCl_3 + 36\ NaOH \rightarrow 12Fe\ (OH)_3 + 36NaCl$$

$$BaCl_2 + 2\ NaOH \rightarrow Ba(OH)_2 + 2NaCl$$

Nucleation of Nano Crystals

$$12Fe(OH)_3 \rightarrow 6Fe_2O_3 + 18H_2O$$

$$Ba(OH)_2 \rightarrow BaO + H_2O$$

Growth of Nano Crystals

$$BaO + 6Fe_2O_3 \rightarrow BaFe_{12}O_{19}$$
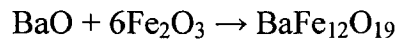
The DSC/DTG/TG traces of the sample S1 ($SrFe_{12}O_{19}$) carried out at the heating rate of 10, 30 and 50 K/min are shown in Figures 5.3 (a-c) respectively. The endothermic peak at about 794°C is attributed to the formation of multiple phases like αFe_2O_3 (JCPDS card No.05-637) and $SrFe_{12}O_{19}$ (JCPDS card No.5-637). This is also confirmed by the XRD analysis (Figure 5.4) of the powder obtained after the heat treated at 800°C (temperature of completion of reaction). The endothermic peak at 1051°C is attributed to the synthesis of pure $SrFe_{12}O_{19}$ (JCPDS card No.5-637) which is also confirmed by the XRD of the powder heat treated at 1200°C in the nitrogen atmosphere (Figure 5.4). The heat treatment temperature required for the synthesis of single phase strontium hexaferrite is observed to be higher than heat treatment temperature needed for the synthesis of single phase barium hexaferrite. In all the three cases, thermal gravimetry, TG analysis of strontium hexaferrite powder shows a weight loss of ~55% in the temperature range of 24 to1189°C after that no weight loss is observed. This is also probably due to the loss of moisture and degassing during the heat treatment process (Tyagi 2009; 2010; 2011; 2011). After the second endothermic reaction in all the cases, DTG and TG curves become smoother, this indicates the completion of reaction i.e. pure M-type strontium hexaferrite nanoparticles are formed. For the endothermic reaction resulting in the synthesis of single phase strontium hexaferrite nanoparticles, the area under the DSC curve (enthalpy of reaction) and T_m (temperature of reaction) for various heating rates (10, 30 and 50 K/min) are given in Table 5.2.

(a)

(b)

82

(c)

DSC uW / TG % / DTG mg/min plot

82Cel
0.125mg/min

302Cel
0.090mg/min

DTG

776Cel
0.147mg/min

1181Cel
2.352mg/

1.66 mJ/mg

313Cel
17uW

DSC

85.2 mJ/mg

32.6 mJ/mg

85Cel
1uW

170 mJ

804Cel
-18.3uW

1184Cel
-39uW

24Cel
100.00 %

299Cel
95.38 %

603Cel
93.96 %

900Cel
91.62 %

100Cel
97.94 %

TG %

804Cel
92.58 %

1001Cel
87.80 %

1225C
1099C 84.61
75.14 %

1189Cel
45.08 %

Temp Cel
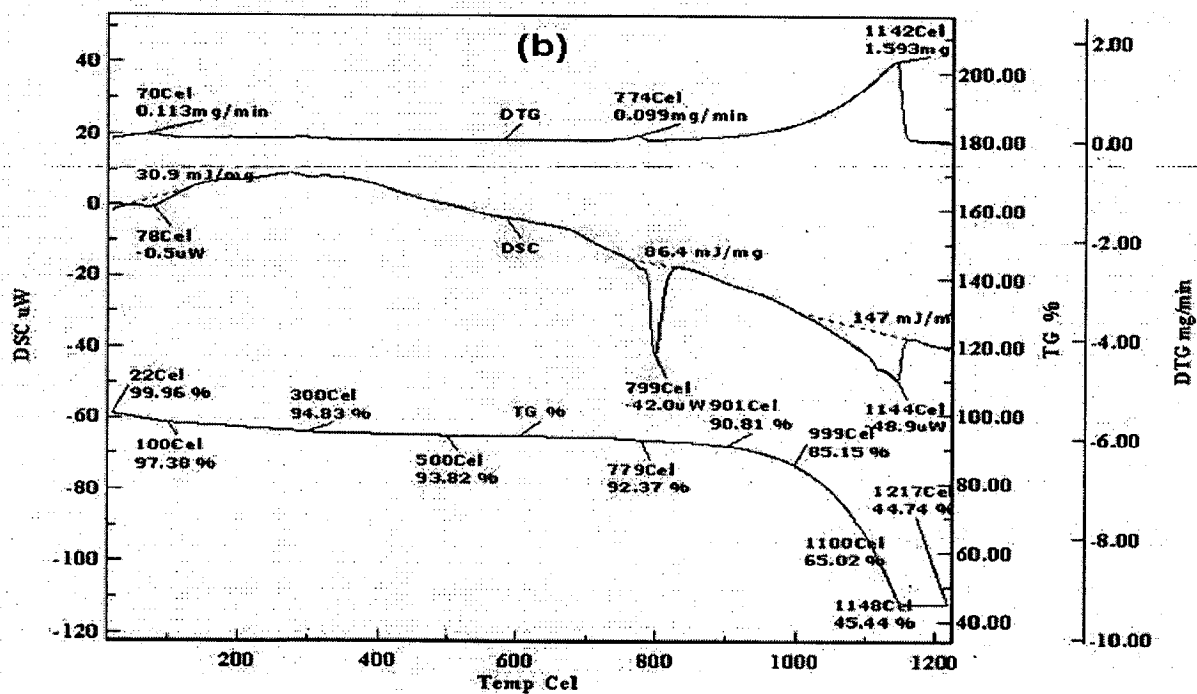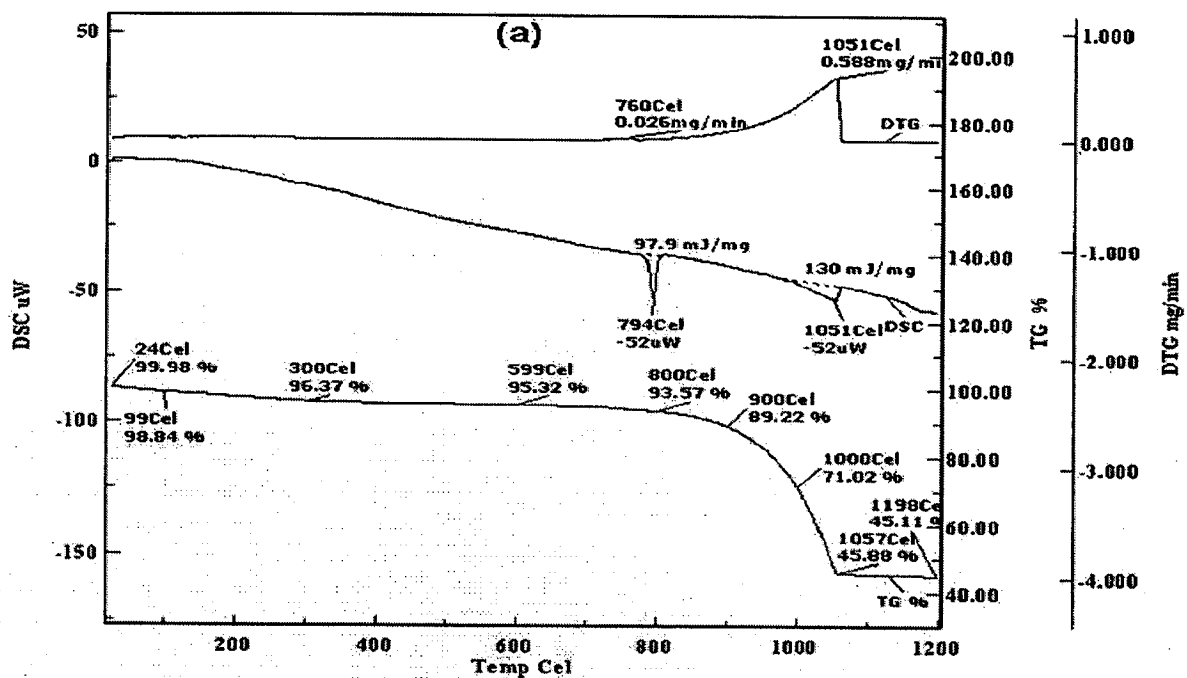
Fig. 5.3: The DSC/DTG/TG traces of the samples S1 synthesized by co-precipitation method at the heating rate of a) 10, b) 30 and c) 50 K/min.

XRD patterns

—α-Fe$_2$O$_3$ ◆ —SrFe$_{12}$O$_{19}$

at 1200 °C

at 800 °C
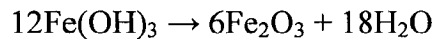
as synthesized

Intensity (a.u)

2θ

Fig. 5.4: XRD patterns of sample S1 in 'as synthesized' and heat treated at 800 and 1200°C in nitrogen atmosphere.

83

From the XRD and DSC study, it is observed that like barium hexaferrite nanoparticles first the hydroxide of strontium and iron is converted to their oxides. Further with increase in heat treatment temperature, they are observed to convert to strontium hexaferrite nanoparticles and are described by the following chemical reactions.

Neutralization with Sodium hydroxide

$$12FeCl_3 + 36\ NaOH \rightarrow 12Fe\ (OH)_3 + 36NaCl$$

$$SrCl_2 + 2\ NaOH \rightarrow Sr(OH)_2 + 2NaCl$$

Nucleation of Nano Crystals

$$12Fe(OH)_3 \rightarrow 6Fe_2O_3 + 18H_2O$$

$$Sr(OH)_2 \rightarrow SrO + H_2O$$

Growth of Nano Crystals

$$SrO + 6Fe_2O_3 \rightarrow SrFe_{12}O_{19}$$
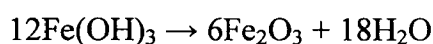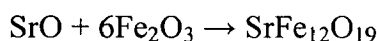
The DSC/TG traces of the sample SC ($SrFe_{12}O_{19}$, $CoFe_2O_4$) carried out at the heating rates of 10, 30 and 50 K/min in nitrogen atmosphere are shown in Figures 5.5 (a-c) respectively. DSC analysis carried out at all the heating rates also shows only endothermic peaks indicating that magnetic composite of strontium hexaferrite and cobalt spinel ferrite ($SrFe_{12}O_{19}$, $CoFe_2O_4$) is also synthesized by the endothermic reaction. The endothermic peak at about 806°C (Figure 5.5a) is attributed to the reaction resulting in the synthesis of multiple phases like αFe_2O_3 (JCPDS No.05-637), $CoFe_2O_4$ (JCPDS card No. 01-1121) and $SrFe_{12}O_{19}$ (JCPDS card No.5-637) which is confirmed by the XRD analysis of the powder heat treated at 900°C in the nitrogen atmosphere (Figure 5.6). The second endothermic peak at 1122°C is attributed to endothermic reaction resulting in the synthesis of desired magnetic phases like $SrFe_{12}O_{19}$ and $CoFe_2O_4$ with increasing crystallinity and is also confirmed by the XRD analysis of the powder heat treated at1200°C in nitrogen atmosphere (Figure 5.6). In case of magnetic composite the temperatures of reaction (806 and 1122°C) are observed to be higher than the temperature of reactions (794 and 1051°C) observed pure strontium hexaferrite nanoparticles. This might be due the formation of spinel ferrite along with hexaferrite nanoparticles. The synthesis of multiple phases might be restraining the growth of each other and resulting in the shifting of synthesis temperature toward the higher side. Thermal gravimetry, TG analysis of 'as synthesized' powder (Figure 5.5a) shows a weight loss of ~62 % in the temperature range of 25 to 1133°C. It may be due to the degassing and loss of moisture during the heat treatment process. Thereafter no weight loss is observed.
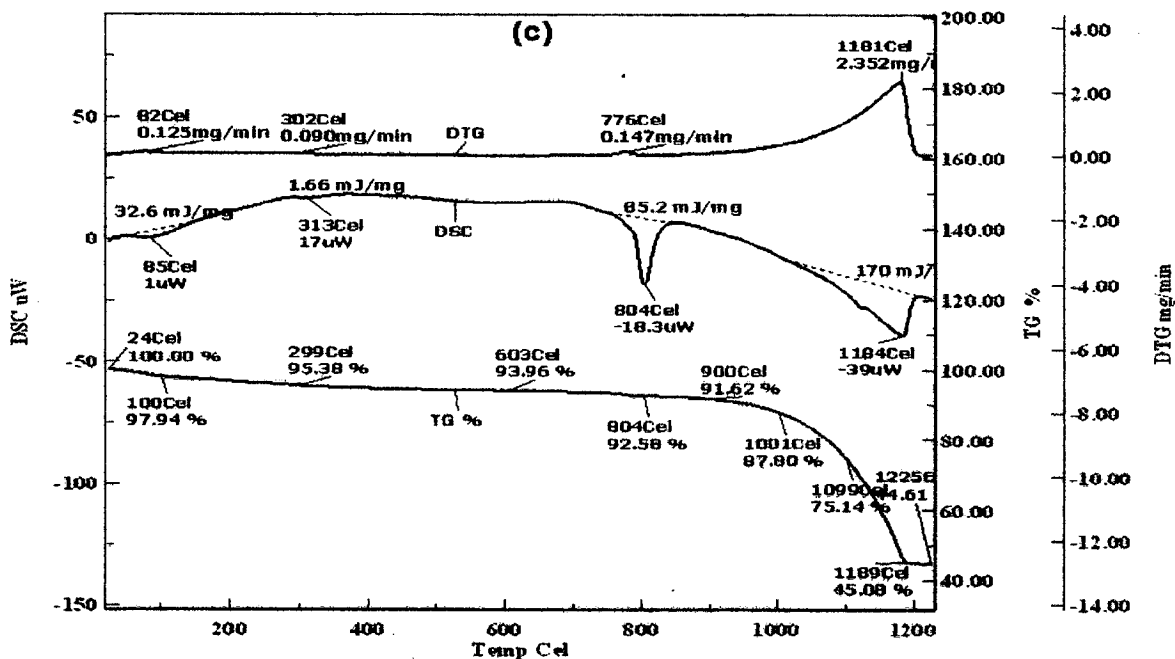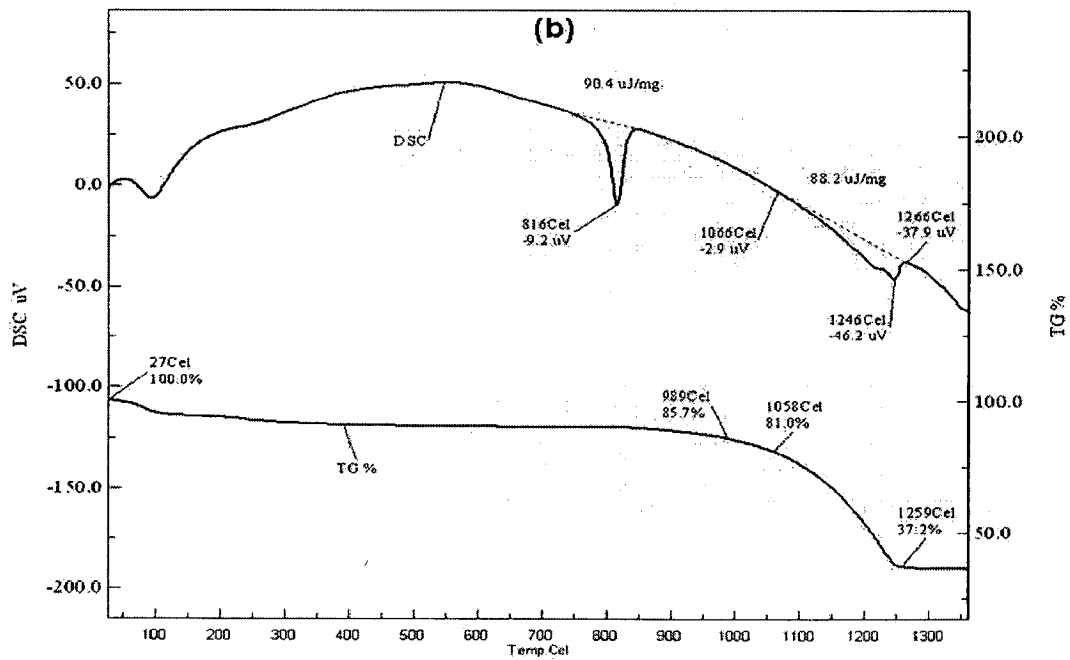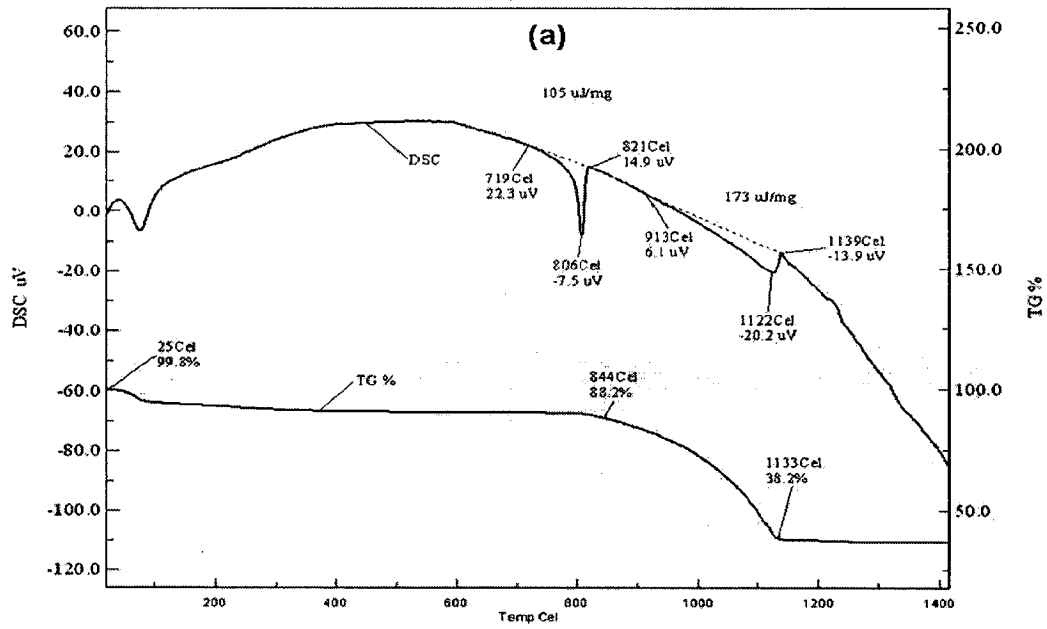
Figure 5.5: The DSC/DTG/TG traces of the samples SC synthesized by Co- Precipitation method at the heating rate of a) 10, b) 30 and c) 50 K/min
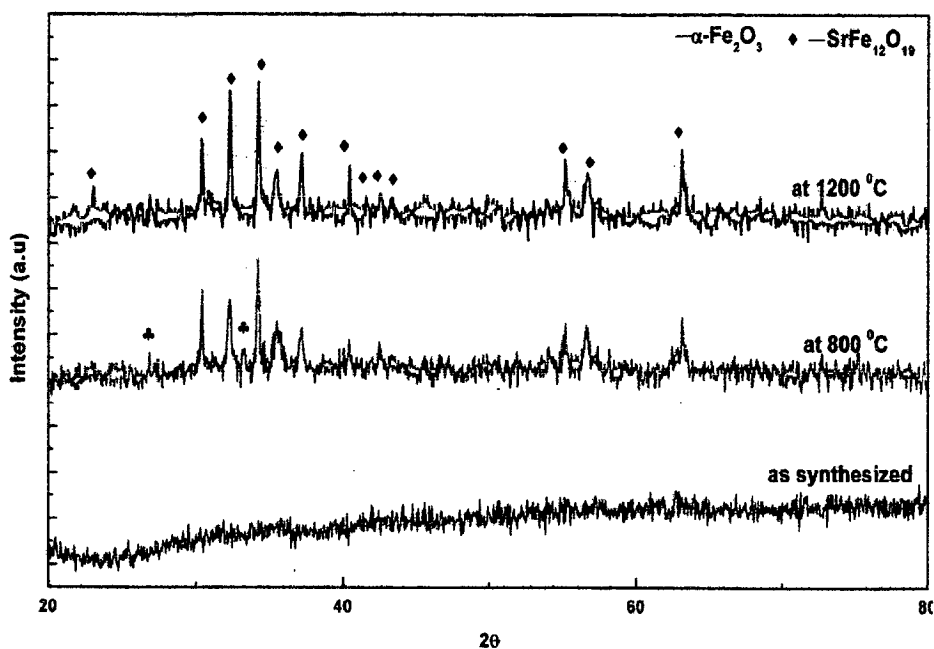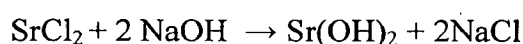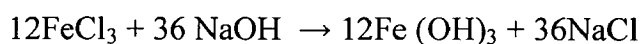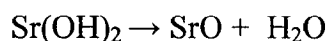

Figure 5.6: XRD patterns of samples SC in 'as synthesized' and heat treated at 900 and1200°C in nitrogen atmosphere.

Like single phase barium and strontium hexaferrite nanoparticles, the magnetic composite of $SrFe_{12}O_{19}$ and $CoFe_2O_4$ is also synthesized during the post synthesis calcinations stage and can be described by the following chemical reactions.

Neutralization with Sodium hydroxide

$$12FeCl_3 + 36\ NaOH \rightarrow 12Fe\ (OH)_3 + 36NaCl$$

$$CoCl_2 + 2\ NaOH \rightarrow Co(OH)_2 + 2NaCl$$

$$SrCl_2 + 2\ NaOH \rightarrow Sr(OH)_2 + 2NaCl$$

Nucleation of Nano Crystals

$$12Fe(OH)_3 \rightarrow 6Fe_2O_3 + 18H_2O$$

$$Co(OH)_2 \rightarrow CoO + H_2O$$

$$Sr(OH)_2 \rightarrow SrO + H_2O$$

Growth of Nano Crystals

$$CoO + Fe_2O_3 \rightarrow CoFe_2O_4$$

$$SrO + 6Fe_2O_3 \rightarrow SrFe_{12}O_{19}$$
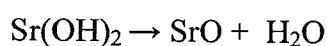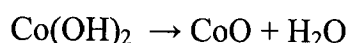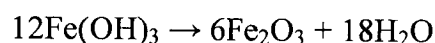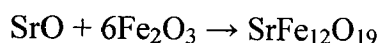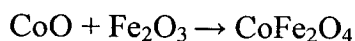
For the endothermic reaction resulting in the synthesis of magnetic composite of strontium hexaferrite and spinel cobalt ferrite, the area under the DSC curve (enthalpy of reaction) and T_m (temperature of reaction) for various heating rates (10, 30 and 50 K/min) are given in Table 5.2. In case of magnetic composite containing strontium hexaferrite and spinel ferrite (binary and ternary magnetic composite), the same trend of DSC/DTG/TG pattern is observed (Figures 5.7, 5.9, 5.11, 5.13 and 5.15). The formations of different magnetic phases synthesized at different temperatures are also confirmed by their XRD analysis (Figures 5.8, 5.10, 5.12, 5.14 and 5.16). For remaining samples (SN, SZ, SNZ, SNC and SCZ), the area under the DSC curve and T_m for various heating rates (10, 30 and 50 K/min) are also given in Table 5.2. In some cases (Figures 5.7 and 5.9), one endothermic peak is also observed at $\sim299^{\circ}C$. This peak is attributed to the conversion of hydroxide to oxides phases (Ataie, 2001; 2002). In all the cases the temperature of maximum reaction point is shifting toward the higher side with increase in heat treatment temperature. This is due to the fact that, with increase in heat treatment temperature the particles find lesser time for their formation and growth and leads to increase in temperature of reaction.

(a)

71 Cel
0.359 mg/min

DTG

1125 Cel
1.041 mg/min

300.0

DSC

15.4 uJ/mg

99.2 uJ/mg

87.1 uJ/mg
299 Cel
15.8 uW

73 Cel
-9.7 uW

813 Cel
-11.9 uW

124 uJ/mg

1129 Cel
-28.7 uW

31 Cel
100.1%

299 Cel
98.5%

TG%

80 Cel
95.3%

799 Cel
88.8%

1131 Cel
37.7%

DSC uW

TG %

DTG mg/min

Temp Cel

(b)

87 Cel
0.579 mg/min

DTG

1214 Cel
2.609 mg/min

180.0

DSC

14.8 uJ/mg

72.7 uJ/mg

98.8 uJ/mg
328 Cel
29.1 uW

92 Cel
-6.5 uW

819 Cel
-2.4 uW

70.6 uJ/mg

1218 Cel
-35.8 uW

31 Cel
99.7%

TG%

799 Cel
86.8%

1227 Cel
38.3%

DSC uV

TG %

DTG mg/min

Temp Cel

88

Fig. 5.7: The DSC/DTG/TG traces of the samples SN synthesized by Co-Precipitation method at the heating rate of a) 10, b) 30 and c) 50 K/min.
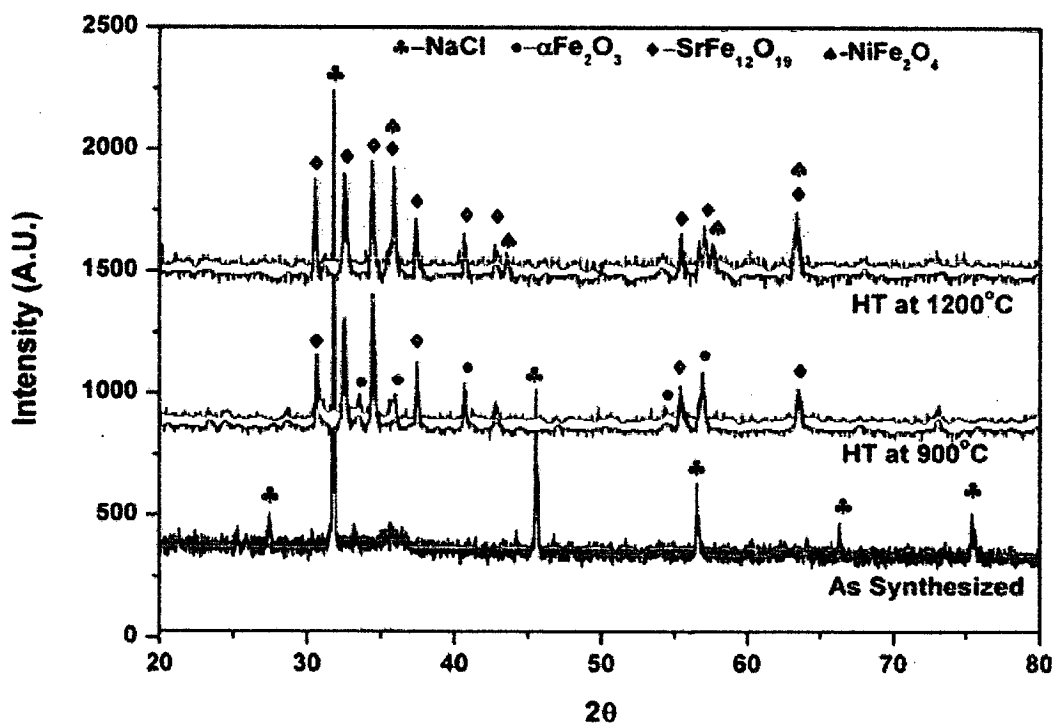
Fig. 5.8: XRD patterns of samples SN in 'as synthesized' and heat treated at 900 and1200°C in nitrogen atmosphere.
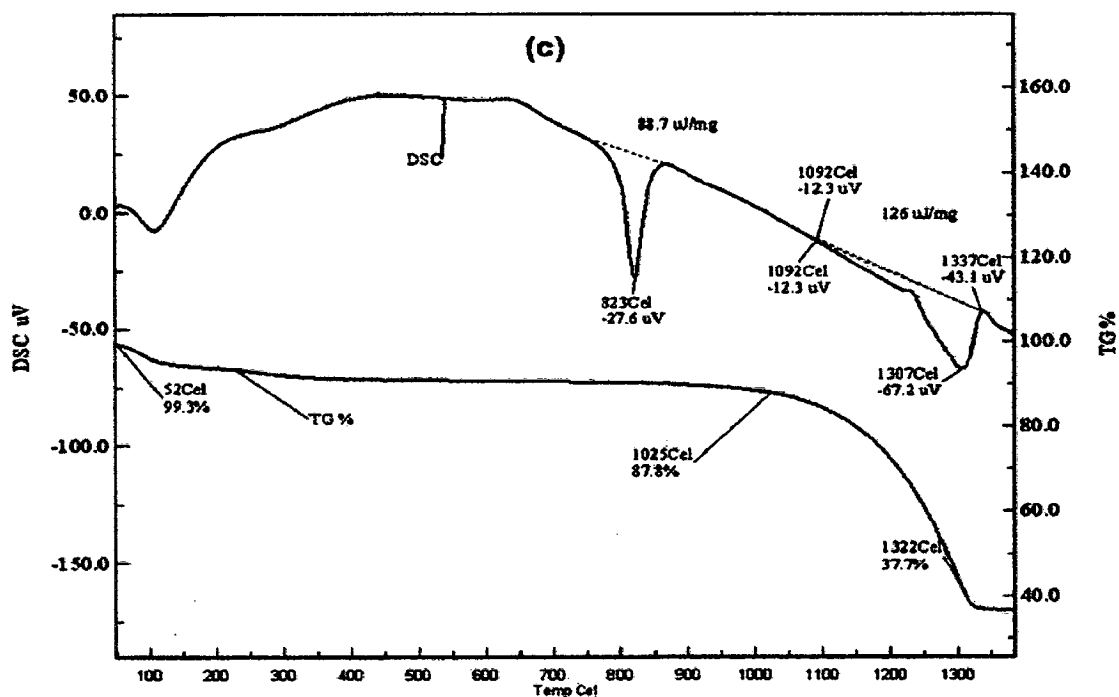
(a)

(b)

90
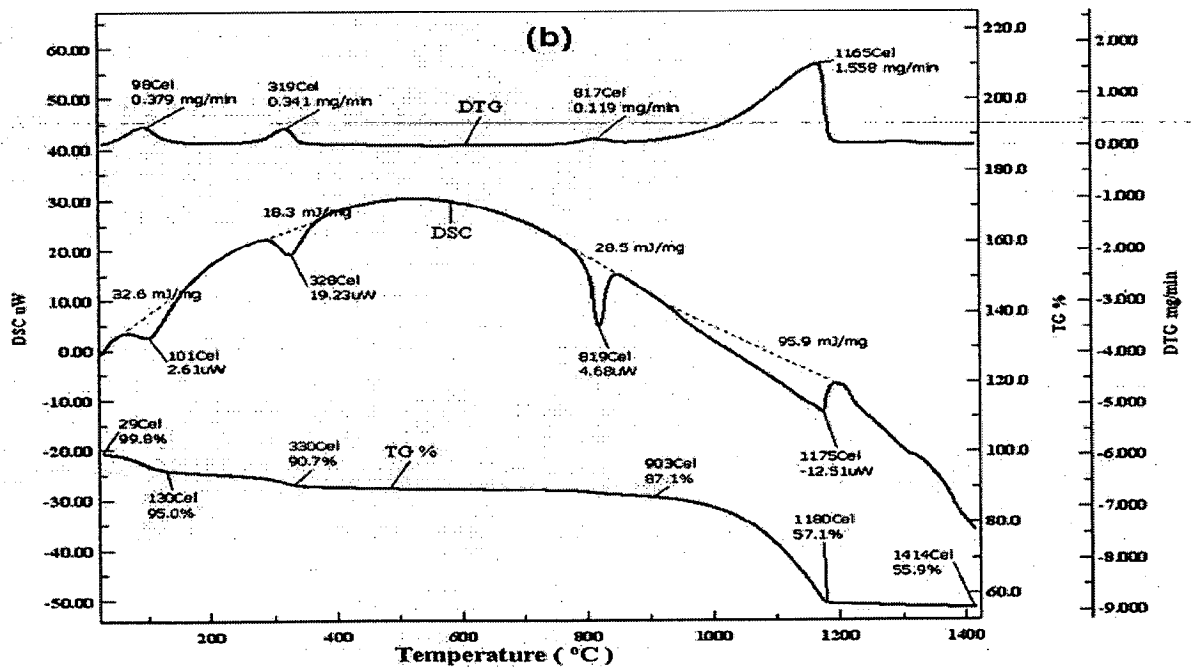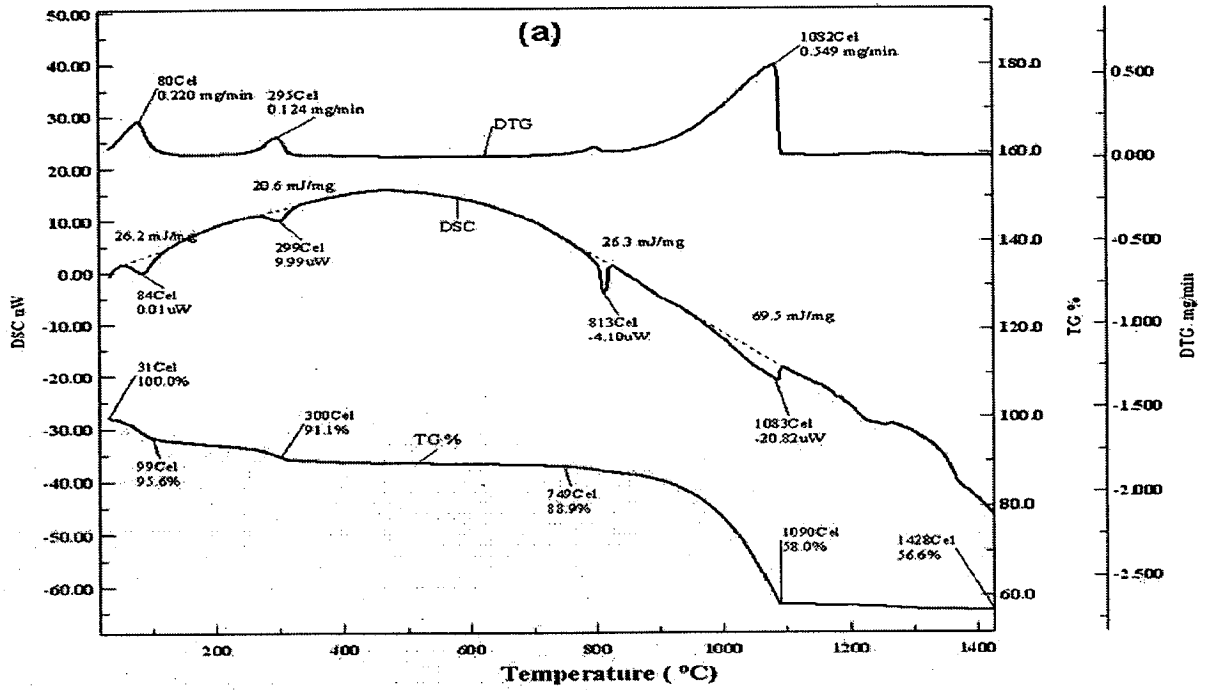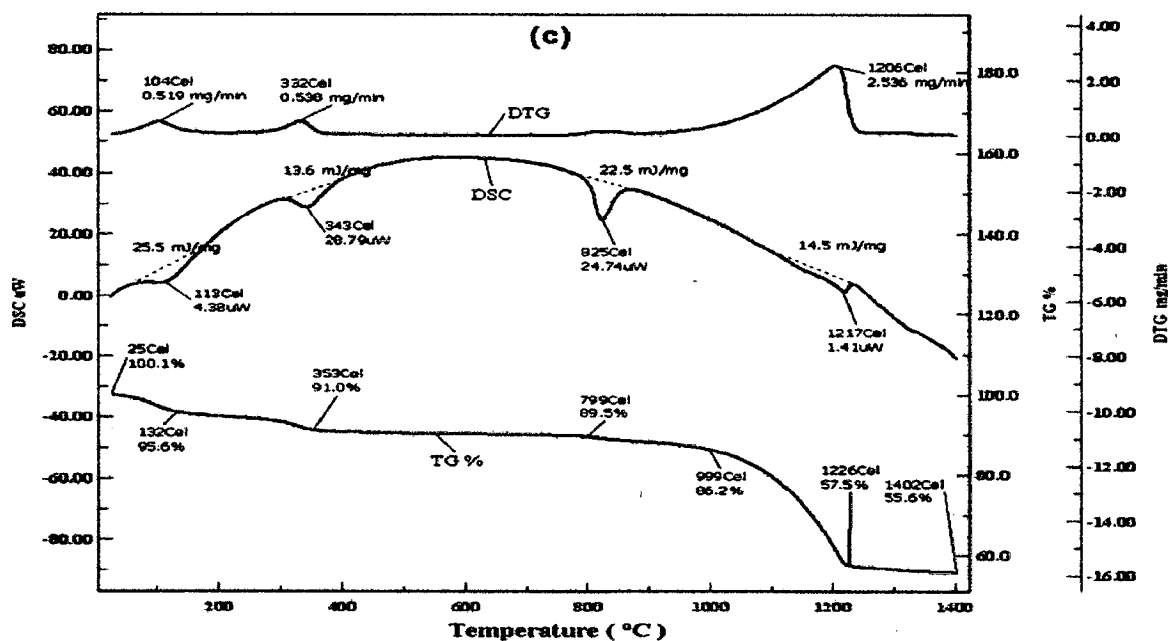
Fig. 5.9: The DSC/DTG/TG traces of the samples SZ synthesized by co-precipitation method at the heating rate of a) 10, b) 30 and c) 50 K/min.
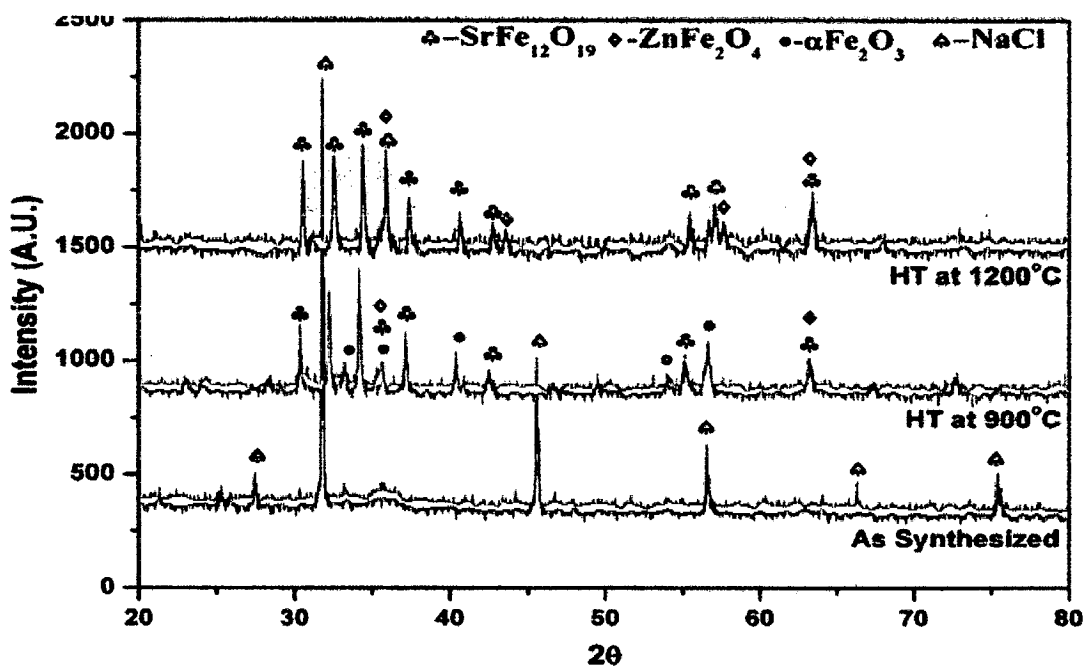
Fig. 5.10: XRD patterns of samples SZ in 'as synthesized' and heat treated at 900 and 1200°C in nitrogen atmosphere.

(a)

(b)

92
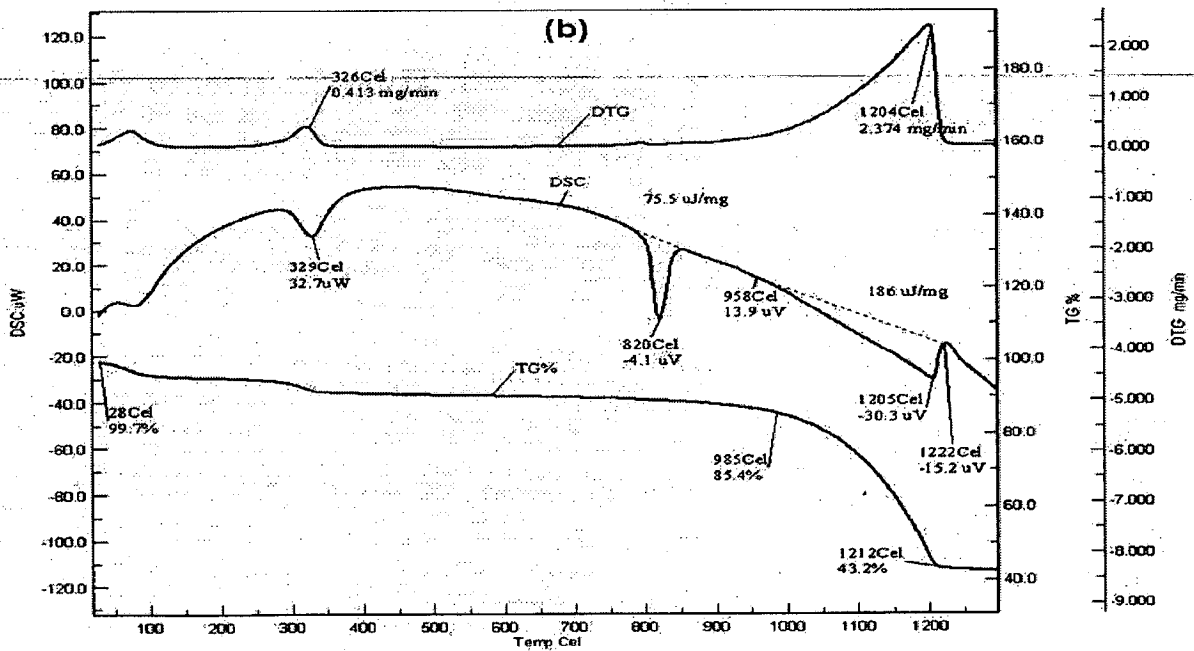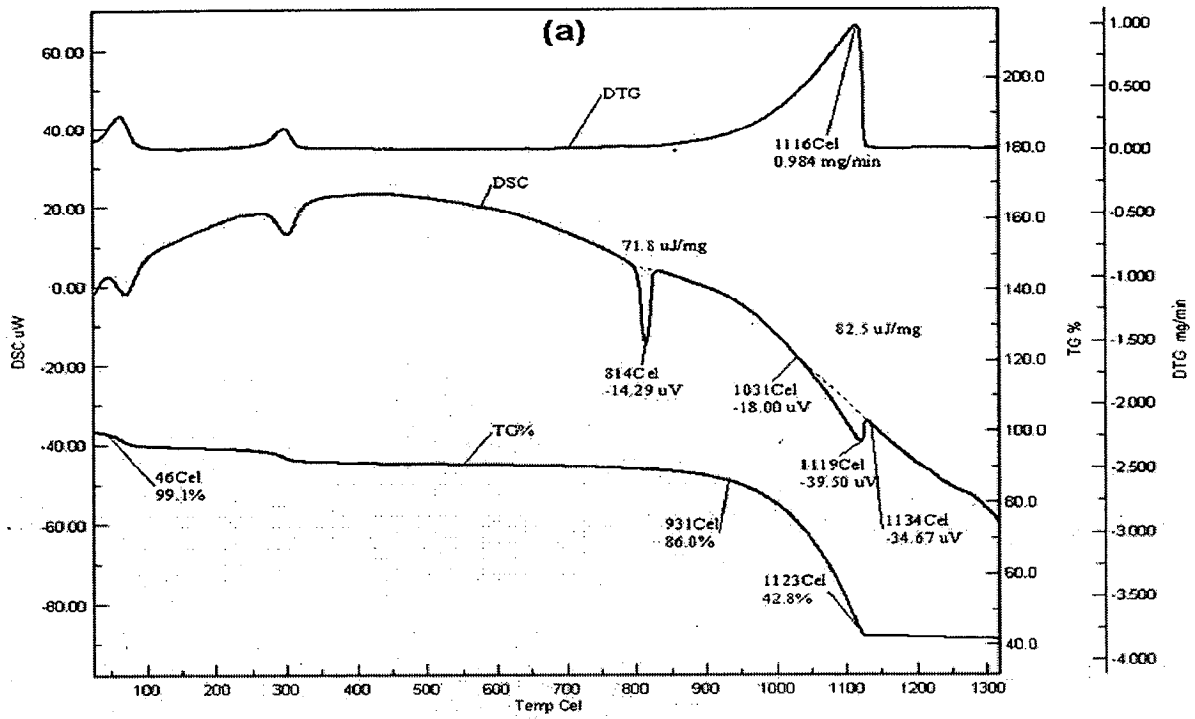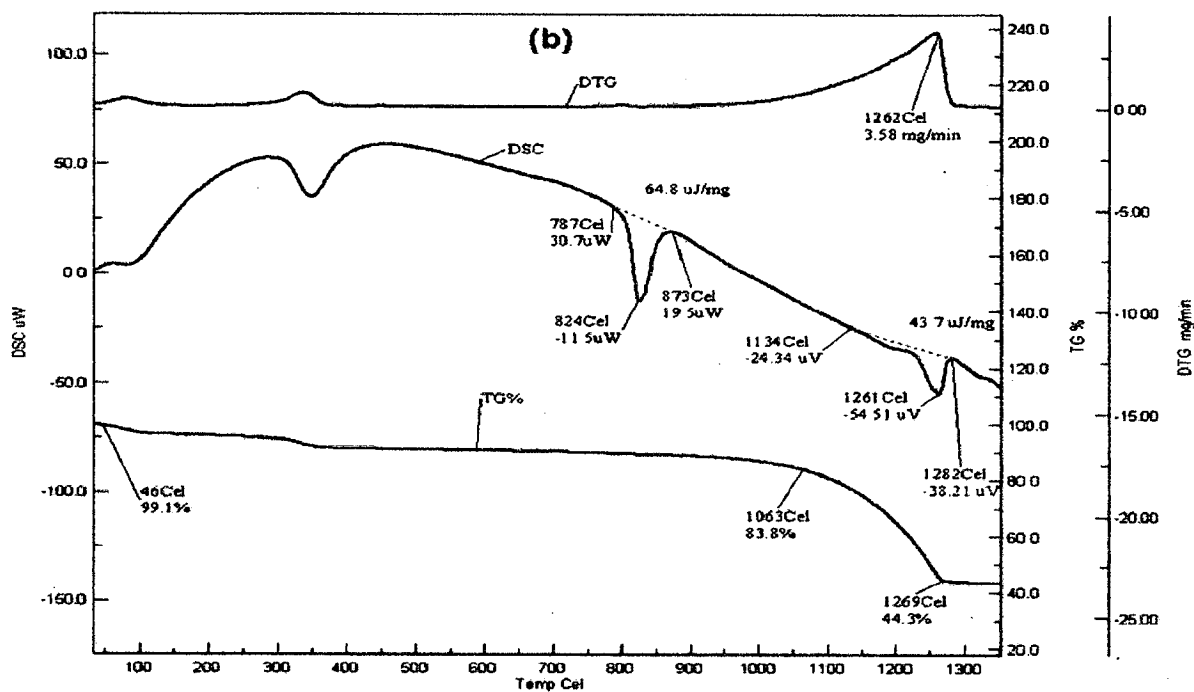
Fig.5.11: The DSC/DTG/TG traces of the samples SNZ synthesized by co-precipitation method at the heating rate of a) 10, b) 30 and c) 50 K/min
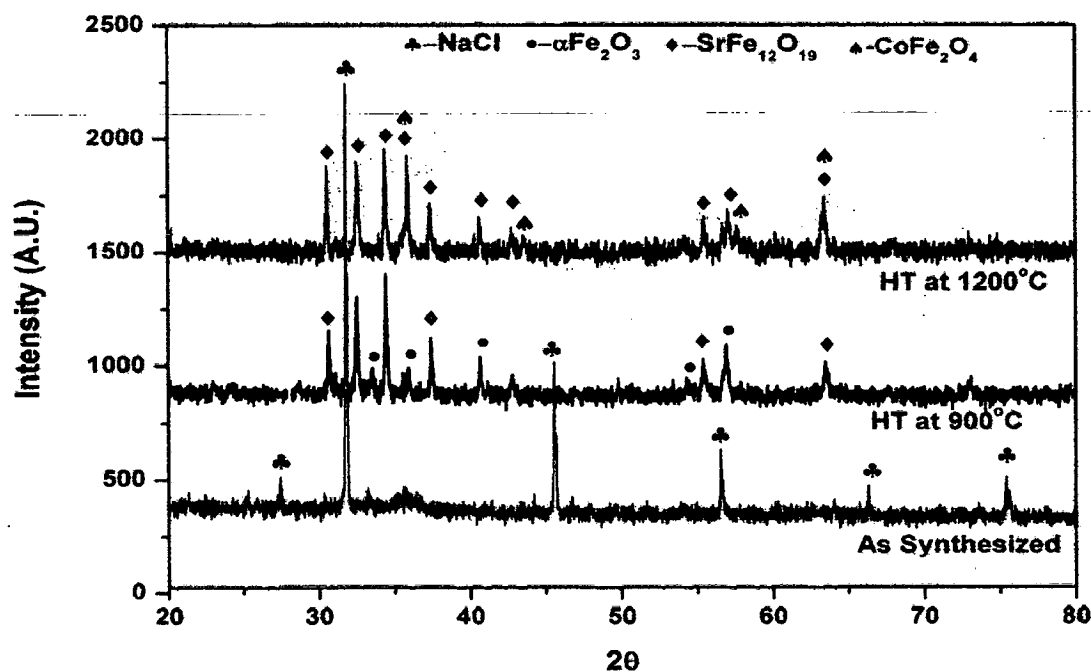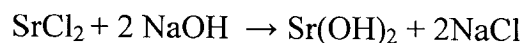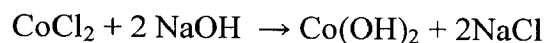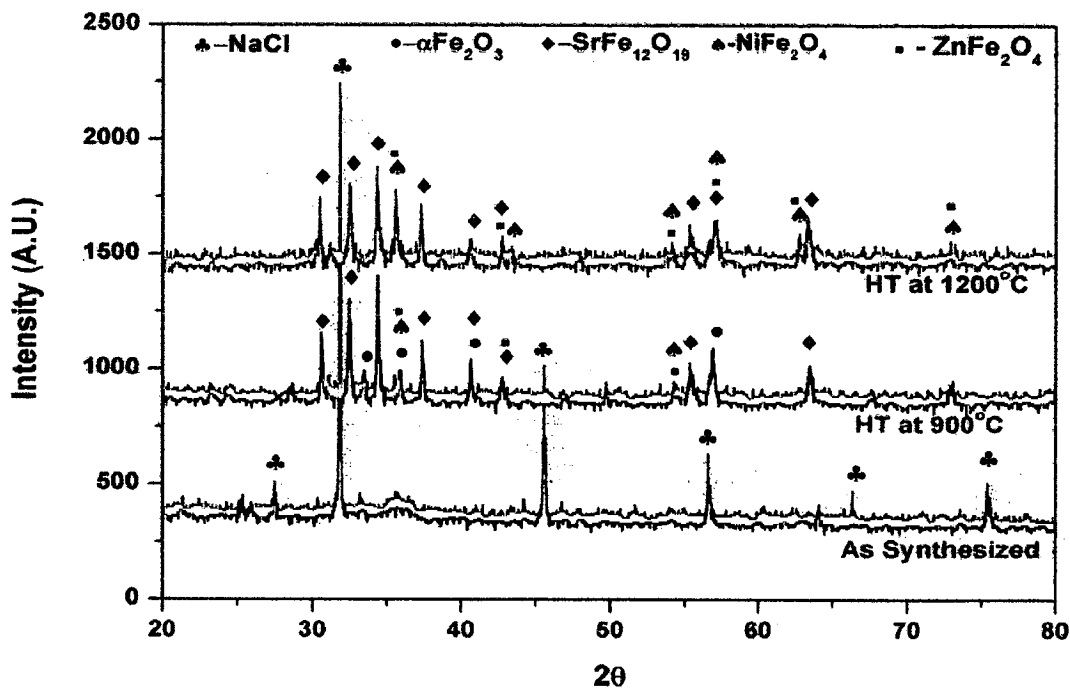

Fig. 5.12: XRD patterns of samples SNZ in 'as synthesized' and heat treated at 900 and 1200°C in nitrogen atmosphere.

(a)

DSC uw

TG %

DTG mg/min

Temp Cel

299 Cel
0.06 mg/min

1072 Cel
0.50 mg/min

35.7 mJ/mg

305 Cel
0.1 uw

93.5 mJ/mg

421 mJ/mg 1090 Cel
-30.1 uw

809 Cel
-25.0 uw

917 Cel
-21.1 uw

1074 Cel
-36.0 uw

16 Cel
100.0 %

15.7 Cel
99.99 %

900 Cel
85.99 %

1000 Cel
74.18 %

1085 Cel
44.9 %

110

(b)

DSC uw

DTG mg/min

TG %

Temp Cel

320 Cel
0.1 mg/min

416 Cel
0.2 mg/min

DTG

1165 Cel
1.4 mg/min

32.9 mJ/mg

DSC

90.9 mJ/mg

330 Cel
15.9 uw

1185 Cel
-11.9 uw

954 Cel
-3.4 uw

448 mJ/mg

814 Cel
-11.9 uw

16 Cel
100.0 %

1001 Cel
83.44 %

1156 Cel
-27.5 uw

TG %

16.4 Cel
99.98 %

900 Cel
87.90 %

1170 Cel
44.4 %

94

Fig. 5.13: The DSC/DTG/TG traces of the samples SNC synthesized by co-precipitation method at the heating rate of a) 10, b) 30 and c) 50 K/min
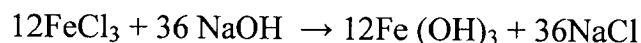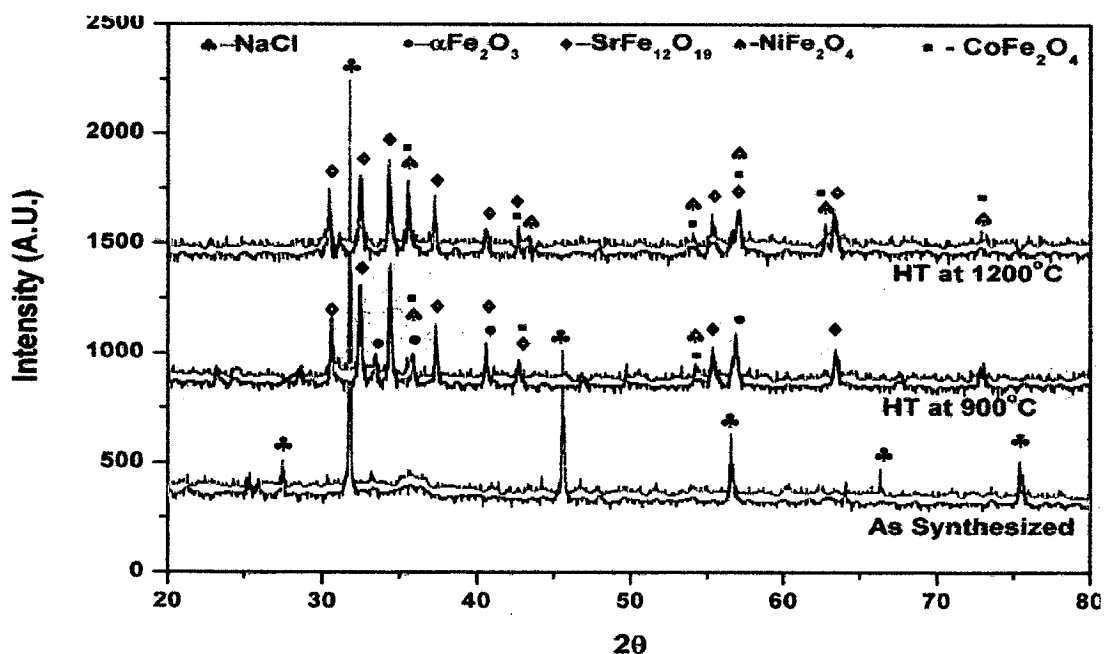

Fig. 5.14: XRD patterns of SNC nanocrystals in 'as synthesized' and heat treated at 900 and1200°C in nitrogen atmosphere.

(a)

(b)

96
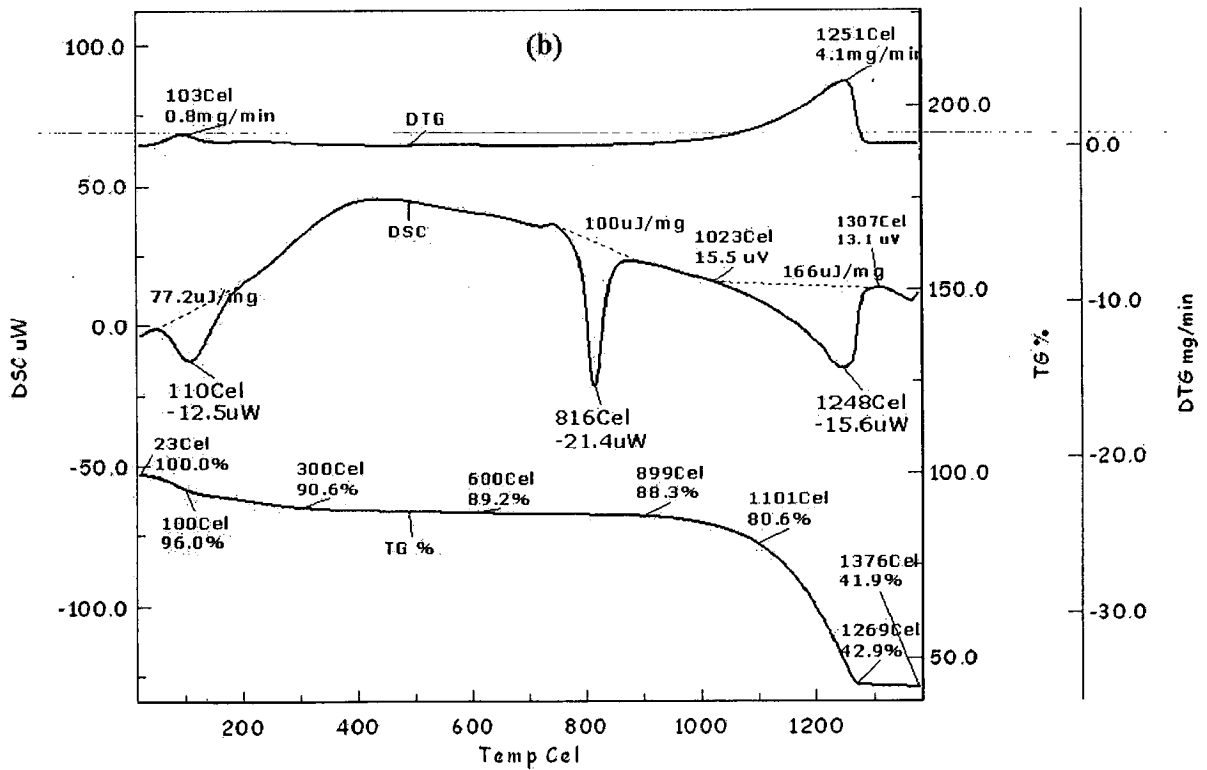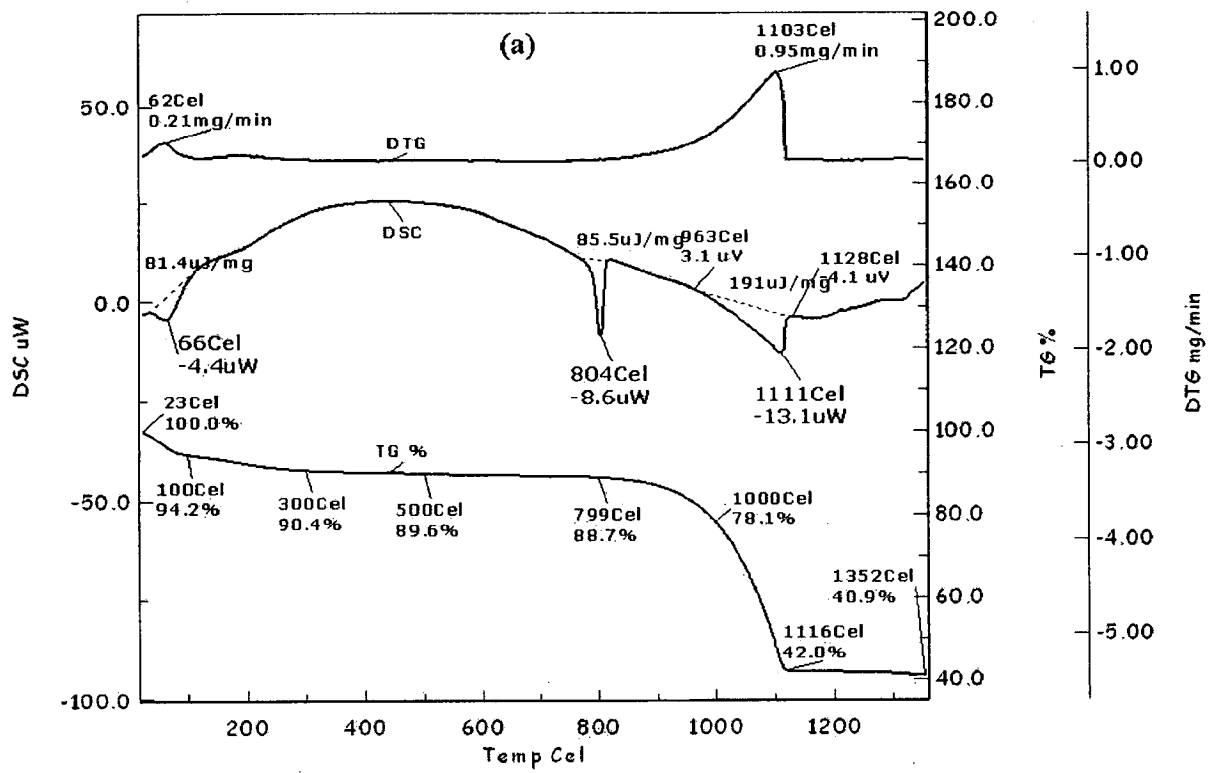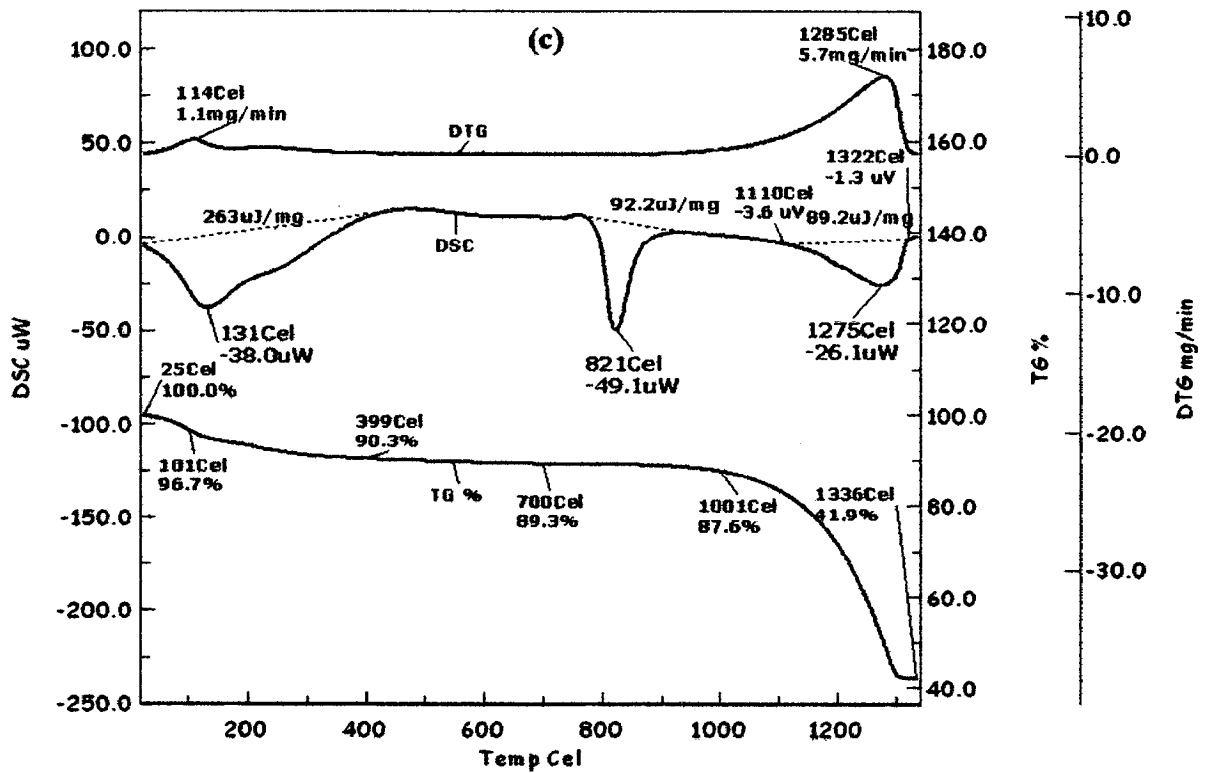
Fig. 5.15: The DSC/DTG/TG traces of the samples SCZ synthesized by co-precipitation method at the heating rate of a) 10, b) 30 and c) 50 K/min.
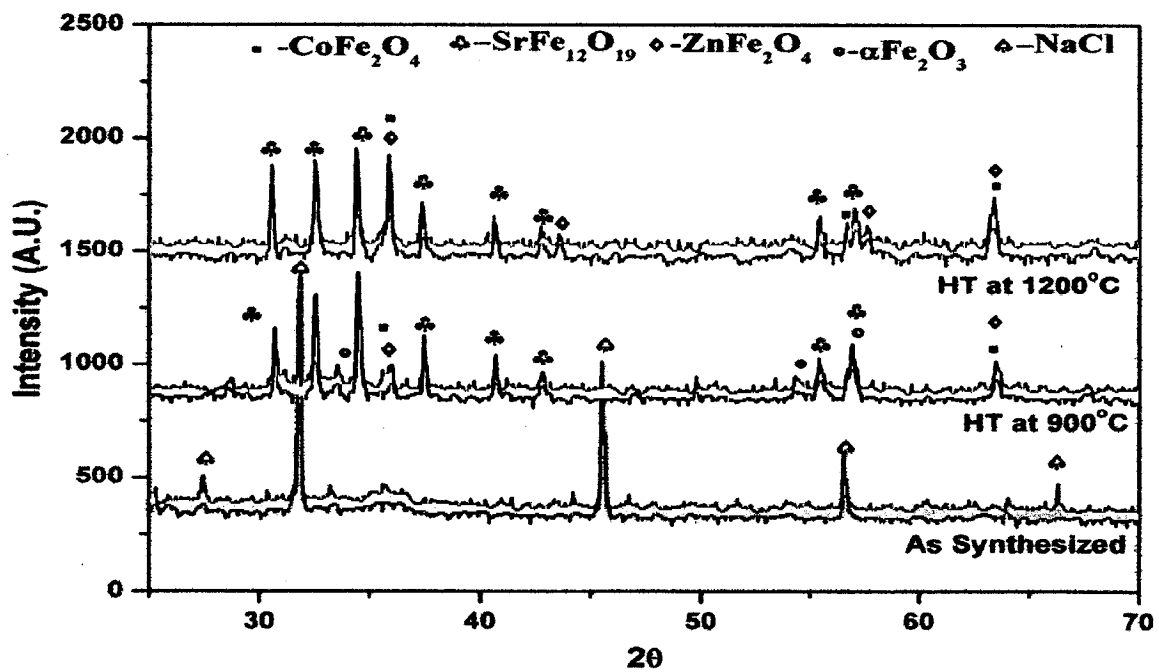
Fig. 5.16: XRD pattern of samples SCZ in 'as synthesized' and heat treated at 900 and 1200°C in nitrogen atmosphere.

5.3.1 Theoritical Background for Calculating The Activation Energy And Avrami Index Parameter

Different models have been applied to study the reaction kinetics of phase transformation in various systems (Wang, 1994; Wang, 2002; Friedman, 1963; Pant, 2007; Gupta, 2009; Agarwala, 2005; Criado, 1987; Joraid, 2005; Holubova 2000; Hou, 2008; Teng, 2007; Xie, 2007). Among various models, popular JMA model have been extensively 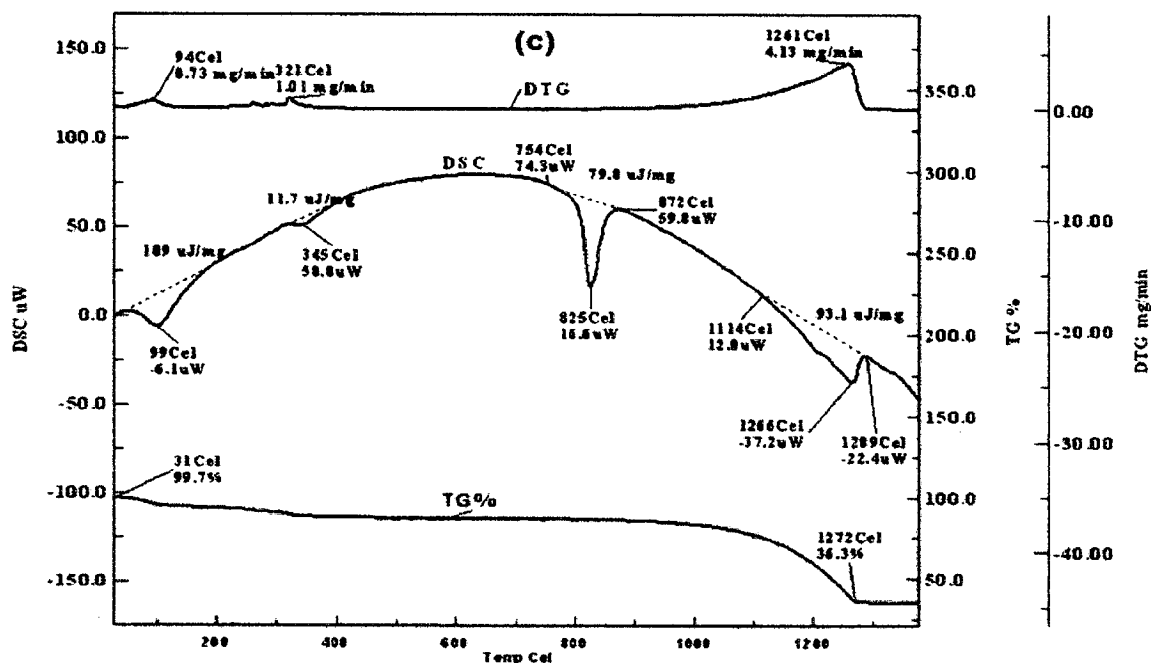used and its limitation for non-isothermal reaction kinetics of some specific systems has been reported (Wang, 1994). It is also reported that for the reaction occurring at relatively higher temperatures (800-1200°C), the kinetics obtained by non-isothermal method is found to be applicable (Wang, 1994). Considering the above fact, JMA model has been applied in the present study, which provides sufficient indications on the kinetics of hexaferrites and composite of hexaferrite and spinel ferrite formation in various reactions carried out under present study.

The reaction rate of solid state transformation obeying JMA kinetic model can be written in the following form (Criado, 1987)

$$d\alpha/dt = An (1-\alpha) [\ln 1/(1-\alpha)^{(n-1/n)} \exp (-E/RT)] \tag{5.1}$$

Where

α is the transformed fraction, t is time of transformation, T is the absolute temperature, R is the gas constant (R= 8.314 J/mol/K), n is Avrami index parameter depending on the nucleation mechanism and number of growth dimensions, E is the activation energy, A is the pre exponent factor. The above equation is differentiated and equated to zero ($d^2\alpha/dt^2=0$) for maximum reaction rate at T_m temperature to obtain final equation.

$$\ln \beta/T_m^2 = -E/RT_m + C_1 \tag{5.2}$$

Where

β is the heating rate, T_m is maximum reaction rate point, C_1 is constant. For all the different heating rates T_m is calculated from the DSC plots with the assumption that the peak of respective DSC plot for a particular heating rate (β) is maximum reaction rate point. The plot for $\ln \beta/T_m^2$ versus $1/T_m$ is linear and slope of this curve gives the value of activation energy E.

Integrating equation (5.1) and taking double natural logarithm and using Doyle's approximation (Doyle, 1962).

$$\ln[\ln(1/1-\alpha)] = C_2 - 1.05 \, nE/RT \qquad (5.3)$$

Where C_2 is a constant

Thus, slope of the $\ln[\ln(1/1-\alpha)]$ versus $1/T$ plot gives the value of nE. Ratio of slopes of this plot and E (slope of plot for $\ln \beta/T^2_m$ versus $1/T_m$) would thus give value of 'n' for the reaction under a particular heating rate.

The above model is for pressure less systems. In case of pressure assisted systems, all the kinetic parameters will change due to change in onset temperature, enthalpy of reaction, maximum reaction point etc. However, kinetic studies through DSC of pressure less powder mixture provide useful indications about the trend of reaction for pressure assisted systems also. It is important to mention that, mainly two factors can be affected due to application of pressure in a reaction. First is change in maximum reaction point temperature (T_m), which is likely to decrease due to closer contact of reactant and resulting in higher and easy availability of reactant specifically at higher heating rate i.e. 50°C/min. Second factor is the change in activation energy which is likely to decrease, due to similar reason. Decrease in activation energy is an indication of low energy barrier for reaction, which means early start of reaction. It means Avrami index parameter (n) value is likely to increase due to decrease in activation energy (from JMA equations) helping in multidimensional nucleation/ growth of product phase. Therefore, from the above discussion, it is clear that DSC study of pressure less system is limiting condition of pressure assisted system from the point of progress of reaction.

5.3.2 Determination of Activation Energy (E) and Kinetics Parameter (n)

Using the non-isothermal kinetics as per equation 5.2, plot of $\ln\beta/Tm^2$ versus $1/T$ for different samples (B1, S1, SC, SN, SZ, SNZ, SNC and SCZ) are shown in Figures 5.17 a-h. From the slope of these curves the activation energy for the reaction resulting in the synthesis of various magnetic phases is calculated and given in Table 5.3. Values of nE are evaluated from $\ln[\ln 1/(1-\alpha)]$ vs $1/T$ plots based on the relationship depicted in equation 5.3. These plots for different samples used in the present study are shown in Figures 5.18-5.25 at heating rates of 10 K/min, 30 K/min and 50 K/min. The nE values are obtained from the slopes of these curves shown in Figures 5.18-5.25. The values of n are computed by dividing these slopes by activation energy and are given in Table 5.4.
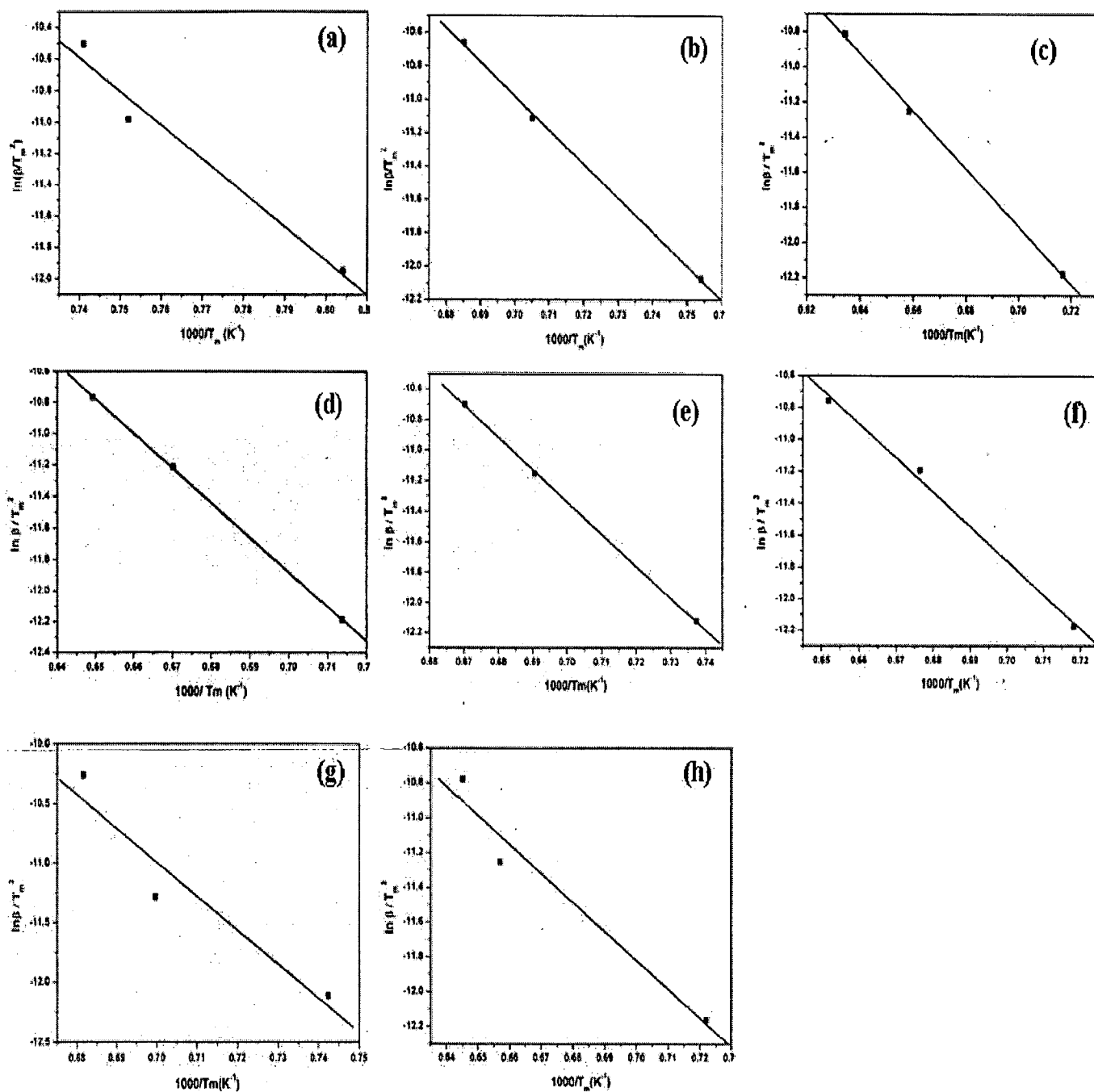
Fig. 5.17: Plot of $\ln\beta/T_m^2$ versus $1000/T_m$ obtained at three heating rates 10, 30 and 50 K/min for samples a) B1, b) S1, c) SC, d) SN, e) SZ, f) SNZ, g) SNC, and h) SCZ.

Table 5.3: Activation Energy of magnetic RAM synthesized in present investigation.

S. No.	Sample	Phases	Activation Energy (KJ/mol)
1	B1	$BaFe_{12}O_{19}$	178.15
2	S1	$SrFe_{12}O_{19}$	168.33
3	SC	$SrFe_{12}O_{19}$, $CoFe_2O_4$	185.33
4	SN	$SrFe_{12}O_{19}$, $NiFe_2O_4$	183.72
5	SZ	$SrFe_{12}O_{19}$, $ZnFe_2O_4$	175.94
6	SNZ	$SrFe_{12}O_{19}$, $NiFe_2O_4$, $ZnFe_2O_4$	176.79
7	SNC	$SrFe_{12}O_{19}$, $NiFe_2O_4$, $CoFe_2O_4$	235.22
8	SCZ	$SrFe_{12}O_{19}$, $CoFe_2O_4$, $ZnFe_2O_4$	182.84
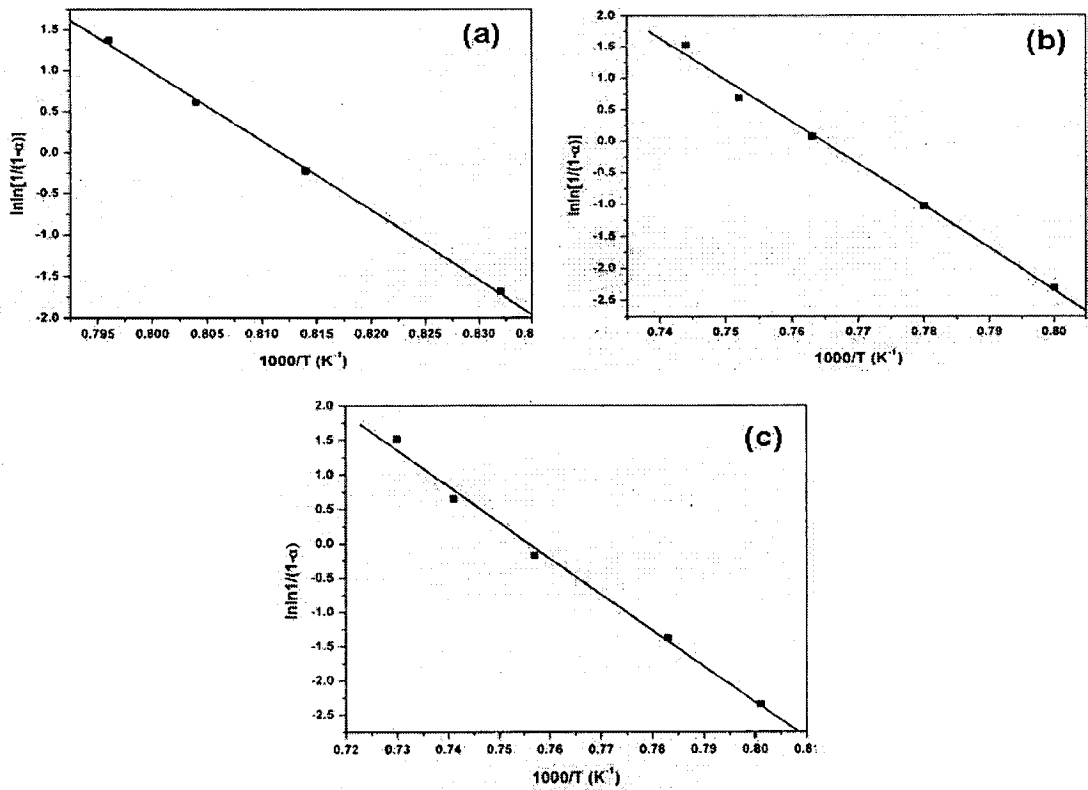
Fig.5.18: Plot of $\ln[\ln 1/(1-\alpha)]$ versus $1/T$ plots of sample B1 at different heating rates, a) 10K/min, b) 30 K/min, c) 50 K/min.

Fig. 5.19: Plot of ln[ln 1/(1- α)] versus 1/T plots of sample S1at different heating rates, a) 10K/min, b) 30 K/min, c) 50 K/min.

Fig. 5.20: Plot of ln[ln 1/(1- α)] versus 1/T plots of sample SC at different heating rates, a) 10K/min, b) 30 K/min, c) 50 K/min.

102

Fig. 5.21: Plot of ln[ln 1/(1- α)] versus 1/T plots of sample SN at different heating rates, a) 10K/min, b) 30 K/min, c) 50 K/min.

Fig. 5.22: Plot of ln[ln 1/(1- α)] versus 1/T plots of sample SZ at different rates, a) 10K/min, b) 30 K/min, c) 50 K/min.

Fig. 5.23: Plot of ln[ln 1/(1- α)] versus 1/T plots SNZ at different heating rates, a) 10K/min, b) 30 K/min, c) 50 K/min.

Fig. 5.24: Plot of ln[ln 1/(1- α)] versus 1/T plots of sample SNC at different heating rates, a) 10K/min, b) 30 K/min, c) 50 K/min.

Fig. 5.25: Plot of ln[ln 1/(1- α)] versus 1/T plots of sample SCZ at different rates, a) 10K/min, b) 30 K/min, c) 50 K/min.

Table 5.4: Slopes of ln[ln1/1- α] versus 1/T plots and calculated n values from the obtained DSC curve.

Sample	Slope, nE/R at different heating rate			n		
	10 °C/min	30 °C/min	50 °C/min	10 °C/min	30 °C/min	50 °C/min
B1	79.0×10^3	59.71×10^3	53.73×10^3	3.68	2.78	2.50
S1	71.7×10^3	71.5×10^3	72.5×10^3	3.54	3.53	3.58
SC	53.91×10^3	63.18×10^3	64.32×10^3	3.30	3.86	3.93
SN	89.10×10^3	92.46×10^3	89.34×10^3	4.03	4.14	4.04
SZ	73.0×10^3	74.68×10^3	78.44×10^3	3.44	3.52	3.70
SNZ	94.85×10^3	89.47×10^3	89.11×10^3	4.46	4.20	4.19
SNC	52.76×10^3	44.89×10^3	44.76×10^3	1.86	1.58	1.58
SCZ	71.5×10^3	62.18×10^3	79.2×10^3	3.52	3.84	3.64

The activation energy for the reaction resulting in the synthesis of barium hexaferrite is observed to be 178.15 KJ/mole (Table 5.3). The value of Avrami exponent was observed to be in the range of 2.50-3.68 (Table 5.4). The mechanism for reactions resulting in the synthesis of barium hexaferrite can thus be termed as, instantaneous nucleation and three-dimensional growth (Criado, 1987; Doyle, 1962). The activation energy for the reaction resulting in the synthesis of strontium hexaferrite is calculated to be 168.33 KJ/mole. This value is observed to be lesser than the barium hexaferrite nanoparticles. This might be due to the lesser ionic radii of strontium (132 pm) than barium (149 pm) which in turn result in more diffusivity and reactivity of strontium at that temperature. The value of Avrami exponent for the synthesis of strontium hexaferrite was calculated to be in the range of 3.53 to 3.58 (Table 5.4). The mechanism for this reactions can also be termed as, instantaneous nucleation and three-dimensional growth (Criado, 1987; Doyle, 1962). The activation energy for the reaction resulting in the synthesis of magnetic composite of strontium hexaferrite and spinel ferrite ($CoFe_2O_4$, $NiFe_2O_4$ and $ZnFe_2O_4$) in binary as well as in ternary magnetic composite system is observed to be higher than observed for single phase strontium hexaferrite nanoparticles (Table 5.3). This might be due to the fact that, the growth of multiple phases could be restrained by each other, which leads to higher value of activation energy (Tyagi, 2009; 2010; 2011; 2011). The calculated Avrami ·index parameter for sample SC, SZ and SCZ was observed to be in the range of 3.30-3.93, 3.40-3.70 and 3.52-3.64 respectively. The mechanism for these reactions is termed as, instantaneous rate of nucleation and three-dimensional growth (Criado, 1987; Doyle, 1962). On the other hand the calculated values of Avrami exponent for the sample SN and SNZ were observed to be in the range of 4.03-4.14 and 4.46-4.19 respectively (Table 5.4). For theses reaction some angular growth might be taking place in addition of three dimensional growths. The activation energy (E) for the reaction resulting in the synthesis of sample SNC is observed to be highest (235.221 kJ/mole) than all the other reactions. The calculated values of Avrami index parameter is found to be lesser and lie in the range of 1.582 to 1.864 (Table 5.4). Based on Avrami exponent values (n), the mechanism for these reactions can thus be termed as, instantaneous rate of nucleation with two-dimensional growth (Criado, 1987; Doyle 1962).

SUMMARY

Reaction kinetics studies of magnetic RAM composition of single phase (sample B1 and S1) binary phase (sample SC, SN and SZ) and ternary phase (sample SNZ, SNC and SCZ) have been carried out through non-isothermal differential scanning calorimetry method. DSC/DTG/TG is conducted at three heating rates (10, 30 and 50 K/min). The formation of different phases like single phase hexaferrite and composite of hexaferrite and spinel ferrite during heat treatment are confirmed by XRD analysis of the powder heat treated at same temperature and under same atmosphere as of DSC analysis. The difference in thermodynamic data like onset and completion temperature of reaction, enthalpy of reaction of binary and ternary phases from single phase is due to formation of spinel ferrite ($NiFe_2O_4$, $CoFe_2O_4$ and $ZnFe_2O_4$) along with strontium hexaferrite. In all the cases, endothermic peak at about $800^\circ C$ results in the formation of one impurity phase (αFe_2O_3) along with desirable magnetic phases like strontium hexaferrite and composite of strontium hexaferrite and spinel ferrite. In all the cases, the endothermic peak at about $1200^\circ C$ results in the synthesis of desirable magnetic phases only. Therefore, the reaction kinetic of the endothermic reaction occurring at about $1200^\circ C$ is carried out in all the cases. The activation energy for the strontium hexaferrite nanoparticle synthesis is observed to be lesser than the barium hexaferrite nanoparticle synthesis. This may be due to the lesser ionic radii of strontium (132 pm) than barium (149 pm) which in turn result in more diffusivity and reactivity of strontium at that temperature. The formation of zinc spinel ferrite along with strontium hexaferrite does not affect much the activation energy of reaction. The addition of cobalt, nickel and composite of nickel and cobalt ferrite along with strontium hexaferrite results in large increment in activation energy of the reaction. This might be due to the growth of multiple kinds of phases ($SrFe_{12}O_{19}$, $NiFe_2O_4$ and $CoFe_2O_4$) which might have been restrained by each other and leads to higher value of activation energy. The value of Avrami parameter (n) for endothermic reaction is found to be in the range of 1.58 to 4.46 for various compositions. Reaction mechanisms are found to be different for different compositions. All the composition indicates that 'as synthesis' nano particles obtained after co-precipitation prefer to grow along multi dimensional growth of reaction product. Thus DSC/DTG/TG studies are not only useful in obtaining the kinetics parameters for the reaction but, it also provides parameters for reaction by showing onset temperature, completion temperature and enthalpy of reaction.

CHARATERIZATION OF MAGNETIC RAM POWDER

6.1 INTRODUCTION

Recently, there has been a great increase in the number of electronics devices that utilize GHz range microwave radiation (Soon, 2001; Thakur, 2007), largely due to high rate of data transfer. In particular, the use of mobile phones or wireless network system is rapidly increasing. The developments in microwave absorber technology have resulted in magnetic materials that can effectively reduce the reflection of electromagnetic signals and have good physical performance (Cheng, 2000; Das, 2000). There are variety of microwave absorber materials that can be used to suppress electromagnetic interference (EMI) depending on whether they are suitable for low and high frequency application (Natio 1971; Dishovaski, 1994; Grunberger, 1991; Nedkov, 1990, Shin, 1993). As far as microwave absorber thickness and working frequency bandwidth are concerned, magnetic composites have obvious advantages. Resin composite of either spinel ferrite or hexaferrite can be used as microwave absorber, due to the large value of magnetic loss (μ"), which is induced by their natural resonance phenomena in GHz frequency range. It is expected that, with the passage of time, the dominant frequency range will shift to higher range in order to increase the transfer rate. However, the (μ_r") of soft magnetic material become small in accordance with Snoek's limit (Maeda, 2004), and these material alone can not function as a microwave absorber in the frequency range above 10 GHz. The natural resonance frequency (f_r) of uniaxial anisotropic material is related to its anisotropy field (H_A) as shown by equation ((Maeda, 2004).

$$2\pi f_r = \gamma H_A \qquad\qquad 6.1$$

Where γ is the gyromagnetic ratio. So it is possible to use magnetic material with large magnetic anisotropy as a microwave absorption material in higher frequency range. As compared to the usual spinel ferrites, the hexaferrites with large planar magnetic anisotropy are of great interest for use as electromagnetic energy dissipation in GHz range (Ghasemi, 2008). It is reported that heat treated hexaferrite and its resin composite are useful as a microwave absorber (Ghasemi, 2008; Sharma. 2008; Tyagi, 2009; 2009; 2010; 2011; 2011;

2011). Hexaferrites are classified into four classes, depending on chemical composition and crystalline structure. These include hexaferrites of M, W, Y and Z type, which correspond to (SrO + MeO): Fe_2O_3 ratios of 1:6, 3:8, 4:6 and 5:12 respectively (Vishwanathan, 1990). Among various classes of magnetic materials, hexagonal hard ferrites such as strontium and barium based M type hexaferrites ferrite have attracted much attention because of their potential application in permanent magnets, microwave devices and magnetic recording media (Shirk, 1969). As far as bulk material is concerned, strontium based hexaferrite is found to have better hard magnetic properties (Shirk, 1969) like large value of magnetic anisotropy ($3.57x10^6$ erg/cc) and lower density (5.11gm/cc) than barium based hexaferrite ($3.25x10^6$ erg/cc, 5.28gm/cc). The practical application of strontium ferrite as permanent magnet is well known and is also used as a dielectric or magnetic filler in the electromagnetic filler attenuation materials (EAM). Recently, demand for various electromagnetic wave absorbers has increased; single material cannot fulfill these demands (large absorption peak and wide working frequency bandwidth). In order to improve electromagnetic absorption properties of magnetic materials, many studies have focused new systems comprising composite of hard and soft magnetic materials (Masala, 2006; Liu, 2006; Tyagi, 2010; 2011; 2011; 2011). It is reported that (Maeda, 2004) exchange interaction between hard and soft magnetic phases improve the magnetic, dielectric and microwave absorption properties. Zinc ferrite ($ZnFe_2O_4$), nickel ferrite ($NiFe_2O_4$) and cobalt ferrite ($CoFe_2O_4$) which has a cubic spinel structure is a kind of soft magnetic material and has been widely studied as microwave absorbing material (Peng, 2005; Yusoff, 2004; Qiu, 2004; Sunny, 2010; Giannakopoulou, 2002).

In view of this, the present work describes the development of hexaferrite and magnetic composite comprising of hexaferrites and spinel ferrite synthesized by different chemical routes like modified flux method and low combustion synthesis method. The specification of composition used in the present study and their characterization has been described in the subsequent sections.

6.2 SPECIFICATIONS

Eight different compositions of hexaferrite and composite of hexaferrite and spinel ferrite (described in chapter 4) were prepared for morphological, phase analysis, magnetic, dielectric and microwave absorption studies. All the compositions have been given a sample code and are listed in Table 4.1.

6.3 CHARATERIZATION

All the presented composition has been synthesized by co-precipitation and low combustion synthesis method. The details of synthesis methods have been described in the chapter 4. In this chapter the morphological, phase analysis, magnetic, dielectric and reflection loss study of the presented compositions have been discussed in the subsequent sections.

6.3.1 Morphological Study

The FESEM micrograph of 'as synthesized' and heat treated hexaferrite and composite of hexaferrite and spinel ferrite upto the various heat treatment temperatures are shown in Figures 6.1-6.11. In the 'as synthesized' condition, in all the compositions, particles seem to have needle and spherical morphology when the heat treatment temperature is increased to 1200°C, the particles grow and constitute multiple morphologies. With increasing heat treatment temperature, the systematic growth of particles with sharp plane of crystals is observed. It is observed that few of needle or spherical shaped particles in the 'as synthesized' condition were transformed to hexagonal pyramidal structure and most of the crystals are found to have hexagonal plate like structures with increase in heat treatment temperatures. This process of crystal growth and morphological evolution can be described in term of Ostwald ripening (Ostwald, 1900) which involves the formation of many nano crystals in the system initially, but slowly disappear except for the few that grow larger, at the expense of small nano crystals. The crystals of small size act as a "nutrients" for bigger crystals. This is a self working process that occurs because larger particles are energetically more favored to grow further than smaller particles. According to literature (Sharma, 2007; 2008; 2008 Tyagi, 2009; 2010; 2011; 2011; 2011), hexaferrite nano particles with multiple morphology like hexagonal pyramidal and hexagonal plate shapes are observed to be potential materials for the electromagnetic wave absorption applications.

Fig. 6.1: FESEM micrographs showing the effect of heat treatment temperature on the morphology of sample B1, a) 'as synthesized' and heat treated at b) 800°C, c) 1000°C and d) 1200°C in nitrogen atmosphere.

Fig. 6.2: FESEM micrographs showing the effect of heat treatment temperature on the morphology of sample S1, a) 'as synthesized' and heat treated at b) 800°C and c) 1200°C in nitrogen atmosphere.

In case of both barium (Figure 6.1) and strontium (Figure 6.2) hexaferrite, the hexagonal plate and hexagonal pyramidal shape of particles are observed. The 'as synthesized' particles, in both case seems to have needle shape morphology. The particles observed in case of strontium hexaferrite are found to have smaller average particle size (80-90nm) than barium hexaferrite (400-500nm) for the powder heat treated at 1200°C. These particles shows the three dimensional growth which is also confirmed by Avrami index parameter (n) values (Table 5.4) obtained for the synthesis of barium and strontium hexaferrite nanoparticles and has been discussed in chapter 5. Being small in particle size with multiple morphologies, strontium hexaferrite form the basis to be used for further study in pure and magnetic composite form.

The TEM micrographs of 'as synthesized' and heat treated composite powder of sample SC at 900 and 1200°C are shown in Figure 6.3. In the 'as synthesized' condition, the agglomerated particles seem to have spherical shape with size range of 10-20nm. On raising the heat treatment temperature, the particles grow (~ 70 nm) and constitute multiple morphologies (Figure 6.3 c).

Fig. 6.3: TEM micrographs showing the effect of heat treatment temperature on the morphology of sample SC, a) 'as synthesized' and heat treated at b) 900 and c) 1200°C in nitrogen atmosphere.

Fig. 6.4: FESEM micrographs showing the effect of heat treatment temperature on the morphology of sample SN, a) 'as synthesized' and heat treated at b) 900 and c) 1200°C in nitrogen atmosphere.

The FESEM micrographs of sample SN composite in 'as synthesized' and heat treated condition at various heat treatment temperatures are shown in Figure 6.4. In the 'as-synthesized' condition, the particles seem to have similar spherical and needle shaped morphology like strontium hexaferrite with particle size in the range of 20-25nm. With increasing heat treatment temperature, the particles grow and constitute multiple morphologies. At 1200°C, $SrFe_{12}O_{19}/NiFe_2O_4$ nanoparticles (with size in the range of 80-90nm) having hexagonal plate shape are observed (Figure 6.4 c). This is also evidenced by TEM micrograph of the powder in 'as synthesized' and heat treated condition (Figure 6.5). The similar trend of morphological transformation as a function of heat treatment temperature is also observed for sample SZ magnetic composite and is shown in Figure 6.6. The confirmation of particle size and shape of the composite has also been done by TEM study of sample SZ and is shown in Figure 6.7.

Fig. 6.5: TEM micrographs showing the effect of heat treatment temperature on the morphology of sample SN, a) 'as synthesized' and heat treated at 1200°C in nitrogen atmosphere.
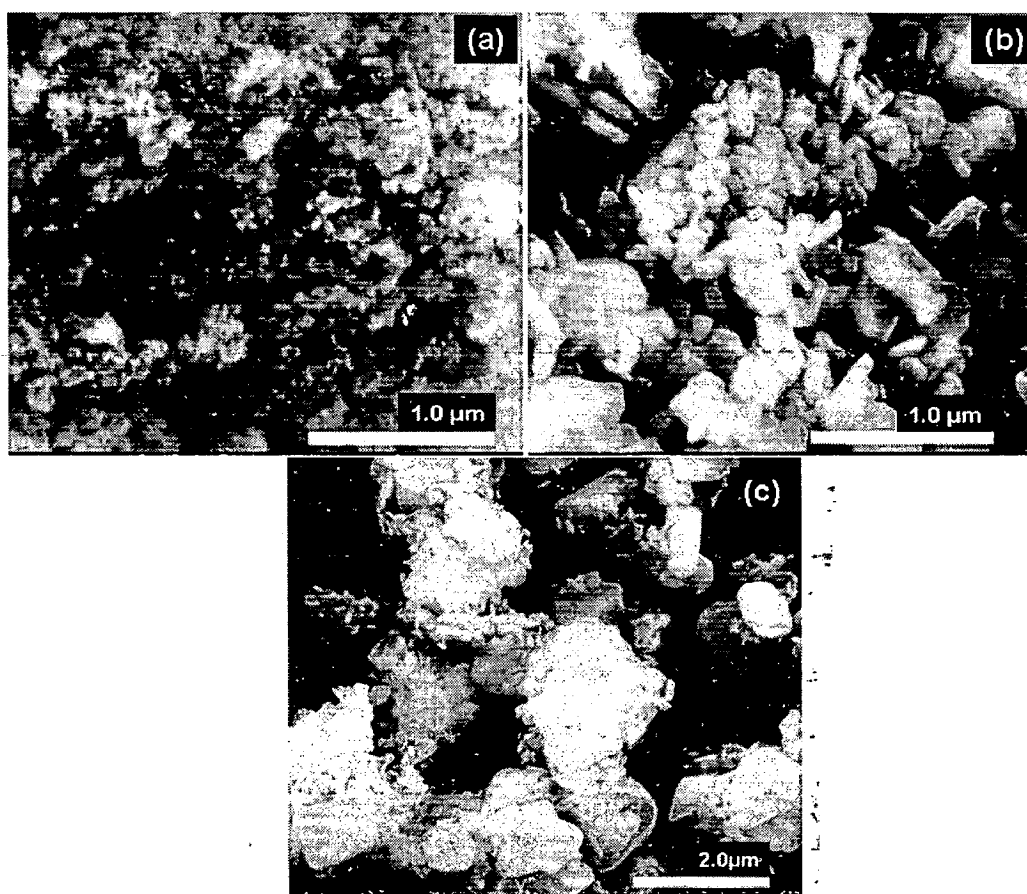
Fig. 6.6: FESEM micrographs showing the effect of heat treatment temperature on the morphology of sample SZ, a) 'as synthesized' and heat treated at b) 900°C, and c) 1200°C in nitrogen atmosphere.
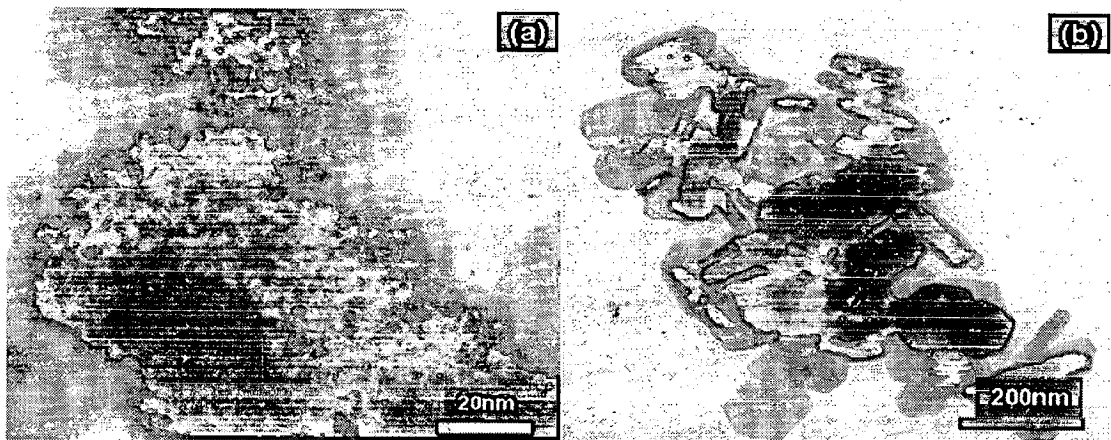
Fig. 6.7: TEM micrographs showing the effect of heat treatment temperature on the morphology of sample SZ, a) 'as synthesized' and heat treated at 1200°C in nitrogen atmosphere.

Agglomeration of 'as synthesized' particles can be seen in the TEM micrograph (Figure 6.7). The heat treated powder at 1200°C for 4h in nitrogen atmosphere under TEM study shows an increase in particle size (~90nm). The particle size in the 'as synthesized' condition is so small (10-20nm) that each particle itself acts as single domain resulting in superparamagnetic nature of material. This is also confirmed by the hysteresis loop obtained for 'as synthesized' powder.

Similar kind of morphology is obtained for the ternary magnetic composite of SNZ. The particle in the 'as synthesized' condition show the needle shape morphology (Figure 6.8) with particle size in the range of 5-10nm. These needle shaped nanoparticles get further transformed to hexagonal pyramidal shape morphology (Figure 6.8). This is also confirmed by the TEM study (Figure 6.9) of the same powder.
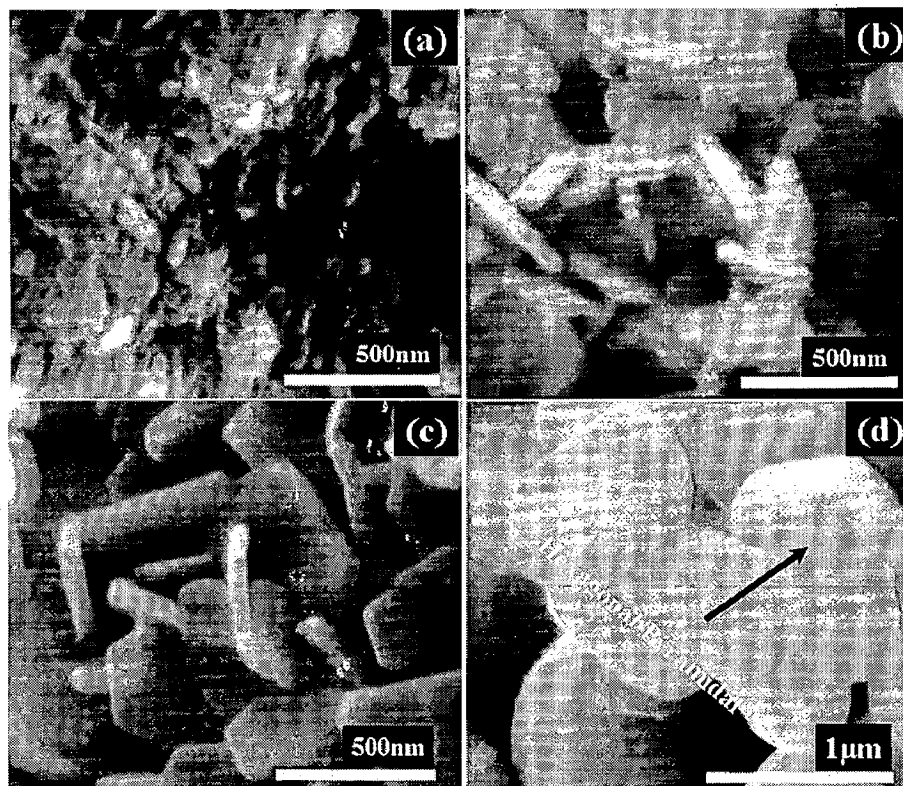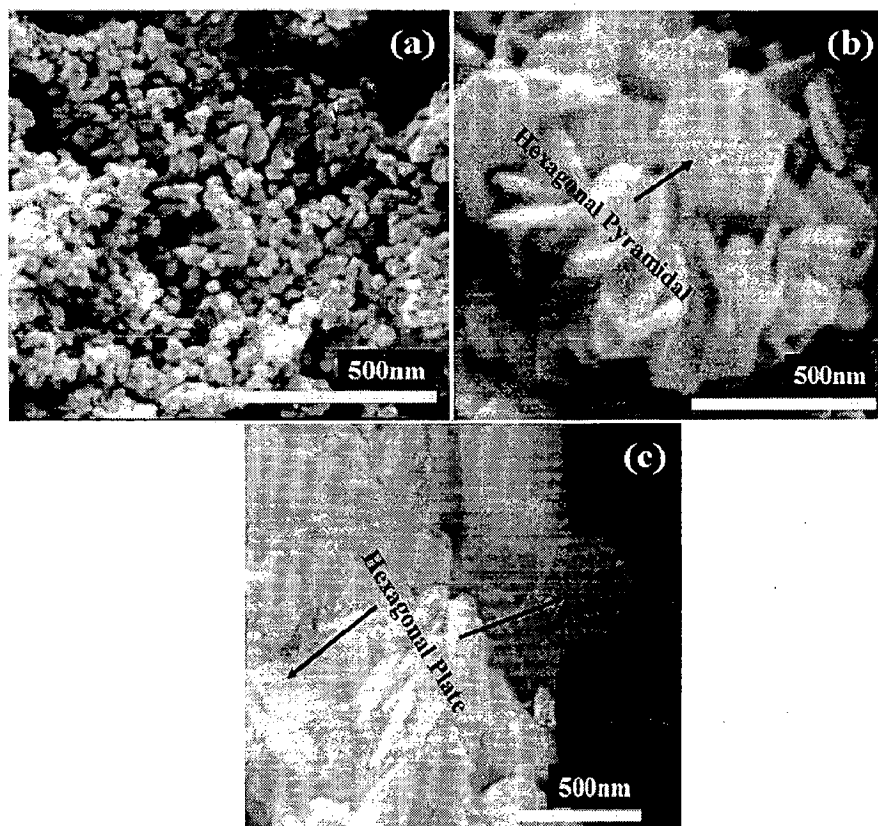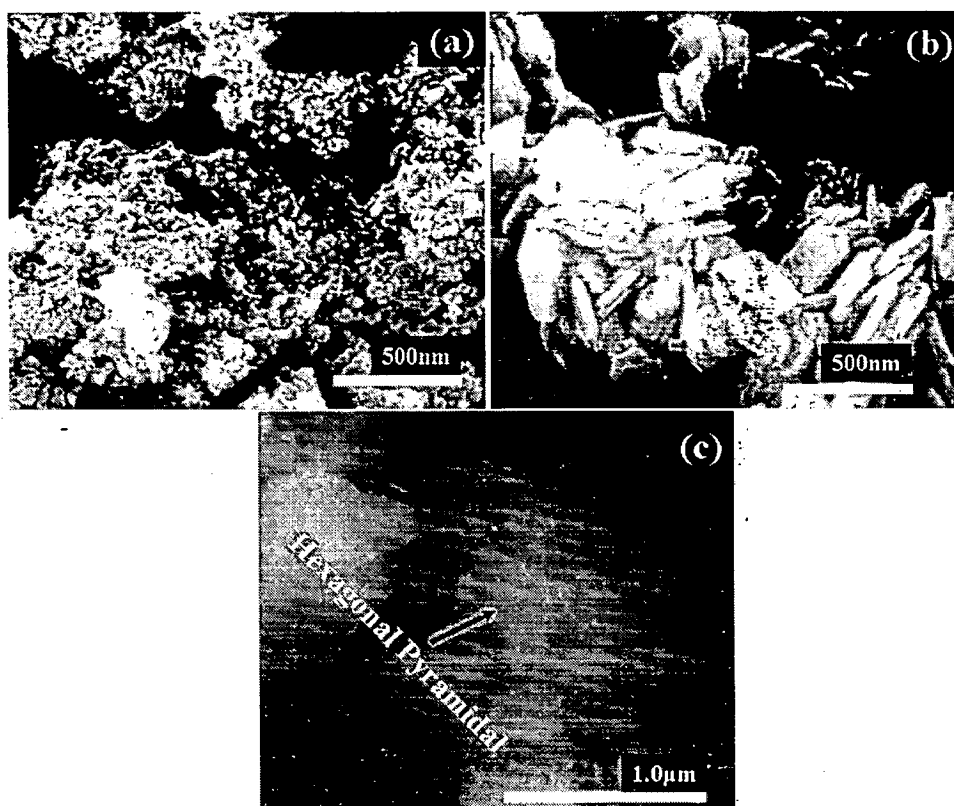
Fig. 6.8: FESEM micrographs showing the effect of heat treatment temperature on the morphology of sample SNZ, a) 'as synthesized' and heat treated at b) 900°C, and c) 1200°C in nitrogen atmosphere.
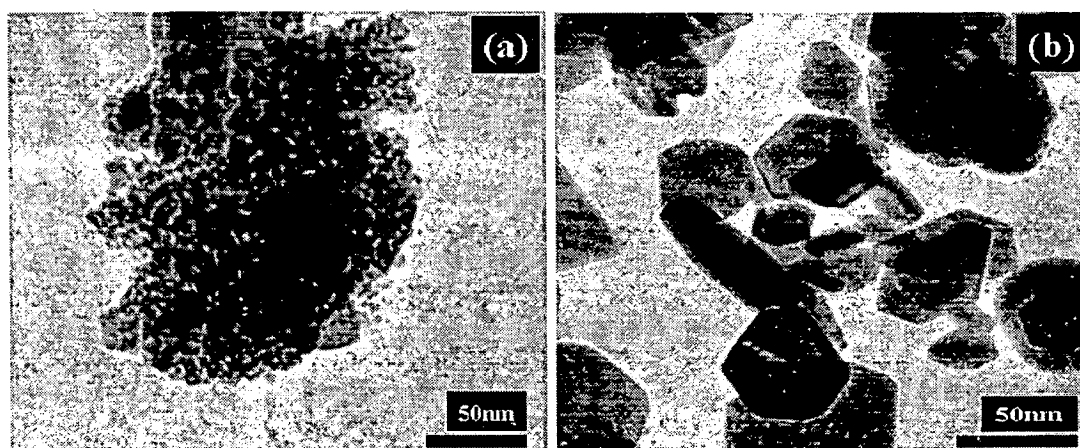
Fig. 6.9: TEM micrographs showing the effect of heat treatment temperature on the morphology of sample SNZ, a) 'as synthesized' and heat treated at 1200°C in nitrogen atmosphere.

The FESEM micrograph for another ternary magnetic composite, SCZ heat treated at 800, 1000 and 1200°C are also shown in Figure 6.10.
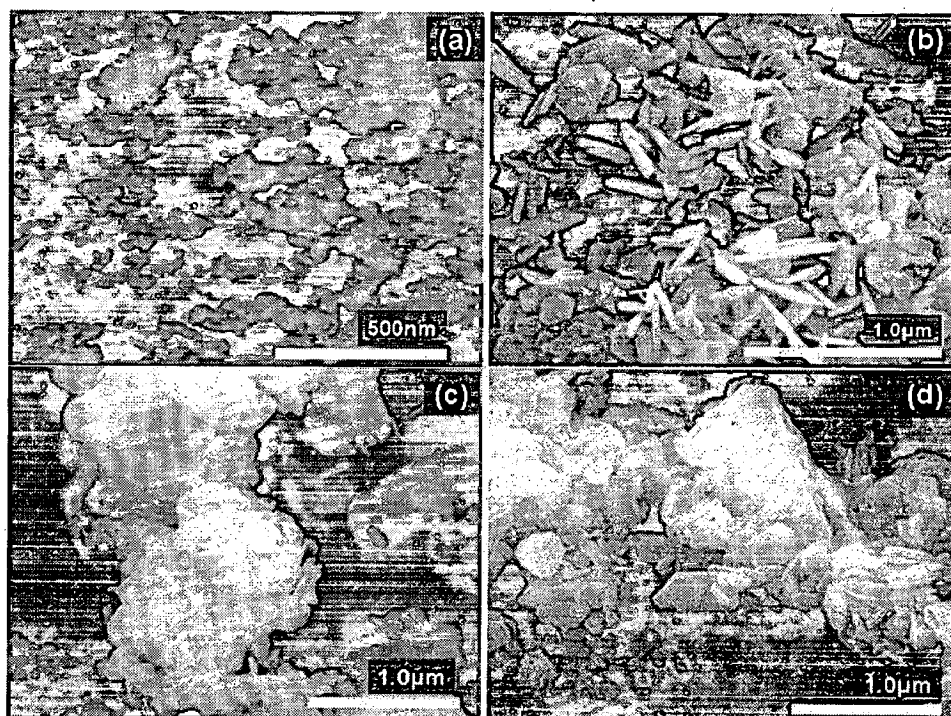
Fig. 6.10: FESEM micrographs showing the effect of heat treatment temperature on the morphology of sample SCZ, a) 'as synthesized' and heat treated at b) 800°C, c) 1000°C and d) 1200°C in nitrogen atmosphere.

For comparative study of two different synthesis methods, the FESEM micrograph of the ternary magnetic composite, SNC synthesized by low combustion synthesis method are shown in Figure 6.11. In this method, the morphology of the particles obtained is different than those obtained for the powder synthesized by co- precipitation method. The particle size is relatively higher which might be due to the self ignition of particle during the synthesis process. This self ignition of nanoparticles during synthesis, impart the heat to the composite to get crystalline which is not observed in the 'as synthesized' particle obtained by co-precipitation method. This is confirmed by the XRD study of the 'as synthesized' particle obtained by co-precipitation (Figure 5.14) and LCS methods (Figure 6.12). In the 'as synthesized' condition the particle are found to have spherical shaped morphology with particle size in the range of 40-50nm. For the powder heat treated at 1000°C, hexagonal plate shape morphology with higher agglomeration is observed. The average particle size increases to ~120nm. Moreover, higher agglomeration in the particle is observed in the powder obtained by LCS method than those observed for powder obtained by co-precipitation method.
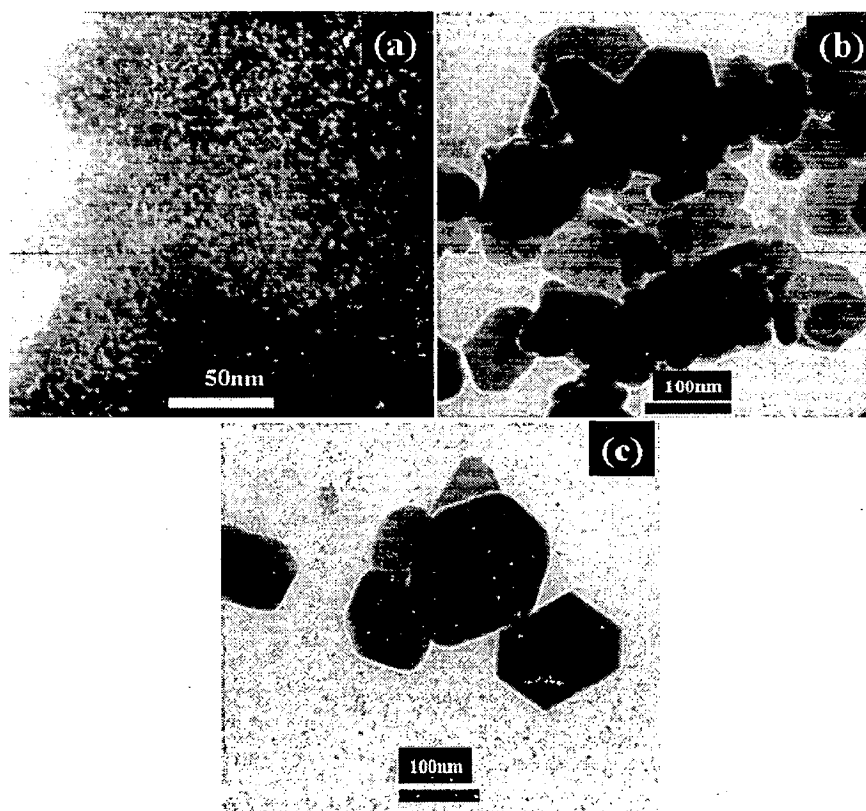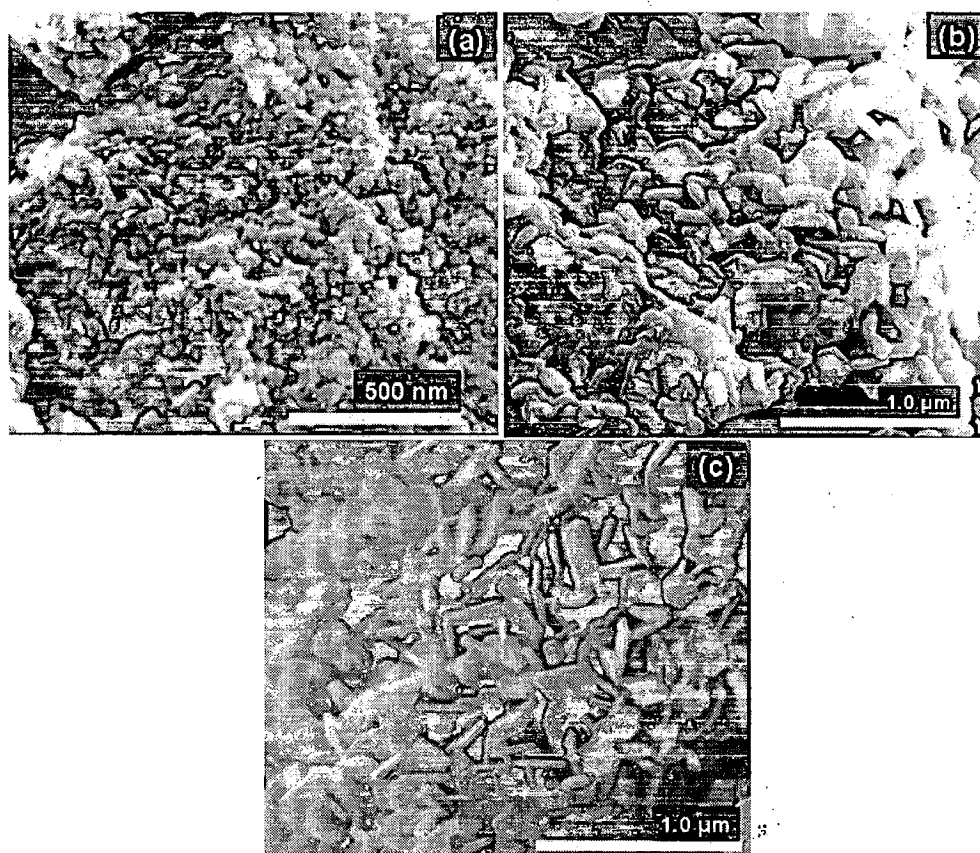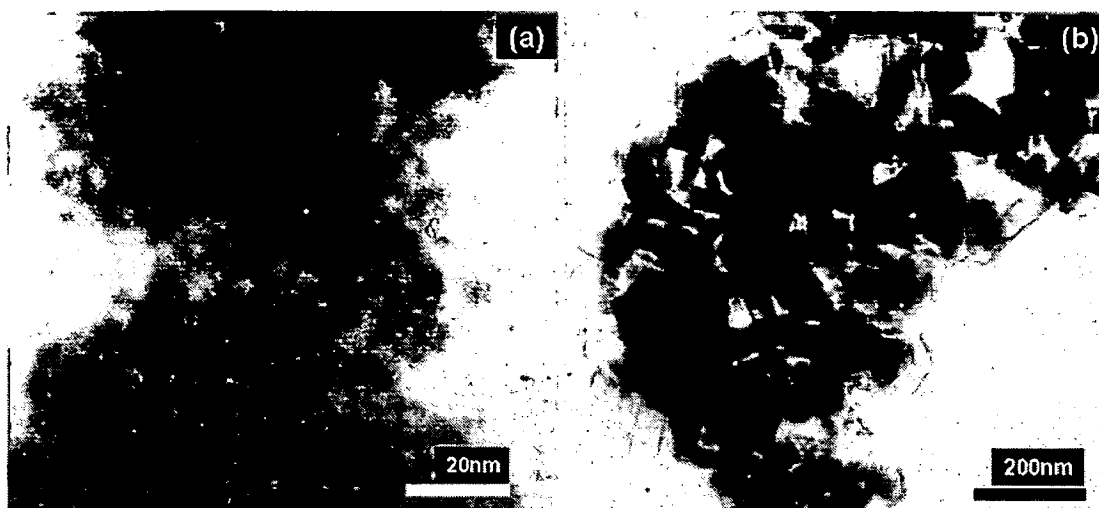
117
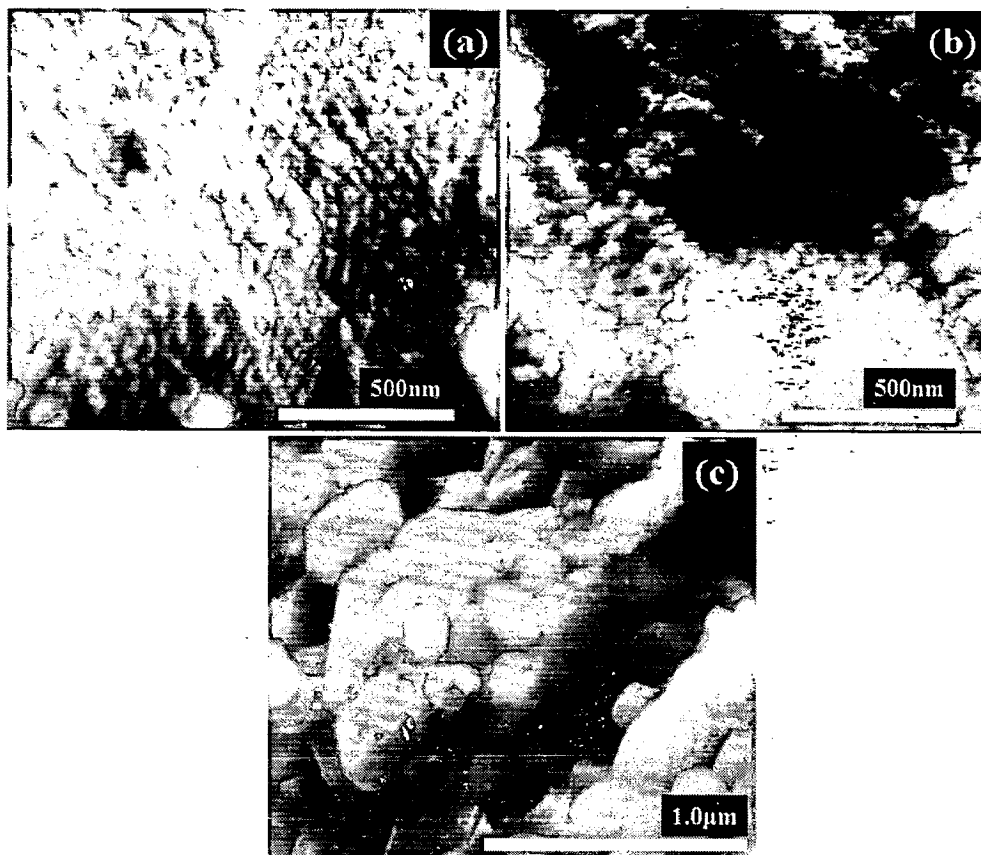
Fig. 6.11: FESEM micrographs showing the effect of heat treatment temperature on the morphology of sample SNC, a) 'as synthesized' and heat treated at b) 800°C, and c) 1000°C in nitrogen atmosphere.

6.3.2 Phase Analysis Study

In this section, out of all eight compositions synthesized by modified flux method, XRD pattern for sample SNC has been explained for the comparative study. The indexed XRD patterns of the sample SNC nanoparticles in 'as synthesized' and after heat treatment at 900 and 1200°C for 4h in the nitrogen atmosphere are shown in Figure 5.14. From the results, it can be inferred that the ferrite powder in 'as synthesized' condition is showing only the peak corresponding to impurity of NaCl (JCPDS Card No.5-637). When annealed at 900°C, $SrFe_{12}O_{19}$ (JCPDS Card No. 24-1207), $NiFe_2O_4$, (JCPDS Card No. 3-875) and $CoFe_2O_4$ (JCPDS Card No. 01-1121) are obtained along with other phase correspond to impurity of αFe_2O_3 (JCPDS Card No.05-637). As expected, the degree of crystallinity and amount of $SrFe_{12}O_{19}$, $NiFe_2O_4$, $CoFe_2O_4$ nanoparticles is further increased by increasing the heat

treatment temperature from 900 to 1200° C (Figure 5.14). On the other hand, for the powder obtained after LCS method, indexed XRD patterns of the sample SNC in 'as synthesized' and after heat treatment at 800 and 1000°C for 4h in the nitrogen atmosphere are shown in Figure 6.12. From the results, it can be inferred that the ferrite powder in 'as synthesized' condition is showing only the peak corresponding to $NiFe_2O_4$ (JCPDS Card No. 3-875) and $CoFe_2O_4$ (JCPDS Card No. 01-1121). When annealed at 800°C, the peak corresponding to $SrFe_{12}O_{19}$, (JCPDS Card No. 24-1207) phase is also observed. The degree of crystallinity and amount of $SrFe_{12}O_{19}$, $NiFe_2O_4$, $CoFe_2O_4$ nanoparticles are further increased by increasing the heat treatment temperature from 800 to 1000°C. In low combustion synthesis method, the desired magnetic composite is observed to obtain at relatively low temperature (1000°C) than co-precipitation method (1200°C).
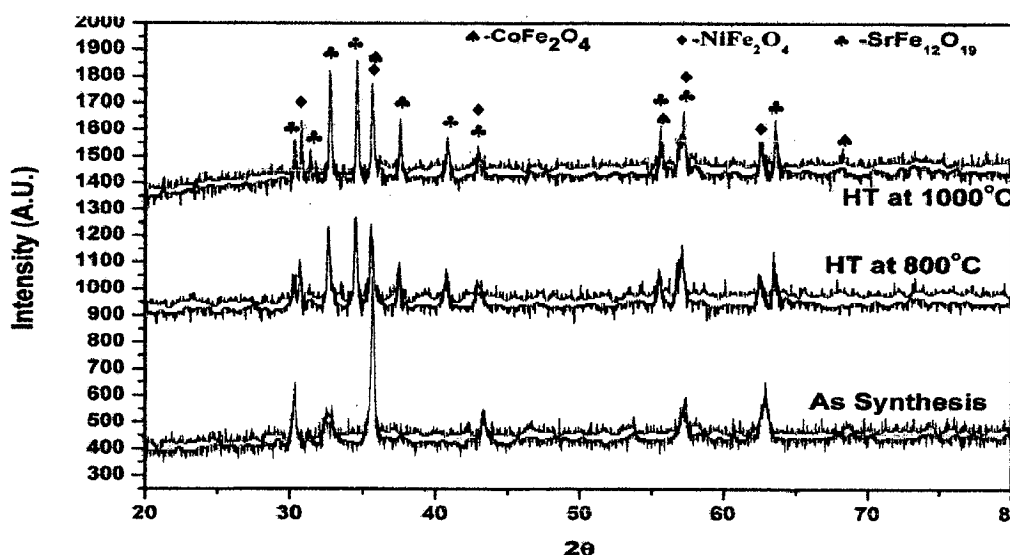
Fig. 6.12:   XRD patterns of sample SNC in 'as synthesized' and heat treated at 800 and 1000°C in nitrogen atmosphere.

6.3.3 Magnetic Study

The vibrating sample magnetometer (VSM) measurements of barium hexaferrite nanoparticles ($BaFe_{12}O_{19}$) show almost negligible coercivity and remanance values (Figure 6.13) in the 'as-synthesized' condition attributing the superparamagnetic behaviour of the material. But when the 'as-synthesized' powders are heat treated (at 800, 1000 and 1200°C),

119

the particles appear to transform from superparamagnetic to ferromagnetic in nature. Saturation magnetization is found to be dependent on HT temperature. It increases from 1.045 to 52.354emu/g with increase in HT temperature (Figure 6.13). The rise in saturation magnetization with the HT temperature can be attributed to the increased formation of barium hexaferrites which is confirmed by X-ray study of powder HT at different temperatures (Figure 5.2) (Hessien, 2008). The coercivity of 3683 Gauss is observed for the powder heat treated at 1000°C and thereafter decreases to 1799 Gauss at 1200°C. This might be due to the presence of αFe_2O_3 up to 1000°C (Figure 5.2); which has a high intrinsic coercive force (Fu, 2005). In addition, the change in morphology and particle size may also affect the magnetic properties (Hessien, 2008). The co-precipitated powder heat treated with NaCl at 1200°C having large hexagonal plate and pyramidal like shape achieved maximum saturation magnetization. While the co-precipitated powder heat treated with NaCl at 1000°C that have small hexagonal plate like structure in addition to αFe_2O_3 achieved a maximum coercivity. Hexaferrite nanoparticles having low coercivity and high saturation magnetization find their applications in magnetic recordings in hard disks, floppy disks, video tapes, etc (Fu, 2005).

Fig. 6.13: The effect of HT temperature on hysteresis loops of sample B1 in 'as synthesized' condition and heat treated at 800, 1000 and 1200°C in nitrogen atmosphere.
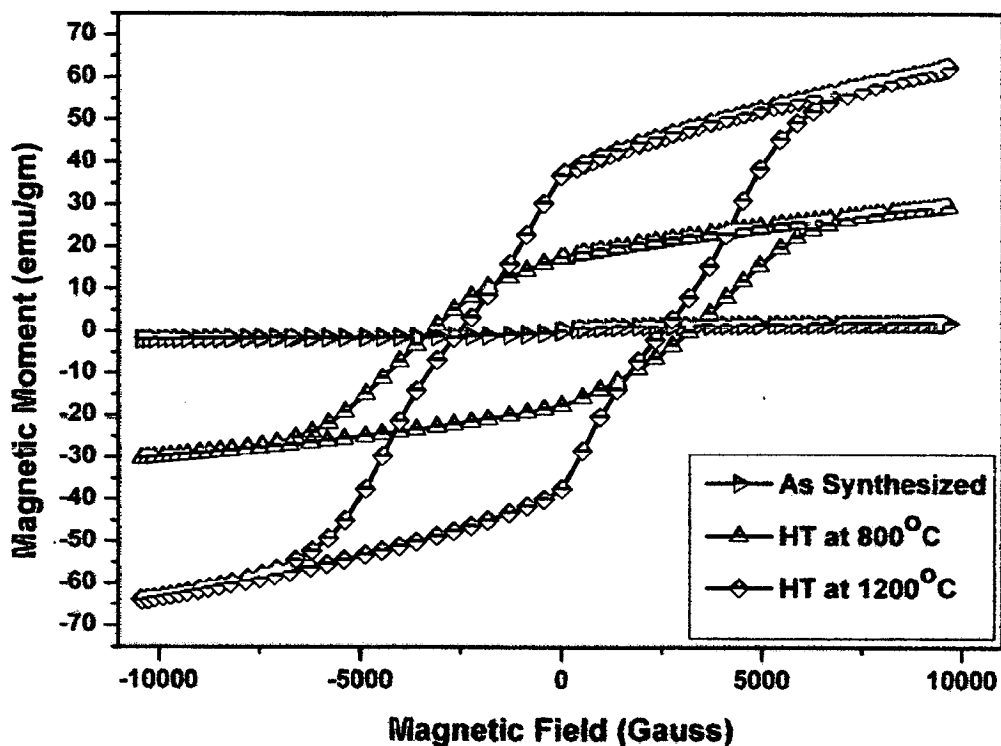
Fig. 6.14: The effect of HT temperature on hysteresis loops of sample S1 in 'as synthesized' condition and heat treated at 800 and 1200°C in nitrogen atmosphere.

In comparison to barium hexaferrite, strontium hexaferrite showed higher saturation magnetization (62.150 emu/gm) and coercivity (2668 Gauss) for the powder heat treated at 1200°C (Figure 6.14). The maximum coercivity of 3176 Gauss is observed for the powder heat treated at 800°C which further decrease to 2668 Gauss for the powder heat treated at 1200°C. This is attributed to the presence of αFe_2O_3 upto the temperature of 800°C which is confirmed by the XRD study of the powder heat treated at 800 and 1200°C (Figure 5.4). According to literature (Shirk, 1969) and on the basis of our findings, the strontium hexaferrite is observed to be more magnetic (higher saturation magnetization and large hysteresis loss) than barium hexaferrite powder. This form the basis of the selection of strontium hexaferrite as base material for the further development of composites containing hard and soft magnetic phases.

121

Fig. 6.15: The effect of HT temperature on hysteresis loops of sample SC in 'as synthesized' condition and heat treated at 900 and 1200°C in nitrogen atmosphere.

The addition of cobalt for the formation of cobalt spinel ferrite ($CoFe_2O_4$) along with ($SrFe_{12}O_{19}$) does not affect the property of the material in the 'as synthesized' condition (Figure 6.15). Like single phase strontium hexaferrite, the composite of strontium and cobalt ferrite is also superparamagnetic in nature in the 'as synthesized' condition. The superparamagnetism transformed to ferromagnetism with increase in heat treatment temperature. Since, the composite is also synthesized by co-precipitation method so trend of property like large coercivity up to the temperature of 900°C (due to the presence of αFe_2O_3) is also observed in the present composition. The presence of cobalt ferrite along with strontium hexaferrite results in higher value of saturation magnetization (84.362 emu/gm) and lower value of coercivity (1274 Gauss) than single phase strontium hexaferrite (62.150 emu/gm, 2668 Gauss). This might be due to the soft magnetic nature of cobalt ferrite (Franco, 2010).

Fig. 6.16: The effect of HT temperature on hysteresis loops of sample SN in 'as synthesized' condition and heat treated at 900 and 1200°C in nitrogen atmosphere.

The formation of nickel ferrite along with strontium hexaferrite does not show much change in magnetic properties (saturation magnetization and coercivity) than single phase strontium hexaferrite. The formation of nickel spinel ferrite along with strontium hexaferrite results in increase in saturation magnetization (65.188 emu/gm) and lowering in coercivity (1375 Gauss) of magnetic composite (Figure 6.16) than observed for single phase strontium hexaferrite (62.150 emu/gm, 2668 Gauss). This also might be due to the formation of soft magnetic nickel ferrite during the heat treatment process (Sunny, 2010).
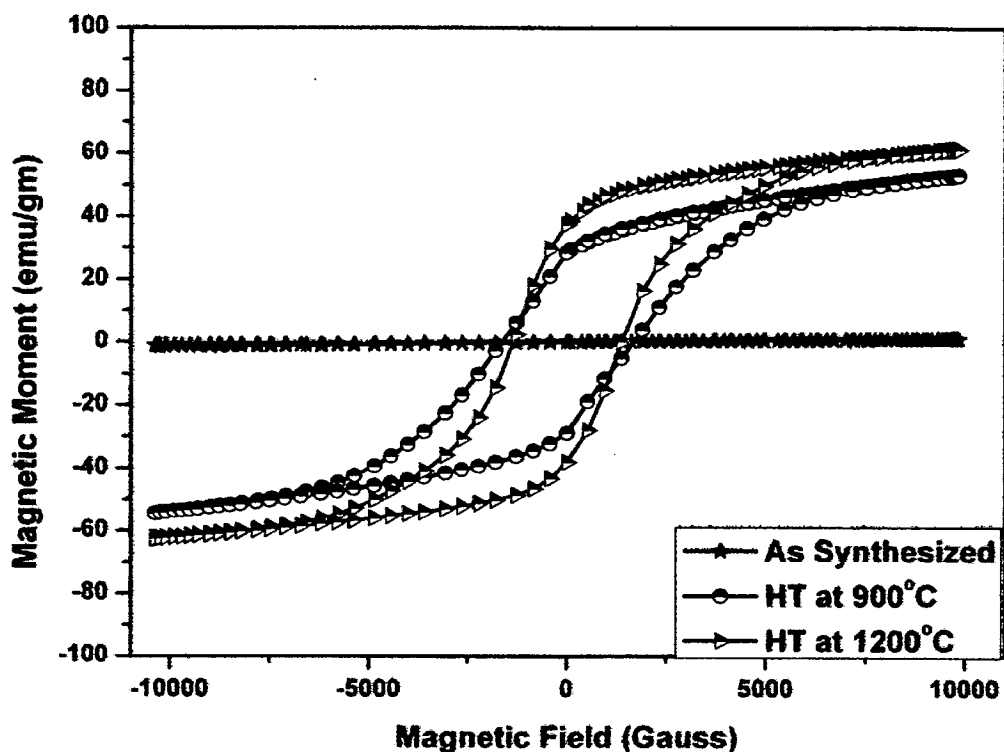
Fig. 6.17: The effect of HT temperature on hysteresis loops of sample SZ in 'as synthesized' condition and heat treated at 900 and 1200°C in nitrogen atmosphere.

The hysteresis loop showing the effect of temperature on the magnetic properties of SZ composite is shown in Figure 6.17. The formation of zinc ferrite $ZnFe_2O_4$ leads to decrease in saturation magnetization (61.227emu/gm) and coercivity (1373 Gauss) than pure strontium hexaferrite nanoparticles. This can also be explained on the basis of soft magnetic behaviour of zinc ferrite than strontium hexaferrite.
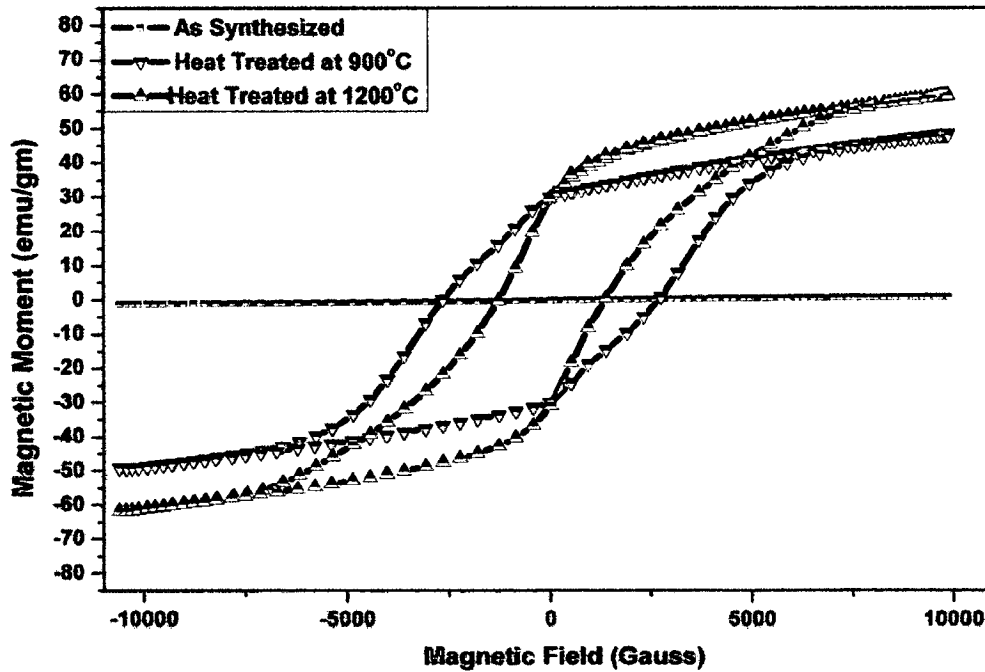
Fig. 6.18: The effect of HT temperature on hysteresis loops of sample SNZ in 'as synthesized' condition and heat treated at 900 and 1200°C in nitrogen atmosphere.

The hysteresis loop showing the effect of heat treatment temperature on the magnetic parameter of ternary magnetic composite of SNZ and SCZ are shown in Figure 6.18 and Figure 6.19 respectively. In both the cases same trend of magnetic properties are observed as in case of single and binary magnetic phases. In case of SNZ magnetic composite the maximum saturation magnetization of 61.227 emu/gm and coercivity of 1265Gauss is observed. While in case of SCZ magnetic composite, the maximum saturation magnetization of 59.011 emu/gm and coercivity of 1289 Gauss is observed. These value are found to be lower than single (62.150 emu/gm, 2668 Gauss) and binary magnetic composite.
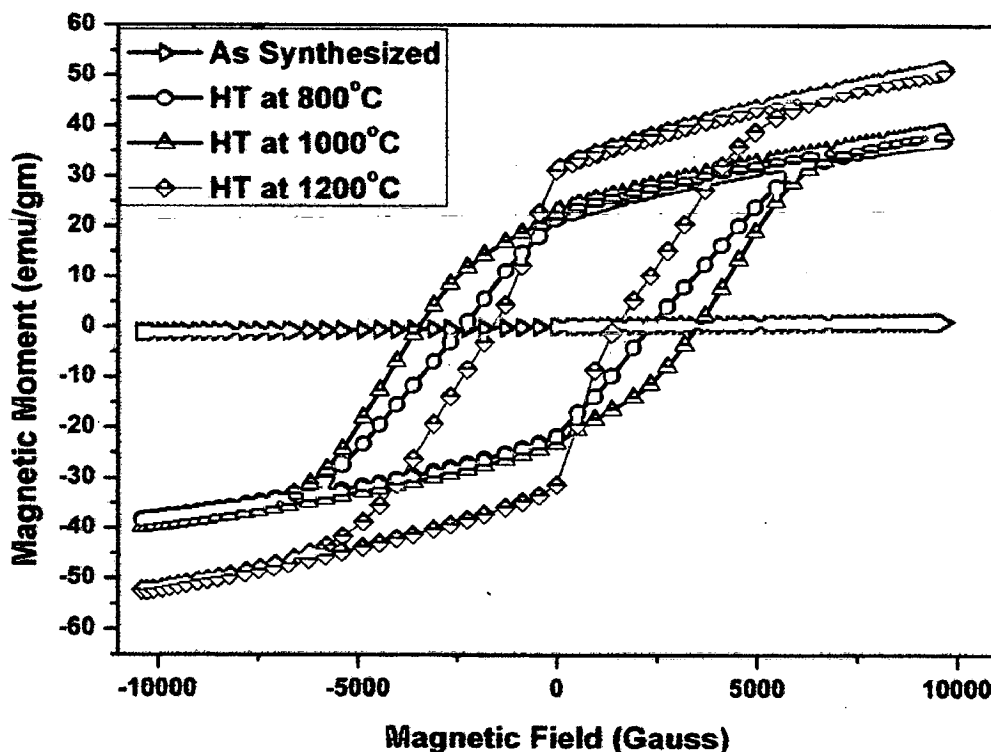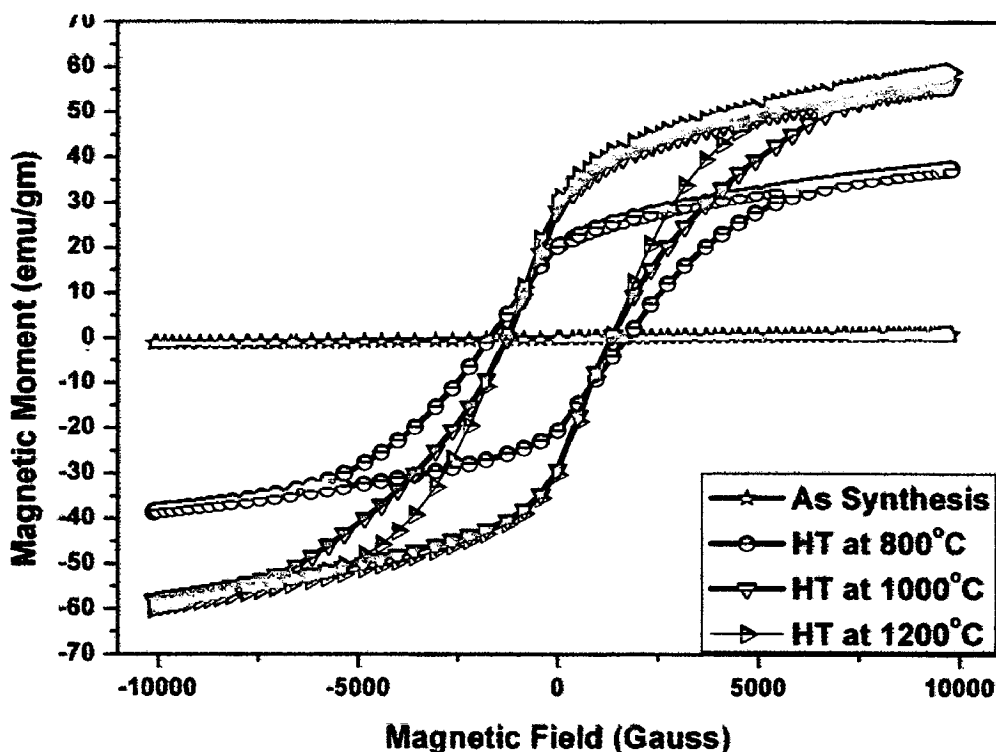
Fig. 6.19: The effect of HT temperature on hysteresis loops of sample SCZ in 'as synthesized' condition and heat treated at 800, 1000 and 1200°C in nitrogen atmosphere.

For comparison, the magnetic properties of ternary magnetic composite of SNC synthesized by low combustion method are also shown in Figure 6.20. The magnetic measurements of SNC nanoparticles have low coercivity (232.583 Gauss) and high saturation magnetization (24.33emu/gm) in the 'as synthesized' condition (Figure 6.20). This indicates the formation of soft magnetic phases ($NiFe_2O_4$/$CoFe_2O_4$) in the 'as synthesized' condition which is also confirmed by XRD pattern (Figure 6.12) of 'as- synthesized' powder. But when the 'as synthesized' powders are heat treated at 800 and 1000°C in nitrogen atmosphere for 4h, the particles appear to transform from soft magnetic to composite of soft and hard magnetic ($SrFe_{12}O_{19}$, $NiFe_2O_4$ and $CoFe_2O_4$) phases (Figure 6.12)
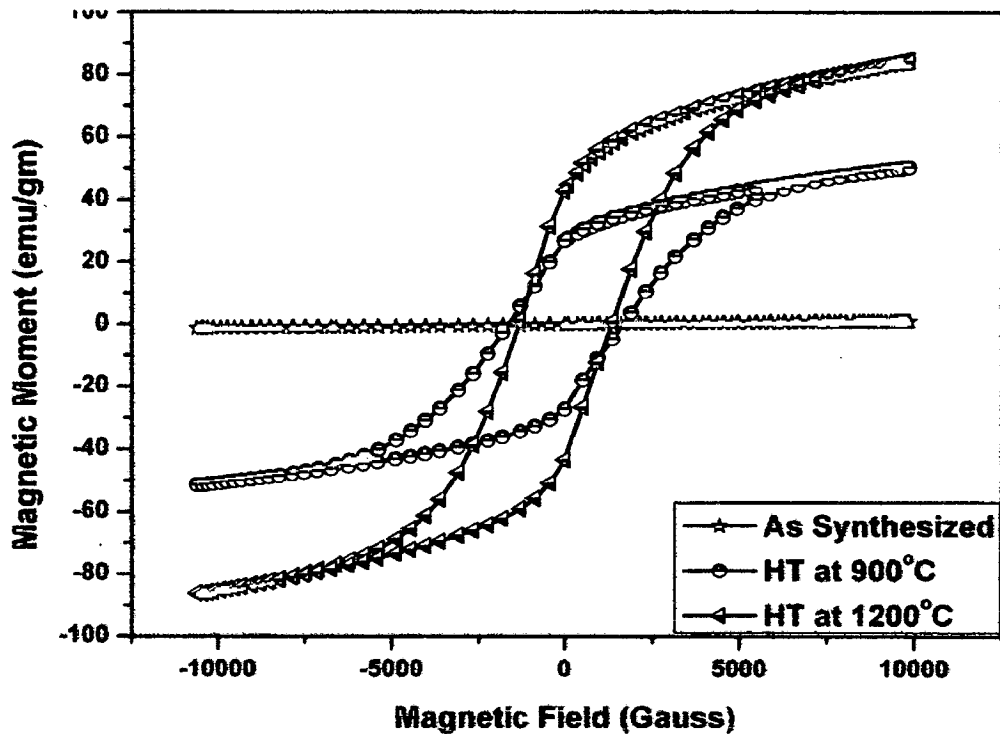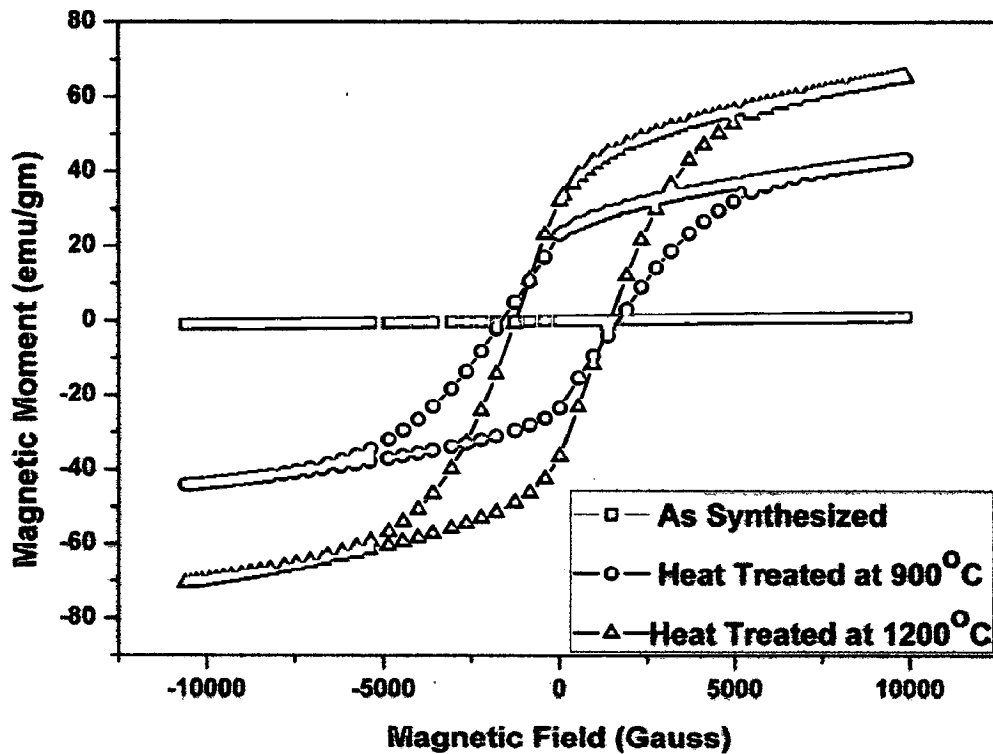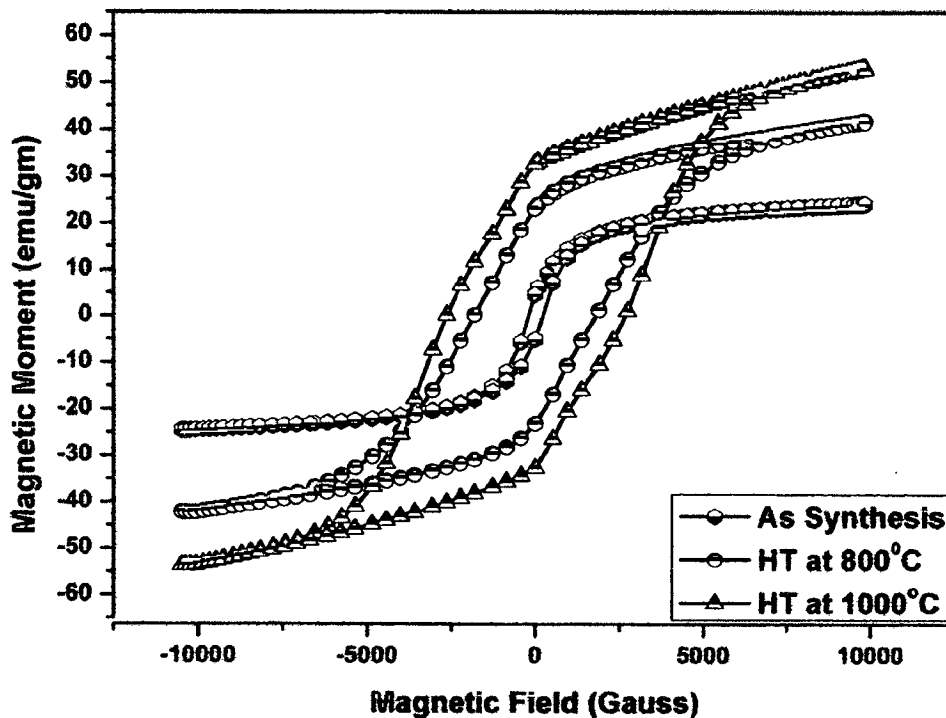
Fig. 6.20: The effect of HT temperature on hysteresis loops of sample SNC in 'as synthesized' condition and heat treated at 800 and 1000°C in nitrogen atmosphere.

Saturation magnetization is found to be dependent on HT temperature. It increases from 24.33 to 53.22emu/gm with increase in HT temperature (Figure 6.20). The rise in saturation magnetization with the HT temperature is attributed to the increased formation of SNC ferrites which is confirmed by X-ray pattern of powder HT at 1000°C (Figure 6.12). The coercivity of 1844Gauss is observed for the powder heat treated at 800°C and thereafter increases to 2709 Gauss at 1000°C. This might be due to the increased formation of strontium hexaferrite with increase in HT temperature which has a high intrinsic coercive force than soft magnetic phases like $NiFe_2O_4$ (Ghasemi, 2008; Tyagi, 2009; 2010). Furthermore, the change in morphology and particle size affects the magnetic properties (Hur, 2004). The coercivity is due to the pinning of the magnetic domains at the grain boundaries (Hur, 2004). As the size of grain increases, the surface to volume ratio increases. Consequently the smaller grains will have more grain boundaries to pin the magnetic domains. So, the materials with smaller grains would have higher coercivity. Thus the synthesis of spinel ($NiFe_2O_4$ and $CoFe_2O_4$) phases along with hexagonal $SrFe_{12}O_{19}$ particles in nano size range results in higher saturation magnetization than those reported for micron size single phase strontium hexaferrite, nickel ferrite, zinc ferrite and cobalt ferrite (Peng, 2005; Sunny, 2010; Ataie, 2001). This study also leads to the conclusion that strontium hexaferrite nanoparticle are observed to be more magnetic than barium hexaferrite nanoparticles. The formation of spinel phase along with hard magnetic phase (strontium hexaferrite) leads to the formation of novel magnetic composite with lesser coercivity and large saturation magnetization than pure strontium hexaferrite nanoparticles (Figures 6.21-6.22).
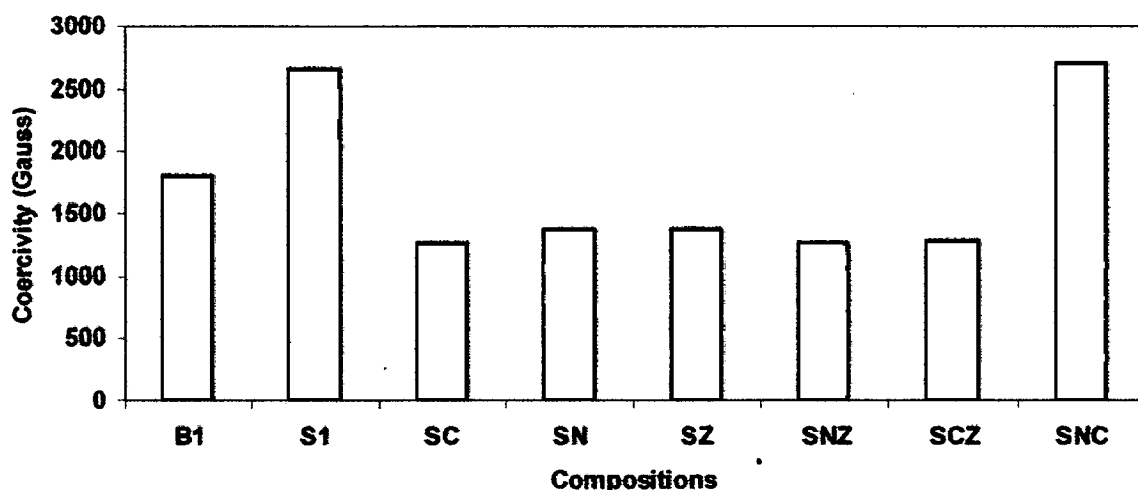
Fig. 6.21: Variation of coercivity with composition of magnetic RAM developed.
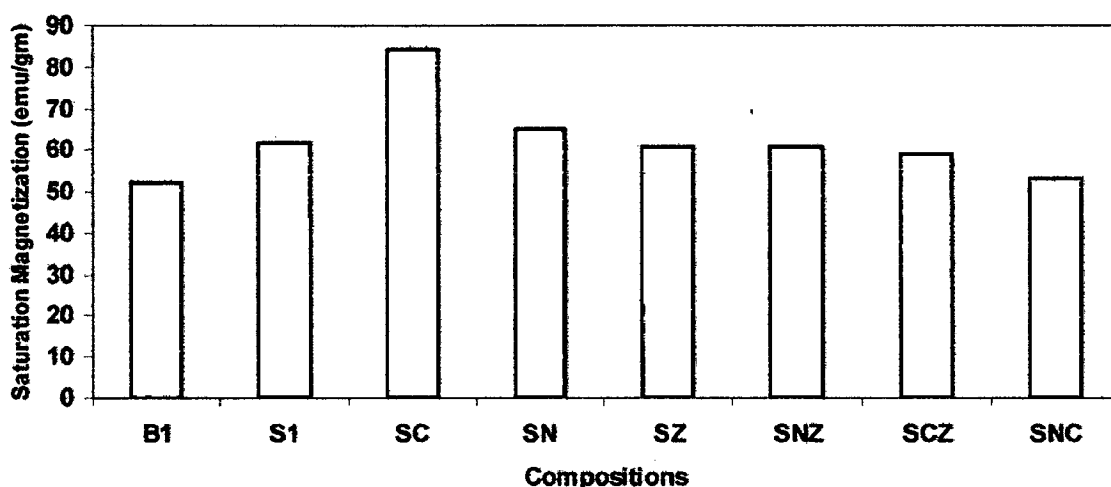
Fig. 6.22: Variation of saturation magnetization with composition of magnetic RAM developed.

6.3.4 Dielectric Study

All the microwave measurements are conducted for X band frequencies because this range is important for defense applications, such as short range tracking, missile guidance, mapping, and marine radar and airborne intercept (Knott, 1993). In a time varying external electric field, some materials exhibits energy dissipation, in which case complex permitivity is expressed as

$$\varepsilon = \varepsilon' - j\varepsilon'' \qquad\qquad 6.2$$

where ε' and ε" are real and imaginary part of permitivity respectively. The ε" associated with electric field loss, results mostly from electric dipole polarization at microwave frequencies. The quantity μ is complex permeability of the material and is dimensionless. In time varying external magnetic field, some materials exhibits energy dissipation, in which case, complex permeability is expressed as

$$\mu = \mu' - j\,\mu''$$ 6.3

where μ' and μ" are real and imaginary part of permeability respectively. The μ" associated with magnetic loss; result from magnetic-dipole polarizarion. A material can absorb EM radiation as long as its ε" and μ" values are not negiligble. The real and imaginary parts of complex permittivity and permeability of magnetic nanocrystals are plotted as a function of frequency in X-band (8.2-12 GHz). It is observed that, with increase in heat treatment temperature from 'as synthesized' condition to 1200°C, both complex permitivity and permeability are observed to increase continuously in all the compositions (Figures 6.23-6.38). This might be due to the increased formation of desired magnetic phases with increase in heat treatment temperature.
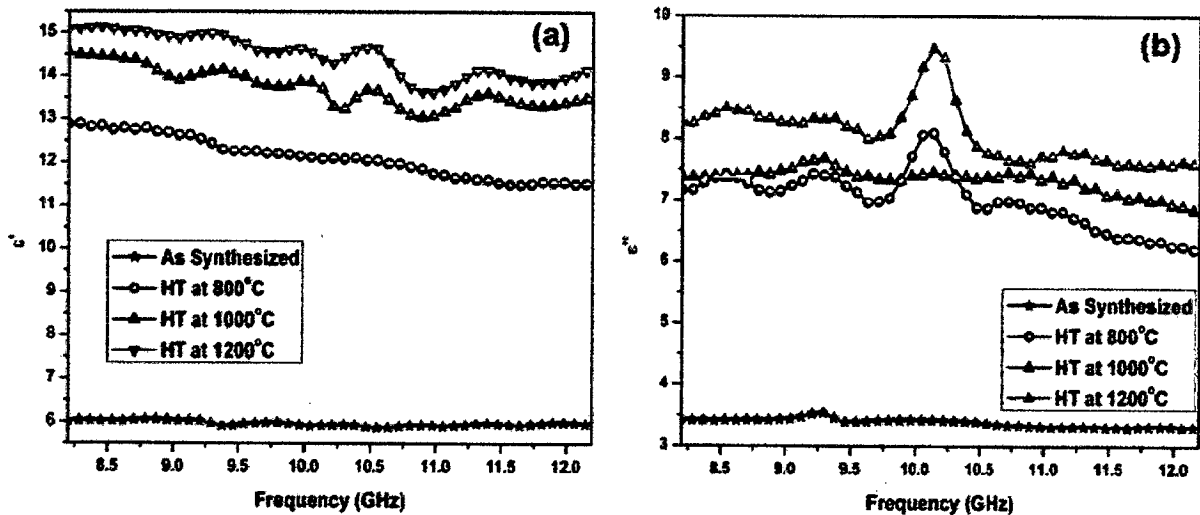
Fig. 6.23: The effect of HT temperature on real (ε') and imaginary (ε") part of permitivity of sample B1 in 'as synthesized' condition and heat treated at 800, 1000 and 1200°C in nitrogen atmosphere.
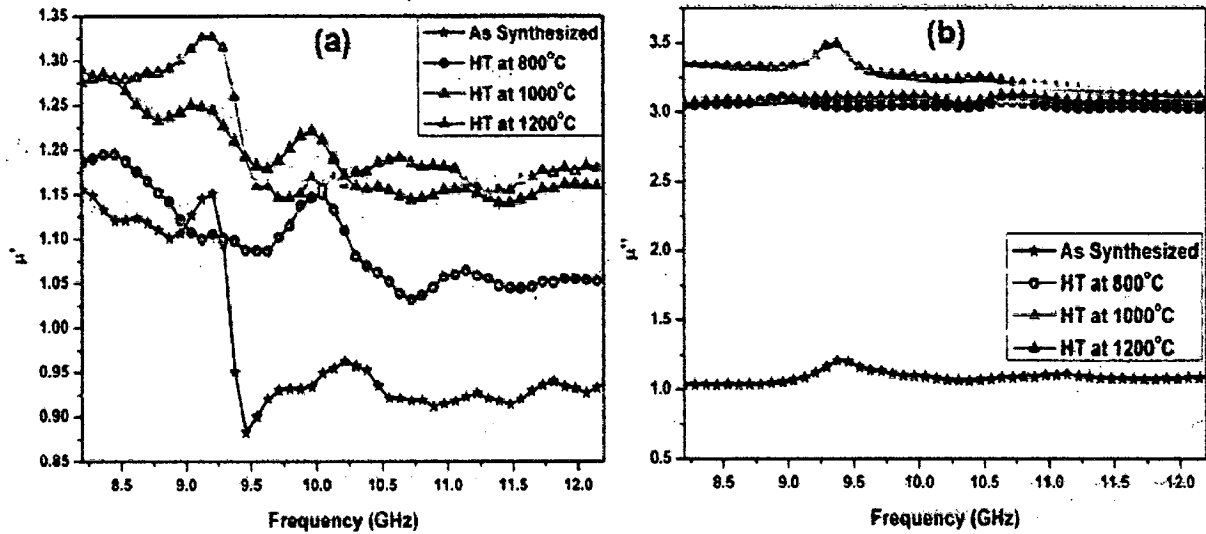
Fig. 6.24: The effect of HT temperature on real (μ') and imaginary (μ") part of permeability of sample B1 in 'as synthesized' condition and heat treated at 800, 1000 and 1200°C in nitrogen atmosphere.
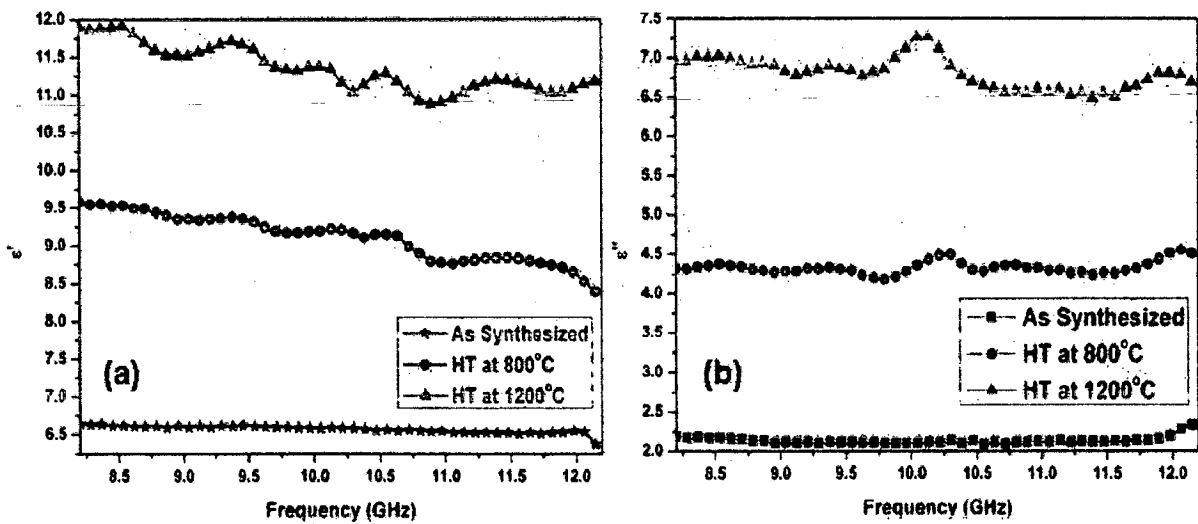
Fig. 6.25: The effect of HT temperature on real (ε') and imaginary (ε") part of permitivity of sample S1 in 'as synthesized' condition and heat treated at 800 and 1200°C in nitrogen atmosphere.

130
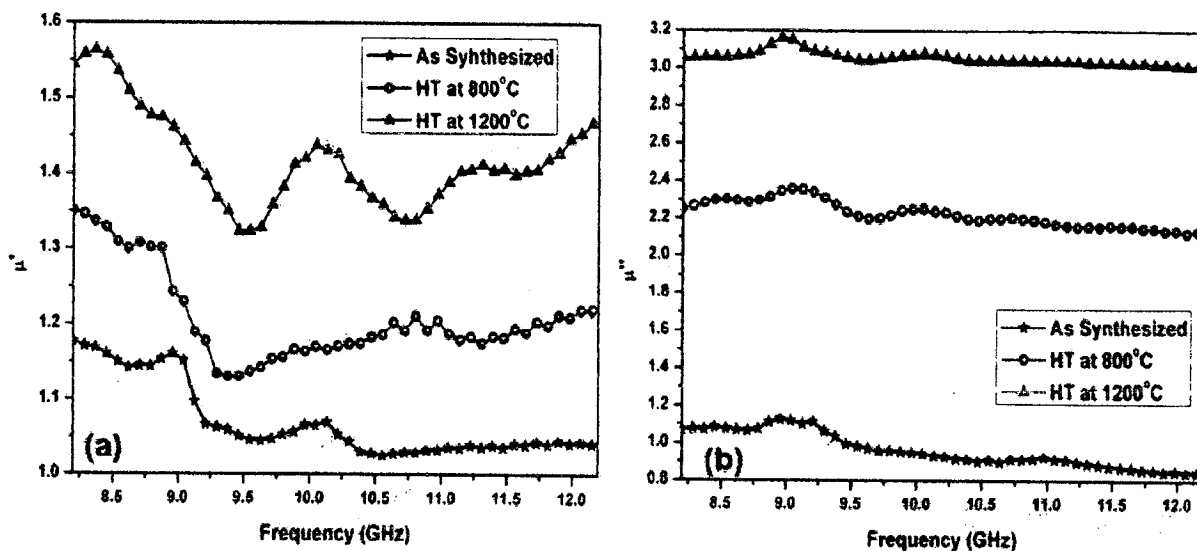
Fig. 6.26: The effect of HT temperature on real (μ') and imaginary (μ") part of permeability of sample S1 in 'as synthesized' condition and heat treated at 800 and 1200°C in nitrogen atmosphere.
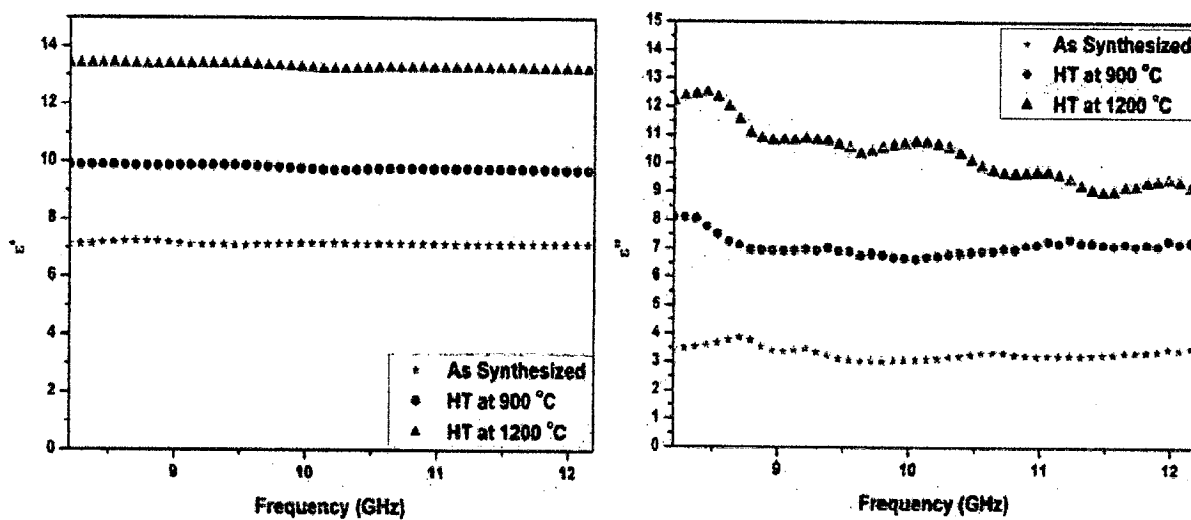
Fig. 6.27: The effect of HT temperature on real (ε') and imaginary (ε") part of permitivity of sample SC in 'as synthesized' condition and heat treated at 900 and 1200°C in nitrogen atmosphere.
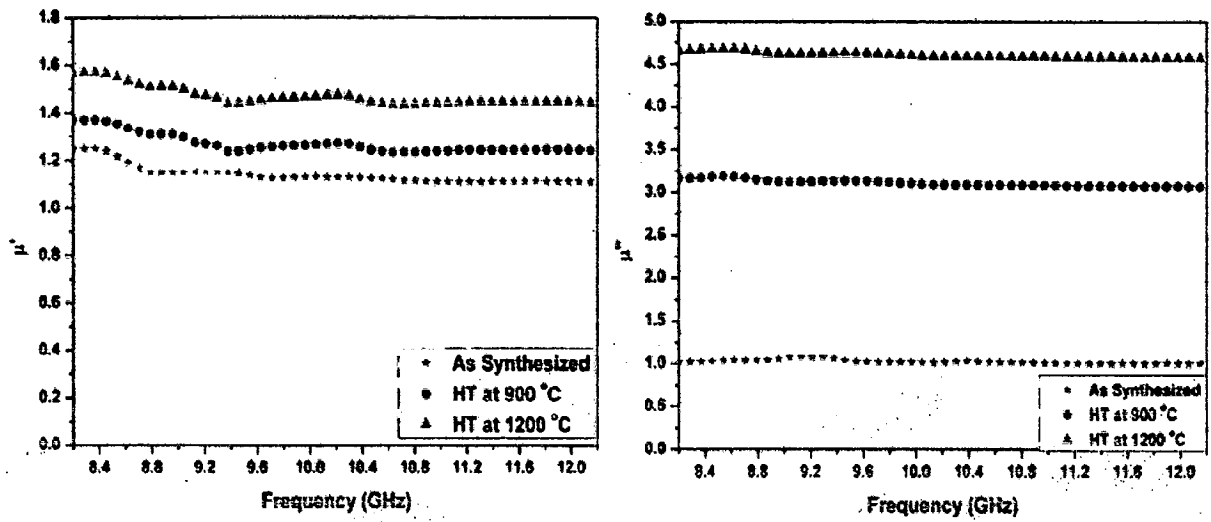
Fig. 6.28: The effect of HT temperature on real (µ') and imaginary (µ") part of permeability of sample SC in 'as synthesized' condition and heat treated at 900 and 1200°C in nitrogen atmosphere.
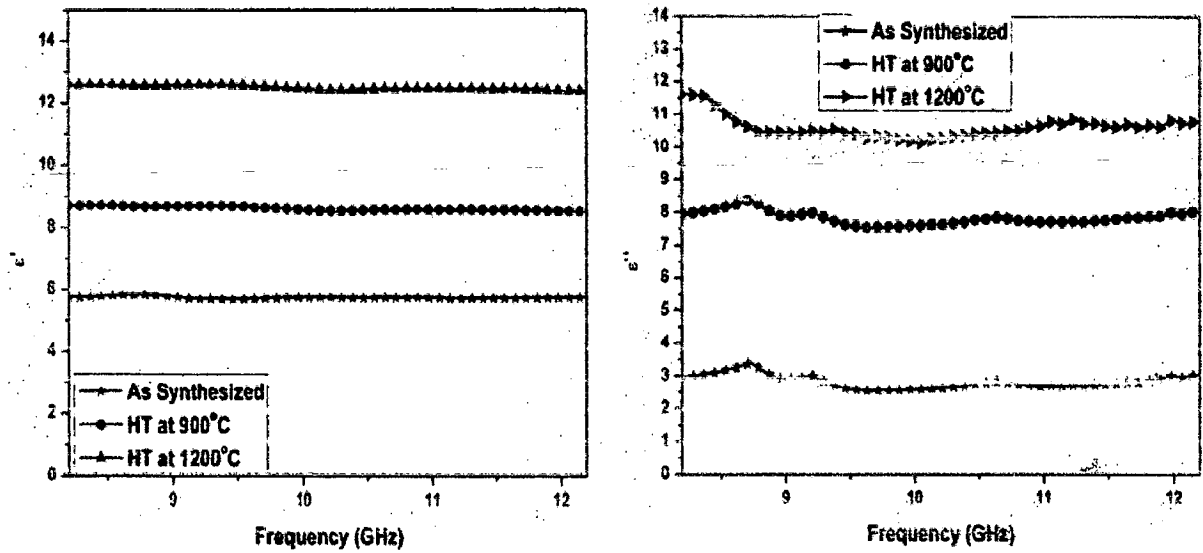
Fig. 6.29: The effect of HT temperature on real (ε') and imaginary (ε") part of permitivity of sample SN in 'as synthesized' condition and heat treated at 900 and 1200°C in nitrogen atmosphere.
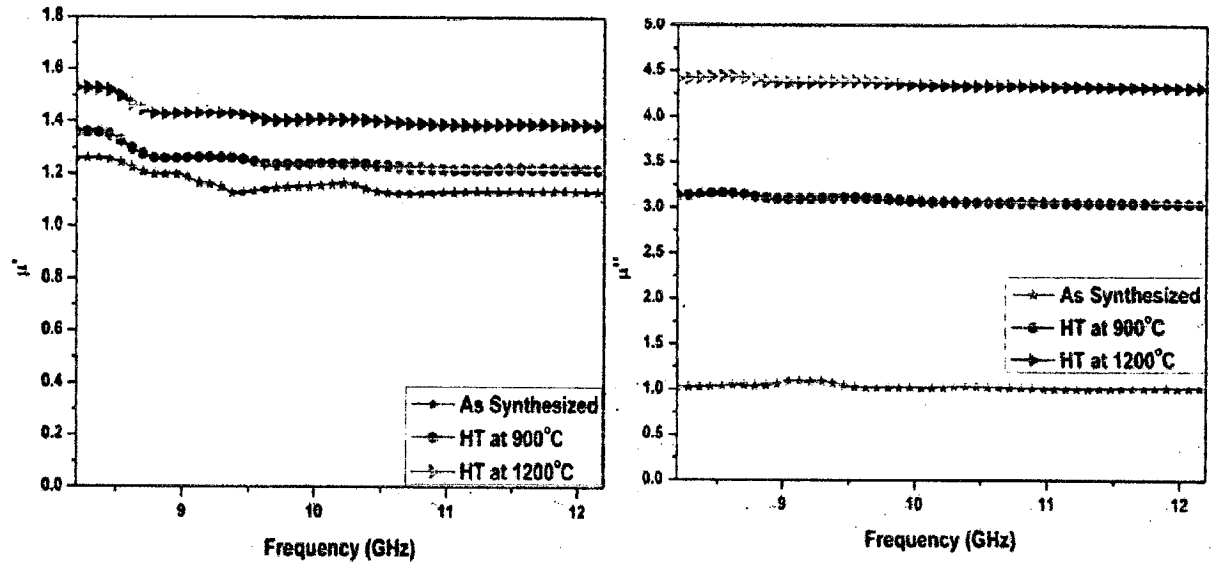
Fig. 6.30: The effect of HT temperature on real (μ') and imaginary (μ'') part of permeability of sample SN in 'as synthesized' condition and heat treated at 900 and 1200°C in nitrogen atmosphere.
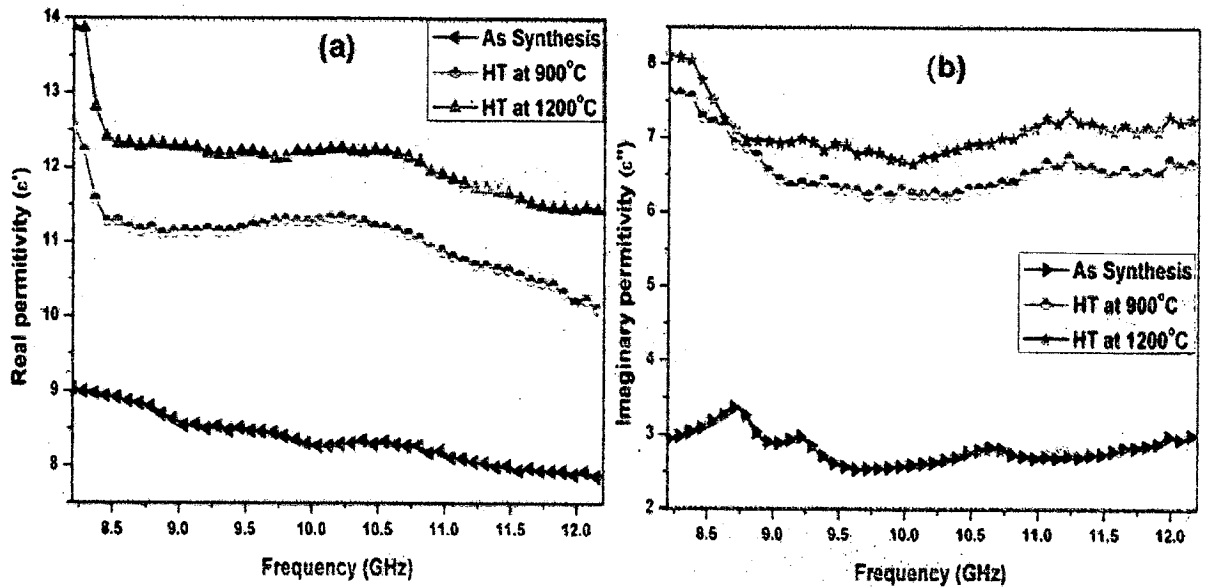
Fig. 6.31: The effect of HT temperature on real (ϵ') and imaginary (ϵ'') part of permitivity of sample SZ in 'as synthesized' condition and heat treated at 900 and 1200°C in nitrogen atmosphere.
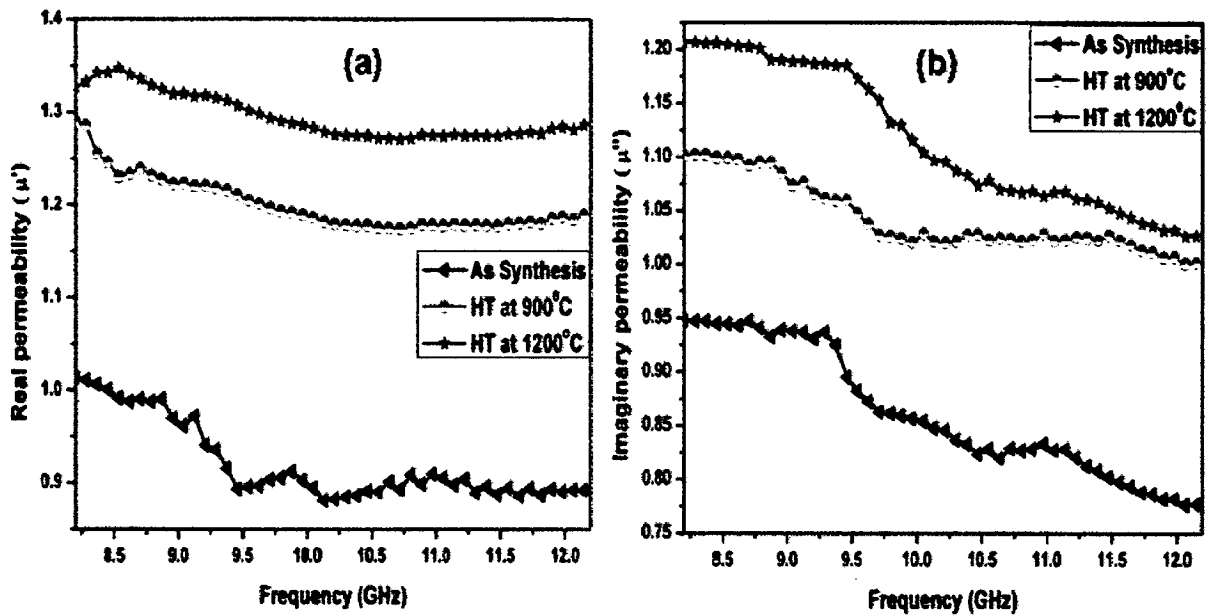
Fig. 6.32: The effect of HT temperature on real (μ') and imaginary (μ") part of permeability of sample SZ in 'as synthesized' condition and heat treated at 900 and 1200°C in nitrogen atmosphere.
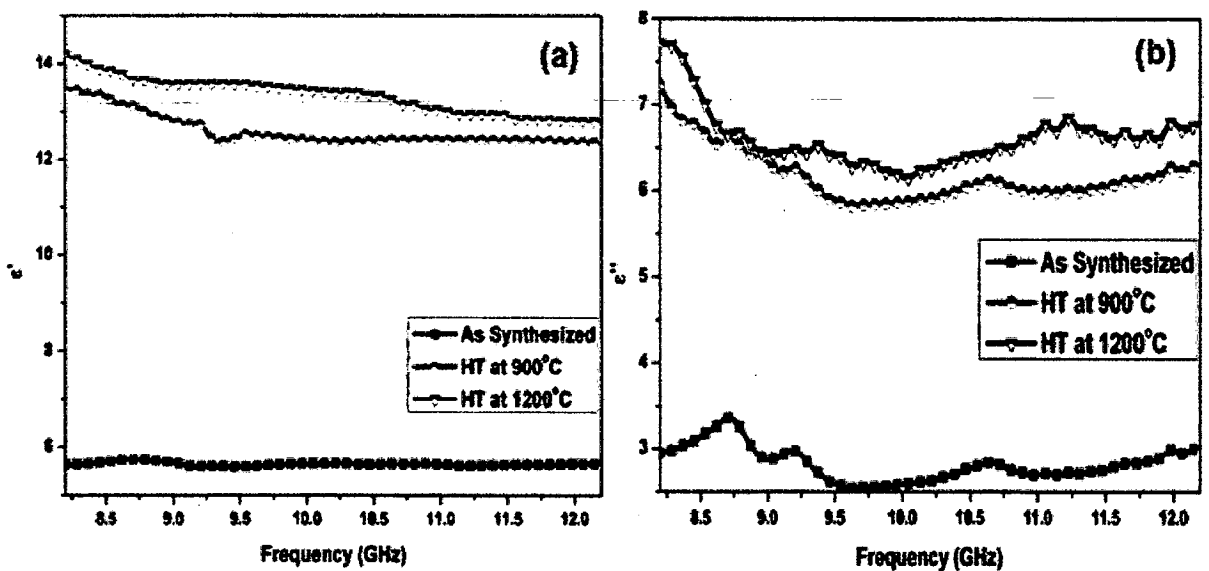
Fig. 6.33: The effect of HT temperature on real (ε') and imaginary (ε") part of permitivity of sample SNZ in 'as synthesized' condition and heat treated at 900 and 1200°C in nitrogen atmosphere.
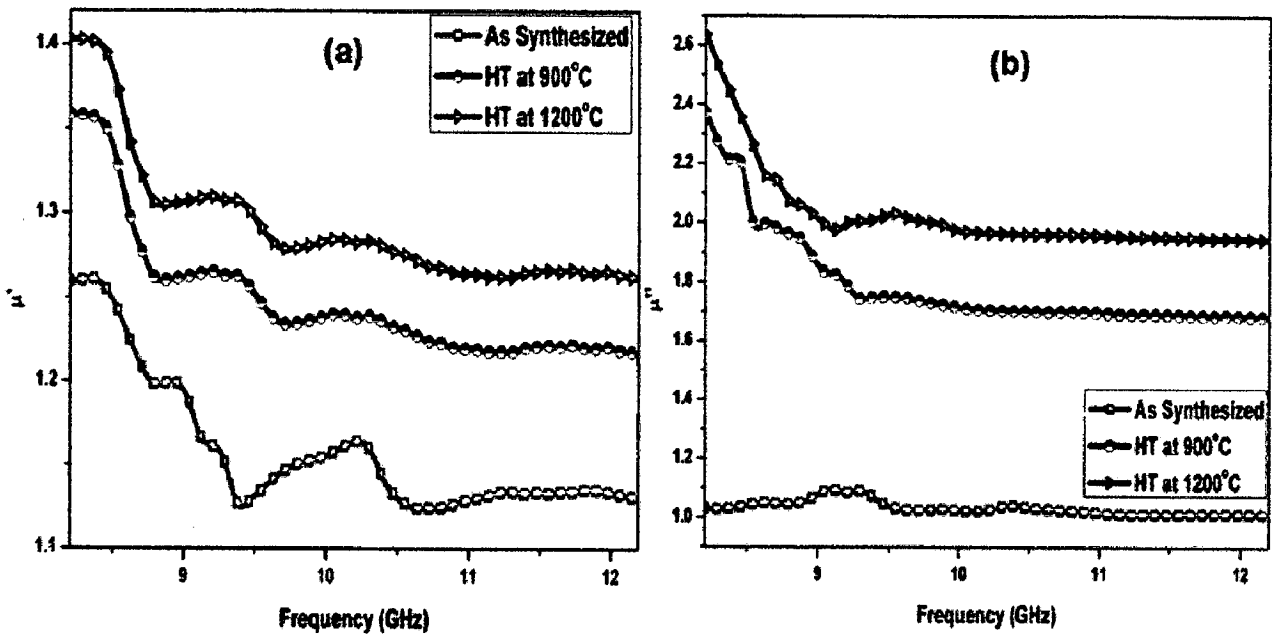
Fig. 6.34: The effect of HT temperature on real (μ') and imaginary (μ'') part of permeability of sample SNZ in 'as synthesized' condition and heat treated at 900 and 1200°C in nitrogen atmosphere.
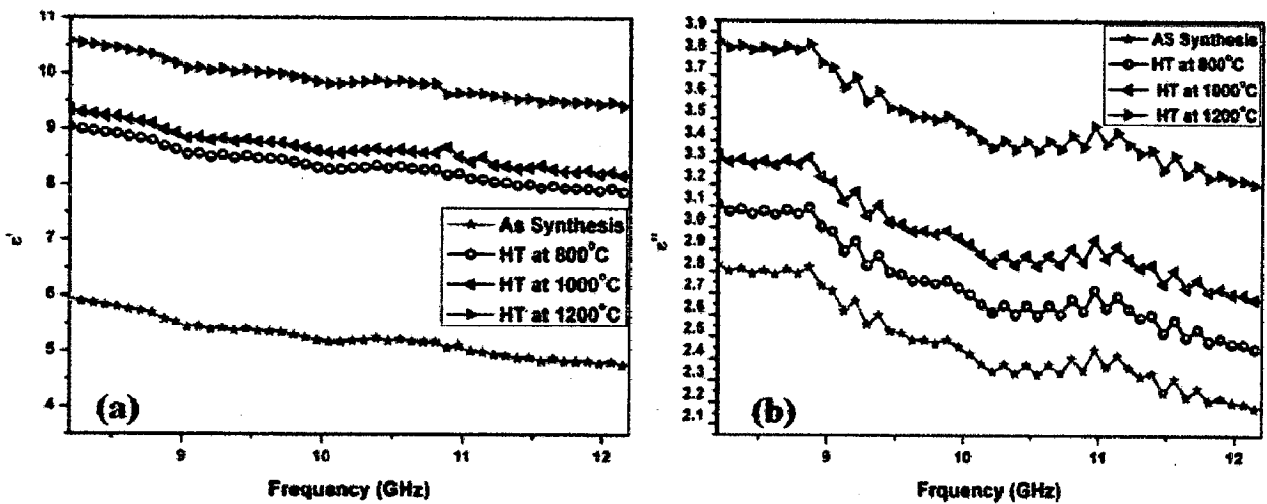
Fig. 6.35: The effect of HT temperature on real (ε') and imaginary (ε'') part of permitivity of sample SCZ in 'as synthesized' condition and heat treated at 800, 1000 and 1200°C in nitrogen atmosphere.
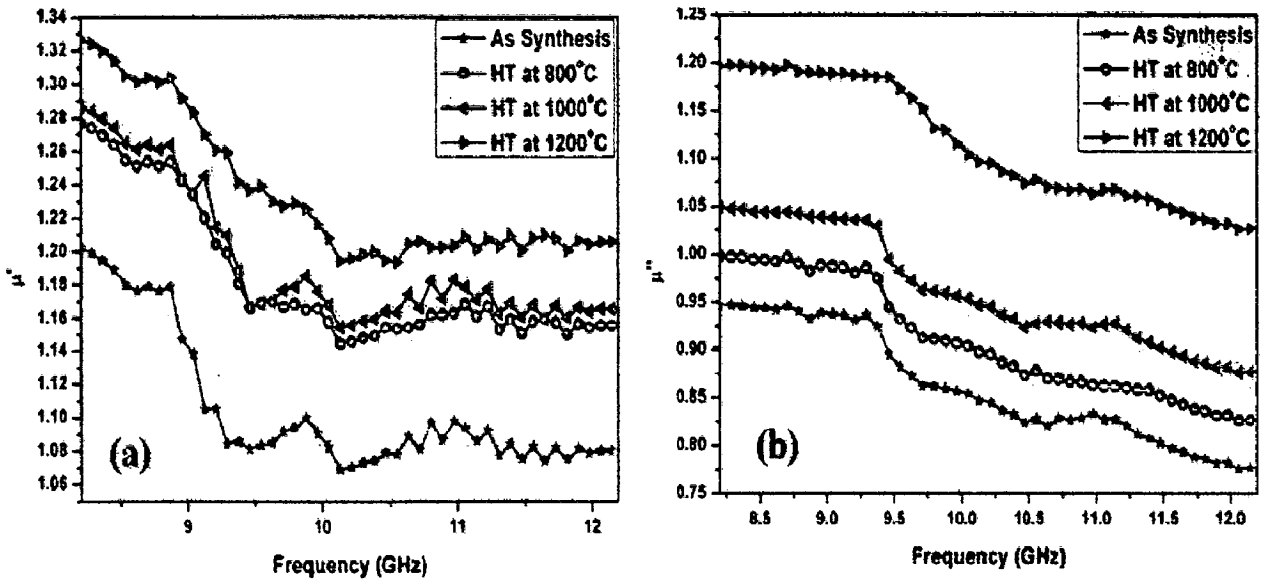
Fig. 6.36: The effect of HT temperature on real (μ') and imaginary (μ'') part of permeability of sample SCZ in 'as synthesized' condition and heat treated at 800, 1000 and 1200°C in nitrogen atmosphere.
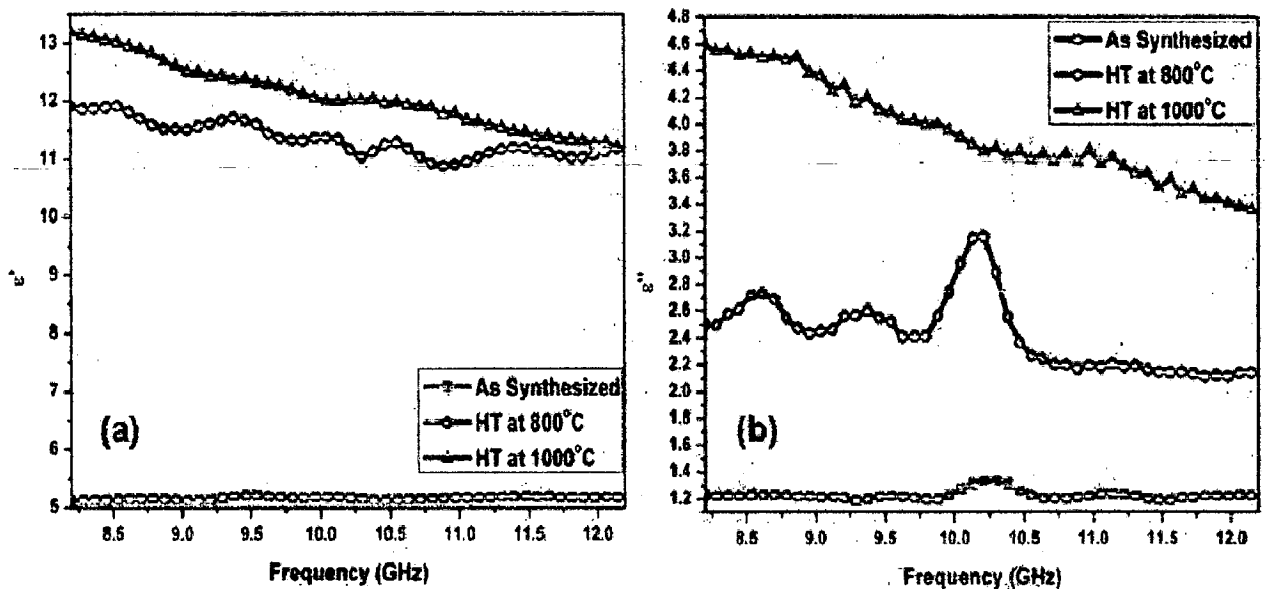
Fig. 6.37: The effect of HT temperature on real (ε') and imaginary (ε'') part of permitivity of sample SNC in 'as synthesized' condition and heat treated at 800 and 1000°C in nitrogen atmosphere.
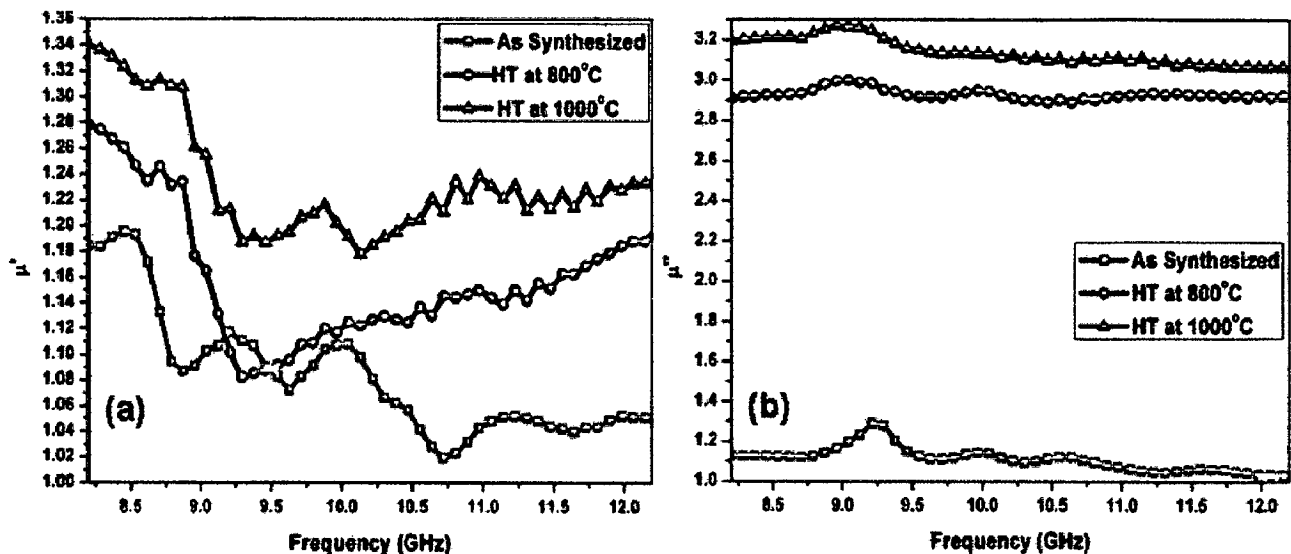
Fig. 6.38: The effect of HT temperature on real (μ') and imaginary (μ'') part of permeability of sample SNC in 'as synthesized' condition and heat treated at 800 and 1000°C in nitrogen atmosphere.

6.3.5 Reflection Loss Study

The reflection losses (RL) for 'as synthesized' $BaFe_{12}O_{19}$ nanoparticles are low for all the frequencies between 8.2 and 12.2GHz (Figure 6.39) and minimum to maximum values are found to be in the range of -3.85 (8.2 GHz) to -6.79dB (9.28 GHz). For $BaFe_{12}O_{19}$ nanoparticles heat treated at 800°C, the reflection loss is evidently improved to - 13.80dB at 10.05GHz and has further enhanced to -22.28dB (10.13GHz) for the material heat treated at 1200°C (Figure 6.39). The increment in reflection loss with increasing heat treatment temperature is attributed to the increased crystallization (Figure 5.2) of $BaFe_{12}O_{19}$ nanoparticles (crystallization effect). The strongest reflection loss and the widest bandwidths of $BaFe_{12}O_{19}$ nanoparticles (for RL >-10dB) with increase in heat treatment temperature are given in Table 6.1. It is reported that, microwave absorption is enhanced, when the particle size is reduced from micron to nano size (Ruan, 2000). This can be supposedly explained on the basis of quantum size effect. In nanocrystalline particles, the quantum size effect makes the electronic energy levels split and the spacing between adjacent energy states increases inversely with volume of the particles. If the particle size of absorber medium is small enough and the discrete energy level spacing is in the energy range of microwave, the electron can absorb the energy as it transit from one level to another, and lead to increase in attenuation.

As expected on the basis of hysteresis loop measurement (big hysteresis area), strontium hexaferrite showed large value of reflection loss with increased bandwidth (-23.12dB, 2.83GHz) than barium hexaferrite nanoparticles (-22.18dB, 2.19GHz). The reflection losses (RL) for 'as synthesized' $SrFe_{12}O_{19}$ nanoparticles are low for all the frequencies between 8.2 and 12.2GHz (Figure 6.40) and minimum to maximum values are found to be in the range of -4.82 (8.2 GHz) to -7.89dB (10.20 GHz). For powder heat treated at 800°C, the reflection loss is evidently improved to -13.62dB at 10.29GHz and has further enhanced to -23.12dB (10.46GHz) for the material heat treated at 1200°C (Figure 6.40). The strongest reflection loss and the widest bandwidths (Table 6.2) of strontium hexaferrite than barium hexaferrite forms the basis of selection of strontium hexaferrite for the development of magnetic composite containing hard ($SrFe_{12}O_{19}$) and soft ferrites ($NiFe_2O_4$, $CoFe_2O_4$ and $ZnFe_2O_4$).

Fig. 6.39: The effect of HT temperature on reflection loss of sample B1 in 'as synthesized' condition and heat treated at 800, 1000 and 1200°C.

Table 6.1: Showing the strongest reflection loss and the widest bandwidths of sample B1 (for RL > 10dB) in 'as synthesized' and heat treated conditions.

Powder	RL (dB) at 8.2 GHz	RL (dB) at 12.2 GHz	The widest bandwidth for RL>10dB (GHz)	The strongest RL (dB)
As Synthesis	-3.85	-3.50	0.0	-6.79 (9.28 GHz)
HT at 800°C	-5.06	-5.01	0.42 (9.88-10.30)	-13.80 (10.05 GHz)
HT at 1000°C	-5.48	-7.61	2.44 (9.20-11.64)	-15.09 (9.45 GHz)
HT at 1200°C	-6.74	-6.85	2.19 (9.20-11.39)	-22.28 (10.13 GHz)

Fig. 6.40: The effect of HT temperature on reflection loss of sample S1 in 'as synthesized' condition and heat treated at 900 and 1200°C.

Table 6.2: Showing the strongest reflection loss and the widest bandwidths of sample S1 (for RL > 10dB) in 'as synthesized' and heat treated conditions

Powder	RL (dB) at 8.2 GHz	RL (dB) at 12.2 GHz	The widest bandwidth for RL>10dB (GHz)	The strongest RL (dB)
As Synthesis	-4.82	-6.20	0.0	-7.89 (10.20 GHz)
HT at 900°C	-4.00	-6.20	0.67 (9.96-10.63)	-13.62 (10.29 GHz)
HT at 1200°C	-7.17	-10.64	2.83 (9.37-12.20)	-23.12 (10.46 GHz)

The addition of divalent ion (Co, Zn and Ni) during synthesis results in the formation of spinel ferrite ($CoFe_2O_4$, $NiFe_2O_4$ and $ZnFe_2O_4$) along with strontium hexaferrite. The maximum reflection loss of -27.60dB at 10.80GHz (Figure 6.41) is observed for sample SC heat treated at 1200°C. The details of strongest reflection losses with working band width for SC magnetic composite are shown in Table 6.3. Similarly the formation of $NiFe_2O_4$ and $ZnFe_2O_4$ along with $SrFe_{12}O_{19}$ in binary composition leads to the increase in reflection loss value with large bandwidth than pure strontium hexaferrite. For the magnetic composite (sample SN) containing $SrFe_{12}O_{19}$ and $NiFe_2O_4$, the maximum reflection loss of -24.92 at 11.1 GHz (Figure 6.42) with bandwidth of 3.4 GHz (RL>-10dB) is observed. The formation of $ZnFe_2O_4$ along with $SrFe_{12}O_{19}$ (sample SZ) result in reflection loss of -29.82 at 10.38 GHz (Figure 6.43) with bandwidth of 2.77 GHz. The strongest reflection loss and the widest bandwidths of sample SN and SZ composite (for RL >-10dB) with increase in heat treatment temperature are given in Table 6.4 and Table 6.5 respectively.

The improvement of reflection loss originated from the formation of hard and soft ferrite which can be explained on the basis of exchange coupling interaction between hard magnetic ($SrFe_{12}O_{19}$) and soft magnetic ($CoFe_2O_4$, $NiFe_2O_4$, $ZnFe_2O_4$) phases, which changes the relative complex permeability of the materials. In this study, the nanocomposite powders were synthesized by modified flux method so multiple types of grains can be combined. The composite powder including hexaferrite ($SrFe_{12}O_{19}$) and spinel ferrite ($CoFe_2O_4$, $NiFe_2O_4$, $ZnFe_2O_4$) coupled to each other by exchange through interface of ferrite particles. There will be more interfaces if the grain size is smaller, and there will be stronger exchange coupling

interaction at the interface. Moreover, the cubic spinal crystal structure of spinel phase ($CoFe_2O_4$, $NiFe_2O_4$, $ZnFe_2O_4$) is similar to the structure of S-block of $SrFe_{12}O_{19}$, so it is possible that the vacancy of spinel phase ($CoFe_2O_4$, $NiFe_2O_4$, $ZnFe_2O_4$) is combined with Fe^{3+} at the $SrFe_{12}O_{19}$ surface, which is another possible reason for strong interface coupling interaction (Maeda, 2004). Thus, exchange coupling interaction existing between hard and soft magnetic phases improves the dielectric and microwave absorption properties (interface effect) (Maeda, 2004) which are in agreement with the present study. The size of particles heat-treated at 1200°C is larger than that of particles heat-treated at 900°C. However, the strongest RL for composites HT 1200°C sample is larger than RL for HT at 900°C. Obviously, there is a competition between interface effect and the crystallization effect on the reflection loss (Tyagi, 2011).

Fig. 6.41: The effect of HT temperature on reflection loss of sample SC in 'as synthesized' condition and heat treated at 900 and 1200°C.

Table 6.3: Showing the strongest reflection loss and the widest bandwidths of sample SC (for RL > 10dB) in 'as synthesized' and heat treated conditions.

Powder	RL (dB) at 8.2 GHz	RL (dB) at 12.2 GHz	The widest bandwidth for RL>10dB (GHz)	The strongest RL (dB) at 10.80 GHz
As Synthesis	-4.84	-7.20	0.1 (10.8-10.9)	-10.78
HT at 900°C	-6.75	-9.90	2.6 (9.4-12.0)	-18.75
HT at 1200°C	-7.80	-10.64	3.1 (9.1-12.2)	-27.60

Fig. 6.42: The effect of HT temperature on reflection loss of sample SN in 'as synthesized' condition and heat treated at 900 and 1200°C.

Table 6.4: Showing the strongest reflection loss and the widest bandwidths (for RL > -10dB) of sample SN in 'as synthesized' and heat treated conditions.

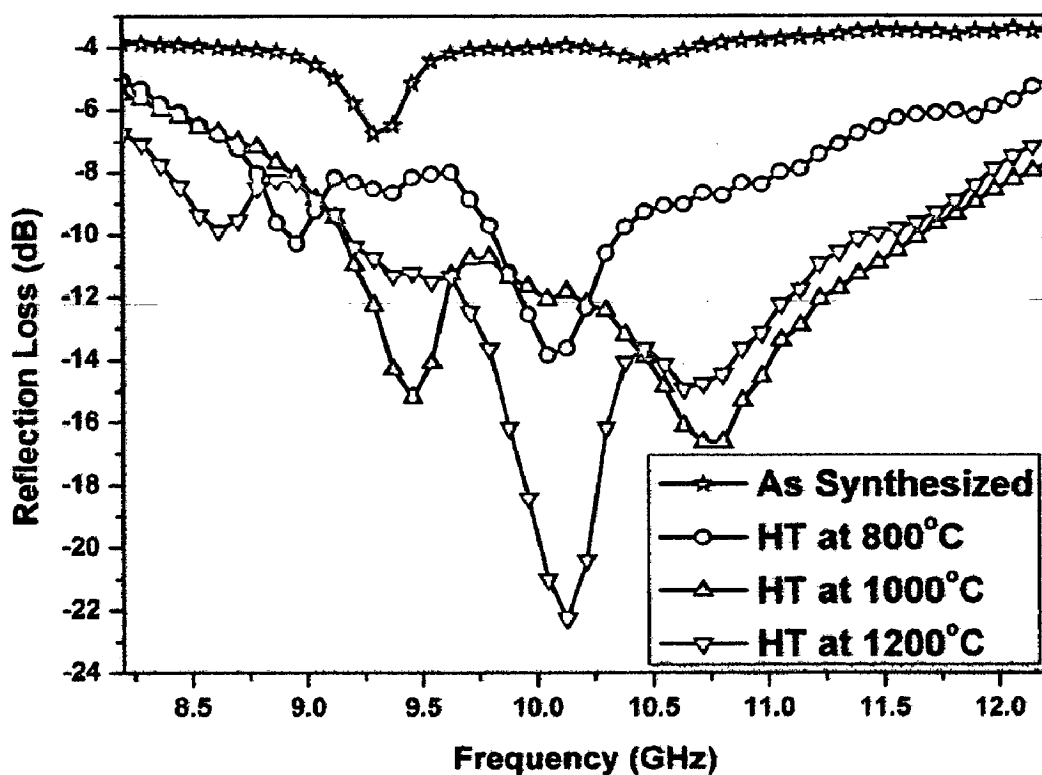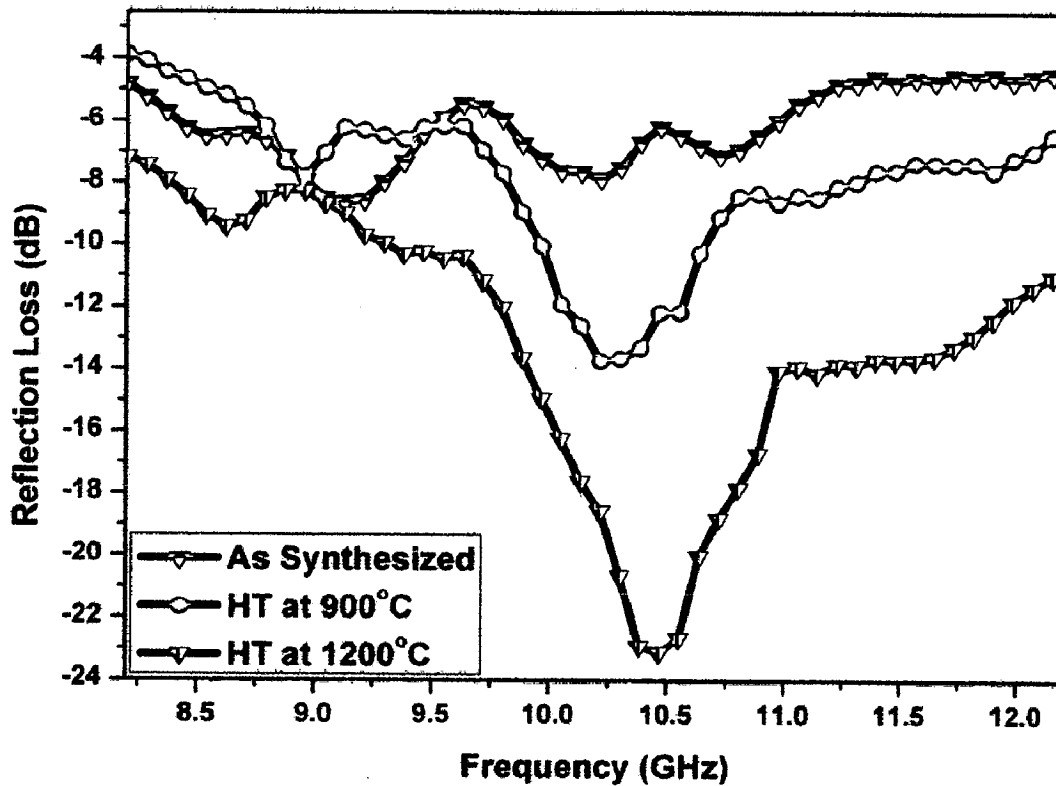| Powder	RL (dB) at 8.2 GHz	RL (dB) at 12.2 GHz	The widest bandwidth for RL>10dB (GHz)	The strongest RL (dB) at 11.1 GHz
As Synthesis	-4.84	-7.80	0.0	-8.83
HT at 900°C	-5.80	-12.25	3.1 (9.1-12.2)	-14.80
HT at 1200°C	-8.83	-12.60	3.4 (8.8-12.2)	-24.92
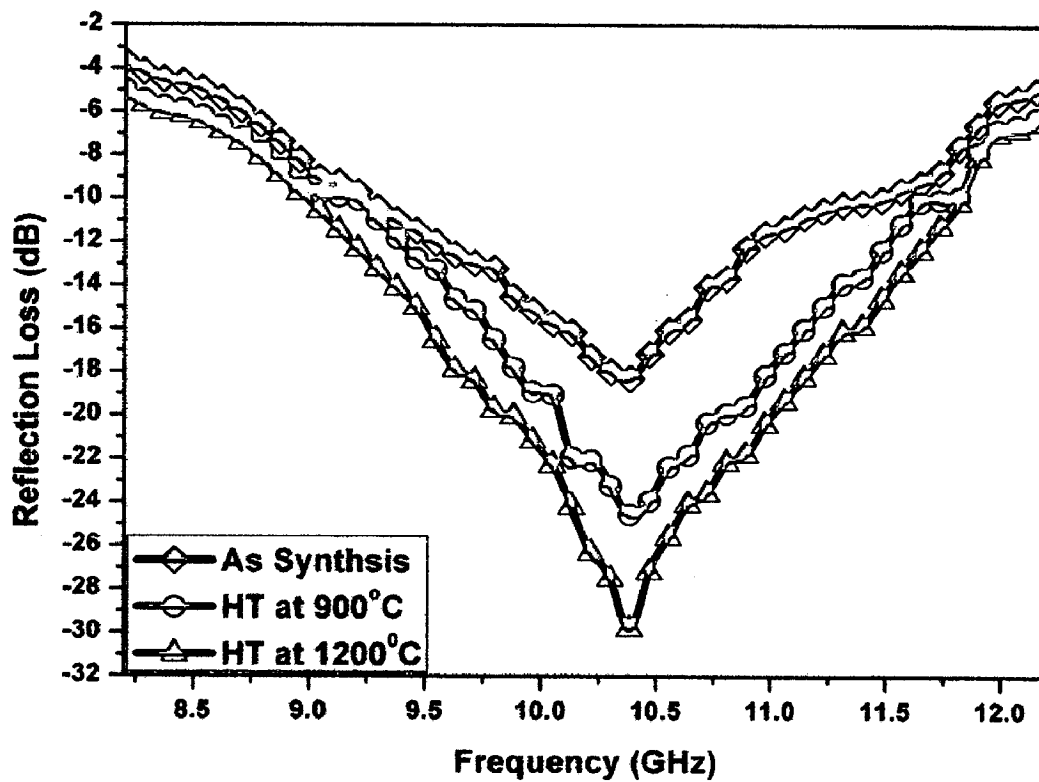
Fig. 6.43: The effect of HT temperature on reflection loss of sample SZ in 'as synthesized' condition and heat treated at 900 and 1200°C.

Table 6.5: Showing the strongest reflection loss and the widest bandwidths (for RL > 10dB) of sample SZ in 'as synthesized' and heat treated conditions.

Powder	RL (dB) at 8.2 GHz	RL (dB) at 12.2 GHz	The widest bandwidth for RL>10dB (GHz)	The strongest RL (dB) at 10.38 GHz
As Synthesis	-3.68	-4.73	2.18 (9.29-1147)	-18.29
HT at 900°C	-4.95	-5.00	2.52 (9.20-11.72	-24.56
HT at 1200°C	-5.20	-5.25	2.77 (9.04-11.81)	-29.82

Similar trend of reflection loss is observed for ternary magnetic composite of SNZ (Figure 6.44) and SCZ (Figure 6.45). The reflection losses (RL) for 'as synthesized' SNZ nanoparticles are also low for all the frequencies between 8.2 and 12.2GHz (Figure 6.44) and minimum to maximum values are found to be in the range of -5.00 (at 8.2 GHz) to   -15.20 dB (at 10.21GHz). For SNZ nanoparticles heat treated at 900°C, the reflection loss is evidently improved to -27.59dB at 10.21GHz and has further enhanced to -29.62dB for the material heat treated at 1200°C (Figure 6.44). Similarly the highest reflection loss of -26.32 dB at 10.63 GHz is observed for the magnetic composite of SCZ (Figure 6.45). The details of strongest reflection loss and the widest bandwidths of SNZ and SCZ composites (for RL >- 10dB) with increase in heat treatment temperature are given in Table 6.6 and Table 6.7 respectively.

For comparative study, the SNC magnetic composite synthesized by low combustion synthesis method, shows the different kind of reflection loss pattern than those observed for co-precipitated particles. The reflection losses (RL) for 'as synthesized' SNC nanoparticles are also low for all the frequencies between 8.2 and 12.2GHz (Figure 6.46) and minimum to maximum values are found to be in the range of -3.85 (at 8.2 GHz) to –8.97dB (at 9.28GHz). For SNC nanoparticles heat treated at 800°C, the reflection loss is evidently improved to -17.59dB at 8.52GHz and has further enhanced to –30.79dB for the material heat treated at 1000°C (Table 6.8).

The present study concluded that, in all magnetic composite, SZ ferrite resin composite is observed to show maximum reflection loss value (Figure 6.47) with almost similar reflection value at extreme frequencies (Figure 6.48) of X band (8.2 and 12.2 GHz). This study form the basis for the selection of sample SZ for fabricating the composite

containing magnetic and non magnetic phases. The higher values of reflection loss are also observed for the ternary composite of sample SNZ and SCZ (Figure 6.47). But the composite with less number of phases with large reflection loss peak (Sample SZ) is observed to be preferable for the further study.

The -10dB absorption bandwidth corresponds to 68% EM wave amplitude attenuation or to 90% power attenuation, whereas a -20 dB absorption bandwidth corresponds to 90% amplitude attenuation or to 99% power attenuation (Liu, 2011). The epoxy resin is an insulator and nonmagnetic; thus, it is transparent to EM waves. In the magnetic ferrite/epoxy composite, the epoxy resin only functions as matrix (Liu, 2011). The reflection loss of the composite mainly stems from the contribution of magnetic ferrite composite. Thus more than 99% power attenuation is observed for all composite material heat treated powders at 1200°C which suits its application in Stealth defense in all military platforms.
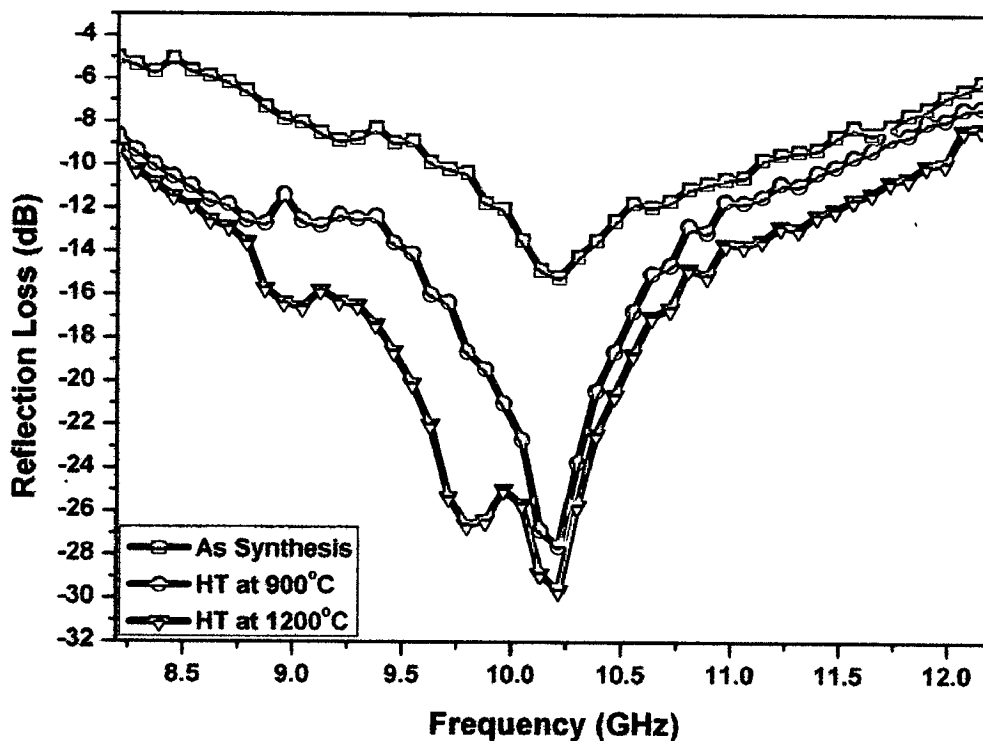
Fig. 6.44:   The effect of HT temperature on reflection loss of sample SNZ in 'as synthesized' condition and heat treated at 900 and 1200°C.

Table 6.6:   Showing the strongest reflection loss and the widest bandwidths (for RL > 10dB) of sample SNZ in 'as synthesized' and heat treated conditions.

Powder	RL (dB) at 8.2 GHz	RL (dB) at 12.2 GHz	The widest bandwidth for RL>10dB (GHz)	The strongest RL (dB) at 10.21 GHz
As Synthesis	-5.00	-5.82	1.48 (9.62-11.10)	-15.20
HT at 900°C	-8.63	-6.88	3.20 (8.36-11.56)	-27.59
HT at 1200°C	-9.13	-8.28	3.70 (8.28-11.98)	-29.62
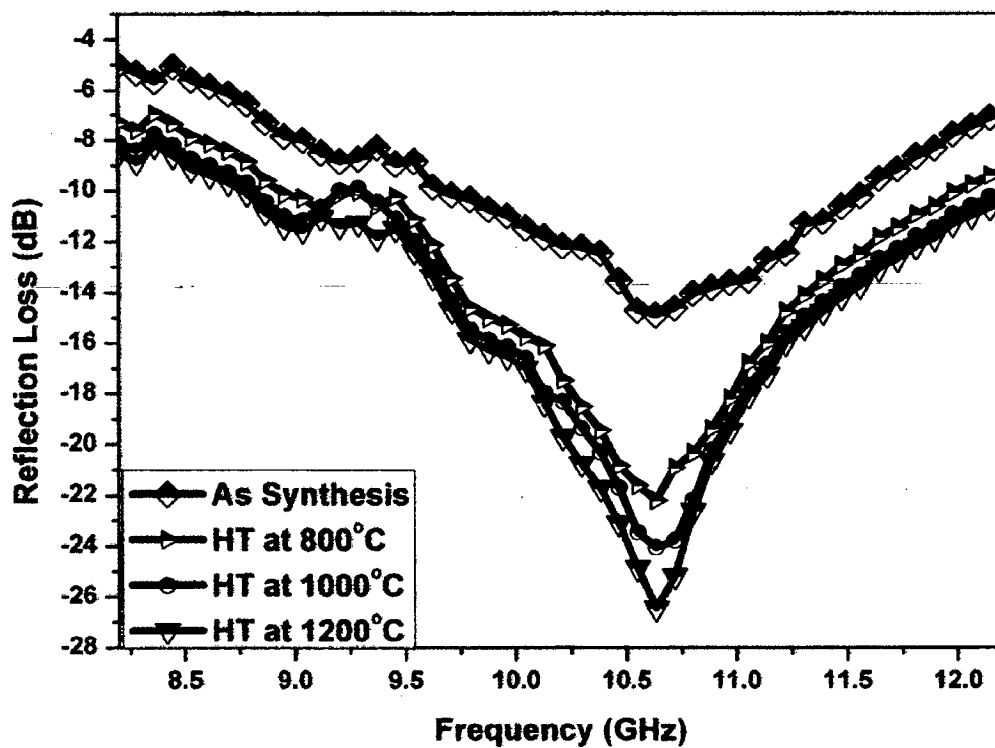
Fig. 6.45:   The effect of HT temperature on reflection loss of sample SCZ in 'as synthesized' condition and heat treated at 800, 1000 and 1200°C.

146

Table 6.7: Showing the strongest reflection loss and the widest bandwidths (for RL > 10dB) of sample SCZ in 'as synthesized' and heat treated conditions.

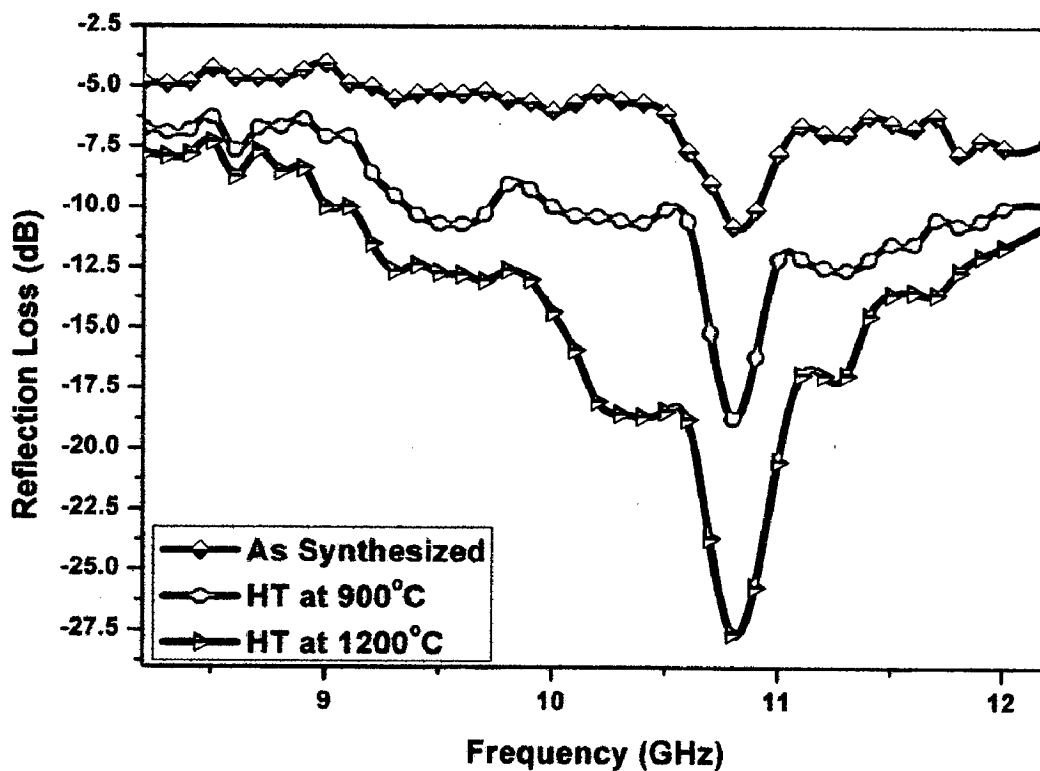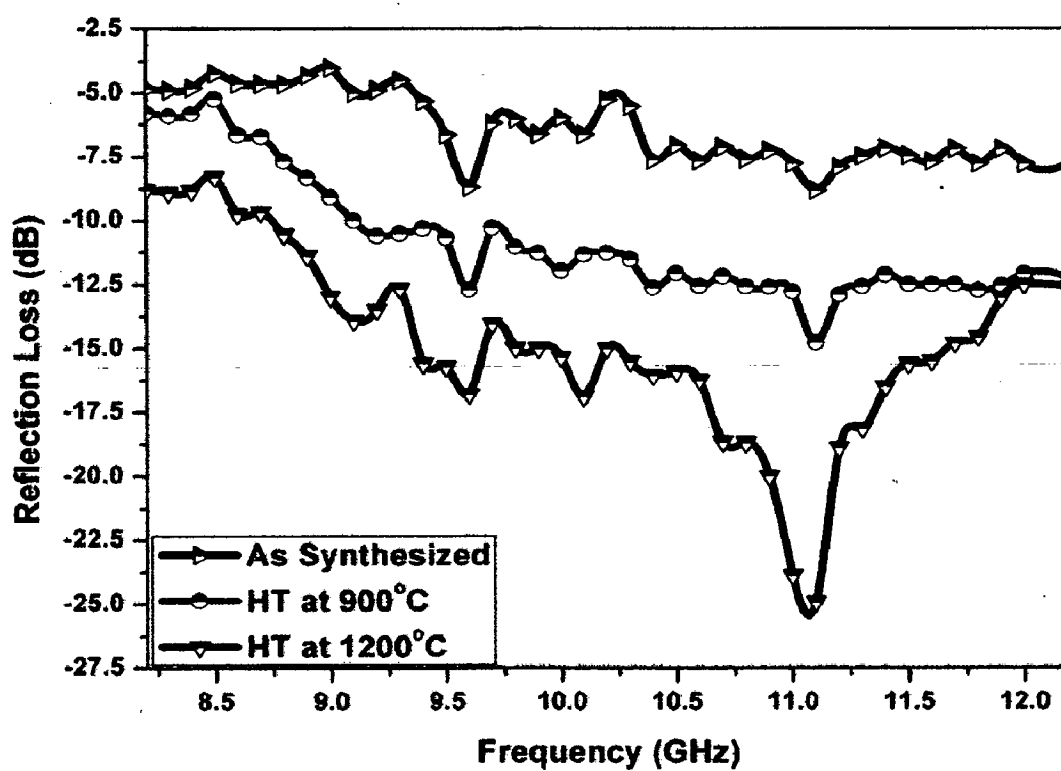| Powder	RL (dB) at 8.2 GHz	RL (dB) at 12.2 GHz	The widest bandwidth for RL>10dB (GHz)	The strongest RL (dB) at 10.63 GHz
As Synthesis	-5.00	-6.82	1.85 (9.71-11.56)	-14.83
HT at 800°C	-7.29	-9.11	3.03 (8.95-11.98)	-22.15
HT at 1000°C	-8.09	-9.97	3.23 (8.87-12.10)	-24.05
HT at 1200°C	-8.55	-10.37	3.42 (8.78-12.20)	-26.32
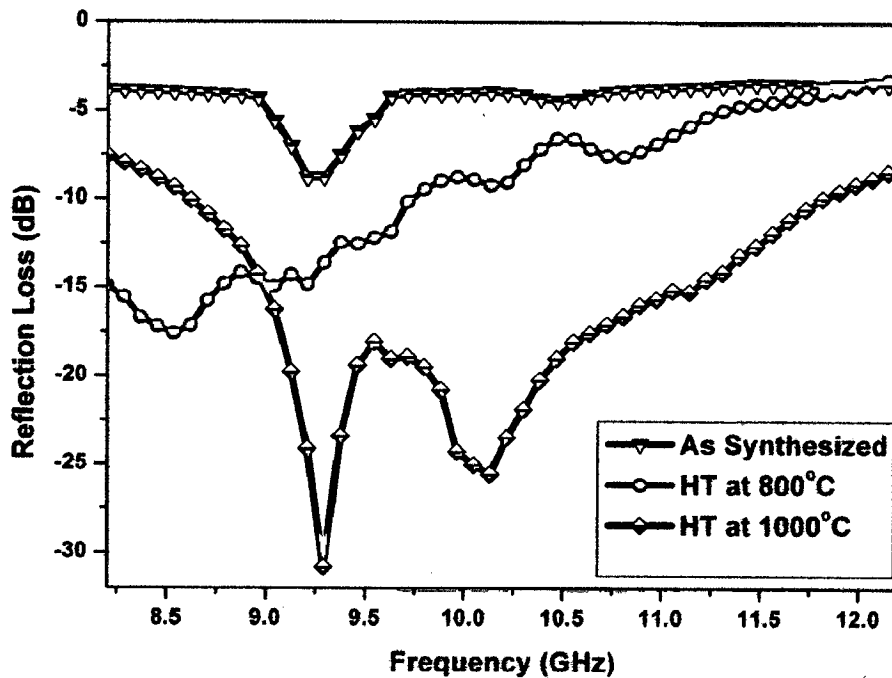
Fig. 6.46: The effect of HT temperature on reflection loss of sample SNC in 'as synthesized' condition and heat treated at 800 and 1000°C.

Table 6.8: Showing the strongest reflection loss and the widest bandwidths (for RL > 10dB) of sample SNC in 'as synthesized' and heat treated conditions.

Powder	RL (dB) at 8.2 GHz	RL (dB) at 12.2 GHz	The widest bandwidth for RL>10dB (GHz)	The strongest RL (dB) at 10.63 GHz
As Synthesis	-3.85	-3.50	0.0	-8.97 (9.28 GHz)
HT at 800°C	-14.92	-3.11	1.51 (8.20-9.71)	-17.59 (8.52 GHz)
HT at 1000°C	-7.56	-8.17	3.10 (8.62-11.72)	-30.79 (9.28 GHz)
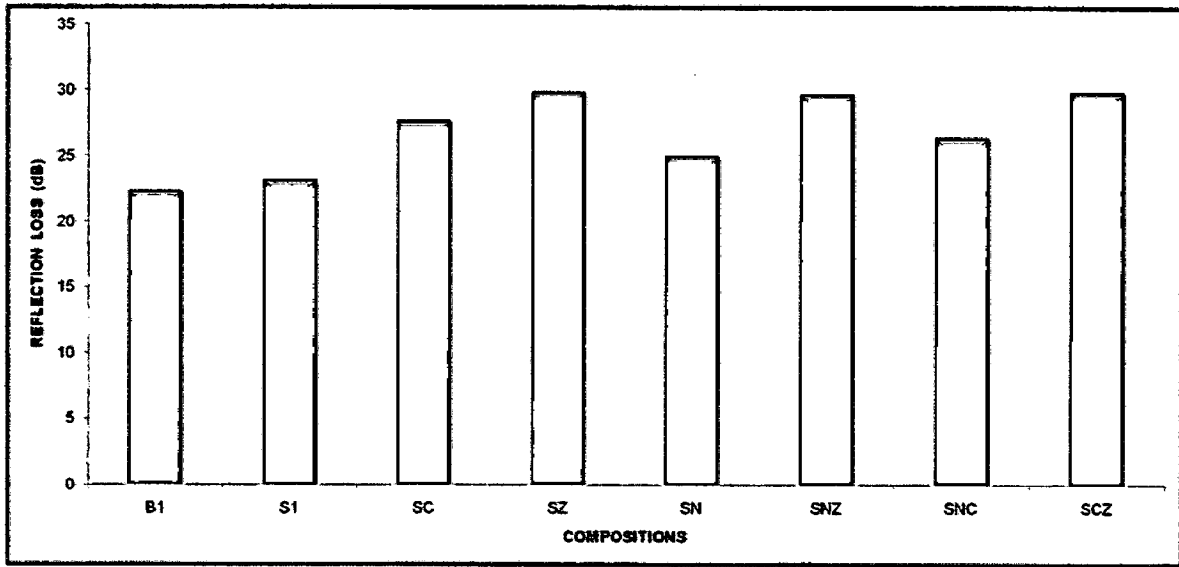
Fig. 6.47: Variation of reflection loss with composition observed for different magnetic RAM.
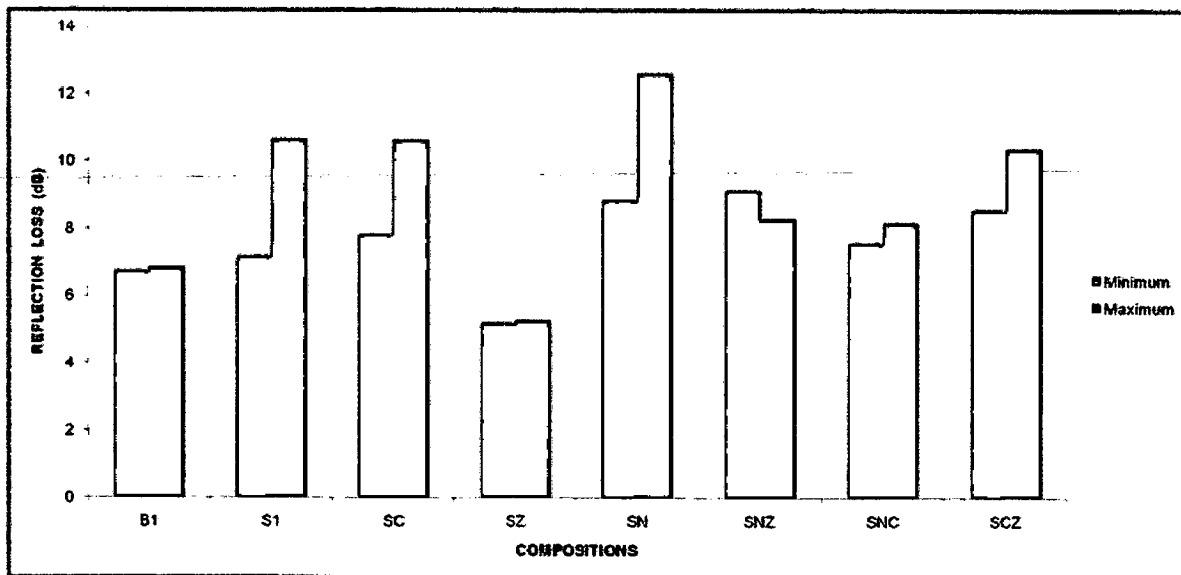
Fig. 6.48: Variation of reflection loss with composition at extreme frequencies of X band (8.2 and 12.2 GHz) observed for different magnetic RAM.

SUMMARY

All developed magnetic compositions have been characterized using instrumentation like XRD, FESEM, TEM, VSM and VNA. Morphological evaluation using FESEM and TEM inferred that, the nanoparticles synthesized by co-precipitation method are showing multiple morphology comprising hexagonal pyramidal and hexagonal plate shapes. The particles synthesized by low combustion synthesis method are found to have only hexagonal shape with increased agglomeration. The magnetic measurement of all the compositions synthesized by co-participation method reveals the superparamagnetic behaviour in 'as synthesized' conditions. All the co-precipitated compositions are observed to transform from superparamagnetic to ferromagnetic after heat treatment at various heat treatment temperatures. The magnetic measurement of all proposed composite inferred that strontium hexaferrite nanoparticles are more magnetic than barium hexaferrite nanoparticles. This is confirmed by the higher value of magnetic parameters like coercivity and saturation magnetization. The synthesis of ferromagnetic based spinel ferrite ($NiFe_2O_4$ and $CoFe_2O_4$) along with strontium hexaferrite results in increase in saturation magnetization of hexaferrite/spinel magnetic composite than single phase strontium hexaferrite. The synthesis of soft ferrite like $ZnFe_2O_4$ along with strontium hexaferrite does not affect the magnetic parameter like saturation magnetization but results in decrease in coercivity of the composite. The magnetic composite SNC synthesized by low combustion synthesis method is found to be soft magnetic in the 'as synthesized' condition and also transformed to ferromagnetic after heat treatment process. The magnetic composite synthesized by LCS method shows higher value of coercivity and saturation magnetization than co-precipitated magnetic composite. The reflection loss measurement of reported composition inferred that strontium hexaferrite nanoparticles show almost similar value of reflection loss like barium hexaferrite nanoparticles with increased bandwidth. The formation of spinel ferrite along with hexagonal ferrite results in increased microwave absorption than single phase hexaferrite. This increment has been explained on the basis of exchange interaction existing between hard and soft magnetic phases during reflection loss measurement. The addition of zinc ferrite is found to show the maximum microwave absorption than all other reported magnetic composites. The composite with less number of phases with large reflection loss peak (Sample SZ) is observed to be preferable for the further study.

DEVELOPMENT OF RAM COMPOSITE CONTAINING MAGNETIC AND NON MAGNETIC MATERIALS

7.1 INTRODUCTION

The details of magnetic and non magnetic materials used for improving the RADAR/microwave absorption applications have already been discussed in chapter 2. The emergence of nanoscience and nanotechnology opened the door for new opportunities to further improve the functionality of electromagnetic wave absorbers. The research pursuing to the development of various magnetic EM wave absorbers has been given much attention. Single material known by literature review namely; barium hexaferrite (Sharma, 2008), strontium hexaferrite (Tyagi, 2010; 2010; 2011; 2010; 2009), nickel ferrite (Sunny, 2010), zinc ferrite (Peng, 2005), cobalt ferrite (Fannin, 2011), silicon carbide, or materials containing carbon like charcoal, carbon black, graphite and carbon nano tubes (Makeiff, 2006; Kim, 2008) alone are not fulfilling the demand of large absorption peak, wide working frequency range and thin absorption layer. In order to improve electromagnetic absorption properties, new systems have been evolved comprising of magnetic and non magnetic phases (Liu, 2011; Maeda, 2004; Sharma, 2008; Zheng, 2008; Che, 2006; 2004; Park, 2009; Zhan, 2011). Strontium and barium hexaferrite, with high coercive force and large saturation magnetization, acted as the traditional microwave absorbing materials (Mishra, 2004, Wang, 2007; Liu, 2010), cannot satisfy the demand of the "ideal" absorbing materials with the defects of small working bandwidth, small absorption peak and mass density. So, it is needed to make composite with other absorbing materials with lesser thickness, high aspect ratio like CNTs (Che, 2006), lower density, high conductivity material like carbon black and SiC (Kim, 2008; Jhao, 2001). Moreover, EM response of material is the result of mutual interaction between the electronic system of the material and EM field. EM wave absorption property of a composite depends on electric (complex permitivty) and magnetic (complex permeability) properties of material. The electric loss of composite depends on ohmic and

polarization loss of energy, which can be obtained by adding fillers like silica, alumina, silicon carbide, carbon black, graphite, CNTs or carbon fiber to a matrix (Jhao, 2001; Jung, 2004; Lee, 1997; Dujardin, 1994; Rajendran, 2009; Ruoff, Soon, 2001; Thakur, 2007; 1993; Zhang, 2001; Hu, 2003; Rauf, 2004; Zhi, 2004, Ugarte, 1996; Manivasakan, 2009). The magnetic loss depends on big hysteresis attenuation, which can be obtained when magnetic material like hexaferrite, spinel ferrite or a composite of hard and soft ferrite is added to a matrix (Tyagi, 2010; 2011; 2011). Hence, ferrite/CNT, ferrite/CB or ferrite/SiC nanocomposite could be an excellent microwave absorbing and shielding material because ferrite and CNT/CB/SiC are the magnetic and dielectric fillers respectively that could enhance both dielectric and magnetic properties of composite.

Recently, modifying the properties of one material by coating it with another type of material has been a popular approach widely documented in the literature (Brookshir, 1961; Gorbunova, 1966; Pai, 1975; Rajagopal, 1989; Pedraza, 1990; Abraham, 1992; Bozzini, 1999; Khoperia, 2003; Peipmann, 2007; Alirezaei, 2007). Tang (2006) has investigated the effect of microwave absorption properties of titania-coated M-type barium ferrite composite powder in the frequency range of 2-20 GHz. Pan (2007) has coated strontium ferrite powder with Co-Ni-P to enhance the microwave absorption properties. Barium and strontium hexaferrite acts as a magnetic core because they have high saturation magnetization and high magnetic anisotropy field, which makes them to give rise to potential magnetic loss material at high frequency and on the other hand coated layer, improves the dielectric properties of material (Sharma, 2007; 2008; 2008).

In view of this, in the present study, an attempt to develop a RADAR absorbing composite medium containing magnetic and non magnetic phases has been made. Also an attempt has been made to develop Ni-P coated RAM powder ($BaFe_{12}O_{19}$ and $SrFe_{12}O_{19}$) and discussed in the subsequent sections.

7.2 SPECIFICATION

Six different composites containing SZ ferrite with non magnetic materials (CNT, CB and SiC) and Ni-P coated ferrite ($SrFe_{12}O_{19}$ and $BaFe_{12}O_{19}$) were prepared for morphological, phase analysis, magnetic, dielectric and microwave absorption study. All the compositions have been given a sample code and are listed in Table 7.1.

Table 7.1: Details of composition and sample code of magnetic and non magnetic composite used in present investigation.

S. No.	Composites	Sample code
1	$SrFe_{12}O_{19}$, $ZnFe_2O_4$, CNT	SZ/CNT
2	$SrFe_{12}O_{19}$, $ZnFe_2O_4$, CB	SZ/CB
3	$SrFe_{12}O_{19}$, $ZnFe_2O_4$, SiC	SZ/SiC
4	$BaFe_{12}O_{19}$, SiC	B1/SiC
5	$SrFe_{12}O_{19}$/(Ni-P)	S1(Ni-P)
6	$BaFe_{12}O_{19}$/(Ni-P)	B1(Ni-P)

7.3 CHATERIZATION

All the presented compositions have been prepared by mixing the magnetic ferrite (sample SZ) and non magnetic materials like CNT, CB and SiC in different proportions in agate pestle mortar. Carbon nanotubes were synthesized by chemical vapor deposition technique and the details of synthesis methods have been described in chapter 3. The commercialized SiC and CB were reduced in size using mechanical alloying at 300 rpm for a period of 50 hrs. The morphological, phase analysis, magnetic, dielectric and microwave absorption properties of different magnetic phases ($BaFe_{12}O_{19}$, $SrFe_{12}O_{19}$ and $SrFe_{12}O_{19}$/$ZnFe_2O_4$) used in the present study have been discussed in chapter 6. The bath composition and coating procedure to coat Ni-P on the hexaferrite powder ($BaFe_{12}O_{19}$ and $SrFe_{12}O_{19}$) have been described in chapter 4. In the present chapter the morphological, phase analysis and magnetic study of prepared non magnetic materials and their effect on dielectric and microwave absorption properties of hexaferrites have been discussed. Also the effect of Ni-P coating on hexaferrite have been studied and discussed in the subsequent sections.

7.3.1 Morphological Study

The microwave absorbing materials are typically constituted of multiple shaped grains with properties that allow electromagnetic wave to penetrate into regions where the electric and magnetic field experience loss (Tyagi, 2011; Knott, 1985). Figure 7.1 shows the typical FESEM of the top view of the CNTs arrays grown over Fe-catalyst. The higher magnification shows long and thin multiwalled carbon nano tubes with diameter in the

range of 30-40nm. The images taken at lower magnification show the grass like appearance of top surface of CNTs array. The FESEM micrographs along with EDAX are also taken at a point (Figure 7.2) and over whole area (Figure 7.3). The EDAX analysis reveals the purity of the multiwalled carbon nanotubes. Here peak correspond to gold with 4.70 and 2.85 wt% is due to the gold coating which has to be done over the CNTs before the FESEM analysis to make them conducting to avoid the charging during FESEM characterization.
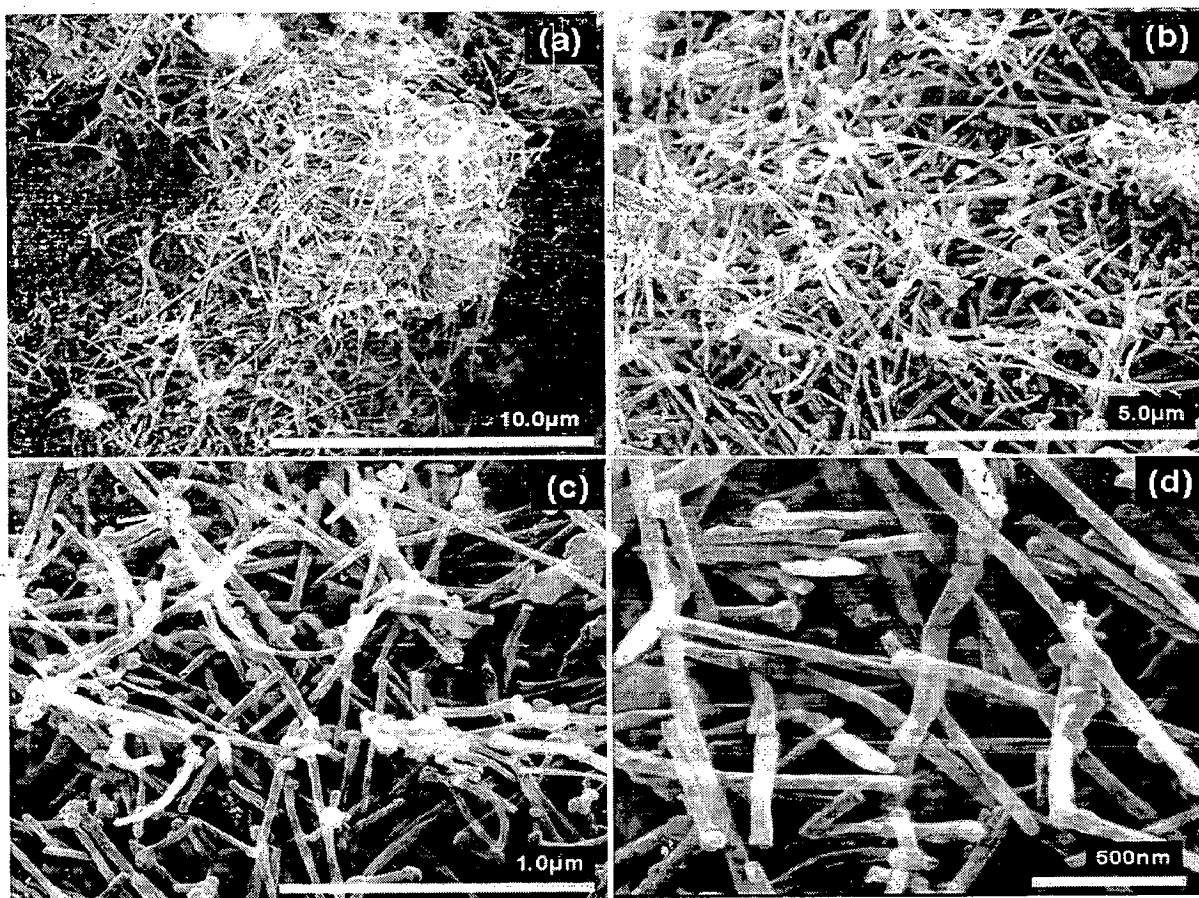
Fig. 7.1: FESEM micrographs showing the growth of CNTs synthesized by the catalytic decomposition of acetylene in the temperature range of 750 to 800°C.
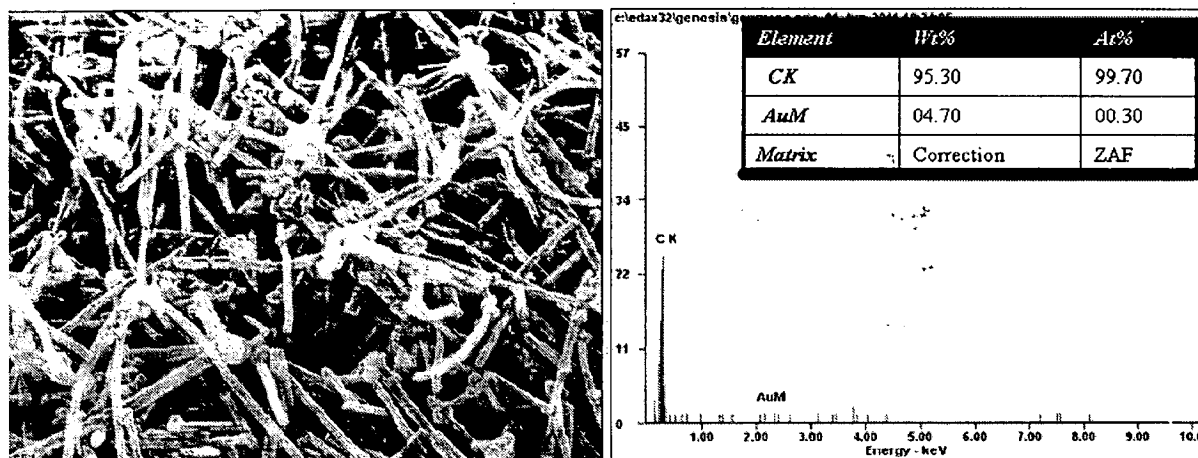
Element	Wt%	At%
CK	95.30	99.70
AuM	04.70	00.30
Matrix	Correction	ZAF

Fig. 7.2: EDAX micrographs showing the atomic and weight percentage of CNTs synthesis by the catalytic decomposition of acetylene gas in the temperature range of 750 to 800°C.

Element	Wt%	At%
CK	97.15	99.82
AuM	02.85	00.18
Matrix	Correction	ZAF
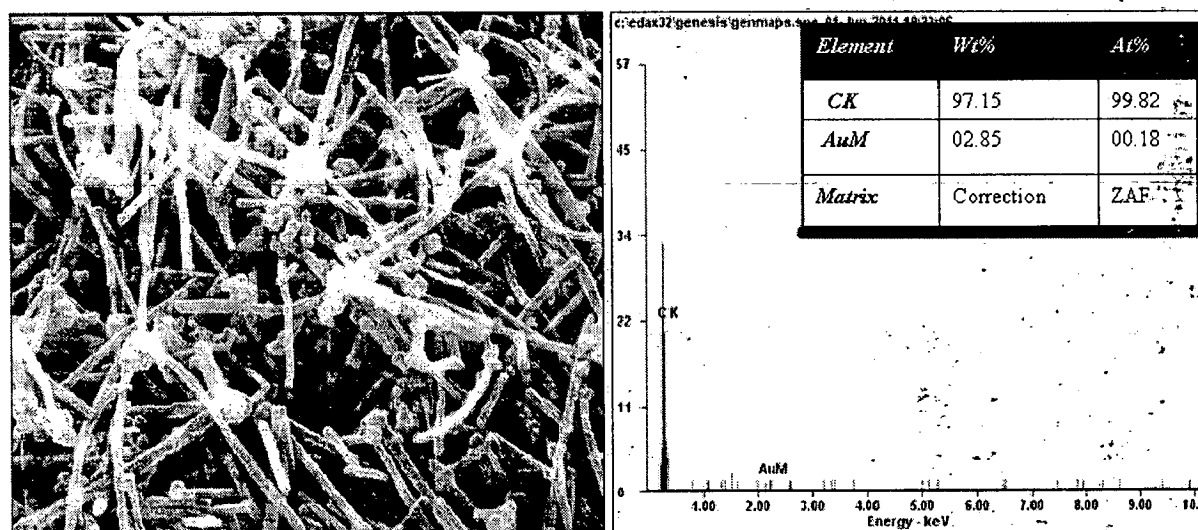
Fig. 7.3: EDAX micrographs showing the atomic and weight percentage of CNTs synthesis by the catalytic decomposition of acetylene gas in the temperature range of 750 to 800°C.

154

Figure 7.4 shows the FESEM images of silicon carbide particles in the 'as received' conditions and the particle obtained after mechanical alloying for different time periods. The FESEM images (Figure 7.4) show that silicon carbide particles are continuously decreasing in size as a function of milling time. It is observed that silicon carbide particle are shaped into irregular cubes with an average size of around 70-80nm. According to literature (Tyagi, 2011; Liu, 2011), the irregular particles possess relatively large surface area, which makes the particle possess large conduction losses and affect the microwave absorbing properties. Figure 7.5 shows the EDAX of the silicon carbide powder obtained after 50hrs milling. The peak corresponding to Fe is attributed to the impurities coming from steel jar and balls during milling. Figure 7.6 shows the FESEM image of CB powder obtained after different milling for 50hrs. CB is one of the traditional representatives of carbon nano materials. The average particle size is found to reduce from 200nm to 120nm with increase in milling time from 0 to 50hrs. These small size particles are found to be severely aggregated and prone to multi-pore structure. These structures, possessing large surface area, leads to plenty of interfacial polarization to weaken the energy of EM waves (Tyagi, 2011; Liu 2011). Figure 7.7 shows the EDAX of the CB powder obtained after 50 hrs milling.
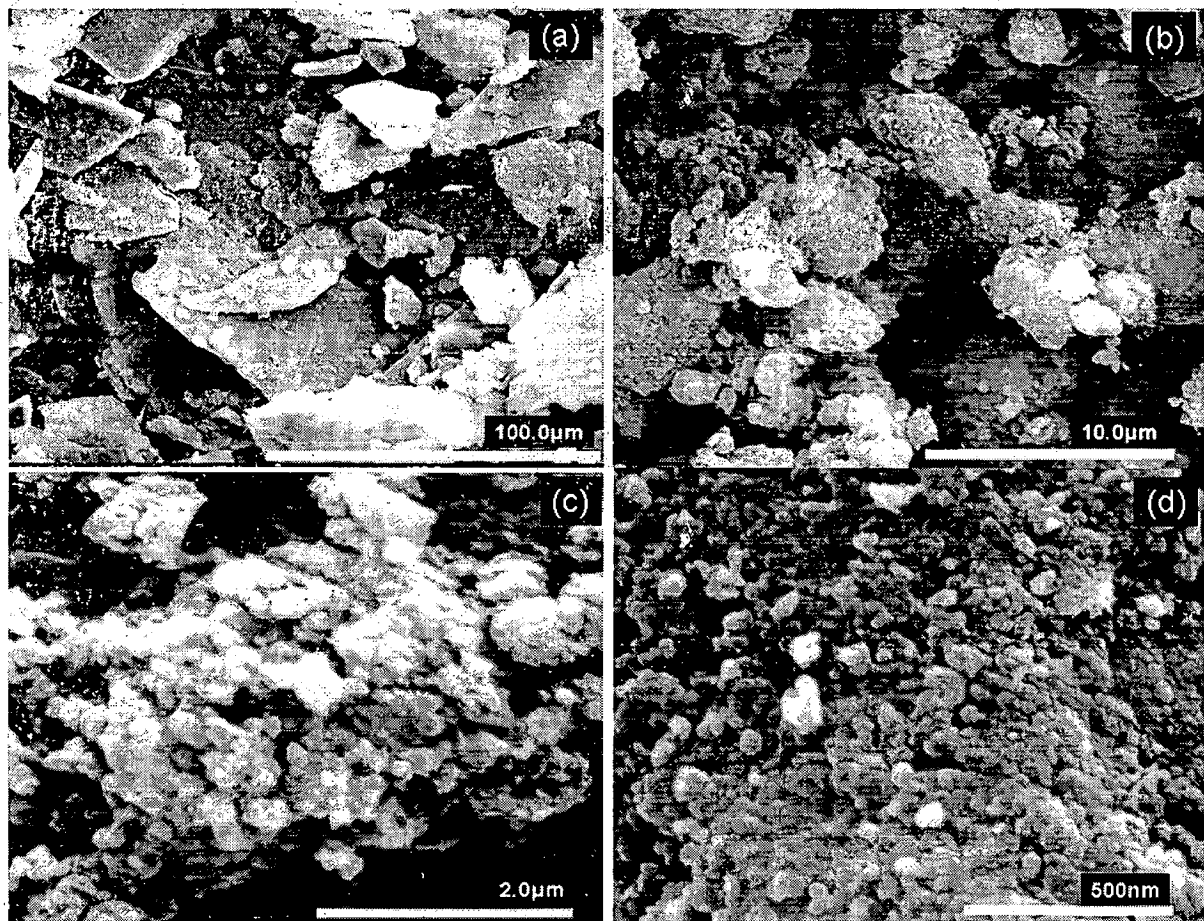
Fig. 7.4: FESEM micrographs of SiC powder, a) as received and milled at 300 rpm for, b) 10h, c) 30h, and d) 50 hrs.
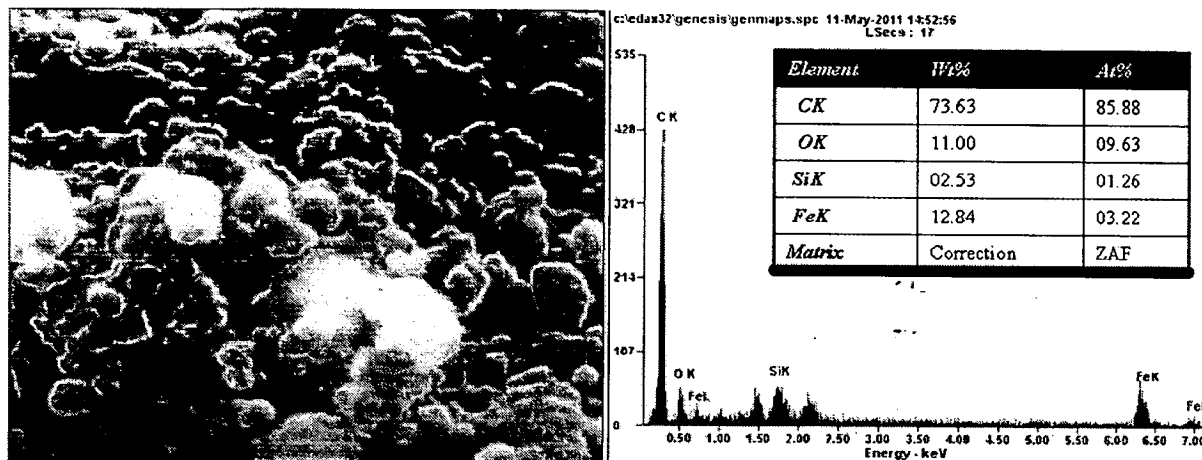
Fig. 7.5: FESEM micrograph with EDAX of SiC powder milled at 300rpm for 50hrs.
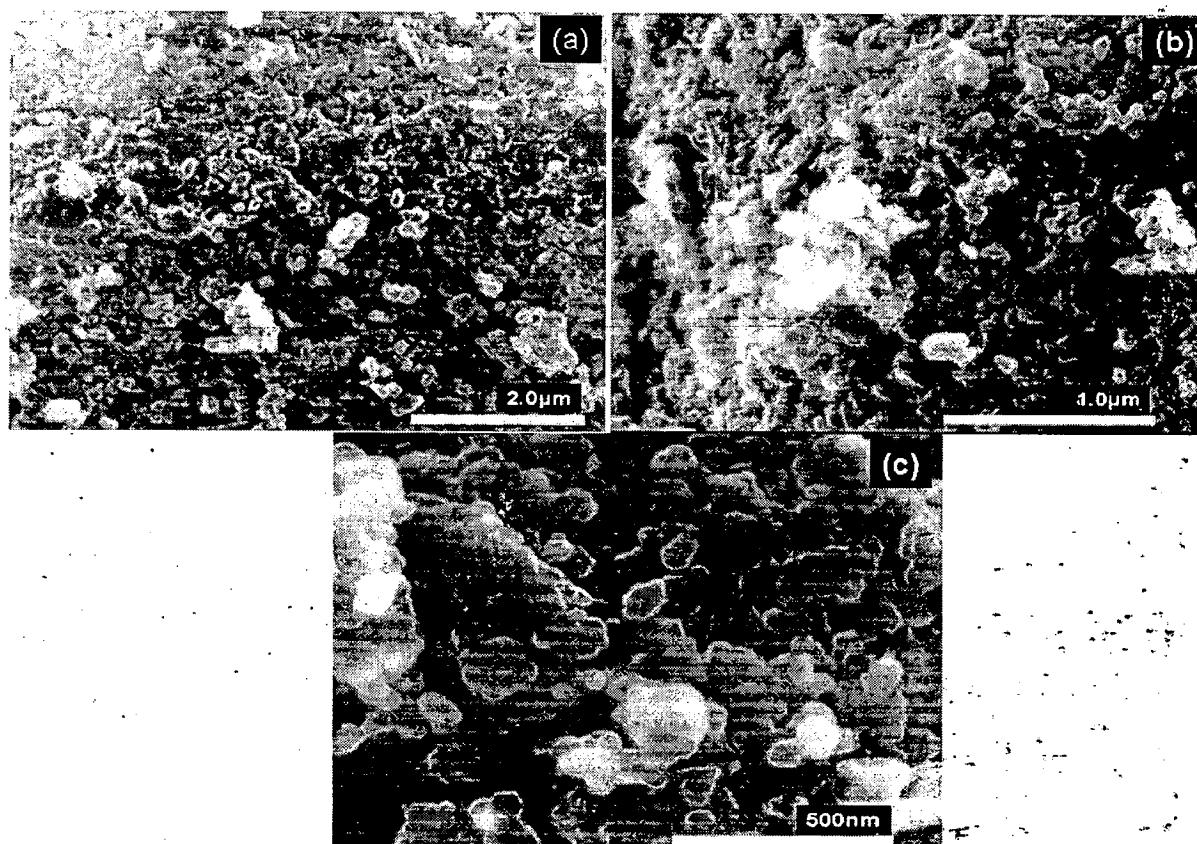
Fig. 7.6: FESEM micrographs showing the decrease in particle size as a function of milling time at 300 rpm for a) as received CB powder, and milled for b) 25h, and c) 50hrs.

Element	Wt%	At%
CK	100.00	100.00
Matrix	Correction	ZAF
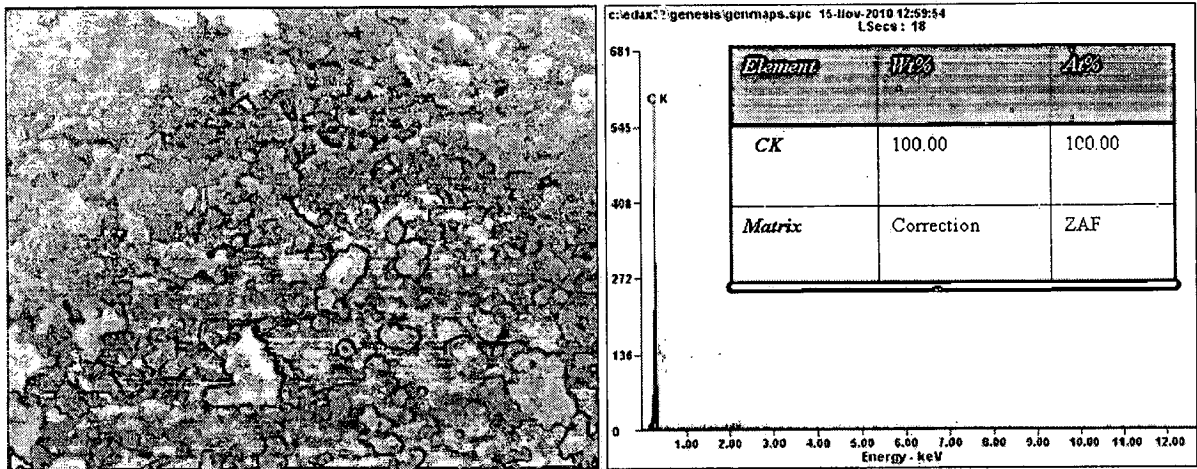
Fig. 7.7: FESEM micrograph with EDAX of CB powder milled at 300rpm for 50hrs.

The FESEM micrographs of EL Ni-P deposition on nano size strontium hexaferrite and barium hexaferrite powder are shown in Figures 7.8 and 7.10 respectively. The Ni-P coating on strontium and barium hexaferrite powder is confirmed through EDAX analysis and shown in Figure 7.9 and 7.11 respectively. The grown EL Ni-P nano globules are marked with arrows (Figures 7.8 and 7.10). The coated layer is uniform throughout the surface with some agglomeration at certain regions that shows the vertical growth. The Ni-P globules are uniformly coated on the nano size strontium hexaferrite (Figure 7.8) and barium hexaferrite powder (Figure 7.10). Figures 7.8 and 7.10 shows the 'as synthesis' Ni-P nanogloubles of 20-30nm size. According to previous study (Sharma, 2007; Sharma, 2008) and the literature available (Pan, 2007) barium and hexaferrite nanoparticles coated with Ni-P are found to be the potential nanocomposite for the RADAR/microwave absorption applications.
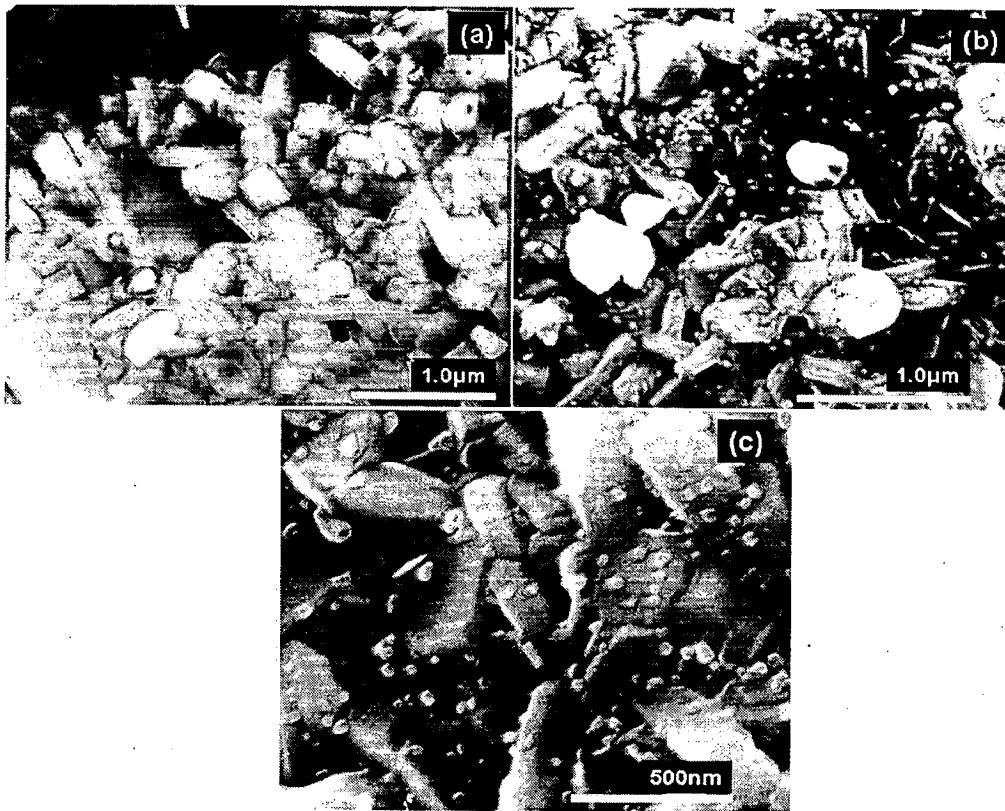
Fig. 7.8: FESEM micrographs of a) $SrFe_{12}O_{19}$ hexaferrite powder, b) coated $SrFe_{12}O_{19}$ (coating seen as layer of Ni-P globules) and c) magnified view of Ni-P coated $SrFe_{12}O_{19}$.

Element	Wt%	At%
OK	02.36	07.84
SrL	03.13	01.90
PK	00.37	00.63
FeK	92.60	88.23
NiK	01.54	01.40
Matrix	Correction	ZAF
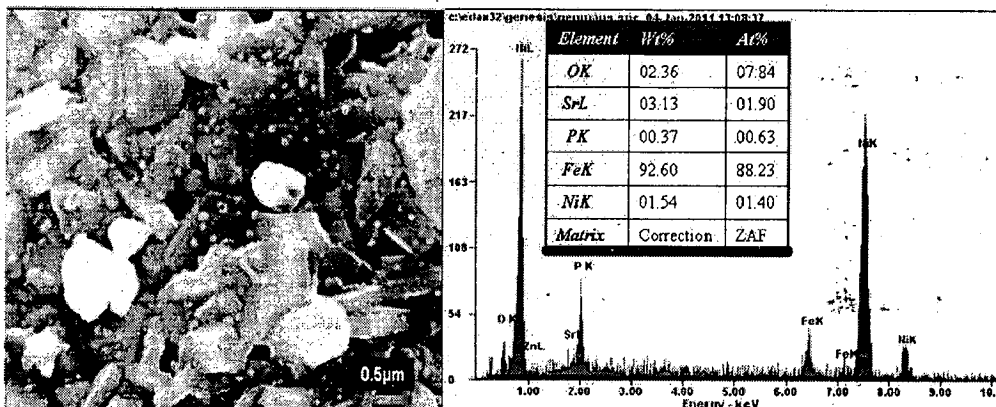
Fig. 7.9: FESEM micrograph with EDAX of nano powder of S1(Ni-P).

158
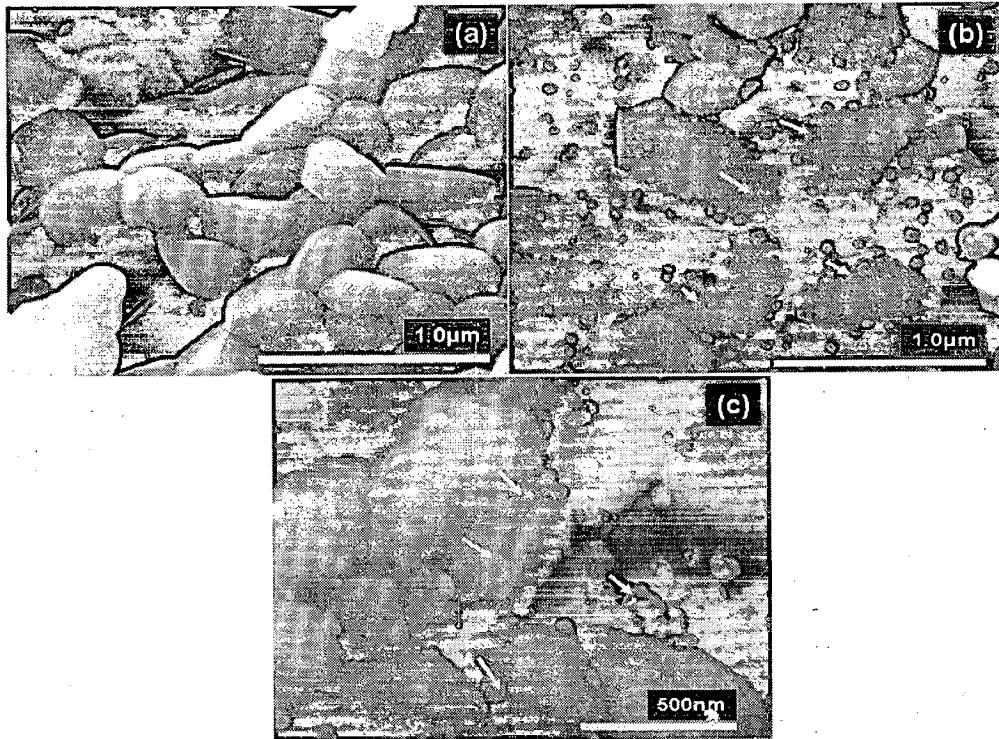
Fig. 7.10: FESEM micrographs of a) $SrFe_{12}O_{19}$ hexaferrite powder, b) coated $BaFe_{12}O_{19}$ (coating seen as layer of Ni-P globules) and c) magnified view of Ni-P coated $BaFe_{12}O_{19}$.

Element	Wt%	At%
OK	13.62	38.10
PK	01.16	01.68
BaL	16.88	05.50
FeK	66.86	53.59
NiK	01.48	01.13
Matrix	Correction	ZAF
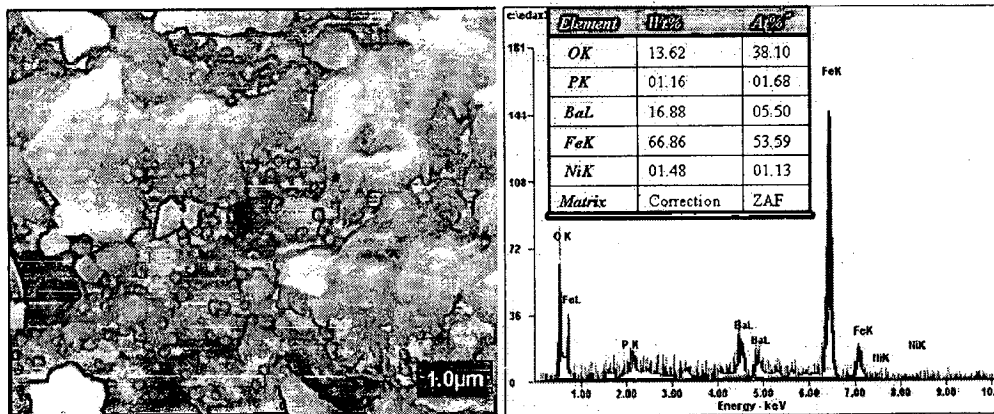
Fig. 7.11: FESEM micrograph with EDAX of nano powder of B1(Ni-P).

7.3.2 Phase Analysis Study

The indexed XRD patterns of the $SrFe_{12}O_{19}$ and $ZnFe_2O_4$ nanoparticles in 'as-synthesized' and heat treatment at 1200°C for 4h in the nitrogen atmosphere are shown in Figure 7.12a. From the results, it can be inferred that the hexaferrite powder in 'as-synthesized' condition was showing the peak only corresponding to impurity of NaCl (JCPDS Card No.5-637). When annealed at 1200°C, the peaks correspond to $SrFe_{12}O_{19}$, $2\Theta=34.386$, $d=2.616$ (JCPDS Card No. 24-1207) and $ZnFe_2O_4$, $2\Theta=35.775$, $d=2.522$ (JCPDS Card No. 02-1043) are observed. This indicates that in 'as-synthesized' condition the XRD broadening ($2\Theta=35.736$) is due to the mixture of amorphous nanoparticles of $SrFe_{12}O_{19}$, and $ZnFe_2O_4$ which needs post calcinations for crystallization. As expected, the degree of crystallinity and amount of $SrFe_{12}O_{19}$ and $ZnFe_2O_4$ nanoparticles were further increased by increasing the heat treatment temperature up to 1200°C. The XRD pattern of CNTs ((JCPDS 01-0640) synthesized by the catalytic decomposition of acetylene gas in the temperature range of 750-800°C is shown in Figure 7.12b. The interlayer spacing (d=002) is found to be 3.40Å are slightly higher than (3.35Å) for pure graphite (JCPDS Card No. 01-0640). The increase in d spacing is perhaps due to the influence of the nature of Fe catalyst used in the present study. The sharpness of the (d=002) interlayer-stacking peak of graphite is a measure of the extent of graphitization, indicating that CNTs synthesized at 800°C are graphitizing in nature. Figures 7.12c and 7.12 d show the indexed XRD pattern of the CB (JCPDS Card No. 03-0401) and SiC (JCPDS Card No. 01-1118) powder obtained after mechanical alloying for the period of 50hrs. In case of SiC, like EDAX no peak corresponding to Fe is observed. This may be due to the lesser weight percentage of iron present in the SiC powder.

Raman spectroscopy (Figure 7.13) gives two main signals from carbon nano tubes, the D peak at around 1300cm^{-1}, which is associated with defect and disorder, and G peak at 1599 cm^{-1}, corresponding to the signal from crystalline graphite. This study in addition with XRD confirmed the synthesis of carbon nanotubes.
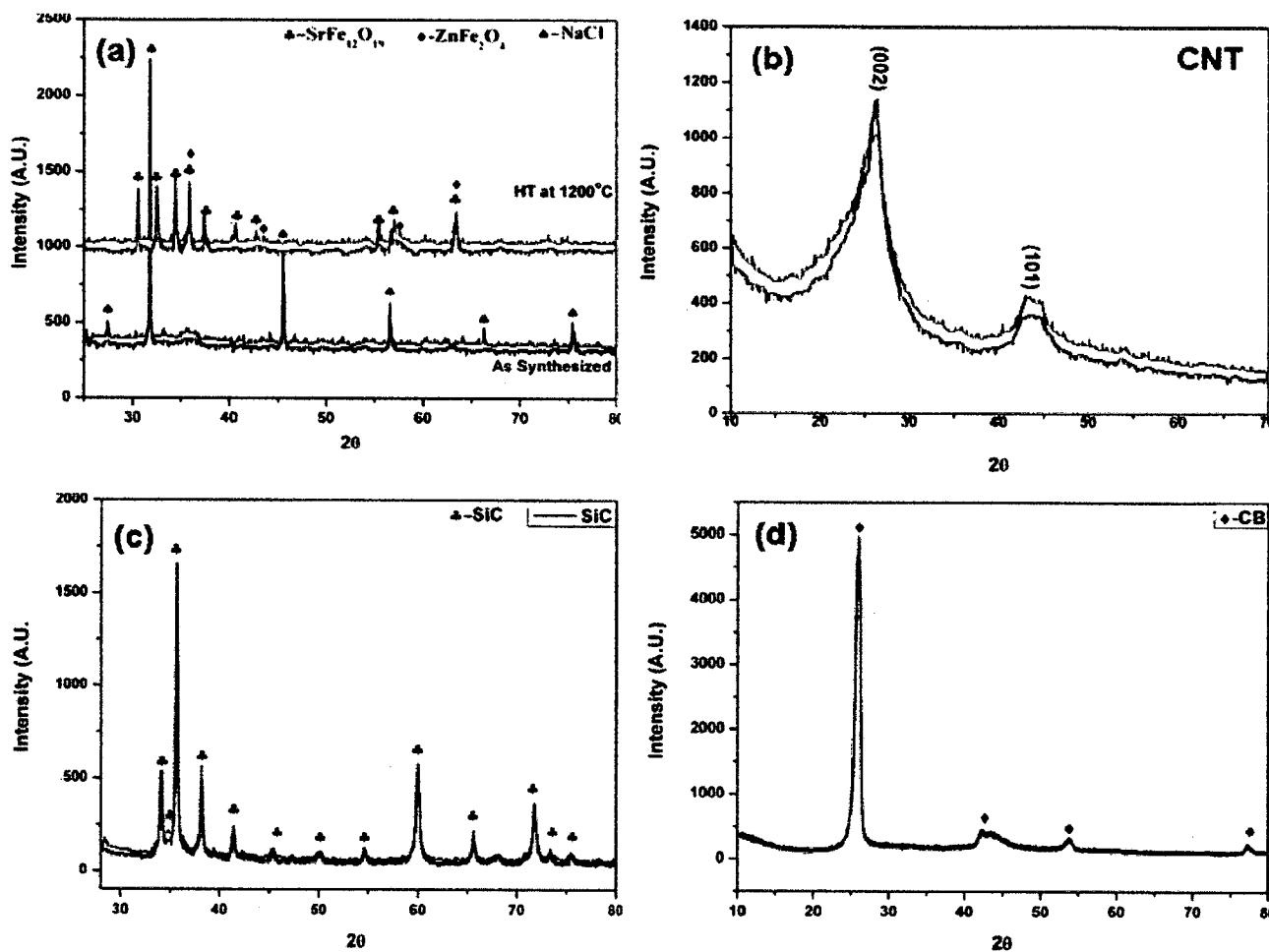
Fig. 7.12: The XRD patterns of different magnetic and non magnetic materials used to fabricate the composites for the present study.
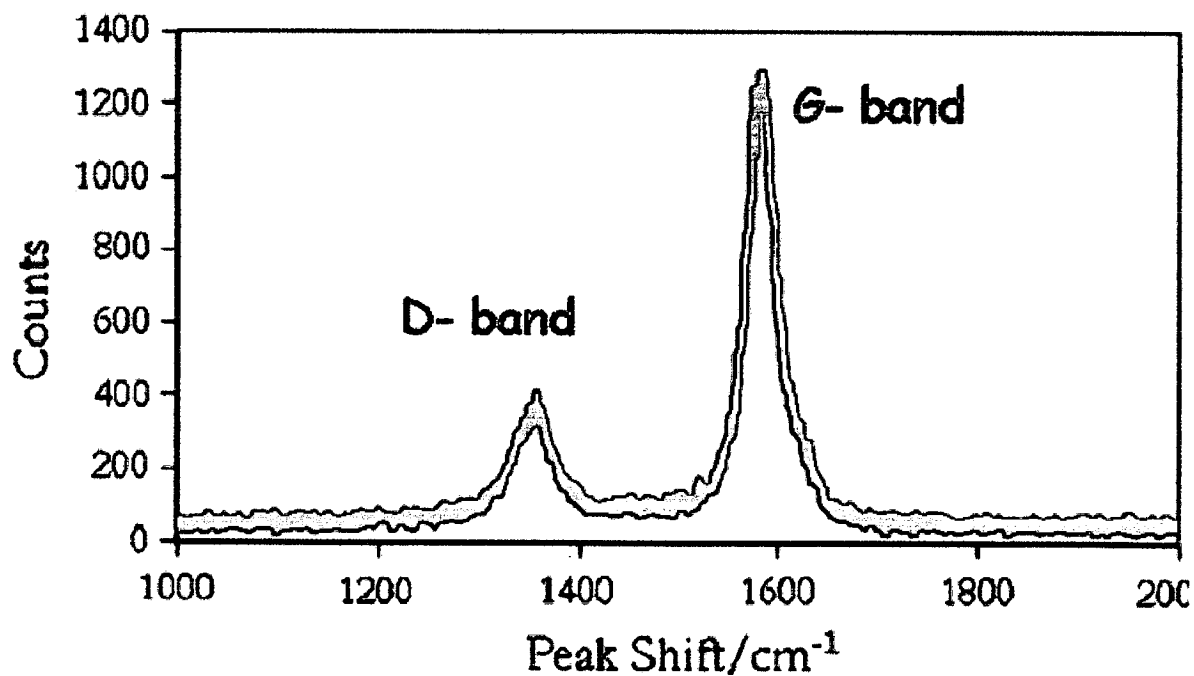
Fig. 7.13: Raman spectrum of 'as synthesized' nanotubes.

161

7.3.3 Magnetic Study

Figures 7.14 (a-d) shows the hysteresis loops of the magnetic (sample SZ) and non magnetic phases (CNTs, SiC and CB) respectively used to fabricate the composite for the present study. The hysteresis loop of magnetic phases (sample SZ) show the typical ferromagnetic behavior (Figure 7.14a) of ferrite with high magnetic parameters like saturation magnetization (61.227emu/gm) and coercivity (1373 Gauss). The hysteresis loop measurement of CNTs, SiC and CB confirm their non magnetic behaviour with negligible coercivity and low saturation magnetization values (Figure 7.14). The highest saturation magnetization for CNTs and CB are observed to be 0.358 and 0.711emu/gm. Similar behavior is observed for hysteresis loop carried out for SiC. It is also observed to be paramagnetic in nature with negligible coercivity and low saturation magnetization (0.585emu/gm). It is reported in literature and also observed in the present study that CNTs and CB are paramagnetic materials which on mixing with magnetic material like spinel ferrite and hexaferrite (Che, 2006) may attain different magnetic properties and improve the microwave absorption property of composite.
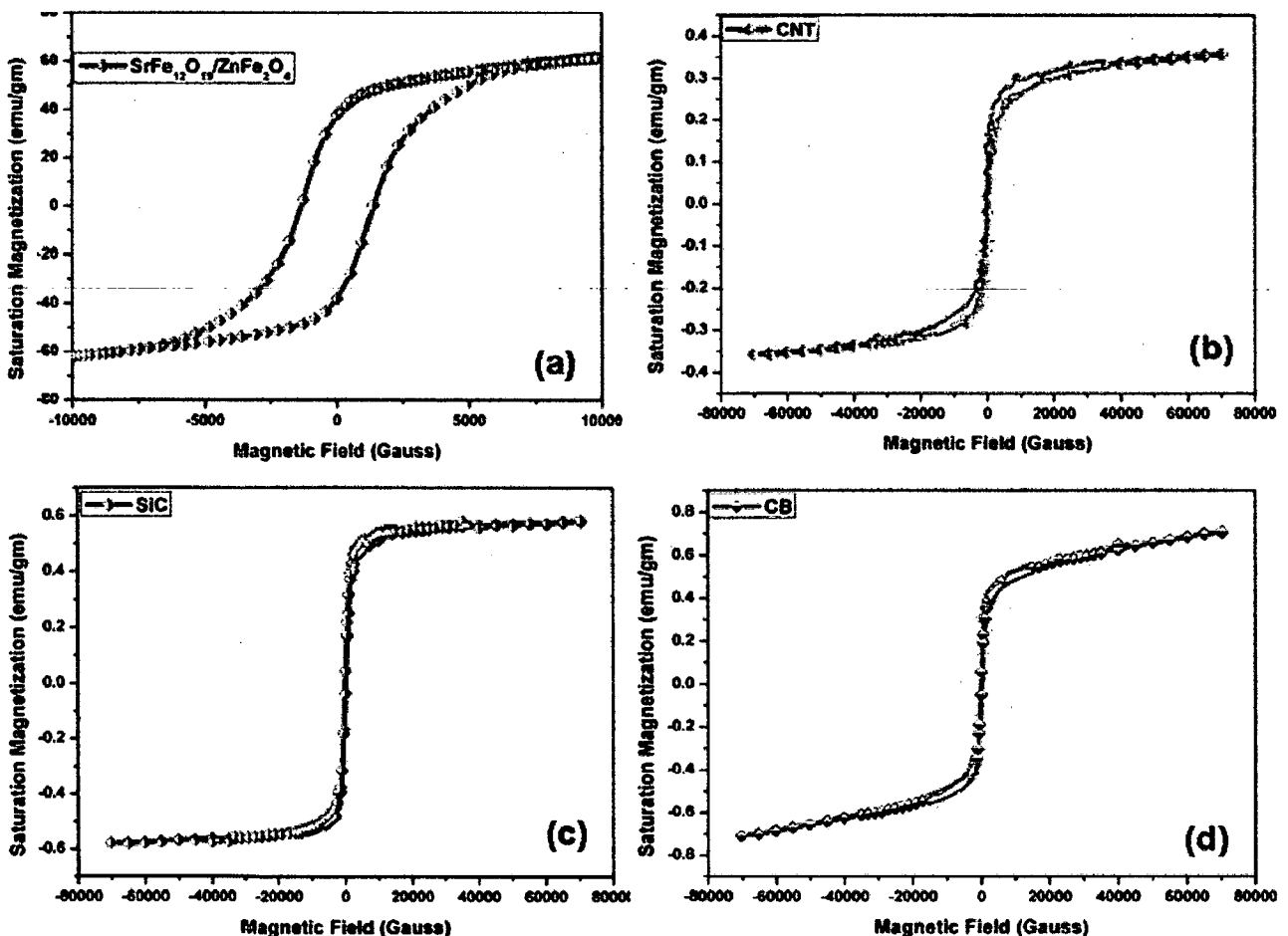
Fig. 7.14: The hysteresis loops of nanoparticles used to fabricate the composites of magnetic and non magnetic phases.

7.3.4 Dielectric Study

The real and imaginary parts of complex permitivity (Figures 7.15a- 7.15b) and permeability (Figures 7.16a-7.16b) of SZ/CNT/EP composite are plotted as a function of frequency in X-band (8-12GHz). Both real and imaginary parts of permitivity of SZ ferrite is observed to increase continuously with increase in wt% of CNTs. The real part of permitivity of SZ ferrite increases from 12.062 (average value) to 17.723 (average value) for composite containing 20 wt % of CNTs, 60 wt % SZ ferrite and 20 wt % EP (Figure 7.15 a). The similar trend is observed for the imaginary part of permitivity. The maximum imaginary permitivity of 8.913 (average value) is observed for composite containing 20 wt% of CNTs, 60 wt% SZ ferrite and 20 wt % EP (Figure 7.15b). The increase in real and imaginary parts of permitivity of composite with increase in wt% of CNTs may be due to the high value of complex permitivity (real and imaginary both) of CNTs which is also measured for pure CNTs (Figures 7.15a- 7.15b). Real part of permeability of SZ/CNT/EP composite is observed to decreases with increase in amount of CNTs (wt %) in the composite. It decreases from 1.294 (average value) for the SZ ferrite to 1.248 (average value) for the composite containing 20 wt % of CNTs, 60 wt % SZ ferrite and 20 wt % EP (Figure 7.16a). The same trend is observed for the imaginary part of permeability. The maximum imaginary permeability of 1.251 (average value) is observed for composite containing 10 wt % of CNTs, 70 wt % ferrite and 20 wt % EP (Figure 7.16b). The decrease in real and imaginary part of permeability of composite with increase in wt% of CNTs might be due to the low value of complex permeability (real and imaginary both) of CNTs which is also measured for pure CNTs (Figures 7.16a-7.16b). The frequency dependence of real and imaginary part of permitivity (Figures 7.17 a-7.17b) and permeability (Figures 7.18a-7.18b) of SZ ferrite as a function of addition of SiC are also plotted here for X band. Both real and imaginary parts of permitivity of SZ ferrite are observed to increase with increase in wt % of SiC. The real part of permitivity attain maximum permitivity of 13.72 (average value) for the composite containing 20 wt % SZ ferrite, 60 wt % SiC and 20wt % EP (Figure 7.17a). Similar trend is observed for the imaginary part of permitivity. The maximum imaginary permitivity of 11.061 (average value) is observed for SZ/SiC/EP composite containing 20 wt % SZ ferrite, 60 wt % SiC and 20wt % EP (Figure 7.17b). The increment in real and imaginary part of permitivity of SZ ferrite with addition of SiC might be due to the higher dielectric values of SiC as compared to ferrite which are also plotted here for comparison (Figures 7.17 a-7.17b). Like SZ/CNT/EP composite, the real and imaginary parts of permeability for

163

SZ/SiC/EP composite are also observed to decrease with increase in wt% of SiC. The minimum value of real and imaginary part permeability are observed to be 1.024 (average value) and 0.047 (average value) respectively for the composite containing 20 wt % SZ ferrite, 60 wt % SiC and 20wt % EP (Figures 7.18a-7.18b).
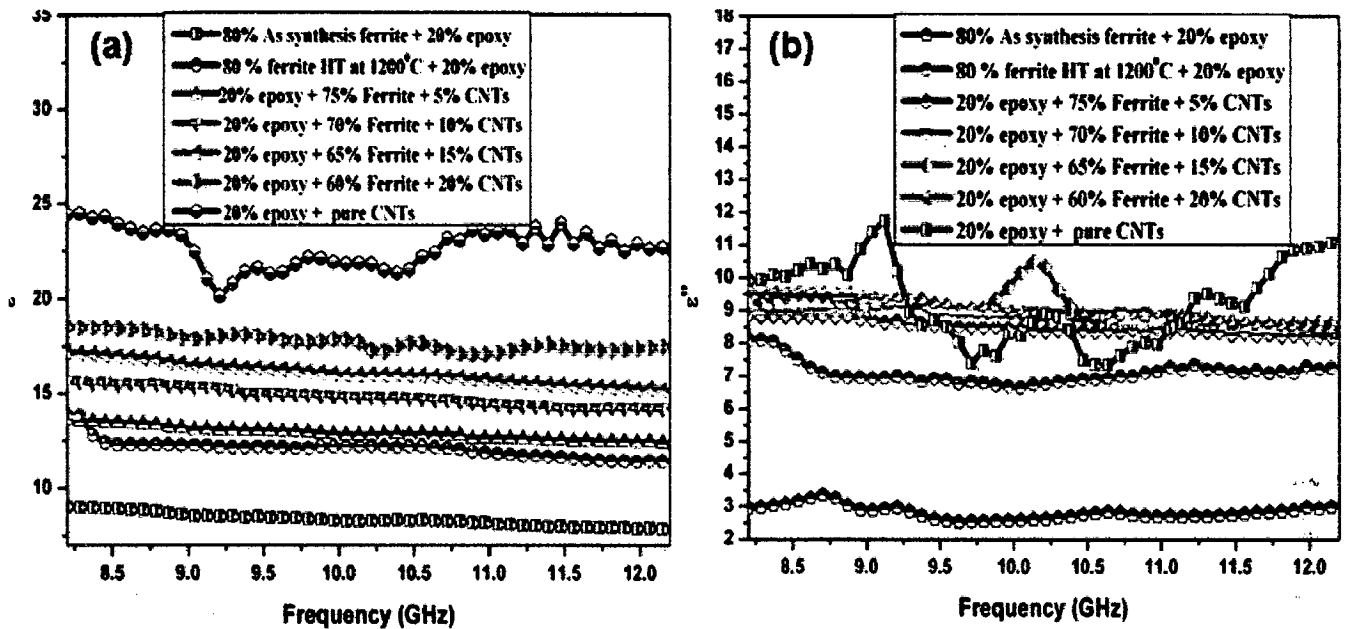
Fig. 7.15: The effect of addition of CNTs on real (ε') and imaginary (ε") part of permitivity of sample SZ.
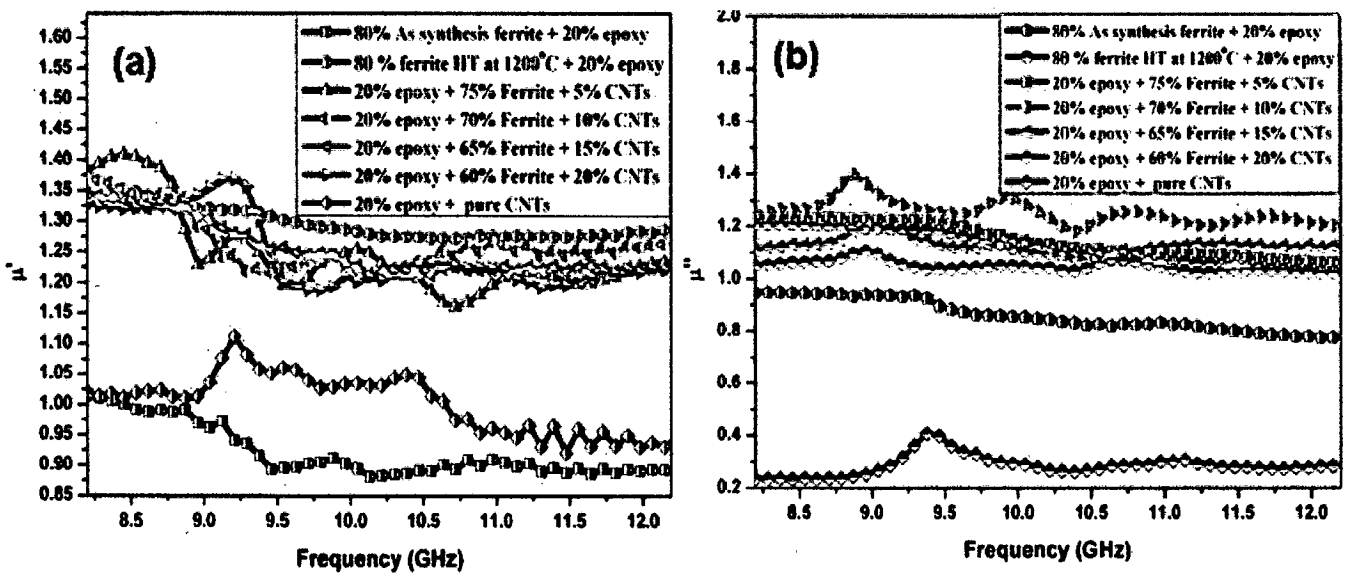
Fig.7.16: The effect of addition of CNTs on real (μ') and imaginary (μ") part of permeability of sample SZ.
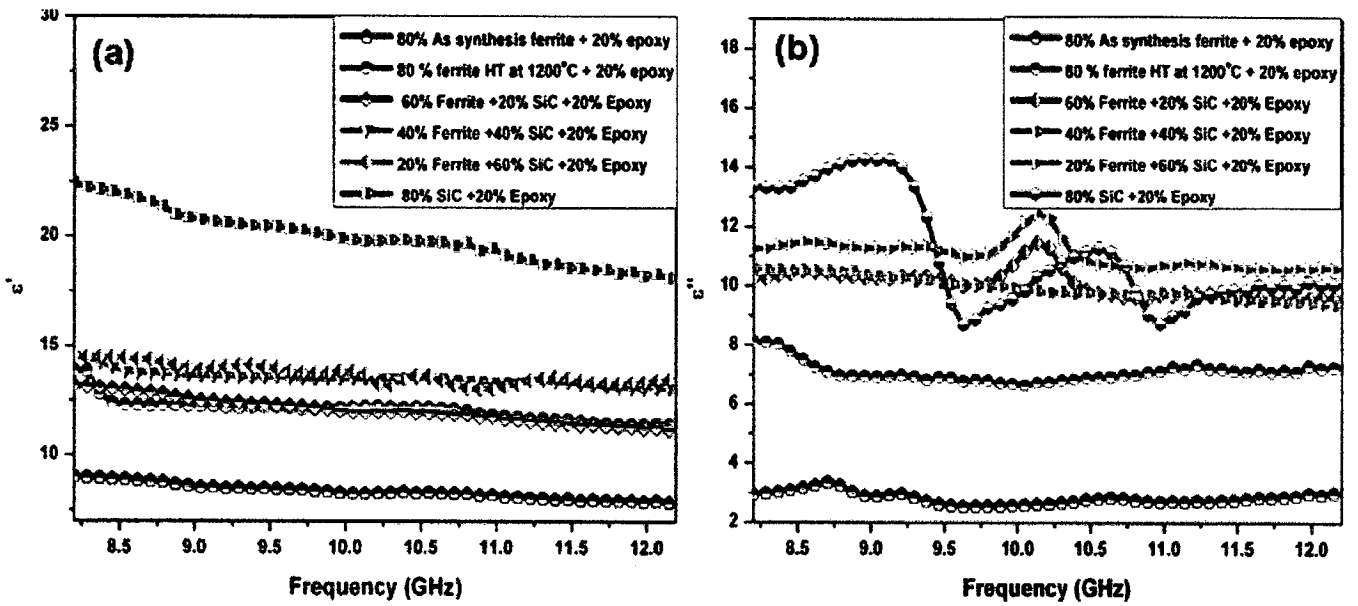
Fig. 7.17: The effect of addition of SiC on real (ε') and imaginary (ε") part of permitivity of sample SZ.
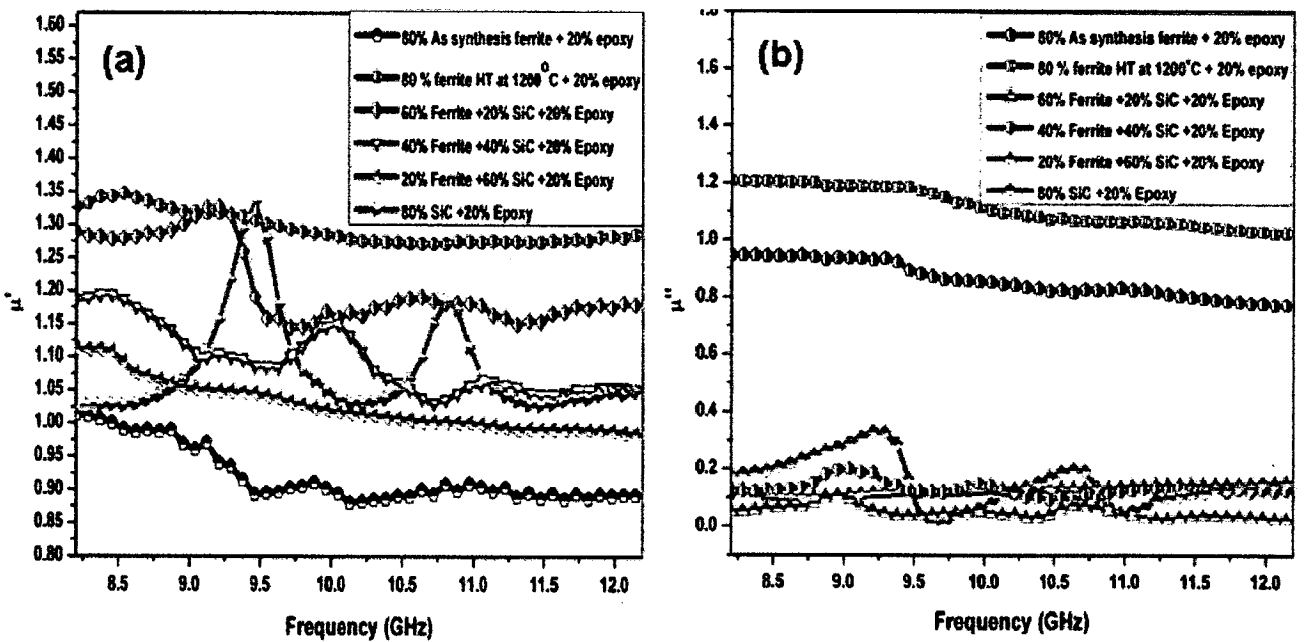
Fig. 7.18: The effect of addition of SiC on real (μ') and imaginary (μ") part of permeability of sample SZ.

For comparative study, real and imaginary parts of complex permitivity (Figures 7.19a- 7.19b) and permeability (Figures 7.20a-7.20b) of composite containing barium hexaferrite and SiC (B1/SiC/EP) are also plotted as a function of frequency in X-band. Both real and imaginary parts of permitivity of B1 ferrite are also observed to increase continuously with increase in wt% of SiC. The real part of permitivity of B1 ferrite increases from 14.449 (average value) to 19.070 (average value) for the composite containing 20 wt % B1 ferrite, 60 wt % SiC and 20wt % EP (Figure 7.19a). The similar trend is observed for the imaginary part of permittivity. The maximum imaginary permitivity of 8.061 (average value) is observed for composite containing 20 wt % B1 ferrite, 60 wt % SiC and 20wt % EP (Figure 7.19b). The increase in real and imaginary part of permitivity of composite with increase in wt% of SiC may be due to the high value of complex permitivity (real and imaginary both) of SiC which is also measured for pure SiC (Figures 7.19a-7.19b). Also, the real part of permeability of B1/SiC/EP decreases with increase in amount of SiC (wt %). It decreases from 1.192 (average value) for the B1 ferrite to 1.127 (average value) for the composite containing 20 wt % B1 ferrite, 60 wt % SiC and 20wt % EP (Figure 7.20a). The same trend is observed for the imaginary part of permeability. The maximum imaginary permeability of 1.994 (average value) is observed for composite containing 60 wt % B1 ferrite, 20 wt % SiC and 20wt % EP (Figure 7.20 b). The decrease in real and imaginary parts of permeability of B1/SiC/EP composite with increase in wt% of SiC might be due to the low value of complex permeability (real and imaginary both) of SiC which is also measured for pure SiC (Figures 7.20a-7.20b).
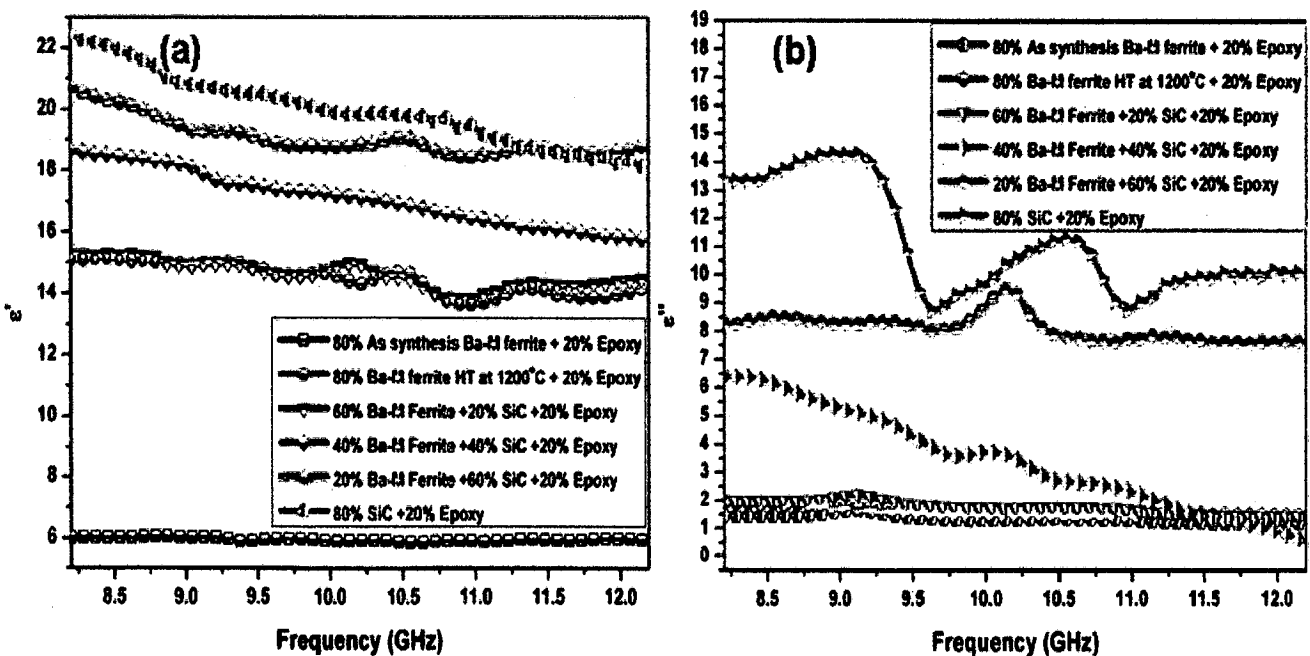
Fig. 7.19: The effect of addition of SiC on real (ε') and imaginary (ε'') part of permitivity of sample B1.
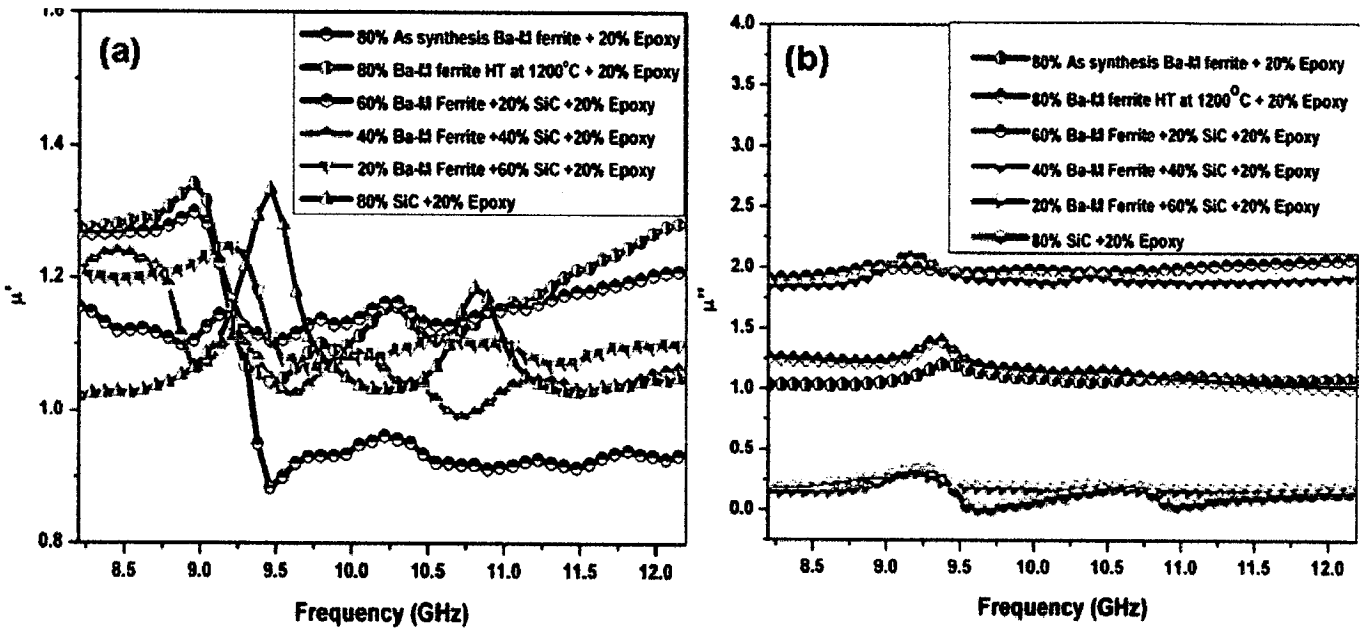
Fig. 7.20: The effect of addition of SiC on real (μ') and imaginary (μ") part of permeability of sample B1.
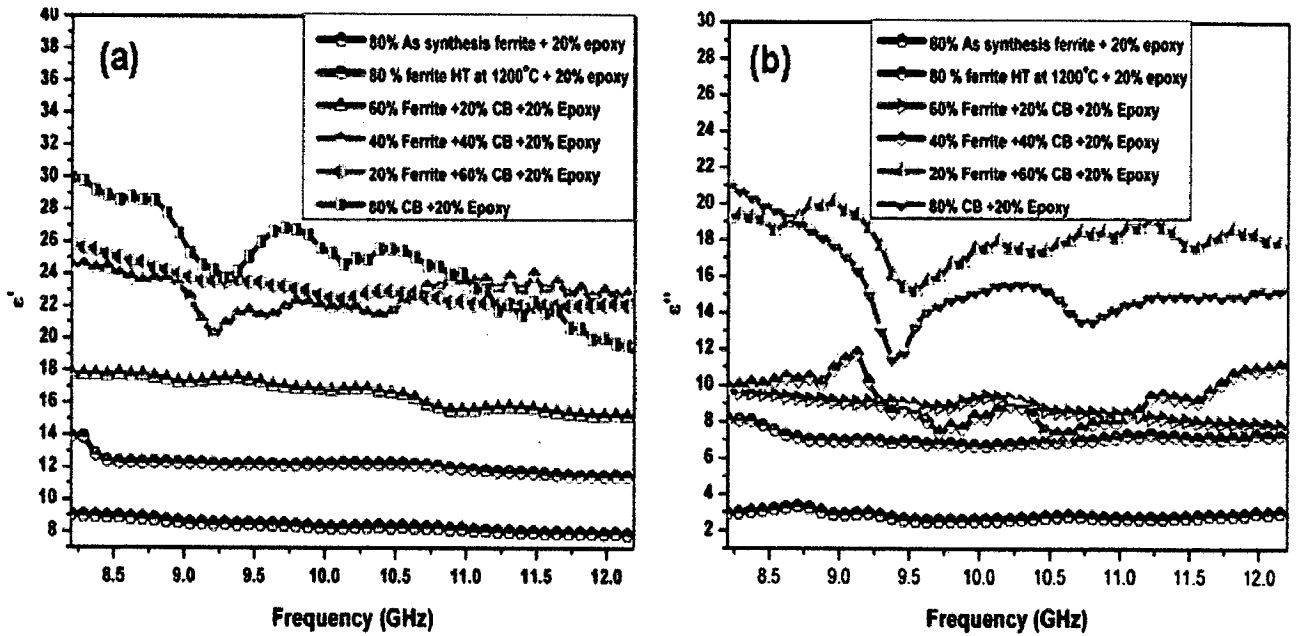
Fig. 7.21: The effect of addition of CB on real (ε') and imaginary (ε") part of permitivity of sample SZ.
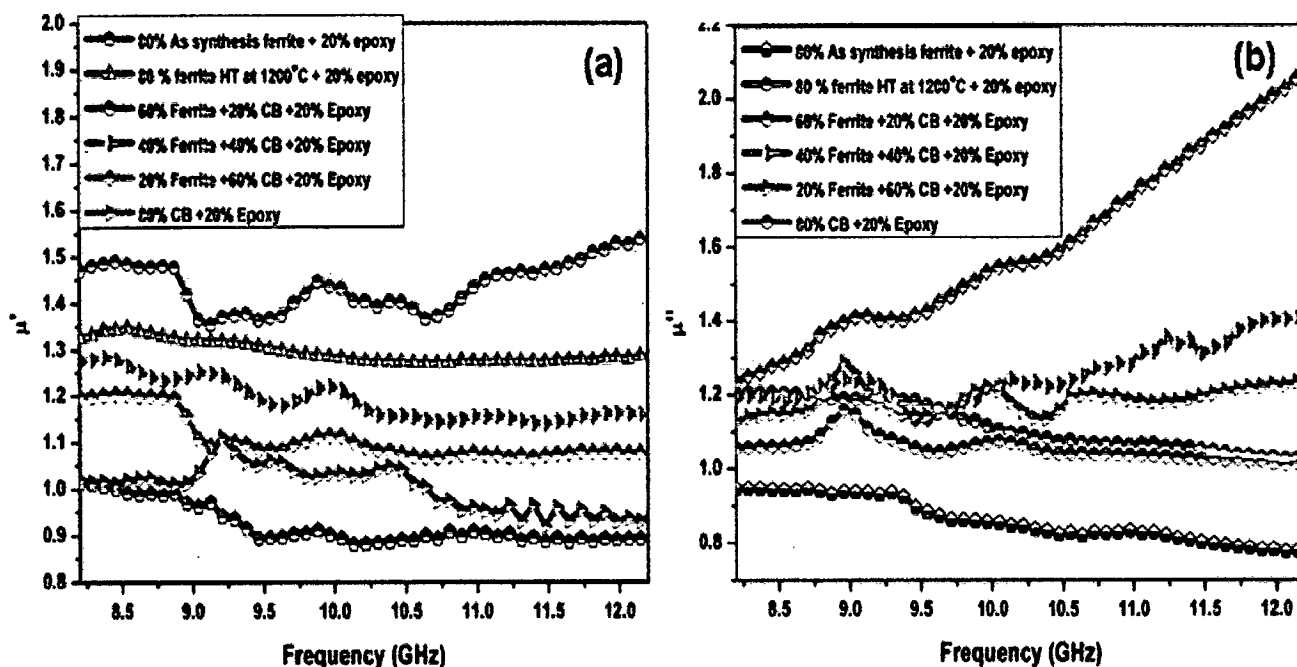
Fig. 7.22: The effect of addition of CB on real (μ') and imaginary (μ") part of permeability of sample SZ.

The frequency dependence of real and imaginary parts of permitivity (Figures 7.21 a-7.21b) and permeability (Figures 7.22a-7.22b) of SZ ferrite as a function of addition of CB are also presented here for X band. Both real and imaginary parts of prmitivity of SZ ferrite is observed to increase with increase in wt % of CB. The real part of permitivity attain maximum value of 23.069 (average value) for the composite containing 20 wt % SZ ferrite, 60 wt % CB and 20wt % EP (Figure 7.21a). Similar trend is observed for the imaginary part of permitivity. The maximum imaginary permitivity of 18.053 (average value) is observed for composite containing 20 wt % SZ ferrite, 60 wt % CB and 20wt % EP (Figure 7.21b). Like SZ/SiC/EP composite, the real and imaginary part of permeability for SZ/CB/EP composite is also observed to decrease with increase in wt% of CB. The minimum value of real and imaginary parts of permeability are observed to be 1.105 (average value) and 1.189 (average value) respectively for the composite containing 20 wt % SZ ferrite, 60 wt % CB and 20wt % EP (Figure 7.22a-7.22b).

The real and imaginary parts of complex permittivity (Figures 7.23a-7.23b) and permeability (Figures 7.24a-7.24b) of Ni-P coated strontium and barium hexaferrite nanoparticles are plotted as a function of frequency in X-band (8-12GHz). Both real and imaginary parts of permitivity of barium and strontium hexaferrite nanoparticles are

observed to increase after coating with Ni-P. The real part of permitivity of strontium hexaferrite increases from 11.341 (average value) to 12.643 (average value). Similarly the real part of permitivity of barium hexaferrite increases from 14.449 (average value) to 15.162 (average value). The similar trend is observed for the imaginary part of permittivity. The maximum imaginary permitivity of 7.202 (average value) is observed for Ni-P coated strontium hexaferrite ferrite and 8.275 for Ni-P coated barium hexaferrite. Real parts of permeability of strontium and barium hexaferrite are also observed to increase after coating with Ni-P. It increases from 1.422 (average value) to 1.460 (average value) for strontium hexaferrite and 1.207 to 1.160 for barium hexaferrite nanoparticles. The maximum imaginary permeability of 3.110 for strontium hexaferrite and 3.420 for barium hexaferrite (average value) are observed after coating with Ni-P.
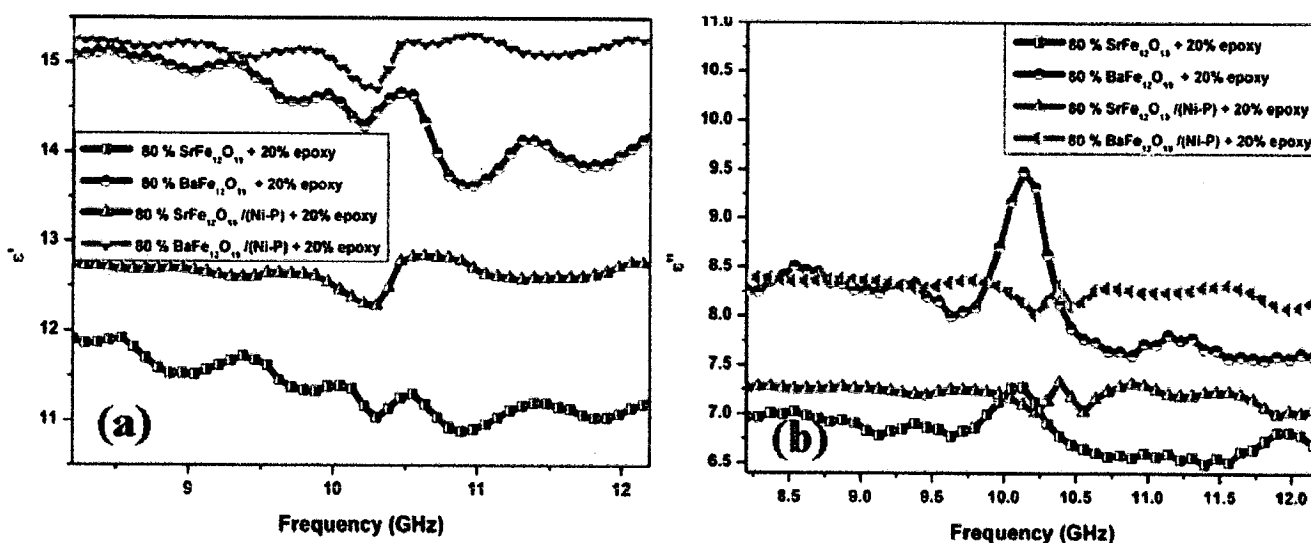
Fig. 7.23: The real (ε') and imaginary (ε'') part of permitivity of uncoated and coated nanoparticles of $SrFe_{12}O_{19}$ and $BaFe_{12}O_{19}$ nanoparticles.
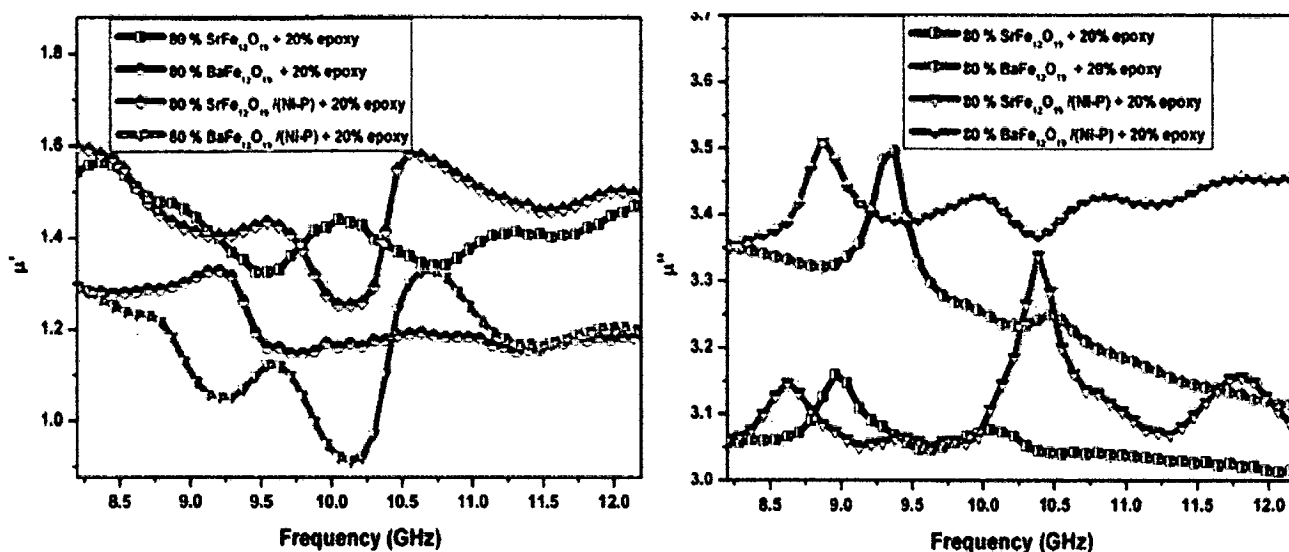
Fig. 7.24: The real (μ') and imaginary (μ'') part of permeability of uncoated and coated nanoparticles of $SrFe_{12}O_{19}$ and $BaFe_{12}O_{19}$ nanoparticles.

7.3.5 Reflection Loss

The relation ship between microwave frequency and reflection loss was measured at 8.2-12.2 GHz range for SZ/CNT/EP composite, ferrite nanoparticles and pure CNTs (Figure 7.25). The reflection loss of pure CNT and ferrite nanoparticles is rather low for all frequencies between 8.2-12.2 GHz and peak values are -14.15dB at 10.72GHz and -29.82 dB at 10.38 GHz respectively. The higher value of reflection loss for pure ferrite is due the exchange interaction existing between hard ($SrFe_{12}O_{19}$) and soft magnetic phases ($ZnFe_2O_4$) which has been explained in chapter 6. For SZ/CNT/EP composites, the microwave absorption evidently improved (higher than that of both pure CNT and ferrite nanoparticles). The maximum reflection loss values are first observed to increase and then decrease with increase in wt % of CNTs in the nanocomposites. The maximum reflection loss of -36.79 dB at 9.29 GHz is observed for the composite contain 70 wt% SZ ferrite, 10 wt% CNTs and 20 wt% EP. The improvement of microwave absorption obviously originates from the combination of CNTs and ferrite nanoparticles. Further analysis of enhancement mechanism is based on the electromagnetic theory and magnetization by hysteresis loop measurements. It is observed that (Che, 2006) microwave absorption would be improved when magnetic contribution matches with dielectric contribution. On the other hand static magnetic properties of SZ ferrite indicate

170

absorption of the composite with SiC and ferrite is suggested to originate from the efficient combination of SiC and ferrite powder. Usually, the excellent microwave absorption of composite material is considered to be related with efficient complementary between complex permitivity and permeability of the material. Mixing ferrite with SiC is an effective way to tailor the complex permitivity and permeability of the composite material and improve the EM wave absorption. In this work composite with 40 wt% ferrite, 40 wt% SiC and 20 wt% EP possess better cooperative interaction than others, resulting in highest microwave absorption.

Fig. 7.26: The effect of addition of SiC on reflection loss of sample SZ ferrite.

Table 7.3: Details of strongest reflection loss and the widest bandwidths (for RL > 10dB) of SZ/SiC/EP composite.

Composite SZ/SiC/EP	RL (dB) at 8.2 GHz	RL (dB) at 12.2 GHz	The widest bandwidth for RL>10dB (in GHz)	The strongest RL (dB)
80% As synthesis SZ+20% EP	-3.68	-4.73	2.18 (9.29-11.47)	-18.29 (10.38 GHz)
80% SZ (HT at 1200°C)+20% EP	-5.20	-5.25	2.77 (9.04-11.81)	-29.82 (10.38 GHz)
60% SZ (HT at 1200°C)+20%SiC+20% EP	-12.73	-8.88	3.69 (8.20-11.89)	-34.63 (10.21 GHz)
40% SZ (HT at 1200°C)+40%SiC+20% EP	-7.82	-8.88	2.94 (8.95-11.89)	-43.34 (10.30 GHz)
20% SZ (HT at 1200°C)+60%SiC+20% EP	-10.03	-6.48	3.10 (8.20-11.30)	-30.50 (9.79 GHz)
80% SiC+20% EP	-10.05	-6.22	0.42 (8.20-8.62)	-10.99 (9.71 GHz)

Fig. 7.27: The effect of addition of SiC on reflection loss of sample B1.

Table 7.4: Details of strongest reflection loss and the widest bandwidths (for RL > 10dB) of B1/SiC/EP composite

Composite B1/SiC/EP	RL (dB) at 8.2 GHz	RL (dB) at 12.2 GHz	The widest bandwidth for RL>10dB (in GHz)	The strongest RL (dB)
80% As synthesis B1 hexaferrite+20% EP	-3.85	-3.50	0.0	-6.77 (9.29 GHZ)
80% B1 (HT at 1200°C) +20% EP	-6.74	-6.85	2.19 (9.20-11.39)	-22.25 (10.04 GHz)
60% B1 (HT at 1200°C)+20%SiC+20% EP	-14.69	-5.17	2.77 (8.20-10.97)	-44.65 (9.20 GHz)
40% B1 (HT at 1200°C)+40%SiC+20% EP	-10.12	-4.18	2.60 (8.20-10.80)	-24.04 (9.12 GHz)
20% B1 (HT at 1200°C)+60%SiC+20% EP	-9.41	-4.43	2.19 (8.36-10.55)	-16.07 (8.87 GHz)
80% SiC+20% EP	-10.05	-6.22	0.42 (8.20-8.62)	-10.99 (9.71 GHz)

For comparison, the microwave absorption properties of composite comprising barium hexaferrite and SiC were also studied. Like SZ/SiC/EP composite, the san of variation in reflection loss with accession of SiC is observed for B1/SiC/EP cor The maximum reflection loss of -44.65 dB (Figure 7.27) is observed for the co; containing 60 wt% B1 ferrite, 20 wt% SiC and 20 wt% EP. The strongest reflect and widest band width (RL>-10dB) are given in Table 7.4. In both the cases, observed that composite containing ferrite (B1 or SZ) and SiC offer excellent mat complex permitivity and permeability data and result in higher reflection (RL>-40dB). Figure 7.28 shows the microwave absorption curve of SZ/Cb/ı composites, which reveals the influence of CB mass fraction on the reflection lo properties of SZ/CB/EP composite. Like other composite studied in the present wor peak of maximum reflection loss shifts to lower frequency. The maximum reflection loss peak initially increase then decrease with increase in mass fraction of CB. The composite containing 60 wt% SZ ferrite, 20 wt% CB and 20 wt% EP shows the maximum value of reflection loss (-34.87 dB at 9.04 GHz) than the other composite containing SZ ferrite and CB (Table 7.5). For comparison, the microwave absorption properties of pure CB and pure SZ ferrite are also plotted and shown in Figure 7.28. It showed that CB mixed with ferrite composite exhibits superior microwave absorption properties than pure CB and pure ferrite. Generally, excellent microwave absorption resulted from efficient

complements between relative permitivity and permeability of materials. Either only magnetic loss or only dielectric loss may induce a weak electromagnetic wave absorption property due to imbalance of electromagnetic match (Che, 2006, Che, 2004). For CB, only dielectric loss contributed to the energy loss of the EM wave, while for the ferrite powder, the effect of magnetic loss was dominate over the dielectric loss. It means that magnetic loss and dielectric loss were out of balance in both the cases, which resulted in poor electromagnetic wave absorption. The improved microwave absorption of SZ/CB/EP composite is originated from combination of diamagnetic CB and ferromagnetic SZ ferrite. The special geometry of the magnetic and non magnetic nanoparticles is the important factor for the above phenomena. It affects the electromagnetic properties through homogenously mixing in the matrix, reducing the magnetic coupling effect between nanoparticles (Liu, 2006; Che, 2006) and constructing the electromagnetic match between the nanosized geometry.
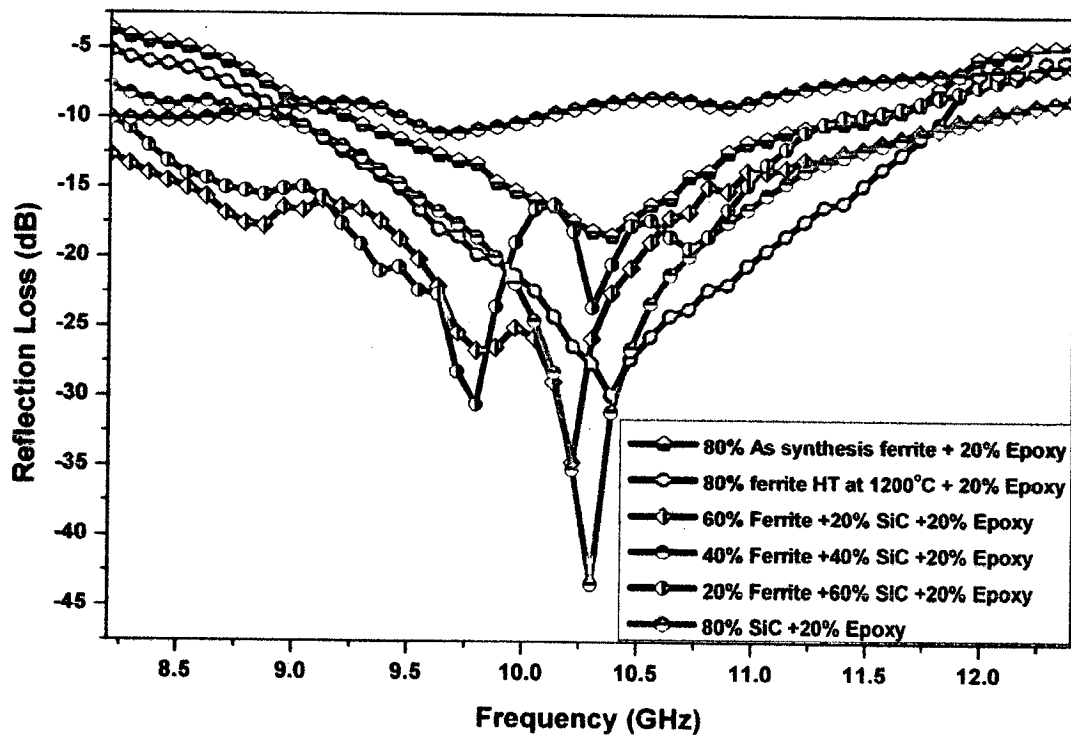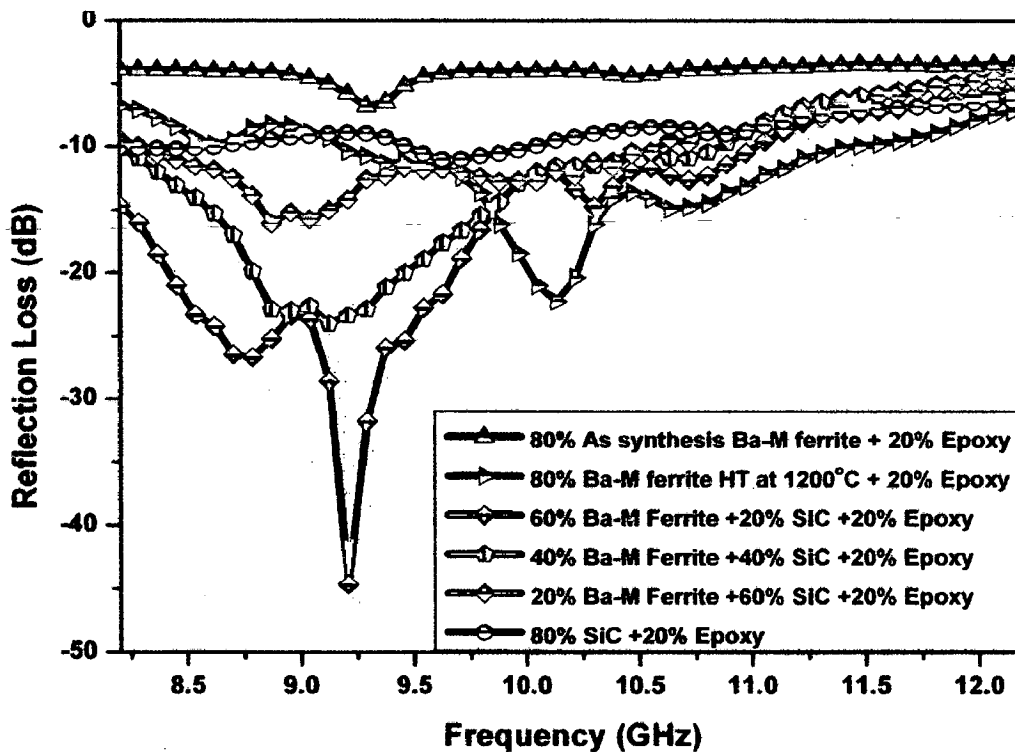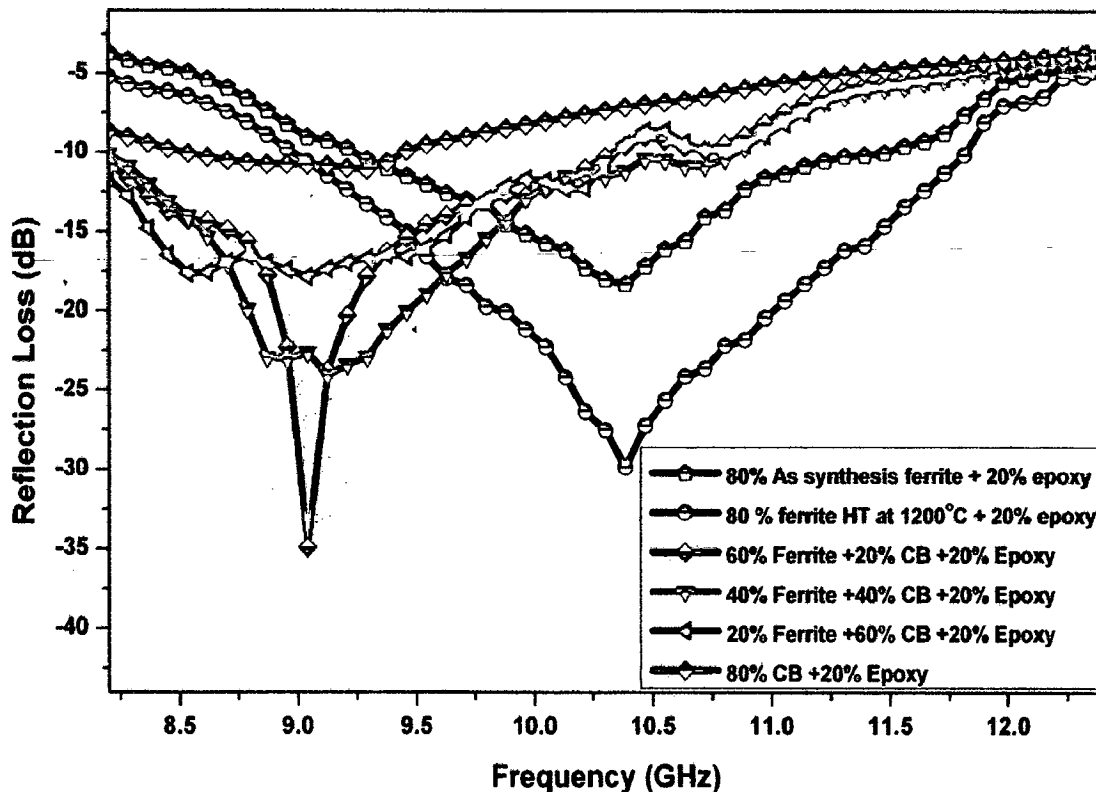

Fig. 7.28: The effect of addition of CB on reflection loss of sample SZ ferrite.

Table 7.5: Details of strongest reflection loss and the widest bandwidths (for RL > 10dB) of SZ/CB/EP composite.

Composite SZ/CB/EP	RL (dB) at 8.2 GHz	RL (dB) at 12.2 GHz	The widest bandwidth for RL>10dB (in GHz)	The strongest RL (dB)
80% As synthesis SZ+20% EP	-3.68	-4.73	2.18 (9.29-11.47)	-18.29 (10.38 GHz)
80% SZ (HT at 1200°C)+20% EP	-5.20	-5.25	2.77 (9.04-11.81)	-29.82 (10.38 GHz)
60% SZ (HT at 1200°C)+20% CB+20% EP	-10.73	-4.02	2.10 (8.20-10.30)	-34.87 (9.04 GHz)
40% SZ (HT at 1200°C)+40%CB+20% EP	-10.12	-4.18	2.60 (8.20-10.80)	-24.04 (9.12 GHz)
20% SZ (HT at 1200°C)+60%CB+20% EP	-11.65	-3.77	2.10 (8.20-10.30)	-17.57 (8.62 GHz)
80% CB +20% EP	-8.64	-3.84	0.84 (8.53-9.37)	-11.08 (9.29 GHz)

The plot showing the variation of reflection loss as a function of frequency for pure and Ni-P coated barium and strontium hexaferrite is shown in Figure 7.29. The maximum reflection loss of -23.12 dB at 10.46GHz is observed for pure strontium hexaferrite nanoparticles which further observed to decrease to -18.81 dB at 10.80 GHz after coating with Ni-P. Similarly the maximum reflection loss of -22.28 dB at 10.13 GHz is observed for pure barium hexaferrite which also further decrease to -18.43 dB at 9.62 GHz after coating with Ni-P. In case of barium hexaferrite, increment in bandwidth (RL>-10dB) is observed after coating with Ni-P (Table 7.6). The decrease reflection loss values of coated barium and strontium hexaferrite than uncoated barium and strontium hexaferrite might be due to the poor matching between relative permitivity and permeability of materials with frequency. Secondly lesser volume fraction of Ni-P globules than observed in previous study (Sharma, 2008; 2007) might be the other reason for the decrease in reflection loss of Ni-P coated barium and strontium hexaferrite nanoparticles.
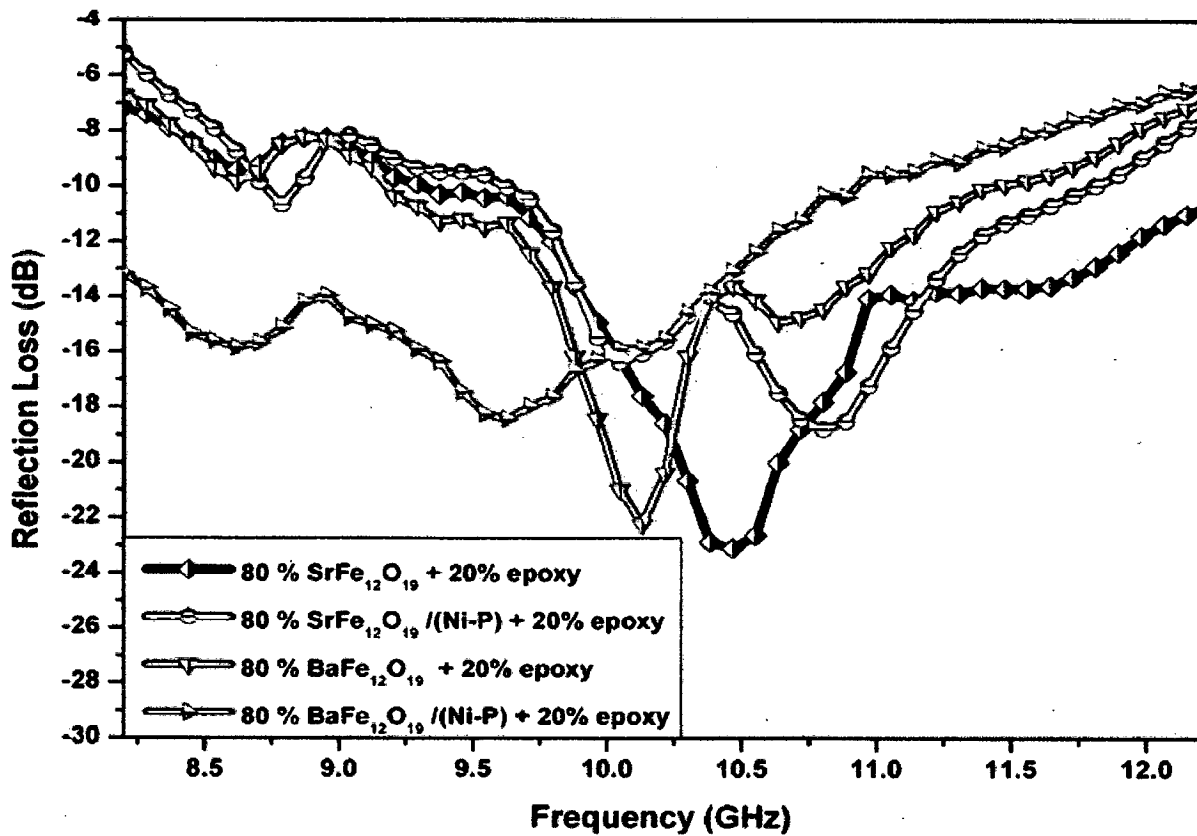
Fig. 7.29: The effect of Ni-P coating on reflection loss of $SrFe_{12}O_{19}$ and $BaFe_{12}O_{19}$ nanoparticles.

Table 7.6: Details of strongest reflection loss and the widest bandwidths (for RL > -10dB) of pure and Ni-P coated $SrFe_{12}O_{19}$ and $BaFe_{12}O_{19}$ nanoparticles.

Composite	RL (dB) at 8.2 GHz	RL (dB) at 12.2 GHz	The widest bandwidth for RL>10dB (in GHz)	The strongest RL (dB)
80% S1 + 20% EP	-7.17	-10.64	2.83 (9.37-12.20)	-23.12 (10.46 GHz)
80% S1/(Ni-P) + 20 % EP	-5.18	-7.48	2.10 (9.62-11.72)	-18.81 (10.80 GHz)
80 % B1 + 20 % EP	-6.74	-6.85	2.19 (9.20-11.39)	-22.28 (10.13 GHz)
80% B1/(Ni-P) + 20 % EP	-13.21	-6.24	2.68 (8.20-10.88)	-18.43 (9.62 GHz)

SUMMARY

All developed magnetic (sample SZ and B1) and non magnetic (CNTs, SiC and CB) constituents of composite have been characterized using instrumentation like XRD, FESEM, VSM, VNA. FESEM of the top view of the CNTs arrays grown over Fe-catalyst at higher magnification shows long and thin multiwalled carbon nano tubes with diameter in the range of 30-40nm. It is observed that SiC particle are shaped into irregular cubes with an average particle size ranging from 70-80nm. These small size particles are found to be severely aggregated and prone to multi-pore structure and possessing large surface area, leads to plenty of interfacial polarization to weaken the energy of EM waves. The magnetic measurement of CNTs, SiC and CB powder reveals the non magnetic nature of these powders which is confirmed by their negligible coercivity and lower saturation magnetization values. This reveals the fact that, for these materials, only dielectric loss contributes to the energy loss of electromagnetic wave while for ferrite material, the effect of magnetic loss such as eddy current loss and hysteresis loss become dominant over the dielectric loss. The dielectric measurements show the increase in complex permitivity of composite with increase in SiC, CB and CNT mass % in the composite. For comparison, the microwave absorption properties of pure non magnetic phase and pure SZ ferrite are also plotted. It shows that non magnetic phase mixed with ferrite composite exhibits superior microwave absorption properties than observed for pure non magnetic and pure ferrite material. Generally, excellent microwave absorption resulted from efficient complements between relative permitivity and permeability of materials. Either only magnetic loss or only dielectric loss may induce a weak electromagnetic wave absorption property due to imbalance of electromagnetic match. It means that magnetic loss and dielectric loss were out of balance in case of pure ferrite and pure non magnetic phases, which resulted in poor electromagnetic wave absorption. The improved microwave absorption of ferrite and non magnetic phase composite is originated from combination of non magnetic phases and ferromagnetic ferrite. In this work, composite of ferrite and SiC possess better cooperative interaction than others, resulting in better microwave absorption properties. The microwave absorption properties is observed to increase with increase in SiC content and reaches a maximum value of -43.34 dB at 10.30GHz for the composite containing 40 wt% SZ ferrite, 40 wt% SiC and 20 wt% EP and -44.65 dB for the composite containing 60 wt% B1 ferrite, 20 wt% SiC and 20 wt%

EP. It is observed that composite containing ferrite (barium, strontium and zinc) and SiC offer excellent match of complex permitivity and permeability data than the other magnetic and non magnetic composite and result in higher value reflection loss (>-40dB). Our findings indicate that ferrite/SiC/EP (ferrite=B1 or SZ) particles nanocomposite may be used as potential stealth material for RADAR/microwave absorption applications.

The present investigation on the "*Studies on Hexaferrite Based Nanocomposite for RADAR/Microwave Absorption Applications*" the following conclusions can be ascribed:

- 'As synthesis' magnetic RAM have been developed by modified flux and low combustion synthesis methods.

- Reaction kinetics studies of magnetic RAM composition of single phase (samples B1 and S1), binary phase (samples SC, SN and SZ) and ternary phase (samples SNZ, SCZ and SNC) have been carried out through non-isothermal differential scanning calorimetry method.

- The activation energy for the reaction resulting in the synthesis of strontium hexaferrite nanoparticles is found to be lesser than the activation energy of the reaction for the formation of barium hexaferrite nanoparticle.

- The value of Avrami parameter (n) for endothermic reaction is found to be in the range of 1.58 to 4.46 for various compositions. All the composition showed that 'as synthesis' nano particles obtained after co-precipitation reaction prefer to have multi dimensional growth during heat treatment.

- The particle synthesized by low combustion synthesized method are found to have only hexagonal shape with increased agglomeration and large particle size than co-precipitated particle in 'as synthesized' as well as in various heat treated conditions.

- The magnetic measurement of all the compositions synthesized by co participation method reveals the superparamagnetic behaviour in 'as synthesized' conditions. All the co-precipitated compositions are observed to transform from superparamagnetic to ferromagnetic behaviour during heat treatment at various heat treatment temperatures.

- The magnetic measurement of all proposed composite inferred that strontium hexaferrite nanoparticles are more magnetic than barium hexaferrite nanoparticles

- The synthesis of ferromagnetic based spinel ferrite ($NiFe_2O_4$ and $CoFe_2O_4$) along with strontium hexaferrite results in increase in saturation magnetization of hexaferrite and spinel ferrite magnetic composite than single phase strontium hexaferrite.

- The reflection loss measurement of reported composition inferred that strontium hexaferrite nanoparticles show almost similar value of reflection loss like barium hexaferrite nanoparticles with increased bandwidth.

- The formation of spinel ferrite along with strontium hexaferrite ferrite results in increase in microwave absorption than single phase strontium hexaferrite.

- The magnetic composite containing zinc spinel ferrite and strontium hexaferrite observed to show the maximum microwave absorption than all other reported magnetic composite.

- The addition of CNTs to SZ ferrite is observed to have highest bandwidth of 3.69 GHz for the composite containing 60% SZ (HT at 1200°C) ferrite, 20%CNT and 20% EP than other composites reported in the present study.

- The composite with SiC and SZ ferrite possess better cooperative interaction than others, resulting in highest microwave absorption. The microwave absorption properties increase with increase in SiC content and reaches a maximum value of - 43.34dB at 10.30GHz for the composite containing 40 wt% SZ ferrite, 40 wt% SiC and 20 wt% EP & -44.65 dB is observed for the composite containing 60 wt% B1 ferrite, 20 wt% SiC and 20 wt% EP.

- For Ni-P coated barium and strontium hexaferrite nanoparticles, the decrease in values of reflection loss with increased bandwidth (for Ni-P coated barium hexaferrite only) than pure barium and strontium hexaferrite is observed.

FUTURE SCOPE

Development of RADAR/microwave absorbing nanocomposite coating has opened the door for new opportunities to further improve the functionality of EM wave absorbers. There is still tremendous future scope for various applications, some are as follows.

- Out of the ultimate goals of any Research and Development work is a commercial field by transitioning a lab environment to production. This involves dealing with many other issues that are not necessarily considered in the lab experiment. A scaling-up issue is one of them.

- Other types of calcium and lead based hexaferrites can also be developed and their reflection loss properties cab be evaluated.

- Multilayer nanocomposite coatings of studied composites can be developed to enhance the reflection loss and bandwidth characteristics as compared to single layer composite.

- Effect of different types of frequency selective surfaces such as triangular shape and hexagonal shape on the performance of microwave absorber can also be studied.

- A fussy model can be made to get the more optimized process parameters that may help to develop best RL properties for a particular set of nanocomposite coating. Such model can be further used for other frequency bands for various applications.

- For defense application, RCS (radar cross section) measurement is still a great area of concern to understand, future RCS measurement of studied composite can be done.

===

PROGRAMME FOR CALCULATING REFLECTION LOSS FROM COMPLEX PERMITIVITY AND PERMEABILITY DATA USING MATLAB.

```
% Opens the file with write permission
fid = fopen('input.txt', 'w');
% Reads the contents back into an array
f = load('output.txt');



fprintf (fid, '%4s \t', 't=2.5' );
for j=1:51
e(j) = f(j,2) - 1i*f(j,3);
u(j) = f(j,4) - 1i*f(j,5);
r(j) = u(j)/e(j);
p(j) = u(j)*e(j);
% Calculates the reflection coefficient



k2 = sqrt(r)*tanh((1i*2*pi*f(j,1)*2.0*0.001 * sqrt(p(j)))/300000000);
R2(j) = 20*log10(abs((k2(j)-1)/(k2(j)+1)));
fprintf(fid, '%4f \t', R2(j) );
end


fclose(fid);
% plotting the results
plot(f(:,1),R2(:),'b','LineWidth',2)
hold on
h1 = xlabel('Frequency');
set(h1,'FontName','Helvetica','FontSize',14, 'FontWeight','bold');
```

```
h2 = ylabel('Reflection Coefficient');
set(h2,'FontName','Helvetica','FontSize',14, 'FontWeight','bold');
x1 = legend('2.0mm');
set(x1,'FontSize',14, 'FontWeight','bold');
hold on
```

REFERENCES

1. **Abbas** S.M., Chandra M., Verma A., Chatterjee R., Goel T.C., (2006), *Composites: Part A,* **Vol.**37, pp. 2148.

2. **Abraham** S., Pai B.C., Satyanarayana K.G., Vaidyan V.K, (1990), *J. Mater. Sci,* **Vol.** 25, pp. 2839.

3. **Abraham** S., Pai B.C., Satyanarayana K.G., Vaidyan V.K., (1992), J. *Mater. Sci* **Vol.** 27, pp. 3479.

4. **Agarwala** R. C., (1987), Ph.D. Thesis, University of Roorkee, Roorkee (Presently Indian Institute of Technology Roorkee, IITR), India.

5. **Agarwala** R.C., Agarwala V., Sharma R., (2006), *Metal-Organic, and Nano-Metal Chemistry (SRINMC), Taylor & Francis Group, LLC,* **Vol.** 36, pp. 493.

6. **Agarwala** V., Baczewska J. K., (2005), *Defect and Diffusion Forum,* **vol.** 237, pp. 653

7. **Aharoni** A., (2000), "Introduction to the Theory of Ferromagnetism", 2nd Ed. *Oxford University Press,* New York.

8. **Ahmad** A.H., and Abdul Sada, J.W., (1990), *IE (I) Journal-ET,* **Vol.** 71, pp. 29.

9. **Alirezaei** S., Monirvaghefi, S.M., Salehi, M., Saatchi, A., (2007), *Wear,* **Vol.** 262, pp. 978.

10. **Apachitei** I., Duszczyk, J., Katgerman, L., Overkamp, P. J. B., (1998), *Scripta Materialia,* **Vol.** 38 (9), pp. 1347.

11. **Ataie** A., Heshmati-Manesh S., (2001), *J. Eur. Ceram. Soc.,* **Vol.** 21, pp. 1951.

12. **Ataie** A., Heshmati-Manesh S., Kazempour H., (2002), *J. Mater. Sci.,* **Vol** 37, pp. 2125.

13. *Baczewska J. K.,* Dymkowski T., Seetharaman S., (1996), *Adv. Powder. Metall. Part. Mater.,* **Vol.** 4 (15), pp.153.

14. **Bakonyi** I., Cziraki, A., Nagy I., Hosso M., (1986), *Z. Metallkd.,* **Vol.** 77, pp. 425.

15. **Balaraju** J.N., Sankaranarayanan T.S.N., Seshadri, S.K., (2003), *J. Appl. Electrochem.,* **Vol.** 33, pp. 807.

16. **Balaraju** J.N., Seshadri S.K., (1999), *Metal Finishing,* **Vol.** 97 (7), pp. 8.

17. **Bangwei** Z., Haowen X., Xiewen X., (1999), *Metal Finishing*, **Vol.** 97 (10), pp. 35.

18. **Baudrand** D.W., (1994), "Electroless Nickel Plating", ASM Hand book, *Surface Engineering*, **Vol.** 15, pp. 290.

19. **Born** E., Wolf E., (1984), "Principles of Optics", *Oxford, New York*, Pergamon Press.

20. **Bozzini** B., Cavallotti P.L., (1997), *Scripta Materialia*, **Vol.** 36 (11), pp.1245.

21. **Bozzini** B., Martin C., Cavalloti P.L., Lanzoni E., (1999), *Wear*, **Vol.** 225 (2), pp. 806.

22. **Brenner** A., (1963), "Electrodeposition of Alloys, Principle and Practice" **Vol.** II, *Academic Press*.

23. **Brenner** A., Riddell G., (1946), *Res. Nat. U. S. Bur. Stand.* **Vol.** 37, pp. 31.

24. **Brookshir** R.R., (1961), *U.S Patent No.* 2, 976, 180.

25. **Bueno** A.R., Gregori M.L., Nobrega M.C.S., (2008), *J. Magn. Magn. Mater,* **Vol.** 320 pp. 864.

26. **Cao** M. S., Song W. L., Hou Z. L., Wen B., Yuan J., (2010), *carbon*, **Vol** .48, pp. 788.

27. **Catuala** F., Molina F., Molina-Sabio M., Rodriguez-Reinoso F., Esteban A, (1995), *J. of Electrochem. Soc.*, **Vol.** 142 (12), pp. 4084.

28. **Chaitanya** K.M.V., (1994), *Ph.D. Thesis,* University of Roorkee (UOR), Presently Indian Institute of Technology Roorkee, Roorkee, India.

29. **Chaitanya** K.M.V., Agrawala, N.K., Gupta, S.C., Misra, P.S., (1995), *IE (I) Journal-ET,* **Vol.** 76, pp. 40.

30. **Che** R., Peng L. M., Duan X., Chen Q., Liang X., (2004), *Adv. Mater.* **Vol.**16, pp. 401.

31. **Che** R. C., Zhi C. Y., Liang C. Y., Zhou X. G., (2006), *Appl. Phys. Lett,* **Vol.** 88, pp. 033105.

32. **Chen** N., Mu G., Pan X., Gan K., Gu M., (2007), *Mater. Sci. Eng., B*, **Vol.** 139, pp. 256.

33. **Cheng** K.B., Ramakrishna S., Lee K.C., (2000), *Composites Part A,* **Vol.** 31, pp. 1039.

34. **Cheong,** W. J., Luan, B.L., Shoesmith, D.W., (2004), *Appl. Surf. Sci,* **Vol.** 229, (1), pp. 282.

35. Choi S.H., Oh J.H., Ko T., (2004), *J. Magn. Magn. Mater*, **Vol.** 272, pp. 2233.

36. Criado J.M., Ortega A., (1987), *Acta Metal.* , **Vol.** 35 pp. 1715.

37. Crobu M., Scorciapino A., Elsener B., Rossi A., (2008), *Electrochim. Acta*, **Vol.** 53(8), pp. 3364.

38. Cullity B.D., Graham C.D., (2008), "Introduction to Magnetic Materials", second ed., *John Wiley & Sons*, New Jersey.

39. Cziraki A., Fogarassy B., Bakonyi I., Tompa K., Hegedns Z., (1980), *J. De Physique*, Collogue C8, Suppliement au no. 8, tome 41, aout C8 – 141.

40. Das N.C., Khastgir D., Chaki T.K., Chakraborty A., (2000), *Composites: Part A*, **Vol.** 31, pp. 1069.

41. Davoodi A., Hashemi B., (2011), *J. Alloys Compd*, **Vol.** 509, pp5893.

42. Dishovski, N., Petkov, A., Nedkov, Razkazov IV, (1994), *IEEE Transaction on Magnetics*, **Vol.** 30 (2), pp. 969.

43. Doyle C.D., (1962), *J Appl. Polym Sci.*, **Vol.** 6, pp. 639.

44. Dujardin E., Ebbesen T. W., Hiura H., Tanigaki K., (1994), *Science*, , **Vol.** 265, pp. 1850.

45. Emerson W.H., (1973), *IEEE Trans. Antenn. Propag*, **Vol.** 21(4), pp. 484.

46. Fan Z., Luo G., Zhang Z., Zhou L., Wei F., (2006), *Mater. Sci. Eng., B*, **Vol.** 132, pp 85.

47. Fannin P. C., Marin C. N., Malaescu I., Stefu N., Vlazan P., Novaconi S., Sfirloaga P., Popescu S., Couper C., (2011), *Mater. Des.* , **Vol.** 32, pp.1600.

48. Fante R. L.; McCormack, (1988), M. *IEEE Transactions on Antennas and Propagation*, **Vol.** *36*, pp. 1443.

49. Feldstein N, (1983), *Metal Finishing*, **Vol.** 82 1 A(2), pp. 408.

50. Franco A., Silva F. C., (2010), *Appl. Phys. Lett*, **Vol.** 96, pp. 172505.

51. Friedman H., (1963), *J. polym. Sci.,* **Vol.** 6C, pp. 183.

52. Fu Y. P., Lin C. H., (2005), *J. Alloys Compd*, **Vol.** 386, pp 222.

53. Gaurilov G. G., (1979), "Chemical (Electroless) Nickel plating", *Porticullis Press*, *Redhill*, England.

54. Gaylor K. (1989) "Radar Absorbing Materials - Mechanisms and Materials," DSTO Materials Research Laboratory.

55. **Ghasemi A.**, Morisakob A., (2008), *J. Magn. Magn. Mate.*, **Vol.** 320, pp. 1167.

56. **Giannakopoulou** T., Kompotiatis L., Kontogeoragakos A., Kordas G., *(2002), J. Magn. Magn. Mater* **Vol.** 246, pp. 360.

57. **Gillespie P.**, (1996), "Electroless Nickel Coatings: Case Study", Surface Engineering Casebook, Edited by Burnell-Gray J. S. and Datta P. K., *Woodhead Publishing Limited,* pp. 49.

58. **Gorbunova** K. M., Nikiforova A. A., Sadkov G. A., (1966), *Electrochemistry (ed.) Melnikova,* M. M., pp. 41.

59. **Grosjean A.**, Rezrazi M., Tachez M., (1997), *Surf. Coat. Technol,* **Vol.** 96 (2-3), pp. 300.

60. **Grunberger W.**, Springman B., Brusberg M., Schmit M., Jahnke R., (1991), *J. Magn. Magn. Mater.,* **Vol.** 101, pp.173.

61. **Gupta R. K.**, Pant B., Agarwala V., Agarwala R. C., Sinha P. P., (2009), *Trans. IIM,* Vol. 62(1), pp. 21.

62. **Gupta** S.C., Agarwal N.K., Chaitanya K. M.V., (1993), *IE (I) Journal-ET,* **Vol.** 39 (3), pp. 197.

63. **Haijun** Z., Xi, Y., Liangying Z., (2002), *J. Magn. Magn. Mater.,* **Vol.** 241, pp. 441.

64. **Halpren O.**, (1945) *U.S. Patent* 2 92.

65. **Harikrishnan K.**, John S., Srinivasan K.N., Praveen J., Ganesan M., Kavimani P.M., (2006), *Metall. Mater. Trans. A,* **Vol.** 37A, pp. 1917.

66. **Hasab** M.G., Ebrahimi S.A.S., Badiei A., (2007), *J. Eur. Ceram. Soc.,* **Vol.** 27, pp. 3637.

67. **Hasab** M.G., Ebrahimi S.A.S., Badiei A., (2007), *J. Eur. Ceram. Soc.,* **Vol.** 310, pp. 2477.

68. **Henry J.**, (1985), *Metal Finishing,* **Vol.** 82 (10), pp. 45.

69. **Hessien** M.M., Rashad M.M., El-Barawy K., (2008), *J. Magn. Magn. Mater.,* **Vol.** 320, pp. 336.

70. **Holubova J.**, Cernosek Z., and Cernoskova E., (2000), *J. of Therm. Anal. Cal.,* **Vol.** 62 pp. 715.

71. **Hou** C., Li T., Zhao T., Zhang W., Cheng Y., (2011), *Mater. Des.,* **Vol.** 33, pp. 413.

72.   **Hou** X., Chou K. C., Zhong X., Seetharaman S. (2008), *J. Alloys Compd.*, Vol. 465, pp. 90.

73.   **Hu** J. Q., Bando Y., Liu Z., (2003), *Adv. Mater.* (Weinheim, Ger.) **Vol. 15**, pp. 1000.

74.   **Hur** N. H., Park J. Y., Dho J., Kim S. J. and Lee E. K., (2004), *IEEE Trans.Magn.* **Vol. 40**, pp. 2790.

75.   **Hwang** Y., (2006), *Mater. Lett.,* **Vol. 60**, pp. 3277.

76.   **Iijima Y.,** Houjou Y., Sato R., (2000), *Proceeding of 2001 IEEE International Symposium on Electromagnetic Compatibility,* **Vol.** 21, pp. 547.

77.   **Ishino K.,** Narumiya Y., (1987), *Ceramic Bulletin,* **Vol.** 66 (10), pp. 1469.

78.   **Jaggard** D. L., Enghcta N., **(1989),** *Elect. Lett.,* **Vol.** *25,* pp. 173.

79.   **Jena** A. K., Chaturvedi M. C., (1992), Phase transformation in materials, *Prentice Hall Inc., Englewood Cliff,* New jersey 07632.

80.   **Jhao** D. L., Zhao H. S., Zhou W. C., (2001), *Physica E.,* **Vol. 9,** pp.679.

81.   **Johnk** C.T.A., (1988), "Elements of Electromagnetic Fields and Waves" *John Wiley & Sons.*

82.   **Joraid** A. A. (2005), *Thermochim. Acta.* **Vol.** 436, pp. 78.

83.   **Jung** H. O., Kyung S. O., Chun G. K., Chang S. H., (2004), *Compos. Part B: Eng.* **Vol.** 35 pp. 49.

84.   **Kasevich** R. S., Broderick F., (1993), *US Patent* 5223849.

85.   **Khanna** R., (1983), *Pramana,* **Vol.** 20 (6), pp. 503.

86.   **Khanna** R., (1983), *Pramana,* **Vol.** 20 (4), pp. 279.

87.   **Khoperia T. N.,** (2003), *Microelectron. Eng,* **Vol.** 69, pp. 384.

88.   **Kim D.I.,** Chung S.M., Park Y.W., Naito Y., (1990), *J. Korean Inst. Navigation,* **Vol.** 14, pp. 9–19.

89.   **Kim D.Y.,** Chung Y.C., Kang T.W., Kim H.C., (1996), *IEEE Transaction on Magnetics,* **Vol.** 32 (2), pp. 555-558.

90.   **Kim** J.B., Lee S. K., Kim C. G., (2008), *Compos. Sci. Technol.,* **Vol.** 68 pp 2909.

91.   **Kim** J. H., Kim S. S., (2011), *J. Alloys Compd,* **Vol.** 509, pp. 4399.

92.   **Kim, S.S.,** Kim, S.T., Yoon, Y.C., and Lee, K.S., (2005), *J. Appl. Phys.* **Vol.** 97, pp. 10F905.

93.   **Kittel, C.,** (1971), "Introduction to Solid State Physics", *Wiley.*

94. **Knott, E.F.,** (1977), *IEEE Transaction on Antennas and Propagation,* **Vol.** Ap-27 (6), pp. 698.

95. **Knott** EF, Shaeffer JF, Tuley MT. (1985), *Radar cross section, Artech House,* Norwood:.

96. **Knott** E.F., Shaeffer J.F., Tuley M.T., (1993) in: E.F. Knott (Ed.), *Radar Cross Section, Artech House Inc.,* Norwood.

97. **Kojima, H.,** in: E.P Wohlfarth (Ed.), (1982), "Ferromagnetic Materials", **Vol.** 3, *North Holland New York (Chapter 5).*

98. **Kotsuka** Y., Yamazaki H., (2000), *IEEE Trans. Electromagn. Comat. ,* **Vol.** 42, pp. 116.

99. **Kumar, A.,** (1987), "Acetylene Black Rubber Target RCS", *Microwave & RF,* pp. 85.

100. **Kwon** H.J., Shin J.Y., Oh T.II., (1994), *J. Appl. Phys.,* **Vol.** 75, pp. 6109.

101. **Lederer, P. G.,** (1986), "An Introduction to Radar Absorbent Materials (RAM)," *Royal Signals and Radar Establishment,* Malvern.

102. **Lee** R. S., Kim H., Fisher J. E., Thess A., Smalley R. E., (1997), *Nature,* **Vol. 388,** pp. 255.

103. **Li** X., Gong, R., Feng, Z., Yan, J., Shen, X., and He., H., (2006), *J. Am. Ceram. Soc.,* **Vol.** 89 (4), pp. 1450.

104. **Li** Y., Wang R., Qi F., Wang C., (2008), *Appl. Surf. Sci,* **Vol.** 254, pp. 4708.

105. **Liu** J.R., Itoh M., Machida K.I., (2006), *Appl. Phys. Lett.* **Vol.** 88, pp 062501.

106. **Liu** L, Duan Y., Lixin M, Liu S., Yu Z., (2010), *Appl. Surf. Sci.,* **Vol.** 257, pp 842.

107. **Liu** X.G., Li B., Geng D.Y., Cui W.B., Yang F., Xie Z.G., Kang D.J., Zhang Z.D., (2009), *Carbon,* **Vol.** 47, pp 470.

108. **Liu** X., Zhang Z., Wu Y., (2011), *Composites: Part B,* **Vol.** 42, pp 326.

109. **Liu** Y., Drew M.G.B, Wang J.P., (2010), *J. Magn. Magn. Mater.,* **Vol.** 322 (3), pp. 366.

110. **Liu** Y., Zhanga Z., Xiao S., Qianga C., Tiana L., Xu J., (2011), *Appl. Surf. Sci.,* **Vol.** 257, pp. 7678.

111. **Maeda** T., Sugimoto S., Kagotani T., Tezuka N., Inomata K., (2004), *J. Magn. Magn. Mater.,* **Vol.** 281, pp. 195.

112. **Mahoney M.W.**, Dynes P.J., (1985), *Scripta Metallurgica*, **Vol.** 19, pp. 539.

113. **Makeiff** D. A., Huber T., (2006), *Synth. Met.* **Vol.**156, pp. 497.

114. **Mallory, G. O.**, (1974), "Influence of the Electroless Plating Bath on the Corrosion Resistance of the Deposits, *Reprinted Courtesy Alied-Kellite products Division*, The Richardson Company, Des laines, Illinois 60018. Originally presented at the 61st Annual Technical Conference, June 18, 1974, American Electroplater's Society, Chicago, Illinois.

115. **Mallory, G. O.**, (1979), "The Electroless Nickel-Myths and Facts" *Reprinted Courtesy Allied- Kellite Products Division*, Originally Presented at Electroless Nickel Conference II, 1980 Cincinati, Ohio.

116. **Manivasakan** P., Rajendran V., Rauta P. R., Sahu B. B., Panda B. K., (2009), *Advanced Materials Research* **Vol.** 67, pp. 143.

117. **Masala** O., Hoffman D., Sundaram N., Page K., Proffen T., Lawes G., Seshadri R., (2006), *Solid State Sci.,* **Vol.** 8, pp. 1015.

118. **Matsumoto M.**, Miyata Y., (1996), *J. Appl. Phys.* **Vol.** 79 (8), pp. 5486.

119. **Meshram M.R.**, Agrawala N.K., Sinha B., Misra P.S., (2002), *Indian J. Radio Space Phys.* **Vol.** 31, pp. 225.

120. **Meshram M.R.**, Agrawala N.K., Sinha B., Misra P.S., (2004), *J. Magn. Magn. Mater.*, **Vol.** 271, pp. 207.

121. **Meyer E.**, Severin H., (1954), Umlauft, G. *Zeitschrift fur Physik*, **Vol.** 138, pp. 465.

122. **Meyer E.**, Severin H., (1956), *Zeitschrift fur angewandte Physik,* **Vol.** 8, pp. 105.

123. **Micheli** D., Apollo C., Pastore R., Marchetti M., (2010), *Compos. Sci. Technol.* Vol. 70, pp 400.

124. **Mishra** D., Anand S., Panda R.K., Das R.P., (2004), *Mater. Chem. Phys.* **Vol.** 86 (1), pp. 132.

125. **Miyata Y.**, Matsumoto M., (1997), *IEEE Transaction on Magnetics*, **Vol.** 33 (5), pp. 3427.

126. **Mohsen** Q. (2010), J. Alloys Compd, **Vol.** 500 pp 125.

127. **Moonir-Vaghefi** S. M., Saatchi A., Hedjazi J., (1997), *Z. Metallkde.*, **Vol.** 88 (6), pp. 498.

128. **Motojima** S., Noda Y., Hoshiya S., Hishikawa Y., (2003), *J. Appl. Phys.*, **Vol.** 94 (4), pp. 2325.

129. **Munk** B. A., (2000), *Frequency Selective Surfaces: Theory and Design*; John Wiley & Sons Inc.: New York.

130. **Musal** H. M., Jr., Smith, D.C., (1990), *IEEE Transaction on Magnetics,* **Vol.** 26 (5), pp. 1462.

131. **Natio** Y., Suetake K., (1971), *IEEE Trans. Microwave Theory Tech.*, **Vol.** 19(1), pp. 65.

132. **Necula** B.S., Apachitei I., Fratila-Apachitei L.E., Teodosiu C., Duszczyk J., (2007), *Journal of Colloid and Interface Science*, **Vol.** 314 (2, 15), pp. 514.

133. **Nedkov** I., Petkov A., (1990), *IEEE Transaction on Magnetics,* **Vol.** 26 (5), pp. 1483.

134. **Nie** *Y.,* He, H.H., Feng, Z.K., Zhang, X.C., Cheng, X.M., (2006), *J. Magn. Magn. Mater.,* **Vol.** 303, pp. 423.

135. **Nortier** J. R., Van der Neut, C.A., Baker, D.E., (1987), *Microwave Journal,* 219.

136. **Oh** J. H., Oh K. S., Kim C. G., Hong C. S., (2004), *Composites: Part B,* **Vol.** 35, pp 49.

137. **Odekerken** (1966), Brit. Pat. 1,041,753, *U. S. Pat.* 3,644,183 and DDR Pat., **Vol.** 41, pp. 406.

138. **Ostwald** W. Z., (1900), *Phys. Chem.* **Vol.** 34, pp 495.

139. **Pai** B.C., Rohatgi P.K., (1975), *Mater. Sci. Eng.,* **Vol.** 21, pp.161.

140. **Pan** *X.,* Mu G., Shen H., Gu M., (2007), Appl. Surf. Sci. **Vol.** 253, pp. 4119.

141. **Pant** B., Agarwala V., Agarwala R. C., Sinha P. P., (2007), *Trans. IIM,* **Vol. 60,** pp. 925.

142. **Park** K. Y., Han J. H., Lee S. B., Kim J.B., Yi J. W., Lee S. K., (2009), *Compos. Sci. Technol.,* **Vol.** 69, pp 1271.

143. **Park** K. Y., Han J. H., Lee S. B., Yi J. W., (2011), *Composites: Part A.* **Vol.** 42, pp. 573.

144. **Park** S.H., Lee D.N., (1988), *J. Mater. Sci.,* **Vol. 23,** pp. 1643.

145. **Patton** C.E., (1967), *Ph.D Thesis,* 1967, Cal Tech.

146. **Pedraza** A. J., Godbole M. J., (1990), *Scripta Metallurgica,* **Vol.** 24, pp. 1185.

147. **Peipmann** R., Thomas J., Bund A., (2007), *Electrochim. Acta,* **Vol.** 52 (19-25), pp. 5808.

148. **Peng** C.H., Hwang C.C., Wan J., Tsai J.S., Chen S. Y., (2005), *Mater. Sci. Engg. B,* **Vol.** 117, pp. 27.

149. **Phang** S. W., Tadokoro M., Watanabe J., Kuramoto N., (2008), *Synth. Met.,* **Vol. 158,** pp. 251.

150. **Pitkethly** M.J., (1992), *Low Profile Absorber and Scatters IEE Colloquium,* **Vol. 7,** pp. 1.

151. **Pozar** D. M., (1998), "Microwave Engineering", *Second Edition, Chapter 9, John wiley & Sons,* New York.

152. **Primc** D., Makovec D., Lisjak D., Drofenik M., (2009), *Nanotechnology* **Vol. 20,** pp 315605.

153. **Qi** X., Yang Y., Zhong W., Deng Y., Au C., Du Y., (2009), *J. Solid State Chem.,* **Vol.** 182, pp. 2691.

154. **Qiang** C. , Xu J., Zhang Z., Tian L., Xiao S., Liu Y., Xu P., (2010), *J. Alloys Compd,* **Vol. 506, pp.** 93.

155. **Qiu** J.X., Wang C.Y., Gu M.Y., (2004), *Mater. Sci. Eng. B.* **Vol.**112, pp. 1.

156. **Radhakrishnan** J. K., Pandian P. S., Padaki V. C., Bhusan H., Rao K. U.,B., Xie J., Abraham J. K., Varadan V. K., (2009), *Appl. Surf. Sci.,* **Vol.** 225, pp 6325.

157. **Raghuraman** K., Pillarsetty N., Prabhu K.R., Katti K.K., Katti K.V., (2004), *Inorg. Chim. Acta,* **Vol.** 357 (10), pp. 2933.

158. **Rajagopal** I., in Sudarshan, T.S., (Ed.), 1989, "Surface Modification Technologies: An Engineering Guide" *Marcel Dekker,* New York

159. **Rajendran** V., (2009), *Advanced Materials Research,* **Vol. 67,** pp. 71.

160. **Rauf** H., Pichler T., Knupfer M., Fink J., Kataura H., (2004), *Phys. Rev. Lett.* **93,** pp. 096805.

161. **Ruan** S., Xu B., Suo H., Wu F., Xiang S., Zhao M., (2000), *J. Magn. Magn. Mater.,* **Vol.** 212, pp. 175.

162. **Ruoff** R. S., Lorents D. C., Chan B., Malhotra R., Subramoney S., (1993), *Science,* **Vol.** 259, pp. 346.

163. **Sadiku** M.N.O., (1995) "Engineering of Electromagnetic" second edition by Oxford University Press.

164. **Salisbury** W.W., (1952), "Absorbent body for Electromagnetic Waves", *U.S. Patent 2 599 944.*

165. **Scade** H.A., (May 1945) "Schornsteinfeger", *U.S. Tech. Mission Europe, Tech. Rep 90-45 Ad-47746.*

166. **Severin** H., (1956), *IRE Trans. Antennas & Propagat., AP-4,* 385.

167. **Shacham** D. Y., Inberg A., Sverdlov Y., Bogush V., Croitoru N., Moscovich H., Freeman A., (2007), *Electrochim. Acta.*, **Vol.** 48 (20-22), pp.2987.

168. **Shafi** K. V. P. M., Gedanken A., (1999), *Nano Srmchmd Materials*, Vol. 12, pp. 29.

169. **Sharbati** A., Choopani S., Azar A.-M., Senna M., (2010), *Solid State Commun*, **Vol.** 150, pp. 2218.

170. **Sharma** R., Agarwala R.C., Agarwala V., (2008), *Mater Lett.*, **Vol.** 62 pp 2233.

171. **Sharma** R., Agarwala R.C., Agarwala V., (2007), *J. Magn. Magn. Mater.*, **Vol.** 312 pp 117.

172. **Sharma** R., Agarwala R.C., Agarwala V., (2008), *J. Nano Res.*, **Vol.** 2, pp 91.

173. **Sharma** S. B., Agarwala R.C., Agarwala V., Ray, S., (2002), *Surf. Eng.*, **Vol.** 18, pp. 344.

174. **Sharma** S. B., Agarwala R.C., Agarwala V., Ray, S., (2002), *Journal of Materials and Manufacturing Processes*, Marcel Dekkar Publication, **Vol.** 17(5), pp. 637.

175. **Sharma** S. B., Agarwala R.C., Agarwala V., and Satyanarayana K.G., (2005), *Metall. Trans. B*, **Vol.** 36 (1), pp. 23.

176. **Shen** G., Xu M., Xu Z., (2007), *Mater. Chem. Phys*, **Vol.** 105, pp 268.

177. **Shibli** S.M.A., Dilimon V.S., (2007), *Int. J. Hydrogen Energy*, **Vol.** 32 (12), pp. 1694.

178. **Shin** J.Y., Oh J.H., (1993), *IEEE Transaction on Magnetics*, **Vol.** 29 (6), pp. 3437.

179. **Shirk** B. T., R. W., (1969), *J Appl. Phys.* Vol., 40, pp 1294.

180. **Simmons** A., Emeson, W., (1953), *Tele-Tech*, **Vol.** 12 (7).

181. **Singh** P., Babbar V.K., Razdan A., Srivastava S.L., Puri R.K., (1999), *Mater. Sci. Eng. B*, **Vol.** 67, pp. 132.

182. **Smith** J., Wijn H.P.J., (1959), "Ferrites", *Philips Technical Library*, pp. 177.

183. **Soon** L. P., Gupta M., (2001), *J. Mater. Sci. Lett* **Vol.** 20, pp. 323.

184. **Srivastava** A., Mohan S., Agarwala V., Agarwala, R.C., (1992), *Z. Metallkunde,* **Vol.** 8(3), pp. 251.

185. **Srivastava** A., Mohan S., Agarwala V., Agarwala, R.C., (1992), *Z. Metallkunde* **Vol.** 8 (4), pp. 254-257.

186. **Srivastava** G.P., Singh P.P., Nath J., (1992), *1992 Microwave Conference Asia Pacafic*, **Vol.** 1, pp. 239.

187. **Stadeley** K.J.. (September 1971), "Oxide Magnetic Materials", *Oxford University Press,* Ely House, London, Chapter 2.

188. **Stonier** RA. (1991), Stealth aircraft and technology from World War II to the Gulf (Part I: History and Background). *SAMPE J;*27(5): pp. 9.

189. **Sunny** V., Kurian P., Mohanan P., Joy P.A., Anantharaman M.R., (2010), *J. Alloys Compd.* **Vol.** 489 pp 297.

190. **Suslick** K.S., Ultrasound: Its chemical, Physical and Biological Effects, *VCH, Weinheim,* 1988.

191. **Tabatabaie F.,** Fathi M.H., Saatchi A., Ghasemi A., (2009), *J. Alloys Compd,* **Vol.** 470, pp 332.

192. **Takabayashi H.,** Kato Y., Kagotani T., Book D., Sugimoto S., Homa M., Ota h., Houjou Y., (2000), *Material transaction JIM.,* **Vol.** 41 (9), pp. 1184.

193. **Tang X.,** Zhao B.Y., Tian Q., Hu K.A., (2006), *J. Phys. Chem. Solids,* **Vol.** 67, pp. 2442.

194. **Teng** L., Noguchi S., Seetharaman S., (2007), *Metall. Mater. Trans. B,* **Vol.** 38B, pp. 55.

195. **Thakur** S. K., Kwee G. T., Gupta M. (2007), *J Mater Sci.,* 42:10040–10046 DOI 10.1007/s10853-007-2004-0.

196. **Ting** T.H., Yu R.P., Jau Y.N., (2011), *Mater. Chem. Phys.,* **Vol.** 126, pp. 364.

197. **Tyagi** S., Agarwala R. C., Agarwala V., (2010), *Trans. of Ind. Inst. of Metals.* **Vol.** 63, pp. 15

198. **Tyagi** S., Agarwala R.C., Agarwala V., (2010), *J. Nano Res.* **Vol.** 10, pp. 19.

199. **Tyagi** S., Baskey H. B, Agarwala R. C., Agarwala V. (2011), Shami T. C., *J. Electron. Mater.,* doi: 10.1007/s11664-011-1693-y.

200. **Tyagi** S., Baskey H. B, Agarwala R. C., Agarwala V., Shami T. C. (2011), *Transaction of Indian Institute of Metals,* **Vol.** 64 (3), pp. 271.

201. **Tyagi** S., Baskey H. B, Agarwala R. C., Agarwala V., Shami T. C. (2011), *Ceram. Int.,* doi:10.1016/j.ceramint.2011.04.012.

202. **Tyagi** S., Agarwala R.C., Agarwala V. (2010), *J. Mater. Sci. - Mater. Electron,* doi 10.1007/s10854-010-0265-x.

203. **Tyagi** S., Agarwala R.C., Agarwala V. (2009), *International Journal of Material Science*, **Vol.** 4, pp 125.

204. **Tyagi** S., Agarwala R.C., Agarwala V. (2009), *Advance Materials Research,* **Vol.** 67, pp 203.

205. **Ugarte** D., Chatelain A., de Heer W. A., (1996), *Science*, **Vol.** 274, pp. 1897.

206. **Vaia** R.A., Giannelis, E.P., (2001), *MRS Bulletin,* **Vol.** 26, pp. 392.

207. **Van** D. P., Barel G., Schweicher A.,, E. *Antennas and Propagation, IEEE Transactions on,* **1989**, *37*, 1327.

208. **Varadan** V. K., Varadan V. V., (1990), *US Patent* No. **Vol.** 4, pp. 948.

209. **Verma** A., Mendiratta R.G., Goel T.C., Dube D.C., (2002), *J. Electroceram.*, **Vol.** 8, pp. 203.

210. **Vinoy** K.J., Jha R.M., (1996), *Boston: Kluwer Academic Publishers.*

211. **Vishwanathan** B., Murthy V.R.K., (1990), Ferrite Materials Science and Technology, *Narosa,* New Delhi:.

212. **Wallace** J. L., (1993), *IEEE Transaction on Magnetics,* **Vol.** 29 (6), pp. 13.

213. **Wang** X, Sohn H. Y, Schlesinger, M. E., (1994), *Mater Sci Eng A.* **Vol.** 186, pp. 151.

214. **Wang** T., Liu R. Y., Zhu M. L. And Zhang J. S., (2002), *J. of Therm. Anal. Cal.,* **Vol.** 70, pp. 507.

215. **Wang** L.X., Huang Q., Mu L., Zhang Q.T., (2007), *J. Rare Earths*, **Vol.** 25 (2), pp. 216.

216. **Wang** G., Chen X., Duan Y., Liu S., (2008), *J. Alloys Compd*, **Vol.** 454, pp 340.

217. **Wang** W., Li Q., Chang C., (2011), *Synth. Met.,* **Vol.** 161, pp 44.

218. **Wilhelm** H.Van Aulock, (1965), "Hand Book of Microwave Ferrite Materials", *Academic Press New York*, London, pp. 269, 451.

219. **Wright** R.W., and Emerson, W.H., (1954), "Broadband Absorbing Materials for Use in Darkrooms", *in Pro. Con. Radio Interface Reduction.*

220. **Wu** K.H., Ting T.H., Liu C.I., Yang C.C., Hsu J.S., (2008), *Compos. Sci. Technol.*, **Vol.** 68, pp. 132.

221. **Wu** K.H., Ting T.H., Wang G. P., Ho W.D., Shih C.C., (2008), *Polym. Degrad. Stab.* **Vol.** 93, pp 483-488.

222. **Xie** J., Teng L. Chen N., Seetharaman S.,(2007), *Metall. Mater. Trans. B,* **Vol.** 38B, pp. 93.

223. **Xu** H., Yanga Z., Lia M.K., Shia Y.L., Huanga Y., Lia H.L., (2005), *Surf. Coat. Technol.*, **Vol.** 191, pp.161.

224. **Yang** Y., Zhang, B., Weidong X., Yingbing S., Ningsheng Z., Huaixian L., (2003), *J. Magn. Magn. Mater.*, **Vol.** 256, pp. 119.

225. **Yashuhiro** K., Norinobu Y., Ichiro, F., (1989), *IEEE International Symposium on Electromagnetic Compatibility,* **Vol.** 31 (3), pp. 323.

226. **Yu** X., Wang H., Yang Z., Yin P., Xin X., (2000), *Appl. Surf. Sci.*, **Vol.** 158, pp.335.

227. **Yusoff** A.N., Abdullah M.H., (2004), *J. Magn. Magn. Mater.* **Vol.** 269, pp. 271.

228. **Zeng** H., Sun S.H, Li J., Wang Z.L, Liu J.P., (2004), *Appl. Phys. Lett.* **Vol.** 85, pp. 792

229. **Zhan** Y., Zhao R., Lei Y., Meng F., Zhong J., Liu X., (2011), *Appl. Surf. Sci*, **Vol.** 257, pp. 4524.

230. **Zhang** L., Li Z., (2009), *J. Alloys Compd*, **Vol.** 469, pp 422.

231. **Zhang** L., Hong Z., (2009), *Mater. Lett*, **Vol.** 63, pp. 272.

232. **Zhang** X. X., Wei H. L., Zhang Z. Q., Zhang L. Y., (2001), *Phys. Rev. Lett.* **Vol.** 87, pp. 157203.

233. **Zhang** X. F., Dong X. L., Huang H., Liu Y. Y., Wang W. N., Zhu X. G., Lv B., Lei J. P., Lee C. G., (2006), *Appl Phys Lett.*, **Vol.** 89, pp. 053115.

234. **Zhao** D. L, Li X., Shen Z. M., (2009), *J. Alloys Compd*, **Vol.** 471, pp. 457.

235. **Zhao** Dong-Lin, Li X. , Shen Z. M. (2008), *Compos. Sci. Technol*, **Vol.** 68, pp. 2902.

236. **Zhao** H., Sun X., Du C. M. J., (2009), *Physica B*, **Vol.** 404, pp. 69.

237. **Zheng** Z. Xu B. Huang L. He L. Ni X., (2008), *Solid State Sci.,* **Vol.** 10, pp 316.

238. **Zhi** C. Y., Zhong D. Y., Wang E. G., (2004), *Chem. Phys. Lett.*, **Vol.** 381, pp. 715.